Properties of Quark Gluon Plasma at Weak and Strong Coupling

by

Mindaugas Lekaveckas

Submitted to the Department of Physics
in partial fulfillment of the requirements for the degree of

Doctor of Philosophy in Physics

at the

MASSACHUSETTS INSTITUTE OF TECHNOLOGY

June 2014

Signature redacted

Author .....
Department of Physics
May 23, 2014

Signature redacted

Certified by .....
Krishna Rajagopal
Professor of Physics
Thesis Supervisor

Signature redacted

Certified by .....
Hong Liu
Associate Professor of Physics
Thesis Supervisor

Signature redacted

Accepted by ..
Krishna Rajagopal
Associate Department Head for Education

Properties of Quark Gluon Plasma at Weak and Strong Coupling

by

Mindaugas Lekaveckas

Submitted to the Department of Physics
on May 23, 2014, in partial fulfillment of the
requirements for the degree of
Doctor of Philosophy in Physics

Abstract

In this thesis properties of probe particle traveling through quark gluon plasma as created in heavy ion collisions are investigated. In the first part, probability distribution $P(k_\perp)$ is calculated for an energetic parton that propagates for a distance L through a weakly coupled medium without radiating to pick up transverse momentum $k_\perp$. Results for $P(k_\perp)$ in weakly coupled quark gluon plasma are compared to expectations from holographic calculations that assume a plasma that is strongly coupled at all length scales. It is found that the shape of $P(k_\perp)$ at modest $k_\perp$ may not be very different in weakly coupled and strongly coupled plasmas, but $P(k_\perp)$ must be parametrically larger in a weakly coupled plasma than in a strongly coupled plasma at large enough $k_\perp$.

In the second part of the thesis the drag force acting on a heavy quark propagating through the matter which is far from or close to equilibrium in a strongly coupled gauge theory that can be analyzed holographically is computed and studied. It is found that fluid velocity and temperature gradients affect the drag force but does not substantially modify it as long as fluid is close to equilibrium. When quark is away from equilibrium, the modification of drag force manifests in terms of the delay time with respect to equilibrium expectations. These aspects are illustrated for the example of two colliding shockwaves where fluid is far from equilibrium at early times as well as for any fluid close to equilibrium in which case drag force expressions are obtained analytically.

Thesis Supervisor: Krishna Rajagopal
Title: Professor of Physics

Thesis Supervisor: Hong Liu
Title: Associate Professor of Physics

Acknowledgments

For all the experiences I first of all would like to thank my advisors Krishna Rajagopal and Hong Liu who continuously challenged and guided me throughout the years. I would also like to thank Krishna for active mentoring and for support when solving problems outside of research.

I thank my collaborators Paul Chesler, Francesco D'Eramo, Christopher Lee and Andrey Sadofyev from whom I learnt a lot and had great experiences while working together. Also, I would like to thank my thesis committee members Iain Stewart and Bolek Wyslouch for their interest in my work.

I thank all the people at Center for Theoretical Physics for creating friendly and motivating environment which is more than ideal for involved problem solving. I thank fellow CTP students Mark Mezei, Ethan Dyer, Deniele Bertoilini, S. Josephine Suh, Ian Moult, Lina Necib and many others for making PhD experience fun and full of great moments.

I would like to thank all people who were involved with the International Fulbright Science & Technology Award, their strong support and commitment made my arrival and subsequent studying as smooth and enjoyable as possible. I am thankful for fellow Fulbright friends Rainer Küngas, Jonathan Ramseder, Allan-Hermann Pool and many others for sharing the difficulties and joys along the way.

Finally, I thank my family. I thank my sister Kristina Lelešienė for providing her perspective on various issues throughout the studies and I especially thank my parents Vytautas and Janina Lekaveckai for continued support, encouragement and much more.

Contents

List of Figures

Preamble

Over the years of PhD studies I had opportunity to work on multiple projects which are described in this thesis in great detail. All topics have a common purpose: to provide better description of quark gluon plasma created in the heavy ion collisions by analyzing how energetic probe partons (quarks or gluons) interact with the medium at finite temperature.

In a fraction of heavy ion collision events, a hard interaction takes place and a pair of energetic partons is created with each parton outgoing in opposite directions. If the hard interaction takes place at the periphery of the nuclei, one particle escapes the collision forming a jet as if in a proton-proton collision while the second particle travels through the created medium and typically undergoes multiple interactions. If the original particle has enough energy and does not thermalize after interactions, the particle forms a jet with energy smaller than the jet which just escaped the medium. There are multiple effects on which the properties of the modified jet depends (*e.g.*, in medium fragmentation functions) but physically the most important is the interaction of the particle with the medium before the jet is formed. Comparing the properties of these two jets we can indirectly learn about the in-medium scattering and energy loss which encodes the information about the quark gluon plasma.

The interaction strength governing the scattering of the probe particle depends on the temperature T that can be assigned to the medium. Most of the kicks that a particle receives are of order of T, but there are rare scattering events with transverse momentum much higher than T. Because of the asymptotic freedom of QCD, kicks with large enough transverse momentum are expected to be governed by weak coupling. Depending on the value of T, the dominant scatterings might be at weak

coupling as well, but at current heavy ion collisions the temperature of original fireball might not be high enough to guarantee weak coupling. Therefore, it is important to understand probe particle interactions with medium at both weak and strong coupling.

In the first part of the thesis, the weak coupling is assumed and transverse momentum broadening $P(k_\perp)$ is evaluated. Previously in the literature, low and high $k_\perp$ limits were investigated using various theories, but in this work calculation is done from first principles using thermal field theory techniques in all transverse momentum $k_\perp$ region. In the end of part I, new calculations at weak coupling are compared to previously obtained $P(k_\perp)$ in strongly coupled $\mathcal{N} = 4$ SYM theory. It is found that at large $k_\perp$ scattering probabilities at weak and strong coupling are substantially different – large $k_\perp$ scattering at weak coupling are much more likely than at strong coupling. This observation suggests that once clear experimental measurements become feasible to identify events with large $k_\perp$ scatterings (with respect to the original hard parton), it will be possible to confirm or disconfirm weak coupling nature of these scattering events. The discussion in the first part of the thesis is largely based on the paper [1] and on the conference proceedings [2].

In the second part of the thesis, quark energy loss far from equilibrium and close to equilibrium at strong coupling is considered. Since it is currently not possible to evaluate the quark energy loss rate in strongly coupled QCD, conformal $\mathcal{N} = 4$ SYM theory is used with the help of holographic principle. In short, holographic principle (also known as AdS/CFT correspondence) says that conformal field theory at strong coupling in 4 dimensions and with large number of colors N_c is described by dynamics of the classical string theory in 5 dimensional anti de Sitter space-time. In this work, pre-equilibrium quark energy loss at strong coupling is calculated for the first time for dynamical medium modeling the collision of two heavy ions. It is found that pre-equilibrium energy loss rate is not substantially different from the equilibrium energy loss rate. It is also found that fluid velocity gradients play substantial role for heavy quark energy loss when quark is traveling close to the ion collision axis. Motivated by this observation, the effect of fluid gradients is investigated for general fluid that

is locally close to equilibrium. When results are applied to the case of colliding sheets of energy, it is found that equilibrium together with gradient energy loss components describe the actual energy loss rate well. It is also observed that there is energy loss delay time that is proportional to $1/T$ and is described by first order gradients when fluid is close to equilibrium. The work presented in the second part of the thesis is largely based on the papers [3, 4] and conference proceedings [5].

Part I

Transverse momentum broadening in weakly coupled quark-gluon plasma

Chapter 1

Introduction to part I

In this part brief introduction to the QCD phase diagram and phase of quark gluon plasma is given. We discuss the motivation for studying quark gluon plasma and how experimental programs at heavy ion colliders help to answer questions of interest. We then discuss the probes that are used to describe the interactions and why they turn out to be of interest. We will particularly concentrate on transverse momentum broadening probability and transport coefficient associated with the second moment of the distribution – jet quenching parameter. We then describe how effective theory (SCET) can be used to take into account large number of very soft interactions by associating transverse momentum broadening with the Wilson loop in thermal medium. Finally, we give a brief introduction to the thermal field theory approach to calculate the Wilson loop and discuss the consequences.

1.1 Quark gluon plasma, phase diagram of QCD and heavy ion collisions

One of the important forces of nature is the strong force, also known as Quantum Chromodynamics (QCD). QCD is an SU(3) non abelian gauge theory which describes the interactions between particles which have color charge associated with it (quarks) and is transmitted with massless gauge boson fields - gluons. QCD has total number

of charges $N_c = 3$ and total number of six quark types (plus antiquarks), which correspond to $N_f = 3$ number of flavors. A unique property of QCD, as opposed to other forces of nature, is asymptotic freedom – at high energies the theory is interacting weakly, $\alpha_s \ll 1$, while at low energies, at around $\Lambda_s \approx 200$ MeV, the theory becomes strongly coupled and confined.

Interesting property of QCD is that in the limit of zero quark masses, the theory has chiral symmetry. Chiral symmetry says that left-handed and right-handed particles should be the same. Nevertheless, quark masses are non-zero and chiral symmetry of QCD is spontaneously broken. The associated Goldstone bosons are lightest hadrons of the theory – pions and kaons, with masses much smaller than the rest of the hadrons observed. Therefore, at zero temperature we do not observe chiral symmetry directly, but it turns out that because of asymptotic freedom at high temperature chiral symmetry is restored quarks and gluons do not form hadrons. The critical temperature above which the symmetry is restored is estimated to be $T_{cr} \sim 170$ MeV at zero baryon chemical potential. The phase diagram of QCD is outlined in Figure 1-1.

Our universe fractions of seconds after the big band was hot enough so that quarks and gluons were in the phase of quark gluon plasma. Since the baryon-antibaryon asymmetry was violated only slightly in the beginning of the universe, baryon chemical potential was very small and therefore it is expected that phase transition happened at temperature $T_{cr} \sim 170$ MeV. Unfortunately, this phase of the universe evolution is not observable directly via astrophysical observations because the universe became transparent only much later when hydrogen atoms were formed corresponding to temperature $T_i \sim 14$ eV.

One way how thermodynamic properties of QCD can be investigated is via lattice calculations. Using imaginary time formalism QCD partition function is calculated in Euclidean space-time with periodic time direction of length $1/T$. Any thermodynamic quantity can then be obtained by differentiating the partition function. This gives a very powerful tool which can be used at strong coupling and nicely supplements the perturbative approach at weak coupling. Lattice calculations indicate a sharp

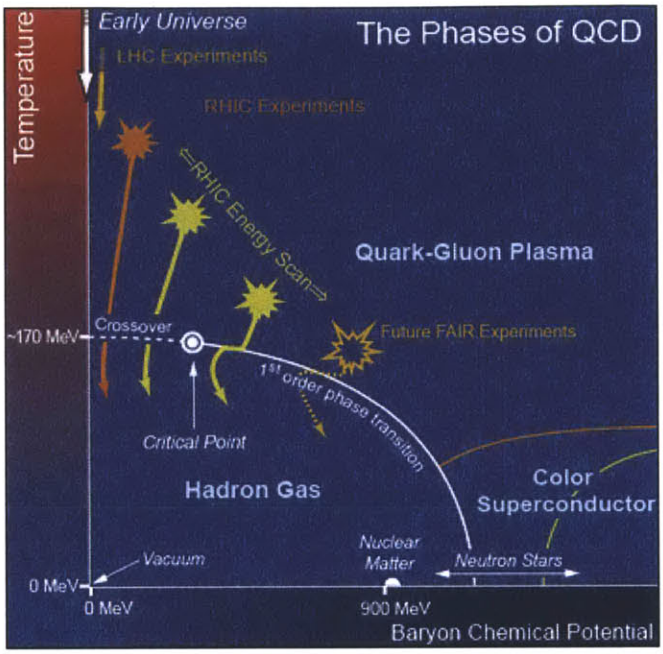

Figure 1-1: Cartoon of phase diagram of QCD with baryon chemical potential on the $x-$axis, and temperature on the $y-$axis.

transition at temperature T_{cr} [6, 7] as can be seen in the Figure 1-2. It can also be seen that the energy density deviates substantially from the Stefan-Boltzmann result for a free gas of noninteracting gluons and massless quarks (indicated by arrow in the plot). The associated critical energy density at T_{cr} is ~ 1 GeV/fm^3, which is the energy density of one nucleon in a cube of 1 fm size. On the other hand, lattice QCD can only be used for zero baryon chemical potential because of sign problem. Also, calculations are restricted by computational power and only static quantities can be calculated on the lattice.

The only physical way to recreate the phase of quark gluon plasma for short period

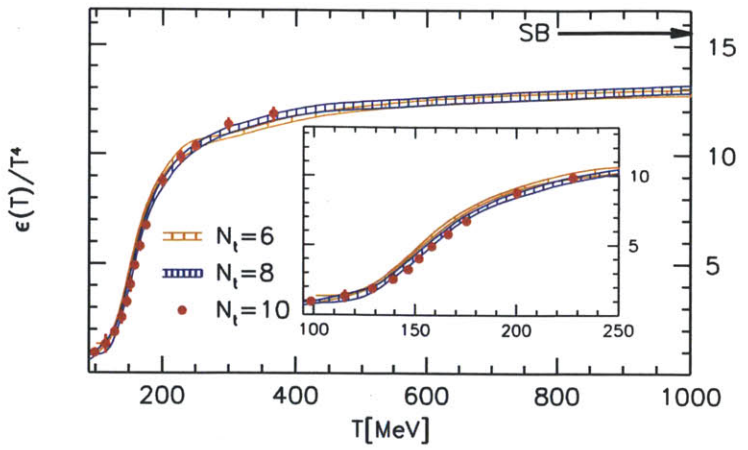

Figure 1-2: Energy density of the QCD as a function of temperature T and normalized with T^4 [6].

of time is using relativistic heavy ion collisions. In experiments at RHIC and LHC, heavy ions are accelerated and collided at the center of mass energy per pair of nucleon $\sqrt{s_{NN}}$ (at RHIC maximum energy is $\sqrt{s_{NN}} = 200$ GeV and $\sqrt{s_{NN}} = 2.76$ TeV at LHC). After the collision, a dense fireball is created at high temperature which immediately starts expanding. During the expansion, the fireball cools down and when it reaches temperatures approximately equal to $155 - 180$ MeV (at RHIC), chemical freeze-out happens and hadronic matter becomes dilute enough not to change the abundance ratios. Formed particles are then observed in the detectors and transverse momentum (with respect to collision plane) is measured. The measurements can be used to infer the information about quark gluon plasma and one of the key measurement is jet quenching or hard probe energy loss.

1.2 Hard probes

The droplets of quark gluon plasma (QGP) produced in heavy-ion collisions can be studied via analyzing the "shape" (in various senses including almost literally) of the explosion of hadrons it decays into and via analyzing their effects on various internally generated "probes". High energy partons, produced in hard parton-parton

scattering events occurring at the earliest moments within a heavy ion collision, are particularly useful probes. After their production they will propagate through as much as $5-10\,\mathrm{fm}$ of the hot and dense medium produced in the collision. In proton-proton collisions, the production rates and decay products (jets) of such high energy partons are well measured and well understood, meaning that in heavy ion collisions they constitute well calibrated probes of the plasma. The suite of observables that indicate the ways in which high energy partons interact with the plasma, for example losing energy to it, are collectively known as "jet quenching". The suppression of the production rates for high-p_T hadrons in heavy ion collisions at RHIC with respect to expectations based on scaling with the number of binary nucleon-nucleon collisions was the earliest manifestation of jet quenching to be discovered [8]. Jet quenching manifests itself in many observables, which contain clues about how the fragmentation of a high energy parton is affected by the presence of the plasma and how the medium responds to the energy and momentum that a fragmenting parton transfers to it. Jet quenching has by now been seen in many ways, both at RHIC and at the LHC. At the LHC, jet energies are high enough that the jets can be detected calorimetrically event-by-event, and the phenomenon of jet quenching is manifest in single events with, say, a jet with an energy greater than 200 GeV back-to-back with a jet with an energy less than 100 GeV [9, 10, 11, 12, 13, 14, 15, 16]. The first measurements of heavy ion collisions at the LHC in which a hard parton (manifest in the final state as a jet) was produced back-to-back with a single hard photon have recently been reported [14, 17], and early results on energetic hadrons back-to-back with a single hard photon in heavy ion collisions at RHIC have also been reported [18]. Since the photon tells us the initial transverse momentum and direction of the parton that produced the jet, analyzing sufficiently large data sets of such events can tell us how the plasma produced in heavy ion collisions affects the energy, fragmentation, and direction of hard partons plowing through it.

Theoretical analyses of how the energy and momenta of hard partons are modified by passage through weakly coupled quark-gluon plasma have been developed by many authors [19, 20, 21, 22, 23, 24, 25, 26, 27, 28, 29, 30] and are reviewed in Refs. [31, 32,

33, 34, 35, 36, 37, 38]. In the limit of high parton energy, parton energy loss occurs dominantly via the radiation of nearly collinear gluons, an effect that is distinct from the changes in the direction of the momentum of the hard parton via (repeated, soft) elastic collisions. The latter effect is often called "transverse momentum broadening", where the word "transverse" here and throughout the remainder of this thesis means perpendicular to the original direction of the energetic parton, not perpendicular to the beam direction. Transverse momentum broadening describes the accumulation of changes to the direction of the momentum of the hard parton as it propagates through a medium. Transverse momentum broadening plays a central role in all the calculations of radiative energy loss, since the incoming and outgoing partons and the radiated gluons are all continually being jostled by the medium in which they find themselves.

1.3 Effective theory approach

Analysis of an energetic parton propagating through a medium immediately involves (at least) two well-separated energy scales, $Q \gg T$, where Q is the energy of the hard parton and T refers to any of the soft scales that characterize the medium itself. In the case of weakly coupled quark-gluon plasma, "T" could refer to the temperature T itself or to even softer scales like gT or g^2T, with g the QCD coupling. This separation of scales suggests the use of Effective Field Theory (EFT), which takes advantage of a separation of energy scales to simplify calculations and enhance predictive power by identifying relevant degrees of freedom, simplifications, or new symmetries that appear in the limit of large scale separation. The hierarchy $Q \gg T$ makes Soft Collinear Effective Theory (SCET) [39], the natural EFT with which to describe hard partons in a medium. (SCET was introduced in other contexts in which both energetic (collinear) partons and soft degrees of freedom are relevant.) The work of Ref. [40], which builds upon the earlier analysis of transverse momentum broadening in Ref. [30], was the first use of SCET to analyze partons in medium. These authors looked at the transverse momentum broadening of partons produced

in deep inelastic scattering on large nuclei. In particular, they discovered that the transverse momentum broadening of an energetic parton is induced by its interactions with the gluons from the medium in a particular kinematic regime, known as "Glauber gluons", that were not present in the original formulation of SCET. Upon choosing coordinate axes such that the three-momentum of the energetic parton is initially along the negative z-axis, meaning that its initial four-momentum is

$$q_0 \equiv \left(q_0^+, q_0^-, q_{0\perp}\right) = (0, Q, 0) \ . \tag{1.1}$$

(in light-cone coordinates defined by $q^\pm = \frac{1}{\sqrt{2}}(q^0 \pm q^3)$) Glauber gluons are gluons whose momenta are parametrically of order [41]

$$\left(\frac{T^2}{Q}, \frac{T^2}{Q}, T\right) \ . \tag{1.2}$$

After absorbing or emitting any number of Glauber gluons, the momentum of the energetic parton is parametrically of order $(T^2/Q, Q, T)$, meaning that it is off-shell only by of order T^2 and so does not radiate either collinear or soft gluons [41]. And yet, repeated absorption and emission of Glauber gluons continually kicks the hard parton and can result in significant transverse momentum broadening. In Ref. [41] SCET formulation for the calculation of transverse momentum broadening in any medium was developed which accounts for arbitrarily many interactions between the energetic parton and the Glauber modes from the medium. SCET has also been used to study momentum broadening and collinear gluon radiation to first order in opacity in Ref. [42]. In this thesis, the general result of [41] is evaluated for the specific case of a weakly coupled quark-gluon plasma, in QCD, in thermal equilibrium.

1.4 Transverse momentum broadening

Transverse momentum broadening is described by $P(k_\perp)$, the probability density that after propagating through the medium for a distance L without radiating, the energetic parton has acquired momentum transverse to its initial direction given by

$k_\perp$. The probability distribution is normalized as

$$\int \frac{d^2k_\perp}{(2\pi)^2} P(k_\perp) = 1 \ . \tag{1.3}$$

$P(k_\perp)$ depends on the medium length L, but we will keep this dependence implicit in our notation. $P(k_\perp)$ is obtained by summing over infinitely many Feynman diagrams, accounting for the interactions between the energetic parton with any number of Glauber gluons from the medium. In Ref. [41] this calculation was performed by treating the Glauber gluons as background fields, analyzing the propagation of the energetic parton in the presence of any background field configuration, and then averaging the result over all possible background field configurations.

The final result for the differential probability distribution reads [41]

$$P(k_\perp) = \int d^2x_\perp \, e^{-ik_\perp \cdot x_\perp} \, \mathcal{W}_\mathcal{R}(x_\perp) \ , \tag{1.4}$$

where $\mathcal{R}$ is the $SU(N_c)$ representation to which the energetic particle belongs and $\mathcal{W}_\mathcal{R}(x_\perp)$ is the expectation value of two light-like Wilson lines with spatial extent L (and therefore length $L^- \equiv \sqrt{2}L$ along the light cone) in representation $\mathcal{R}$ separated from each other in the transverse plane by the vector $x_\perp$.[1] The explicit definition of $\mathcal{W}_\mathcal{R}(x_\perp)$ is given at the beginning of Section 2.1. The expression (1.4) was obtained previously using different methods in Refs. [35, 43]. The nature of the medium — for example whether it is weakly coupled or strongly coupled — does not enter in the analysis of the propagation in any one background field configuration, and therefore does not affect the expression (1.4) [41]. This distinction, or indeed any property of the medium, only becomes relevant when one averages over all possible background field configurations, which is to say when one *evaluates* the expectation value $\mathcal{W}_\mathcal{R}(x_\perp)$.

[1] The expression (1.4) is gauge invariant only after the ends of the lightlike Wilson lines are closed with transverse segments, completing a Wilson loop. However, in the limit $L \gg 1/T$ the contribution of these transverse segments is subleading in any covariant gauge, meaning that the gauge invariant result can be obtained by evaluating (1.4), which includes only the two long lightlike Wilson lines, in any covariant gauge [41]. In lightcone gauge, the expectation value of the lightlike lines vanishes and the same result is obtained entirely from the transverse segments [41, 47]. In the thesis, covariant gauge is used to obtain the gauge invariant result directly from (1.4).

If the medium of interest is in thermal equilibrium, the expectation value $\mathcal{W}_{\mathcal{R}}(x_\perp)$ is a thermal average that can be evaluated in equilibrium thermal field theory. If the medium of interest is not in equilibrium, the expectation value $\mathcal{W}_{\mathcal{R}}(x_\perp)$ is much harder to evaluate but the expression (1.4) remains correct. If the medium of interest is cold nuclear matter, for example in approaches to understanding the Cronin effect in proton-nucleus collisions via transverse momentum broadening of the incident parton from the proton before its hard scattering [44, 45, 46], then the relevant $P(k_\perp)$ is also given by (1.4). In all these contexts, the result (1.4) is valid only in the high energy limit for the propagating parton. Specifically, it requires that $Q \gg k_\perp^2 L$, as this is the criterion that ensures that the trajectory of the hard parton in position space remains well-approximated as a straight line, even as the parton picks up transverse momentum $k_\perp$. In this limit, $P(k_\perp)$ is given by (1.4) and is therefore independent of the energy of the hard probe, depending only on the properties of the medium through the thermal expectation value $\mathcal{W}_{\mathcal{R}}(x_\perp)$. Transverse momentum broadening without radiation thus "measures" a field-theoretically well-defined property of the medium.

In Ref. [41], an explicit evaluation of the thermal average $\mathcal{W}_{\mathcal{R}}(x_\perp)$ and hence $P(k_\perp)$ was provided only for the plasma of $\mathcal{N} = 4$ supersymmetric Yang-Mills (SYM) theory in the large number of colors (N_c) and strong coupling limit, in which this strongly coupled plasma has a holographic description, allowing the calculation to be done via gauge/gravity duality.[2] In this plasma (and, quite likely in any plasma in the strong coupling limit) $P(k_\perp)$ is Gaussian in $k_\perp$ and transverse momentum broadening can be understood as diffusion in $k_\perp$-space due to repeated, even continuous, interactions between the hard parton and the strongly coupled medium.

In this thesis QCD plasma in equilibrium at high enough temperatures is considered so that physics at scales $\sim T$ is weakly coupled. We shall evaluate the thermal average $\mathcal{W}_{\mathcal{R}}(x_\perp)$ perturbatively, using standard methods from thermal field theory. From this we then obtain $P(k_\perp)$ and hence momentum broadening in a weakly cou-

[2]The result so obtained [41] confirms one obtained first in Ref. [48], and eliminates certain subtleties in the earlier derivation.

pled quark-gluon plasma by applying (1.4). We shall present this calculation over the course of Sections 2.1, 2.2 and 2.3. We set up the general formalism and identify the leading order contribution in the gauge coupling g (assumed $\ll 1$) to the expression in (1.4). In doing so, we resum an infinite class of diagrams which are enhanced by the medium length L. For a thick medium, the resummation alters $P(k_\perp)$ at small $k_\perp$, as we will show explicitly. Once we have set up the formalism and identified the expression that we need to evaluate, we find that $P(k_\perp)$ depends on the retarded gluon propagator. In Section 2.2, we show how this propagator can be expressed in terms of self-energies, which we compute. We compute the self-energies first using ordinary perturbation theory, for any value of the external momentum. Since our goal is to compute the probability distribution in (1.4), which manifestly depends on a gluon correlator in coordinate space, we need the gluon propagator for any value of the external momentum. Famously, perturbation theory for non-Abelian gauge theories at finite temperature breaks down in the infrared [49, 50]. In the case of the gluon propagator this happens when the external momentum is of order g^2T, and we recover this pathology from our expression. We take care of the infrared problem by using the hard thermal loop (HTL) effective theory [51], which is valid for momenta of order gT and below and which restores a consistent perturbative expansion. We work in the weak-coupling regime, where the hierarchy $g^2T \ll gT$ guarantees that the infrared problem does not show up in our calculation. In Section 2.3 we discuss this in detail, and we explain how we use full or HTL retarded self-energies in the appropriate regimes, as well as how we match them at an intermediate scale. The reader only interested in our results, not in their derivation, can jump directly to Section 3. There we present our results, compare them to results at strong coupling [48, 41], and compare them to other weak-coupling results in the literature for $P(k_\perp)$ and its second moment, which is called the jet quenching parameter $\hat{q}$ [30, 52, 53, 54, 55].

The most important qualitative feature of our result is that $P(k_\perp) \propto 1/k_\perp^4$ in the large $k_\perp$ regime. Since this is parametrically larger than a Gaussian at large $k_\perp$ this means that at sufficiently large $k_\perp$ $P(k_\perp)$ is greater in a weakly coupled plasma than in a strongly coupled one. We close Section 3 by exploring this comparison, semi-

quantitatively. In Section 3.5 we conclude and look ahead. We do not expect that our result for weakly coupled quark-gluon plasma describes $P(k_\perp)$ for quark-gluon plasma produced in heavy ion collisions correctly at all $k_\perp$. Heavy ion collisions do not reach the asymptotically high temperatures at which $g \ll 1$ at scales of order the temperature. Instead, there are many indications that the plasma produced in heavy ion collisions at both RHIC and LHC is a strongly coupled liquid, with no well-defined quasiparticles (i.e. no quasiparticles with mean free paths long compared to $1/T$). At small $k_\perp$, we therefore expect that its $P(k_\perp)$ is more similar to that in the strongly coupled $\mathcal{N} = 4$ SYM plasma [48, 41] than to that we calculate in this paper. However, QCD is asymptotically free meaning that at short enough distance scales the strongly coupled liquid must be described by weakly interacting quark and gluon quasiparticles. We do not incorporate the running of g with $k_\perp$ in our calculation. Nevertheless we expect that, because g *does* run, $P(k_\perp)$ for the strongly coupled liquid produced in heavy ion collisions *is* well described at large enough $k_\perp$ by the result of our weakly coupled calculation of $P(k_\perp)$. This means that if $P(k_\perp)$ can be measured over a sufficiently wide range of $k_\perp$ it could yield insights into how quark-gluon plasma with liquid-like properties at length scales of order $1/T$ emerges from a weakly coupled gauge theory at short distances.

Chapter 2

Tools and calculation of transverse momentum broadening

2.1 Setting up the formalism

In this section, we derive an expression valid to leading order in the QCD coupling constant, and hence in a weakly coupled QCD plasma, relating the general result for $P(k_\perp)$, derived in Ref. [41] and given in (1.4), to the retarded gluon propagator. We see in (1.4) that the probability distribution $P(k_\perp)$ that describes momentum broadening is the Fourier transform of $\mathcal{W}_\mathcal{R}(x_\perp)$, the expectation value of two light-like Wilson lines in representation $\mathcal{R}$ separated from each other by a distance $x_\perp$ in the transverse plane. We begin by defining $\mathcal{W}_\mathcal{R}(x_\perp)$ explicitly:

$$\mathcal{W}_\mathcal{R}(x_\perp) \equiv \frac{1}{d\,(\mathcal{R})}\Big\langle \mathrm{Tr}\left[W^\dagger_\mathcal{R}[0,x_\perp]\,W_\mathcal{R}[0,0]\right]\Big\rangle\,, \tag{2.1}$$

where each Wilson line along the light-cone is in turn defined by

$$W_\mathcal{R}\left[y^+,y_\perp\right] \equiv P\left\{\exp\left[ig\int_0^{L^-} dy^-\,A^+_\mathcal{R}(y^+,y^-,y_\perp)\right]\right\}\,. \tag{2.2}$$

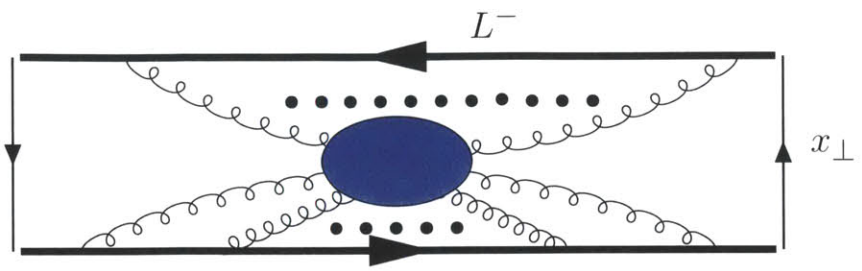

Figure 2-1: Diagrams contributing to the expectation value of the Wilson loop, $\mathcal{W}_{\mathcal{R}}(x_\perp)$. The length of each of the long light-like sides of the loop is $L^- = \sqrt{2}L$. The light-like Wilson lines are separated in the transverse direction by a distance $x_\perp$.

Next, we Taylor expand (2.1), and in doing so we define

$$\mathcal{W}_{\mathcal{R}}(x_\perp) \equiv 1 + \sum_{j=2}^{\infty} \mathcal{W}_{\mathcal{R}}^{(j)}(x_\perp) = 1 + \mathcal{W}_{\mathcal{R}}^{(2)} + \mathcal{W}_{\mathcal{R}}^{(3)} + \dots \ , \tag{2.3}$$

where $\mathcal{W}_{\mathcal{R}}^{(j)}$ denotes the contribution in which j gluon fields are evaluated at points on the light-like Wilson lines or, equivalently, the contribution from those diagrams (see Fig. 2-1) in which gluon propagators end at j vertices on the light-like Wilson lines. We have dropped the explicit denotation of the $x_\perp$-dependence on the right-hand side of (2.3), and will do so at many points below. Each term on the right-hand side of (2.3) is itself a series,

$$\mathcal{W}_{\mathcal{R}}^{(j)} = \sum_{k=0}^{j} W_{\mathcal{R}}^{(k,j-k)} \tag{2.4}$$

where the contribution from a diagram with k gluon vertices on the light-like line at the perpendicular position $x_\perp$ and $j-k$ gluon vertices on the light-like line at the origin of the perpendicular plane is given by

$$W_{\mathcal{R}}^{(k,j-k)} = \frac{(-i)^k \, i^{j-k} \, g^j}{d(\mathcal{R}) \, k! \, (j-k)!} \int_0^{L^-} dy_1^- \dots dy_j^- \\ \left\langle \mathrm{Tr} \left[\mathcal{P} \left\{ A_{\mathcal{R}}^+(y_1^-, x_\perp) \dots A_{\mathcal{R}}^+(y_k^-, x_\perp) A_{\mathcal{R}}^+(y_{k+1}^-, 0_\perp) \dots A_{\mathcal{R}}^+(y_j^-, 0_\perp) \right\} \right] \right\rangle \ . \tag{2.5}$$

Here, g is the $SU(N_c)$ gauge coupling constant, $\mathcal{P}$ stands for path ordering of the gluon fields and the trace is taken over $SU(N_c)$ color indices. We need not specify

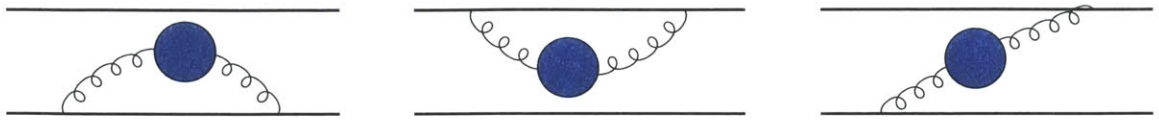

Figure 2-2: Diagrams contributing to $\mathcal{W}_{\mathcal{R}}^{(2)}$. Here, the blue blobs stand for full interacting gluon two-point Green functions.

the y^+ coordinates at which the gluon fields in (2.5) are evaluated because they are evaluated on the light-cone described by varying y^- at fixed y^+, and we can use the translational invariance of the medium to set all of the y^+ coordinates to 0. The gluon fields in (2.5) can each be written as the product of an operator and a group matrix: $A^+_{\mathcal{R}} = A^{a+} t^a_{\mathcal{R}}$. Note, finally, that since the expectation value of a single gluon field vanishes, there is no $j = 1$ contribution in the expansion (2.3). We have now specified the $\mathcal{W}_{\mathcal{R}}$ of (2.1) fully explicitly. The probability distribution $P(k_\perp)$ that describes momentum broadening is then given by the Fourier transform of $\mathcal{W}_{\mathcal{R}}$, as in (1.4).

Both the gluon operators A^{a+} and the group matrices $t^a_{\mathcal{R}}$ within $\mathcal{W}_{\mathcal{R}}$ are ordered along the path as indicated by arrows in Fig. 2-1, in contrast with the time ordered operators in a conventional Wilson loop [41]. Hence, the expectation value $\mathcal{W}_{\mathcal{R}}$ should be described by a Schwinger-Keldysh contour with one light-like Wilson line on the $\mathrm{Im}\, t = 0$ segment of the contour and the other one on the $\mathrm{Im}\, t = -i\epsilon$ segment. The infinitesimal displacement in imaginary time ensures that the operators from the two lines are ordered such that all operators from one line come before any operators from the other. The Schwinger-Keldysh formalism relevant to our calculation is reviewed in Appendix A. A typical diagram contributing to $\mathcal{W}_{\mathcal{R}}(x_\perp)$ is shown in Fig. 2-1.

We are looking for the leading order contribution to $\mathcal{W}_{\mathcal{R}}$, leading in the $g \ll 1$ limit. The first non-trivial and non-vanishing contribution appears for $j = 2$, and is given by the diagrams in Fig. 2-2. Upon writing each gluon field as $A^+_{\mathcal{R}} = A^{a+} t^a_{\mathcal{R}}$, the propagator that arises in $\mathcal{W}_{\mathcal{R}}^{(2)}$ reads

$$\left\langle \mathrm{Tr}\left[A^+_{\mathcal{R}}(y_1^-, y_{1\perp}) A^+_{\mathcal{R}}(y_2^-, y_{2\perp})\right]\right\rangle = \mathrm{Tr}\left[t^a_{\mathcal{R}} t^b_{\mathcal{R}}\right] \left\langle A^{a+}(y_1^-, y_{1\perp}) A^{b+}(y_2^-, y_{2\perp})\right\rangle \ , \quad (2.6)$$

where $y_{1\perp}$ and $y_{2\perp}$ can each be either $0_\perp$ or $x_\perp$. The expectation value on the right-

hand side of (2.6) is diagonal in the color indices, making it convenient to define

$$\begin{aligned} \left\langle A^{a\,+}(y_1^-, y_{1\perp}) A^{b\,+}(y_2^-, y_{2\perp}) \right\rangle \equiv \\ \delta^{ab}\, D^>(y_1^- - y_2^-, y_{1\perp} - y_{2\perp}) \ , \end{aligned} \tag{2.7}$$

where the Wightman propagator $D^>$ has no color indices.[1] We can now write

$$\begin{aligned} \left\langle \mathrm{Tr}\left[A^+_{\mathcal{R}}(y_1^-, y_{1\perp}) A^+_{\mathcal{R}}(y_2^-, y_{2\perp}) \right] \right\rangle = \\ d(\mathcal{R})\, C_{\mathcal{R}}\, D^>(y_1^- - y_2^-, y_{1\perp} - y_{2\perp}) \ , \end{aligned} \tag{2.8}$$

where we have identified the quadratic Casimir factor $C_{\mathcal{R}}$ for the $SU(N_c)$ representation $\mathcal{R}$ via the relation

$$\delta^{ab}\, t^a_{\mathcal{R}} t^b_{\mathcal{R}} = C_{\mathcal{R}}\, \mathbf{I}_{\mathcal{R}} \ , \tag{2.9}$$

where $\mathbf{I}_{\mathcal{R}}$ is the identity matrix for the representation $\mathcal{R}$. With all these definitions in place, $\mathcal{W}^{(2)}_{\mathcal{R}}$ now reads

$$\begin{aligned} \mathcal{W}^{(2)}_{\mathcal{R}} = -\, g^2\, C_{\mathcal{R}} \int_0^{L^-} dy_1^- \int_0^{L^-} dy_2^- \times \\ \left[D^>(y_1^- - y_2^-, 0_\perp) - D^>(y_1^- - y_2^-, x_\perp) \right] \ , \end{aligned} \tag{2.10}$$

where $L^- = \sqrt{2} L$. Finally, we perform a change of variables for the integrations over the y^- coordinates, defining

$$Y^- \equiv \frac{y_1^- + y_2^-}{2}, \qquad\qquad y^- \equiv y_1^- - y_2^- \ . \tag{2.11}$$

The integration over the "center of mass" coordinate Y^- is straightforward, and we find

$$\mathcal{W}^{(2)}_{\mathcal{R}} = -g^2 C_{\mathcal{R}} L^- \int dy^- \left[D^>(y^-, 0_\perp) - D^>(y^-, x_\perp) \right] \ . \tag{2.12}$$

In order to determine the leading gauge coupling dependence of $\mathcal{W}^{(2)}_{\mathcal{R}}$, we need to

[1] It would be more precise to call the propagator $D^{>\,++}$, since we only have the + component of the gluon fields. We omit the ++ for notational simplicity. However, we keep the symbol > to remind ourselves that this is the Wightman propagator. We shall later relate $D^>$ to the retarded propagator.

determine how the gluon propagator depends on g. The tree level term in the gluon propagator is proportional to the metric tensor $g^{\mu\nu}$, and since $g^{++} = 0$ this vanishes. The first non-vanishing contribution is found at next order in perturbation theory, when we evaluate the one-loop propagator — i.e. replacing the blue blobs in Fig. 2-2 by single loops. It is straightforward to count the powers of g when the external momentum in the propagator (i.e. momentum in the gluon lines shown explicitly in Fig. 2-2) are greater than the scale gT. In this case, conventional perturbation theory is under control, the one-loop propagator is $\mathcal{O}(g^2)$ and the full expression in (2.12) is $\mathcal{O}(g^4)$. For external momentum in the propagator of the order gT and lower, we shall see below that HTL resummation is necessary. We shall complete the discussion of the g-dependence of our results in Section 3.

Before we move on, we need to check that the $\mathcal{W}_{\mathcal{R}}^{(j)}$ for $j > 2$ are suppressed relative to $\mathcal{W}_{\mathcal{R}}^{(2)}$. Each gluon field from the Wilson lines brings a factor of g with it, meaning that $\mathcal{W}_{\mathcal{R}}^{(j)}$ comes with a factor of g^j from attaching j gluons to the Wilson lines. This, together with the fact that $\mathcal{W}_{\mathcal{R}}^{(3)}$ must include a three-gluon vertex that comes with another g, suggests that all the $\mathcal{W}_{\mathcal{R}}^{(j)}$ for $j > 2$ are suppressed relative to $\mathcal{W}_{\mathcal{R}}^{(2)}$ by a factor of at least g^2. The only way to avoid this conclusion would be if the tree-level contribution to $\mathcal{W}_{\mathcal{R}}^{(3)}$ or $\mathcal{W}_{\mathcal{R}}^{(4)}$ were nonzero, since we saw that $\mathcal{W}_{\mathcal{R}}^{(2)}$ vanishes at tree-level. However, because the three-point gluon vertex has the form $g^{\mu\nu}p^{\rho}$, where p^{ρ} is one of the incoming gluon momenta, and because $g^{++} = 0$, the tree-level contribution to $\mathcal{W}_{\mathcal{R}}^{(3)}$ vanishes. It is also straightforward to check that the tree-level contribution to $\mathcal{W}_{\mathcal{R}}^{(4)}$ vanishes. We conclude that the contribution to the series in (2.3) that is leading order in powers of g is given by $\mathcal{W}_{\mathcal{R}}^{(2)}$, which is related to the gluon propagator $D^{>}$ according to (2.12).

The formalism from Ref. [41] within which (1.4) was derived requires $LT \gg 1$. If we were to require in addition that $g^2 C_{\mathcal{R}} L T \ll 1$, which is satisfied at weak enough coupling for any given L, we would have achieved our goal for this section having derived the relationship (2.12). However, we would prefer to have a result that is valid at large L for any given weak value of the coupling g. For this purpose the leading order contribution to $\mathcal{W}_{\mathcal{R}}$ given by (2.12) does not suffice because it is proportional to

the length of the medium L, meaning that if we evaluate $P(k_\perp)$ by taking the Fourier transform of (2.12) as prescribed in (1.4), we obtain a probability distribution that is proportional to L. This cannot be the correct result at large enough L for any fixed g. In particular, we find that when $g^2 C_{\mathcal{R}} L T \sim 1$ or greater, the perturbative expansion is not under control. In Appendix B we complete the discussion of a "thin medium", in which $g^2 C_{\mathcal{R}} L T \ll 1$, showing how in this circumstance (2.12) yields a correctly normalized probability distribution $P(k_\perp)$. Here, we shall do better.

In order to find a perturbative expansion that is valid for any value of L (and which of course reduces to what we have already derived if $g^2 C_{\mathcal{R}} L T$ is $\ll 1$) we need to consider the L-dependence of each diagram contributing in (2.3). In a translation-invariant medium, each contribution to the series (2.3) is, at minimum, proportional to L. This can easily be seen by starting from the definition in (2.3) and changing the y^- coordinates to a new set including the center-of-mass coordinate Y^-, in analogy to what we have done for $\mathcal{W}_{\mathcal{R}}^{(2)}$ in (2.11). The gluon correlator cannot depend on the center of mass position, and therefore the integration along Y^- is straightforward, giving just a factor of L. If this were the complete story, we would (incorrectly) conclude that power counting in g and L results in

$$\mathcal{W}_{\mathcal{R}}^{(j)} \propto g^{r_j} L \,, \qquad r_j \geq j \,, \tag{2.13}$$

and would further conclude that the previous perturbative expansion needs no modification. In fact, the L power counting in (2.13) is incorrect because its "derivation" assumed that the diagram in Fig. 2-1 is connected. If this were the case, there would be only one global translational invariance, and therefore one single center of mass integration. Disconnected diagrams, however, always have additional translational invariances (corresponding to the freedom to translate disconnected pieces of the diagram independently) that yield additional integrations over center-of-mass coordinates that in turn result in the contribution of the diagram being enhanced by additional powers of L. Thus when $g^2 C_{\mathcal{R}} L T \sim 1$ or greater we will need to resum a suitable set of disconnected diagrams, namely those whose contributions are the most

"length-enhanced". Disconnected diagrams can always be drawn for $j \geq 4$, and the greatest number of translational invariances is reached in diagrams with the greatest number of disconnected pieces.

From the cluster decomposition principle, we expect that when we include all disconnected diagrams, $\mathcal{W}_{\mathcal{R}}(x_\perp)$ can be written in the exponentiated form

$$\mathcal{W}_{\mathcal{R}} = \exp\left(\sum \text{connected diagrams}\right) \ . \tag{2.14}$$

We emphasize that here connected diagrams include diagrams which could be disconnected were the gauge group Abelian. For example, consider the diagrams in Figs. 2-3 and 2-4. The first is clearly disconnected. Naively, the cross diagram within Fig. 2-4 also appears disconnected in coordinate space. However, the contractions in color space restrict the coordinate space integrations, and the cross diagram should in fact be considered connected. Since all connected diagrams come with precisely one factor of L, our earlier power counting of g goes through, but now when applied to the exponent in (2.14). So, to leading order in weak coupling we now have

$$P(k_\perp) = \int d^2x_\perp \, e^{-ik_\perp \cdot x_\perp} \, \exp\left[\mathcal{W}_{\mathcal{R}}^{(2)}\right] \ . \tag{2.15}$$

The proof of (2.14) is almost analogous to the textbook proof of the relation between the connected and disconnected diagrams in, say, $\lambda\phi^4$ theory. There are some additional complications involving path ordering and group contractions. We illustrate how these are resolved in Appendix C, by giving as an example a proof of the exponentiation of $\mathcal{W}_{\mathcal{R}}^{(2)}$, namely (2.15).

We conclude that whereas for a thin medium in which $g^2 C_{\mathcal{R}} L\, T \ll 1$ the leading contribution to $P(k_\perp)$ at weak coupling is given by (1.4) with $W_{\mathcal{R}}$ replaced by just $\mathcal{W}_{\mathcal{R}}^{(2)}$, if $g^2 C_{\mathcal{R}} L\, T$ is not small we must resum all disconnected diagrams involving only $\mathcal{W}_{\mathcal{R}}^{(2)}$ as in Fig. 2-3, obtaining

$$\exp\left[\mathcal{W}_{\mathcal{R}}^{(2)}\right] = 1 + \sum_{n=1}^{\infty} \frac{1}{n!} \left(\mathcal{W}_{\mathcal{R}}^{(2)}\right)^n \tag{2.16}$$

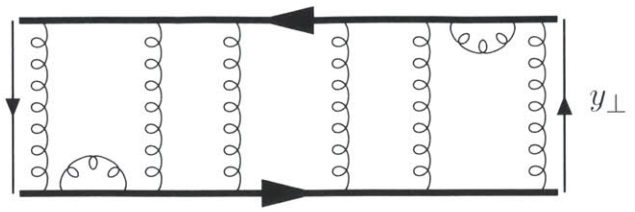

Figure 2-3: A contraction of $n = j/2$ gluons, here with $n = 8$, giving a contribution proportional to L^n. This is an example of a diagram whose contribution is length-enhanced.

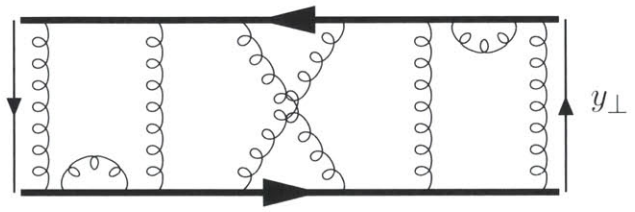

Figure 2-4: A different contraction of $k = j/2 = 8$ gluons giving a contribution which is proportional only to L^7, making it less "length-enhanced" than that of Fig. 2-3. If we neglect powers of g coming from within the propagators, the cross diagram in this figure gives a factor of $g^4 L$ which should be compared with the $g^4 L^2$ factor coming from two disconnected lines. This diagram and that of Fig. 2-3 give contributions proportional to the same power of g but, among all such contributions, that from Fig. 2-3 is one of those that comes with the highest possible power of L while that from this diagram is not. So, the diagram in Fig. 2-3 is one of the length-enhanced diagrams that we resum while this diagram is not.

where $\left(\mathcal{W}_{\mathcal{R}}^{(2)}\right)^n$ contains a "length enhancement" factor L^n. By keeping only the leading order term in the exponent in (2.14) we are resumming those diagrams that have the highest possible power of L for a given power of g. This is illustrated in Figs. 2-3 and 2-4. The diagram in Fig. 2-3 is included in our resummation (2.15); it contributes to the $n = 8$ term in the expansion (2.16). The diagram in Fig. 2-4 arises in (2.14) from a cross-term involving 6 powers of $\mathcal{W}_{\mathcal{R}}^{(2)}$ and one power of $\mathcal{W}_{\mathcal{R}}^{(4)}$. It therefore does not arise in (2.16) or (2.15). It is not included in our resummation because, for its power of g, it is less length-enhanced than the diagram in Fig. 2-3.

The physical interpretation of resumming length enhanced diagrams is that by doing so we are taking into account the possibility that the energetic parton scatters many times over the course of propagating for a distance L through the medium. In

Appendix D we show explicitly that the resummation we have performed is equivalent to considering multiple scattering by deriving and solving a Boltzmann equation for momentum broadening. The rederivation of our results in Appendix D is also helpful in making contact between our results and those in previous literature. To that end, in Appendix D we analyze the Boltzmann equation with a collision kernel that includes only one gluon exchange. The solution to this Boltzmann equation is identical to Eq. (2.15), which we obtained by describing processes with one gluon exchange (via $\mathcal{W}_{\mathcal{R}}^{(2)}$, obtained by evaluating the Wilson line diagrams in Fig. 2-2) and then exponentiating in order to resum length-enhanced diagrams as we have just discussed. From our approach, we know that Eq. (2.15) could be extended to higher orders in the coupling by including further disconnected diagrams in (2.14). Analogously, the calculation in Appendix D can immediately be generalized to analyze a Boltzmann equation with more terms in its collision kernel, and to show that if the collision kernel includes all terms to arbitrarily high orders in the coupling the result of the Boltzmann equation approach would indeed agree with our more general expression (2.14).

The expression for $\mathcal{W}_{\mathcal{R}}^{(2)}$ is given in (2.12) as a function of the gluon propagator in coordinate space. Together with (2.12), the result (2.15) provides an expression for the probability distribution that describes transverse momentum broadening in a weakly coupled plasma of any length L, thick or thin. In Appendix B we complete the analysis of a thin medium, where $g^2 C_{\mathcal{R}} L\, T \ll 1$, disconnected diagrams are not length-enhanced, and only the diagrams in Fig. 2-2 contribute.

We end this Section by rewriting the expression (2.12) for $\mathcal{W}_{\mathcal{R}}^{(2)}$, which appears in the final result (2.15), in Fourier space. We first introduce the Wightman propagator in momentum space through

$$D^{>}(X) = \int \frac{d^4Q}{(2\pi)^4}\, e^{-iQ\cdot X}\, D^{>}(Q)\ . \tag{2.17}$$

Here and below, we denote Lorentz four-vectors by an uppercase character, e.g. Q, and the modulus of the three-vector by lowercase character, e.g. q. Integrating over

y^- in (2.12) (taking $L \to \infty$) yields a delta function $\delta(q^+)$. Keeping in mind that the coordinate-space gluon fields are evaluated on the negative light-cone $y^+ = 0$, we then find that

$$\mathcal{W}_{\mathcal{R}}^{(2)}(x_\perp) = -g^2 C_{\mathcal{R}} L^- \int \frac{dq^- d^2q_\perp}{(2\pi)^3} \left[1 - e^{iq_\perp \cdot x_\perp}\right] D^>(q^-, q_\perp). \tag{2.18}$$

Finally, the propagator $D^>$ can be written as [56]

$$D^>(Q) = \left[1 + f(q^0)\right] 2\,\mathrm{Re}\, D_R(Q) \ , \tag{2.19}$$

where $f(q^0)$ is the Bose-Einstein distribution function and $D_R(Q)$ is the retarded propagator. We see that in a weakly coupled plasma $P(k_\perp)$ depends only on the retarded gluon propagator. Our goal in the next Section will be to derive an explicit expression for the retarded propagator $D_R(Q)$, from which $D^>(Q)$ can be obtained using (2.19), $\mathcal{W}_{\mathcal{R}}^{(2)}$ can then be obtained using (2.18), and the probability distribution describing momentum broadening in a weakly coupled QCD plasma then follows using (2.15).

2.2 Retarded gluon propagator

In this section, we evaluate the real time expression for the retarded gluon propagator using the Schwinger-Keldysh formalism, with the two long light-like segments of the contour separated infinitesimally in the imaginary time direction. We give a brief review of the real-time field theory framework that we use in Appendix A. The retarded gluon propagator $D_{R\,\mu\nu}$ is obtained by solving the Dyson equation

$$D^{-1}_{R\,\mu\nu}(Q) = \left(D^{\text{free}}_{R\,\mu\nu}(Q)\right)^{-1} + i\,\Pi_{R\,\mu\nu}(Q) \ , \tag{2.20}$$

where $D^{\rm free}_{R\,\mu\nu}$ is the free retarded propagator and $\Pi_{R\,\mu\nu}$ is the retarded self-energy. In a generic covariant gauge, the former reads

$$(D^{\rm free}_{R\,\mu\nu}(Q))^{-1} = i\,Q^2\left[g_{\mu\nu} - \left(1-\frac{1}{\xi}\right)\frac{Q_\mu Q_\nu}{Q^2}\right] \ , \tag{2.21}$$

where ξ is the gauge fixing parameter. In this Section, we compute the one-loop expression for the retarded self-energy. With the self-energy in hand we can solve (2.20) and extract the ++ component of the retarded propagator, which is what we need in order to determine the probability distribution $P(k_\perp)$ using the formalism that we set up in the previous Section.

Unlike at zero temperature, the medium breaks Lorentz invariance and the self-energy tensor therefore has four independent components, in principle. We work in Feynman gauge ($\xi = 1$), where the one-loop self-energy is transverse [57, 58, 59, 60], $Q^\mu \Pi_{R\,\mu\nu}(Q) = 0$. In this case we only have two independent components:

$$\Pi_{R\,\mu\nu}(Q) = \Pi^T_R(Q)\,P^T_{\mu\nu} + \Pi^L_R(Q)\,P^L_{\mu\nu} \qquad (\xi = 1) \ , \tag{2.22}$$

where the projectors $P^T_{\mu\nu}$ and $P^L_{\mu\nu}$ are defined in Appendix E. After we substitute the expressions (2.21) and (2.22) into (2.20), we can invert the Dyson equation, obtaining

$$D_{R\,\mu\nu}(Q) = \frac{i\,P^T_{\mu\nu}}{Q^2 - \Pi^T_R(Q)} + \frac{i\,P^L_{\mu\nu}}{Q^2 - \Pi^L_R(Q)} - \frac{i\,K_{\mu\nu}}{Q^2} \ , \tag{2.23}$$

where the projector $K_{\mu\nu}$ is also given in Appendix E.

In what follows, we explicitly evaluate the full retarded gluon self-energy tensor $\Pi_{R\,\mu\nu}(Q)$ at one-loop, and then extract the components $\Pi^T_R(Q)$ and $\Pi^L_R(Q)$. We use the Schwinger-Keldysh formalism presented in Appendix A, with the identification in (A.11) between the retarded self-energy and the components of the self-energy matrix in the Schwinger-Keldysh formalism. There are two main contributions to $\Pi_{R\,\mu\nu}(Q)$, the Yang-Mills sector and the quarks, so we write

$$\Pi^{\mu\nu}_R = \Pi^{\mu\nu}_{R,\,\rm YM} + \Pi^{\mu\nu}_{R,\,\rm quarks} \ . \tag{2.24}$$

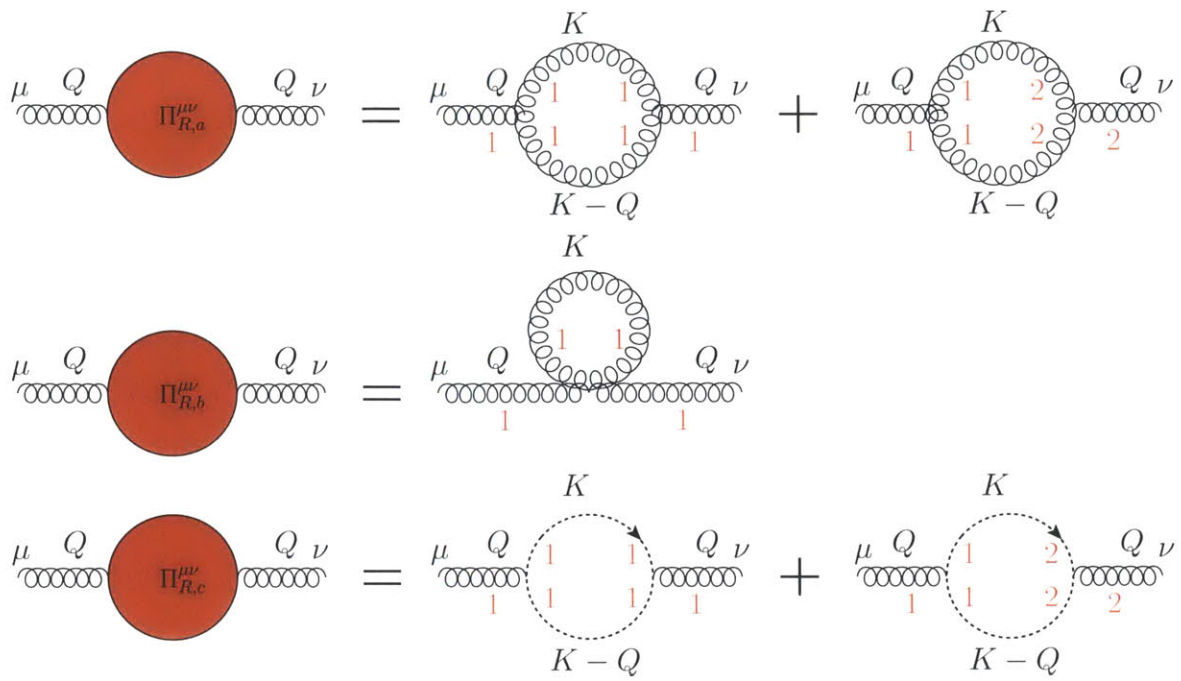

Figure 2-5: Diagrams contributing to $\Pi^{\mu\nu}_{R,\,\mathrm{YM}}$, the contribution to the retarded self-energy from the Yang-Mills sector. The red numbers denote entries of the Schwinger-Keldysh matrix propagator.

In the Yang-Mills sector we have three contributions

$$\Pi^{\mu\nu}_{R,\,\mathrm{YM}} = \Pi^{\mu\nu}_{R,a} + \Pi^{\mu\nu}_{R,b} + \Pi^{\mu\nu}_{R,c} \ , \tag{2.25}$$

corresponding to the different diagrams shown in Fig. 2-5: a) gluon loop with the three-point vertex; b) gluon loop with the four-point vertex; c) ghost loop. We start from the diagrams for $\Pi^{\mu\nu}_{R,a}$ in Fig. 2-5 and use the standard Feynman rules for the three-gluon vertex to obtain the expression

$$\begin{aligned}\Pi^{\mu\nu}_{R,a} = \frac{i}{4}\, g^2 N_c \int \frac{d^4K}{(2\pi)^4} \left[D_R(K) D_S(K-Q) + D_S(K) D_A(K-Q)\right] \times \\ \left[-g^{\mu\nu}\left(5Q^2 + 2K^2 - 2K\cdot Q\right) + 2Q^\mu Q^\nu \right. \\ \left. +5Q^\mu K^\nu + 5K^\mu Q^\nu - 10 K^\mu K^\nu\right] \ .\end{aligned} \tag{2.26}$$

The explicit expressions for the retarded, advanced and symmetric propagators D_R,

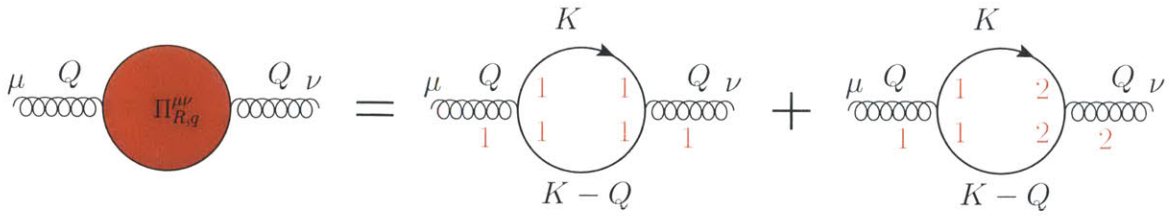

Figure 2-6: Diagrams contributing to $\Pi^{\mu\nu}_{R,\,\text{quarks}}$. Notation as in Fig. 2-5.

D_A and D_S are given in Appendix A. We can combine the first two terms on the right-hand side of (2.26) by changing the loop integration variable $K \to Q - K$ in one of them. The vertex factor is left unchanged, whereas for the propagators we have

$$D_R(K)D_S(K-Q) \;\to\; D_S(K)D_A(K-Q)\;. \tag{2.27}$$

The two contributions are then identical, and we obtain

$$\begin{aligned}\Pi^{\mu\nu}_{R,a} =& \frac{i}{2}\,g^2 N_c \int \frac{d^4K}{(2\pi)^4}\, D_S(K)D_A(K-Q) \\ & \left[-g^{\mu\nu}\left(5Q^2+2K^2-2K\cdot Q\right)+2Q^\mu Q^\nu\right. \\ & \left.+5Q^\mu K^\nu + 5K^\mu Q^\nu - 10K^\mu K^\nu\right]\;.\end{aligned} \tag{2.28}$$

Next we consider the contribution $\Pi^{\mu\nu}_{R,b}$. In this case we have only one diagram, since interaction vertices cannot connect fields on different segments of the Schwinger-Keldysh contour, and it reads

$$\Pi^{\mu\nu}_{R,b} = g^2\,N_c \int \frac{d^4K}{(2\pi)^3}\delta(K^2)\,n_B(k_0)\,(-3\,g^{\mu\nu})\;. \tag{2.29}$$

Finally, since we are working in the Feynman gauge, there is also a contribution $\Pi^{\mu\nu}_{R,c}$ from ghosts in the loop. Its calculation is very similar to the one for the first contribution $\Pi^{\mu\nu}_{R,a}$, and in particular the two sub-diagrams in Fig. 2-6 are combined together by the same shift (2.27). After some algebra, the only difference with respect to the previous case is the interaction vertex, and we have

$$\Pi^{\mu\nu}_{R,c} = i\,g^2 N_c \int \frac{d^4K}{(2\pi)^4}\, D_S(K)D_A(K-Q)\,[K^\mu K^\nu - Q^\nu K^\mu]\;. \tag{2.30}$$

Upon summing (2.28), (2.29) and (2.30), we find that the full gauge contribution to the retarded gluon self-energy is given by

$$\Pi^{\mu\nu}_{R,\,\mathrm{YM}} = g^2 N_c \int \frac{d^4K}{(2\pi)^3}\delta(K^2)\, n_B(k_0)\, \frac{1}{(Q-K)^2 - i\,\mathrm{sgn}(k_0-q_0)\,\epsilon} \times \\ \left[g^{\mu\nu}\left(2Q^2 + 4Q\cdot K - K^2\right) - 2Q^\mu Q^\nu - 6Q^\mu K^\nu - 2K^\mu Q^\nu + 8K^\mu K^\nu\right] . \tag{2.31}$$

We assume that there are N_f quarks in the theory. The fermion loop contribution is shown in Fig. 2-6, and its calculation proceeds analogously to that for the gauge contribution. We find

$$\Pi^{\mu\nu}_{R,\,\mathrm{quarks}} = 4\, g^2 N_f \int \frac{d^4K}{(2\pi)^3}\delta(K^2)\, n_F(k_0)\, \frac{1}{(Q-K)^2 - i\,\mathrm{sgn}(k_0-q_0)\,\epsilon} \times \\ \left[g^{\mu\nu}\left(Q\cdot K - K^2\right) - Q^\mu K^\nu - K^\mu Q^\nu + 2K^\mu K^\nu\right] . \tag{2.32}$$

The full retarded self-energy defined in (2.24) is given by the sum of the two results (2.31) and (2.32). We use the transverse and longitudinal projectors defined in Appendix E to extract its components $\Pi^T_R(Q)$ and $\Pi^L_R(Q)$, defined by (2.22), in order to evaluate the expression for the retarded gluon propagator in (2.23). The longitudinal component is projected out as follows

$$\Pi^L_R = P_{L\,\nu\mu}\,\Pi^{\mu\nu}_R = -\frac{U_\mu U_\nu}{N^2}\Pi^{\mu\nu}_R = \frac{Q^2}{q^2}\Pi^{00}_R \ , \tag{2.33}$$

and we get

$$\Pi^L_{R,\,\mathrm{YM}} = \frac{Q^2}{q^2}\, g^2 N_c \int \frac{d^4K}{(2\pi)^3}\delta(K^2)\, n_B(k_0)\, \frac{2Q^2 + 4Q\cdot K - 2q_0^2 - 8q_0k_0 + 8k_0^2}{(Q-K)^2 - i\,\mathrm{sgn}(k_0-q_0)\,\epsilon} \ , \\ \Pi^L_{R,\,\mathrm{quarks}} = \frac{4\,Q^2}{q^2}\, g^2 N_f \int \frac{d^4K}{(2\pi)^3}\delta(K^2)\, n_F(k_0)\, \frac{k_0^2 + k^2 - 2q_0k_0 + Q\cdot K}{(Q-K)^2 - i\,\mathrm{sgn}(k_0-q_0)\,\epsilon} \ . \tag{2.34}$$

Likewise, the transverse component reads

$$\begin{aligned} \Pi_R^T &= \frac{1}{2}\, P_{T\,\nu\mu}\, \Pi_R^{\mu\nu} = -\frac{1}{2}\left[\Pi_R + \Pi_R^L\right] \ , \\ \Pi_R &\equiv g_{\mu\nu}\Pi_R^{\mu\nu} \ , \end{aligned} \tag{2.35}$$

where the factor of $1/2$ arises because the projector P_T defined in Appendix E has trace -2. In the second equality, we have defined the trace of the retarded self-energy Π_R and we have also identified the longitudinal self-energy just found above. Thus, once we know the longitudinal component, in order to get the transverse component we need only compute the trace of the self-energy and can then use (2.35). We find that the two contributions to the trace are given by

$$\begin{aligned} \Pi_{R,\,\mathrm{YM}} &= g^2 N_c \int \frac{d^4K}{(2\pi)^3}\delta(K^2)\, n_B(k_0)\, \frac{6Q^2 + 8Q\cdot K + 4K^2}{(Q-K)^2 - i\,\mathrm{sgn}(k_0 - q_0)\,\epsilon} \ , \\ \Pi_{R,\,\mathrm{quarks}} &= g^2 N_f \int \frac{d^4K}{(2\pi)^3}\delta(K^2)\, n_F(k_0)\, \frac{8\,Q\cdot K - 2K^2}{(Q-K)^2 - i\,\mathrm{sgn}(k_0 - q_0)\,\epsilon} \ , \end{aligned} \tag{2.36}$$

for the pure gauge and quark contributions, respectively.

In order to obtain an explicit expression for the retarded gluon propagator of Eq. (2.23), we need the longitudinal self-energy given in (2.33), and the transverse component obtained by combining (2.35) and (2.36). The expressions we have obtained so far are valid for any value of the gluon external momentum Q. However, as we have shown in (2.18), we only need the retarded gluon propagator evaluated on the negative light-cone, namely for $q^+ = 0$. For nonzero transverse momentum $q_\perp$ this corresponds to space-like external momentum $Q^2 = -q_\perp^2 < 0$, in which case the self-energy has a non-vanishing imaginary part. This is crucial to our analysis, since what enters the calculation of $P(k_\perp)$ is the real part of the retarded propagator, as shown in Eqs. (2.12), (2.15) and (2.19). The retarded propagator in (2.23) has a real part if and only if the self-energy has an imaginary part. Without this imaginary part, the probability distribution $P(k_\perp)$ in (2.15) would just be a delta function centered at $k_\perp = 0$, and thus we would not have any momentum broadening.

In what follows, we sketch the extraction of the longitudinal component of the

self-energy arising from loops involving gauge bosons and ghosts, and just state the final result for the transverse component. Starting from the explicit expression (2.34), we first integrate over k_0, imposing the on-shell condition for the loop momentum via the delta function. We get two different contributions, for $k_0 = k$ and $k_0 = -k$. The integration over the spatial components of the loop momentum is performed in polar coordinates, with the polar axis defined by the direction of the spatial component $\vec{q}$ of the external momentum. The integration over the azimuthal angle ϕ is straightforward, giving just a 2π factor. The polar angle θ satisfies $\cos\theta = \vec{q}\cdot\vec{k}$, and after we integrate over it we find

$$\Pi^L_{R,\,\mathrm{YM}} = \frac{g^2 N_c T^2}{6}\frac{q_\perp^2}{q^2} + \frac{g^2 N_c}{8\pi^2}\frac{q_\perp^2}{q^3}\int_0^\infty dk\, n_B(k) \left[\left(2q^2 - (2k-q_0)^2\right)\log\left(\frac{q_\perp^2 + 2k(q_0-q) + i\epsilon\ \mathrm{sgn}(k-q_0)}{q_\perp^2 + 2k(q_0+q) + i\epsilon\ \mathrm{sgn}(k-q_0)}\right) + \begin{pmatrix} q_0 \to -q_0 \\ \epsilon \to -\epsilon \end{pmatrix}\right], \tag{2.37}$$

where we have used $\int_0^\infty dk\, k\, n_B(k) = \frac{\pi^2 T^2}{6}$. The logarithms appearing in the expression (2.37) develop an imaginary part for $(q_\perp^2 \pm 2kq_0)^2 < (2kq)^2$. We expand the logarithms in the $\epsilon \to 0$ limit, obtaining a logarithm of the absolute value and a Heaviside step function for the real and imaginary part, respectively. We then identify the real and imaginary part of the longitudinal self-energy, obtaining

$$\begin{aligned}
\mathrm{Re}\,\Pi^L_{R,\,\mathrm{YM}} &= \frac{g^2 N_c T^2}{6}\frac{q_\perp^2}{q^2} + \frac{g^2 N_c}{8\pi^2}\frac{q_\perp^2}{q^3}\int_0^\infty dk\, n_B(k) \left[\left(2q^2 - (2k-q_0)^2\right)\log\left|\frac{q_\perp^2 + 2k(q_0-q)}{q_\perp^2 + 2k(q_0+q)}\right| + (q_0 \to -q_0)\right], \\
\mathrm{Im}\,\Pi^L_{R,\,\mathrm{YM}} &= \frac{g^2 N_c}{8\pi}\frac{q_\perp^2}{q^3}\left[\int_{\frac{q_0+q}{2}}^\infty dk\, n_B(k)\left(2q^2 - (2k-q_0)^2\right) - (q_0 \to -q_0)\right].
\end{aligned} \tag{2.38}$$

The only integrations which are left are over the magnitude of the loop three-momentum. The integral for the real part can only be evaluated numerically, whereas the one for the imaginary part can be expressed in terms of the polylogarithmic functions $\mathrm{Li}_\nu(z)$. The expressions for the real and imaginary part of the longitudinal self-energy com-

ing from quark loop are evaluated analogously, with the main difference being the appearance of the Fermi-Dirac distribution thermal distribution function instead of the Bose-Einstein. After combining the Yang-Mills piece and the contribution from N_f quarks we obtain

$$\begin{aligned}
\mathrm{Re}\,\Pi_R^L =& \left(N_c + \frac{N_f}{2}\right)\frac{g^2T^2}{6}\frac{q_\perp^2}{q^2} + \frac{g^2}{8\pi^2}\frac{q_\perp^2}{q^3}\left[\int_0^\infty dk \log\left|\frac{q_\perp^2 + 2k(q_0-q)}{q_\perp^2 + 2k(q_0+q)}\right| \times \right. \\
& \left. \left[N_c n_B(k) q^2 - (N_f n_F(k) + N_c n_B(k))(4k^2 - 4kq_0 - q_\perp^2)\right] + (q_0 \to -q_0)\right] , \\
\mathrm{Im}\,\Pi_R^L =& \frac{g^2 N_c}{24\pi}\frac{q_\perp^2}{q^3}\left[5q_0^3 + 8q_0T^2\pi^2 + 6q_0q_\perp^2\right] \\
& - \frac{g^2T}{4\pi}\frac{q_\perp^2}{q^2}\left[\frac{N_f}{2}\left(T\,\mathrm{Li}_2\left(-e^{\frac{q_0-q}{2T}}\right) + \frac{2T^2}{q}\mathrm{Li}_3\left(-e^{\frac{q_0-q}{2T}}\right)\right)\right. \\
& \left. - N_c\left(\frac{q}{2}\log\left(1-e^{\frac{q-q_0}{2T}}\right) - 2T\mathrm{Li}_2\left(e^{\frac{q-q_0}{2T}}\right) + \frac{4T^2}{q}\mathrm{Li}_3\left(e^{\frac{q-q_0}{2T}}\right)\right) - (q_0 \to -q_0)\right],
\end{aligned} \tag{2.39}$$

By similar means, we calculate the trace of self-energy tensor (2.36) which we then combine with the longitudinal components in (2.39) to obtain the transverse self-energy according to Eq. (2.35). We find

$$\begin{aligned}
\mathrm{Re}\,\Pi_R^T =& \left(N_c + \frac{N_f}{2}\right)\frac{g^2T^2}{12}\left(1 + \frac{q_0^2}{q^2}\right) + \frac{g^2q_\perp^2}{16\pi^2q^3}\left[\int_0^\infty dk \log\left|\frac{q_\perp^2 + 2k(q_0-q)}{q_\perp^2 + 2k(q_0+q)}\right| \times \right. \\
& \left. \left[2N_c n_B(k) q^2 + (N_c n_B(k) + N_f n_F(k))(q^2 + (2k-q_0)^2)\right] + (q_0 \to -q_0)\right] , \\
\mathrm{Im}\,\Pi_R^T =& \frac{g^2N_c}{48\pi}\frac{q_\perp^2}{q^3}\left[10q_0^3 - 8q_0T^2\pi^2 + 9q_0q_\perp^2\right] + \\
& \frac{g^2T}{4\pi}\frac{q_\perp^2}{q^3}\left[-\frac{N_f}{2}\left(q^2\log\left(1+e^{\frac{q_0-q}{2T}}\right) + 2qT\mathrm{Li}_2\left(-e^{\frac{q_0-q}{2T}}\right) + 4T^2\mathrm{Li}_3\left(-e^{\frac{q_0-q}{2T}}\right)\right) + \right. \\
& \left. N_c\left(q^2\log\left(1-e^{\frac{q-q_0}{2T}}\right) - qT\mathrm{Li}_2\left(e^{\frac{q-q_0}{2T}}\right) - 2T^2\mathrm{Li}_3\left(e^{\frac{q-q_0}{2T}}\right)\right) - (q_0 \to -q_0)\right] .
\end{aligned} \tag{2.40}$$

Thus, we have obtained the components of the gluon self-energy in (2.39) and (2.40) by direct calculation in real-time field theory. In the imaginary time formalism, the gluon self-energies were first computed in Refs. [57, 61].

We end this section by performing a check of our calculation, a check whose results

we shall use in Section 2.3. We recover the HTL self-energies [51], which are valid for external momenta of order gT or below. In this regime, the main contribution to the loop integral comes from hard loop momenta $k \sim T$, so the procedure corresponds to expanding the integrand in powers of q/k. Both the real and imaginary parts of the gluon self-energy that we have obtained above can be computed analytically to leading order in this expansion, resulting in

$$\begin{aligned} \mathrm{Re}\,\Pi_R^L\big|_{HTL} &= \frac{m_D^2 q_\perp^2}{q^2}\left(1+\frac{q_0}{2q}\log\left(\frac{q-q_0}{q+q_0}\right)\right) , \\ \mathrm{Im}\,\Pi_R^L\big|_{HTL} &= \pi m_D^2\left(\frac{q_\perp^2 q_0}{2q^3}\right) , \\ \Pi_R^T\big|_{HTL} &= \frac{m_D^2 - \Pi_R^L\big|_{HTL}}{2} , \end{aligned} \tag{2.41}$$

where m_D^2 is the Debye mass squared

$$m_D^2 = \frac{g^2T^2}{3}\left(N_c+\frac{N_f}{2}\right) . \tag{2.42}$$

As we will show explicitly in Section 2.3, perturbation theory breaks down in the region where the external momentum in a gluon propagator is of order g^2T. We will fix this problem by using the HTL self-energies given in Eq. (2.41), which are well-behaved in the region where ordinary perturbation theory becomes problematic.

2.3 Breakdown of perturbation theory and self-energy matching

The purpose of this work is to evaluate the probability distribution $P(k_\perp)$ in (2.15). In order to do that we have to evaluate the gluon propagator for $q^+ = 0$, and integrate it over $dq^- d^2q_\perp$, as in Eq. (2.18). In particular, we have to integrate the gluon propagator over the region in momentum space where both q^- and $q_\perp$ are of order g^2T or smaller. We shall begin this Section with an explicit demonstration of the breakdown of perturbation theory at the scale g^2T in our self-energy results (2.39)

and (2.40), and then describe how we shall evade this difficulty. This problem in finite temperature non-abelian gauge theory has been known for many years, since the early work of Refs. [49, 50]. Here, we focus on the pure Yang-Mills contribution to the self-energy (setting $N_f = 0$), since the matter fermions are not responsible for the breakdown of perturbation theory in the infrared. We only consider the real part of the self-energies, since that is where the problem arises.

We can find the infrared breakdown of perturbation theory that occurs where both q^- and $q_\perp$ are of order g^2T by focussing on the slice through this region where $q_0 = 0$ and $0 < q_\perp < g^2T$. No problems arise in the longitudinal self-energy: it is gauge independent [50] and, upon taking the appropriate limit in (2.39), we find

$$\mathrm{Re}\,\Pi^L_{R,YM}(q_0 = 0, q_\perp \to 0) \to m_D^2 = \frac{1}{3}g^2 N_c T^2 \ . \tag{2.43}$$

This longitudinal self-energy is responsible for screening the electric modes, giving them a screening mass $m_{\rm el}^2 = g^2 N_c T^2/3$. It does not cause any problems for perturbation theory. The problems arise in the transverse self-energy (2.40). In order to extract the infrared limit, we divide the loop integral dk in (2.40) into hard and soft regions. When $q_0 = 0$, $q_\perp < g^2T$, and the loop integration variable is hard ($k \gtrsim T$ and therefore $k \gg g^2T$) we find that the integrand in the expression (2.40) for $\Pi^T_{R,YM}$ vanishes. We return to this point below but, first, we push ahead into trouble by attempting to evaluate the contribution to $\Pi^T_{R,YM}$ from the region of the dk integral in (2.40) where $k \ll T$. Here we are allowed to use the "soft approximation"

$(n_B(k) \sim T/k)$ in (2.40). We find[2]

$$\begin{aligned} &\mathrm{Re}\,\Pi^T_{R,YM}(q_0 = 0, q_\perp \to 0) \to \\ &\frac{3}{8\pi^2} g^2 N_c q_\perp T \int_0^\infty \frac{dk}{k} \log\left|\frac{q_\perp - 2k}{q_\perp + 2k}\right| = -\frac{3}{16} g^2 T N_c q_\perp \ . \end{aligned} \tag{2.44}$$

We immediately notice that for external momentum $q_\perp \sim g^2 T$, the real part of the transverse self-energy $\mathrm{Re}\,\Pi^T_{R,YM}$ is comparable to $q_\perp^2$. This introduces an unphysical pole at a space-like momentum of order $g^2 T$ in the propagator (2.23). It also invalidates the perturbative expansion of the propagator (2.23), in which Π_R is supposed to be subleading compared to Q^2. Clearly, perturbation theory cannot be trusted anymore at and below the scale $g^2 T$, and neither can the result (2.44).

It is expected that a magnetic mass of order $g^2 T$ arises from nonperturbative effects. Even if this happens, though, perturbation theory still breaks down at the g^6 order, as shown in Ref. [49] by an explicit example. (In contrast, neither perturbative nor non-perturbative effects generate a magnetic mass in an abelian gauge theory [62]. The leading term for the transverse self-energy goes as $g^2 q_\perp^2$, as can be checked from our fermion loop result, and for this reason perturbation theory does not break down in the infrared limit.)

To take care of this problem, we use the HTL self-energy (2.41) in the problematic region. In this approximation, the transverse component of the gluon self-energy is gauge independent [63] and does not give rise to any additional pole at $q \neq 0$, so we do not run into any infrared problems. Along the $q_0 = 0$ slice that we analyzed above, the HTL self-energy is so well-behaved that it in fact vanishes, as we already saw above. Using the HTL self-energy in the $g^2 T$ momentum region avoids all infrared problems and gives us a well-behaved result at the leading order to which we are working, but of course it does not incorporate the effects of the magnetic

[2]Our result is obtained in Feynman gauge ($\xi = 1$). For a general covariant gauge the infrared behavior of the self-energy was first analyzed in [50] using the imaginary time formalism, finding

$$\mathrm{Re}\,\Pi^T_{R,YM}(q_0 = 0, q_\perp \to 0) \to -\frac{8 + (1+\xi)^2}{64} g^2 T N_c\, q_\perp \ ,$$

consistent with our result in the Feynman gauge. This contribution is gauge dependent, but it cannot be set to zero by any gauge choice.

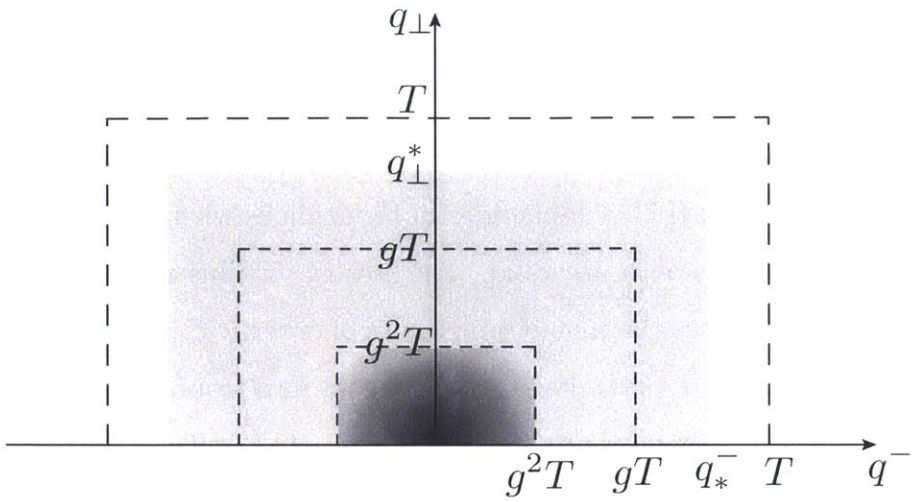

Figure 2-7: Self-energy matching illustration. In the momentum region shaded in grey, where $|q^-| < |q_*^-|$ and $q_\perp < q_\perp^*$, we use HTL self-energies in the integration in (2.18), whereas we use full self-energies elsewhere, in the white regions. The darker grey region, where momenta are $\mathcal{O}(g^2T)$ is the dangerous region where we *must* use HTL self-energies. We do not want to do the matching from grey to white anywhere near this darker region. The HTL self-energies are not valid once momenta are $\mathcal{O}(T)$, so the grey region must not extend this far. We have checked explicitly that for $g \ll 1$ the numerical result for (2.18) is insensitive to where we match from grey to white, as long as $gT < |q_*^-| < T$ and $gT < k_\perp^* < T$.

mass of order g^2T, which is generated only nonperturbatively and so is absent in the HTL self-energy (2.41). In the high-temperature limit of QCD, the nonperturbative physics at momenta of order g^2T is described by matching to a dimensionally reduced long-wavelength effective theory which turns out to be just Euclidean 3-dimensional $SU(N_c)$ gauge theory with the dimensionful coupling constant g_E given by $g_E^2 = g^2T$. Following up on a suggestion by Caron-Huot [54], Laine has very recently shown that the nonperturbative contributions to $P(k_\perp)$ can be related to the static potential in this effective theory and he and others [47, 64] have used this elegant observation to show that the nonperturbative contribution to $P(k_\perp)$ is suppressed parametrically, contributing to $\hat{q}$ (the second moment of $P(k_\perp)$) only at order g^6T^3, and is further suppressed by a numerically small prefactor [64]. This result justifies the neglect of these nonperturbative effects that is inherent in our use of the HTL self-energy at momenta of order g^2T.

Although using the HTL self-energy nicely eliminates the infrared problems in

perturbation theory, we cannot simply use the HTL self-energy throughout our calculation because it is not valid for hard external momenta, which in our case corresponds to $q_0 \sim T$ (and therefore $q^- \sim T$) and $q_\perp \sim T$ in (2.18). The correct procedure is then to use the full or HTL self-energies in the regimes where each is valid, and to match in a region where both are valid. The strategy is illustrated in Fig. 2-7. The darkest shading illustrates the momentum scales of order g^2T where we must use the HTL self energies because perturbation theory runs into troubles if we do not do so. In the regions where momenta are of order T, the HTL self energies are no longer valid and we have to use the full self energies. We must match from HTL to full self energies in a region in which both are valid. As illustrated in Fig. 2-7, we perform the matching at q_*^- and $q_\perp^*$ such that $gT < q_*^- < T$ and $gT < q_\perp^* < T$. We find that the matching is smooth at weak coupling $g \ll 1$, with the exact location of the matching scales q_*^- and $q_\perp^*$ not affecting our final results as long as the matching is performed in the appropriate region.

Before presenting our results in the next Section, we close this Section by comparing our approach to perturbation theory, illustrated in the Fig. 2-7, to that in some previous field-theoretical analyses of momentum broadening in weakly coupled quark-gluon plasma [52, 53, 54, 55]. In the soft region ($k_\perp < T$), these authors use the HTL approximation in their calculations of the probability for momentum broadening. In the notation of our Eq. (2.18), using the HTL approximation is well justified when $q_\perp < T$ only over the regime of the dq^- integration in which $|q^-| < T$, but not over the entire range of the dq^- integration. We have checked, however, that if we were to use the HTL self energies for $q_\perp < T$ over the entire dq^- integration the error introduced is quite small. Our results therefore agree with theirs in this momentum regime, for a thin medium. But, only for a thin medium because once the medium becomes thick one must resum L-enhanced diagrams, as we have done. In the hard region ($k_\perp \gg T$) Arnold and Dogan correctly use the unscreened gluon propagator [52]. In this regime, resumming L-enhanced diagrams does not modify our results significantly (because it is more likely to pick up a very large $k_\perp$ from a single improbable hard kick than from several less hard but still improbable kicks)

and our results therefore agree with those of Ref. [52] for $k_\perp \gg T$. We have been quite careful about how we match from the hard region, including that at $|q^-| \gg T$ at small $q_\perp$, as we have described in Fig. 2-7. This care is unnecessary when $k_\perp \gg T$, and when $k_\perp < T$ it turns out that doing the matching carefully as we do modifies our results less than the resummation of L-enhanced diagrams does. So, we shall see in the next section that our calculation correctly reproduces the results derived with other techniques where it should. However, when the medium is thick enough that the effects of the resummation that we have done become important, we find disagreements with previous results in the soft perpendicular momentum region.

Chapter 3

Results and discussion for part I

In Sections 2.1, 2.2 and 2.3 we have presented a careful derivation of our expression for $P(k_\perp)$ in a weakly coupled plasma and a complete description of how we shall evaluate it. The derivation has turned out to be both subtle and technical at various points, and we therefore promised in Introductions that a reader not interested in subtleties or technical details could skip from the end of Introduction to here. For the benefit of such a reader, we begin here by restating the most salient points from the previous Sections. After expanding the probability distribution for transverse momentum broadening (1.4) in the weak-coupling limit and after resumming an infinite class of "length-enhanced" diagrams that are important if L is large enough that $g^2 C_{\mathcal{R}} L\, T$ is not $\ll 1$, we found that transverse momentum broadening is described by

$$P(k_\perp) = \int d^2x_\perp \, e^{-ik_\perp \cdot x_\perp} \, \exp\left[\mathcal{W}_{\mathcal{R}}^{(2)}\right] \; . \tag{2.15}$$

The physical interpretation of resumming length enhanced diagrams is that doing includes the effect of multiple scattering; we show in Appendix D that the same result (2.15) can equally well be derived by solving a Boltzmann equation for momentum broadening via multiple elastic collisions. In (2.15), the properties of the medium enter through

$$\mathcal{W}_{\mathcal{R}}^{(2)}(x_\perp) = -g^2 C_{\mathcal{R}} L^- \int \frac{dq^- d^2q_\perp}{(2\pi)^3} \left[1 - e^{iq_\perp \cdot x_\perp}\right] D^>(q^-, q_\perp) \; . \tag{2.18}$$

The Wightman gluon propagator $D^>$ is directly related to the retarded gluon propagator by

$$D^>(Q) = \left[1 + f(q^0)\right] \, 2\,\mathrm{Re}\, D_R(Q) \;, \tag{2.19}$$

where $f(q^0)$ is the Bose-Einstein distribution function and $D_R(Q)$ is given in (2.23) in terms of the self-energies that we have then computed explicitly in Section 2.2. In Section 2.3 we explain where and why we use the full self energies or the HTL self energies in our evaluation of (2.23). The full and HTL self energies are given explicitly in Eqs. (2.39,2.40,2.41).

3.1 Results for a thin medium, and comparison to previous results

Let us introduce the dimensionless variable

$$\kappa \equiv \frac{g^2 C_R \, LT}{2\pi} \;, \tag{3.1}$$

proportional to the thickness of the medium L, which determines how important it is to resum L-enhanced diagrams. We begin by presenting our results for the case where $\kappa \ll 1$, meaning that there is no need to resum the L-enhanced diagrams at all. In this thin-medium regime, it is convenient to define the function

$$P_{\rm thin}(k_\perp) \equiv \frac{2\sqrt{2}\pi\,\kappa}{T} \int \frac{dq^-}{2\pi} D^>(q^-, k_\perp) \;, \tag{3.2}$$

because the resummed probability distribution (2.15) reduces to

$$P(k_\perp) = P_{\rm thin}(k_\perp) \quad \text{for} \quad k_\perp \neq 0 \;. \tag{3.3}$$

This is shown explicitly in Appendix B, where we also explain how to handle subtleties at $k_\perp = 0$ correctly, so as to obtain a normalized probability distribution $P(k_\perp)$.

The correct IR and UV behavior of the probability distribution $P_{\rm thin}(k_\perp)$ have

each been obtained previously:

- In the IR region, Aurenche, Gelis and Zaraket showed by explicit calculation that (in our notation) [65]

$$P_{\rm thin}(k_\perp) = P_{\rm thin}^{\rm AGZ}(k_\perp) \quad \text{for} \quad k_\perp \ll T \tag{3.4}$$

  where

$$P_{\rm thin}^{\rm AGZ}(k_\perp) \equiv \kappa \, \frac{2\pi m_D^2}{k_\perp^2 (k_\perp^2 + m_D^2)} \; , \tag{3.5}$$

  with the Debye mass squared as given in (2.42).

- In the UV region, $k_\perp \gg T$, the calculation of Arnold and Dogan shows that (again in our notation) [52]

$$P_{\rm thin}(k_\perp) = P_{\rm thin}^{\rm AD}(k_\perp) \quad \text{for} \quad k_\perp \gg T \tag{3.6}$$

  where

$$P_{\rm thin}^{\rm AD}(k_\perp) = \kappa \, (4N_c + 3N_f) \frac{g^2 \zeta(3) T^2}{\pi k_\perp^4} \; , \tag{3.7}$$

  with $\zeta(3) \approx 1.202$ the Riemann zeta function.

These expressions can each be obtained from our $P_{\rm thin}(k_\perp)$, defined in Eq. (3.2), by taking the IR or UV limits. To obtain the IR expression, we use the HTL self-energy everywhere, make the additional soft approximation, e.g. $n_B(q_0) \sim T/q_0$, and recover (3.5). To take the UV limit, we use the full self-energy rather than the HTL self-energy and keep only the first order solution to the Dyson equation (2.20), and recover (3.7). In Fig. 3-1 we plot $P_{\rm thin}(k_\perp)$ multiplied by factors of $k_\perp^3$ and $k_\perp^4$, and show the agreement in the IR with the AGZ result and in the UV with the AD result. We see that at both $g = 0.1$ and $g = 0.3$, the agreement with the AGZ result is excellent, and extends to values of $k_\perp/m_D$ that are not small at all. In fact, for $g = 0.01$ (which we have not plotted) this agreement extends beyond $k_\perp = 10 m_D$. We also see that although at $g = 0.3$ the matching described in Section 2.3, see Fig. 2-7, is smooth, at $g = 1$ and $g = 2$ it introduces a kink at $k_\perp = q_\perp^*$. This highlights the

fact that a weak-coupling analysis is not quantitatively reliable at these larger values of g. There is a good reason for this: once $g \geq 1$, the separation of the scales g^2T, gT and T that we discussed in Section 2.3 and used as depicted in Fig. 2-7 breaks down. In order to apply our calculation at $g = 1$ and $g = 2$, we need a prescription for how to do the matching described in Fig. 2-7, even when the scales depicted are not separated. What we have done is to choose the matching scale on the horizontal axis of Fig. 2-7 as $q_*^- = T$, thinking it would be unreasonable to choose a larger q_*^- even if it is the case that $gT > T$. Then we have chosen the matching scale $q_\perp^*$ so as to make the probability distribution $P_{\rm thin}(k_\perp)$ continuous at $k_\perp = q_\perp^*$, with a kink there but no discontinuity. Clearly we could instead have chosen a matching prescription at $g > 1$ involving interpolation over a window in $k_\perp$, but this would have been no less arbitrary, given that there is a physical reason why the calculation is not under quantitative control at these large values of g.

For $g < 1$, as discussed in Section 2.3 the matching can be done anywhere in the range $gT < q_\perp^*, q_*^- < T$, because the HTL and full self-energies are in good agreement throughout this region. For $g = 0.1$, the matching was done at $q_*^- = 0.28T$ and $q_\perp^* = 0.3T$ while for $g = 0.3$ it was done at $q_*^- = 0.42T$ and $q_\perp^* = 0.9T$. We have checked that if we vary the locations at which the matching is done within the range between gT and T, the correction to $P_{\rm thin}(k_\perp)$ plotted in Fig. 3-1 is less than the thickness of the curves in the Figure.

A leading order expression for $P_{\rm thin}(k_\perp)$ for all $k_\perp$ was obtained in Ref. [53] by interpolating between the small and large $k_\perp$ regimes. A next-to-leading-order result was derived in Ref. [54], but within the HTL approximation. The HTL result of Ref. [54] was then extended to the $k_\perp > T$ region by making the soft approximation discussed above. Another calculation of $P_{\rm thin}$ valid in the IR can be found in Ref. [55], where the momentum broadening distribution was obtained via a Langevin equation. The solution obtained there using the HTL self-energy reproduces the AGZ result.

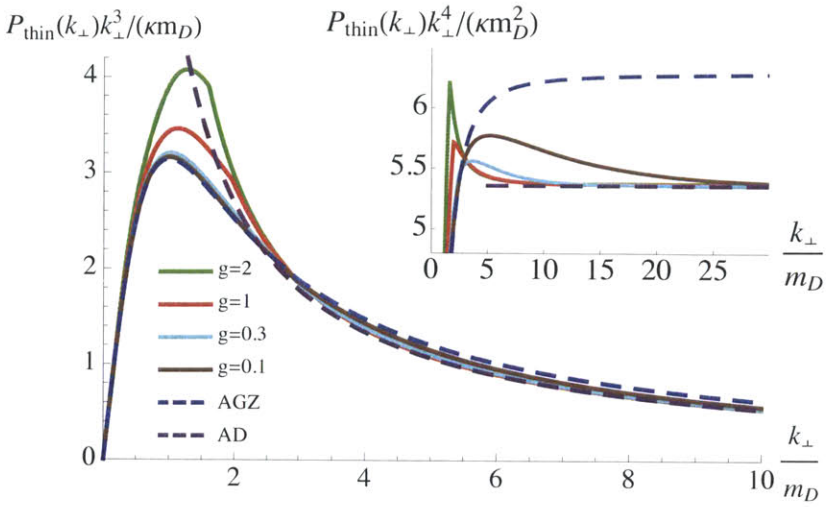

Figure 3-1: The continuous brown, light blue, red and green curves are the probability distribution $P_{\rm thin}(k_\perp)$ for $g = 0.1$, 0.3, 1 and 2 (bottom to top at low $k_\perp$, top to bottom at high $k_\perp$), multiplied by $k_\perp^3$ and $k_\perp^4$. In the IR, $P_{\rm thin}(k_\perp)$ agrees with $P_{\rm thin}^{\rm AGZ}(k_\perp)$ (shown as the dashed dark blue curves) and in the UV, $P_{\rm thin}(k_\perp)$ agrees with $P_{\rm thin}^{\rm AD}(k_\perp)$ (shown as the dashed purple curves). The only L-dependence in $P_{\rm thin}$ arises from it being proportional to κ meaning that, because we have plotted the probability distributions divided by κ, the quantities plotted are L-independent. We have scaled both axes by the appropriate power of the Debye mass m_D to make the quantities plotted dimensionless. Scaling the plots in this way also ensures that $P_{\rm thin}^{\rm AGZ}(k_\perp)$ and $P_{\rm thin}^{\rm AD}(k_\perp)$, shown as the dashed curves, are independent of g. The kinks in the curves for $g = 1$ and $g = 2$ are located at the $k_\perp = q_\perp^*$ where we do the matching described in Fig. 2-7.

3.2 Complete results for the probability distribution $P(k_\perp)$

The probability distribution $P(k_\perp)$ in (1.4) is obtained by Fourier transforming the function $\exp\left[\mathcal{W}_{\mathcal{R}}^{(2)}(x_\perp)\right]$ with $\mathcal{W}_{\mathcal{R}}^{(2)}$ given by (2.18). We see therefore that, if the medium being probed is a weakly-coupled plasma, $\mathcal{W}_{\mathcal{R}}^{(2)}(x_\perp)$ is the only "soft function" through which properties of the medium enter into the probability distribution for momentum broadening. $\mathcal{W}_{\mathcal{R}}^{(2)}(x_\perp)$ is proportional to κ and depends on the gauge coupling constant g, with most of the latter dependence coming via its dependence on the Debye mass m_D given in (2.42). We illustrate this in Fig. 3.2, where we plot $\mathcal{W}_{\mathcal{R}}^{(2)}(x_\perp)/\kappa$ versus $x_\perp m_D$ for several values of g. We have described in detail how we

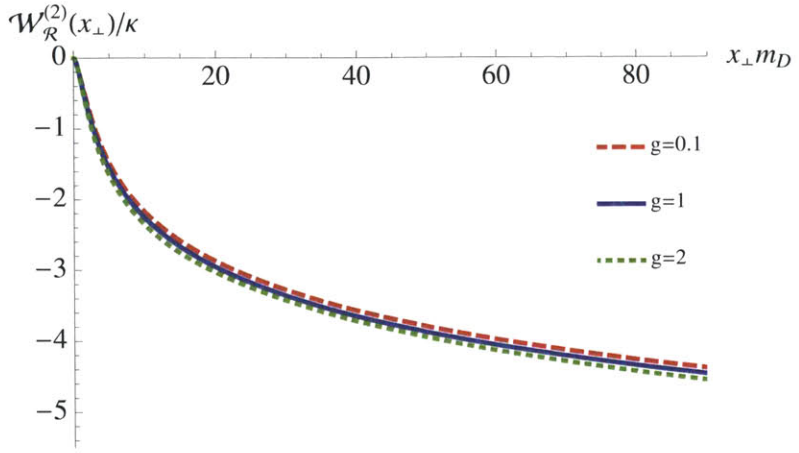

Figure 3-2: $\mathcal{W}_{\mathcal{R}}^{(2)}(x_\perp)/\kappa$ for gauge coupling constants $g = 0.1$, 1 and 2. $\mathcal{W}_{\mathcal{R}}^{(2)}(x_\perp)/\kappa$ is independent of κ and, when plotted versus $x_\perp$ in units of the inverse Debye mass, is almost independent of g.

evaluate $\mathcal{W}_{\mathcal{R}}^{(2)}(x_\perp)$ in Sections 2.2 and 2.3.

In the top panel of Fig. 3-3, we present our numerical results for the fully resummed probability distribution $P(k_\perp)$ that describes momentum broadening in a weakly coupled plasma with gauge coupling constant $g = 0.1$. We show our results for three different values of the thickness of the medium L, meaning three different values of κ. We have also plotted $P_{\rm thin}(k_\perp)$, and we see that when $\kappa = 0.1$ the medium is so thin that $P(k_\perp) \simeq P_{\rm thin}(k_\perp)$, meaning that there is no need to resum L-enhanced diagrams. Although $P_{\rm thin}(k_\perp) \propto \kappa$, meaning that $P_{\rm thin}(k_\perp)/\kappa$ in the Fig. 3-3 is κ-independent, our full result $P(k_\perp)$ has nontrivial κ-dependence at small $k_\perp$. This κ-dependence is better seen in the middle panel of the Fig. 3-3, where we plot $k_\perp^3 P(k_\perp)$. Note that the mean value of $k_\perp^2$, which is proportional to the jet quenching parameter $\hat{q}$ that we shall discuss in Section 3.3, is given by the area under the curves in this middle panel. We see from the Figure that increasing κ steadily shifts probability density away from small $k_\perp$, pushing it out to larger and larger $k_\perp$. This makes sense: as you make the medium thicker, the hard parton spends more time travelling through the medium, getting kicked, and so can pick up more and more transverse momentum. Finally, in the third panel of Fig. 3-3 we highlight the

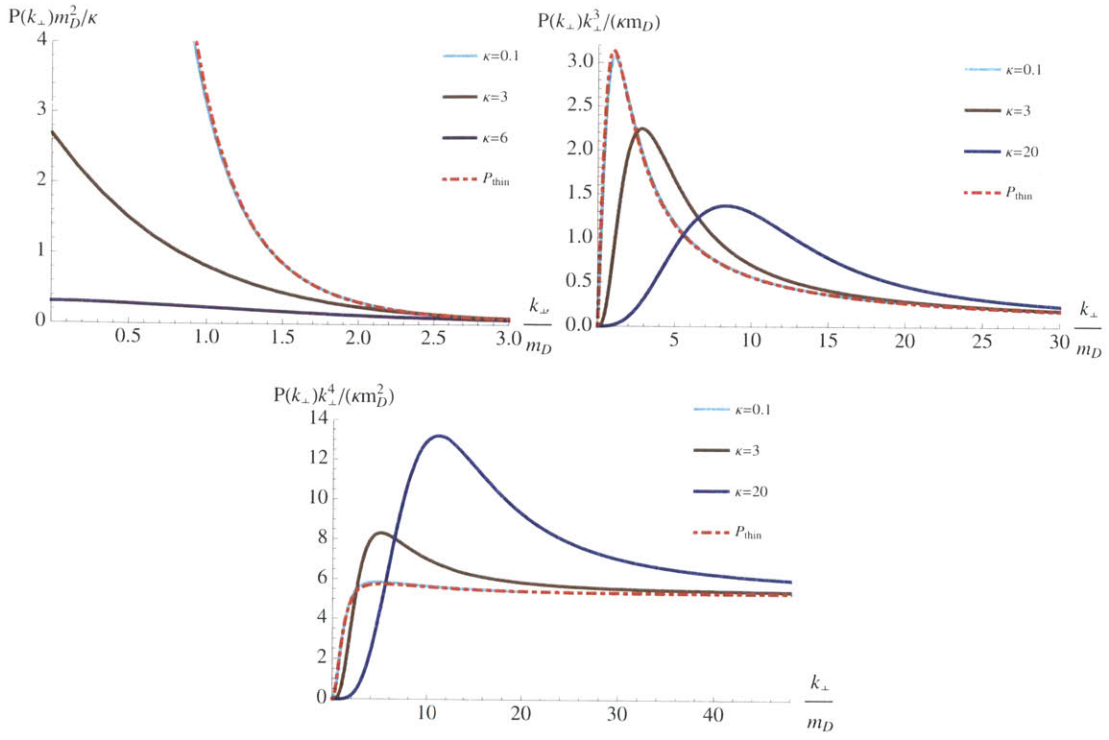

Figure 3-3: In the top left panel, we plot our full result for the probability distribution $P(k_\perp)$, after resumming the contributions of L-enhanced diagrams. We show our results at three different values of κ (κ increases from top to bottom at low $k_\perp$), and confirm that at $\kappa = 0.1$ our result agrees with $P_{\rm thin}(k_\perp)$. In the top right and lower panels, we multiply $P(k_\perp)$ by $k_\perp^3$ and $k_\perp^4$ in order to highlight the behavior at intermediate and large $k_\perp$, as well as at a larger value of κ, namely $\kappa = 20$. The gauge coupling constant is $g = 0.1$ throughout. All the probability distributions are normalized as in (1.3).

behavior of $P(k_\perp)$ at large $k_\perp$. We see that for any value of κ at large enough $k_\perp$ the probability distribution $P(k_\perp)$ approaches $P_{\rm thin}(k_\perp)$, meaning that resummation of L-enhanced diagrams is unnecessary. This is reasonable on physical grounds: for any value of κ there will be some $k_\perp$ that is so large that the most probable way of picking up this improbably large $k_\perp$ is via a single scattering, which is described by $P_{\rm thin}(k_\perp)$.

We expect from Fig. 3.2, and confirm in Fig. 3-4, that once we plot $P(k_\perp)$ relative to $k_\perp/m_D$, there is little remaining g-dependence. We see from Fig. 3-4 that the g-dependence is at most about 10% at $\kappa = 0.1$, and even much smaller than that

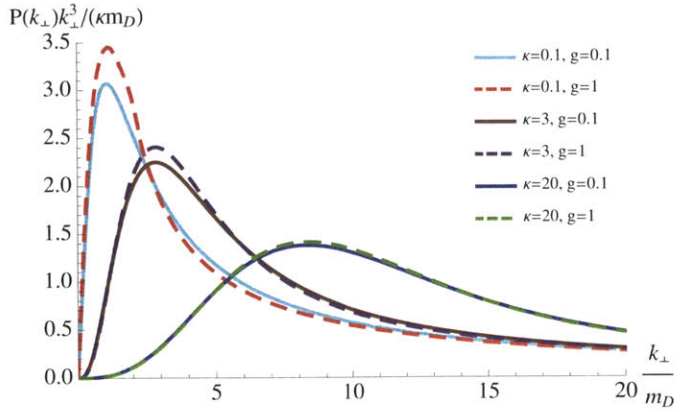

Figure 3-4: Probability distribution $P(k_\perp)$ at three different values of κ, multiplied by $k_\perp^3$ and plotted as in the middle panel of Fig. 3-3, but for two different values of g.

at $\kappa = 20$. Note that what Fig. 3-4 demonstrates is that, when plotted in this way, our results are insensitive to increasing g *at fixed* κ. Increasing g while holding κ fix requires reducing L. If, instead, we increase g at fixed L, this corresponds to increasing κ — which (we see in Figs. 3-3 and 3-4 and below) has a marked effect on our results.

The κ-dependence of $P(k_\perp)$ at small $k_\perp$ manifest in Fig. 3-3 is interesting. For very small κ, $P(k_\perp) \simeq P_{\rm thin}(k_\perp)$, which diverges proportional to $1/k_\perp^2$ at small $k_\perp$, as in (3.5). Plotting our results at many more values of κ than we have shown in Fig. 3-3 indicates that $P(k_\perp)$ diverges as $k_\perp \to 0$ if $\kappa < 2$ and is finite at $k_\perp = 0$ for $\kappa \geq 2$, and indicates that $P(k_\perp)$ is linear in $k_\perp$ at small $k_\perp$ if $\kappa = 3$ (as illustrated in Fig. 3-3) and is quadratic in $k_\perp$ at small $k_\perp$ if $\kappa \geq 4$. All these features of the behavior of $P(k_\perp)$ in the $k_\perp \to 0$ limit can be demonstrated analytically, via approximating $P_{\rm thin}(k_\perp)$ by $P_{\rm thin}^{\rm AGZ}(k_\perp)$ as is valid for $k_\perp \to 0$, and then resumming L-enhanced diagrams. We present this analysis in Appendix F. We expect that the L-resummed $P^{\rm AGZ}(k_\perp)$ will agree with the full $P(k_\perp)$ at small $k_\perp$ because $P_{\rm thin}^{\rm AGZ}(k_\perp)$ agrees with $P_{\rm thin}(k_\perp)$ in this regime. The physical argument behind this expectation follows. For any value of $k_\perp$, resumming the L-enhanced diagrams means taking into account the possibility that the hard parton could pick up this $k_\perp$ via multiple scatterings, summing over the infinite number of ways of adding up individual kicks that yield $k_\perp$ in total. If we

consider some $k_\perp$ that is small enough that $P_{\rm thin}(k_\perp) \simeq P^{\rm AGZ}_{\rm thin}(k_\perp)$, then getting this $k_\perp$ via multiple kicks that each transfer momenta much larger than $k_\perp$ is improbable. The L-resummation is therefore dominated by terms in which each of the multiple kicks transfers momenta that are comparable to or smaller than $k_\perp$, meaning that all the multiple kicks being resummed are small enough that AGZ is a good approximation. We therefore expect that, after resummation, $P(k_\perp) \simeq P^{\rm AGZ}(k_\perp)$. We confirm this by explicit calculation in Appendix F. From the analysis in Appendix F we then learn that as $k_\perp \to 0$, the probability distribution $P(k_\perp)$ includes a term proportional to $k_\perp^2$ as well as a (possibly nonanalytic) term proportional to $k_\perp^{\kappa-2}$, which dominates at small enough $k_\perp$ if $\kappa < 4$. This term explains the qualitative features that we have described above.

We have seen that for $\kappa \geq 4$, the leading small-$k_\perp$ behavior of $P(k_\perp)$ is a constant minus a term quadratic in $k_\perp$. This immediately makes one think of a Gaussian. And, indeed, there is every reason to expect that at large κ we should find a Gaussian probability distribution at small enough $k_\perp$: large κ means a thick medium, meaning that the hard parton picks up its transverse momentum via the sum of many kicks. This means that in the large-κ regime we expect that momentum broadening can be thought of as diffusion in transverse momentum space, with a Gaussian probability distribution $P(k_\perp)$ arising via the central limit theorem. In Fig. 3-5, we illustrate $P(k_\perp)$ for three large values of κ, showing that at small enough $k_\perp$ we do indeed find a Gaussian probability distribution. For each κ, we fit a Gaussian of the form

$$P_{\rm fit}(k_\perp) = A \exp(-a\, k_\perp^2) \tag{3.8}$$

to $P(k_\perp)$ at low $k_\perp$. We determine A by requiring that $P_{\rm fit}(0) = P(0)$ and then determine the width parameter a by fitting the quadratic dependence of $\log P(k_\perp)$ around $k_\perp = 0$, i.e. by fitting the brown dashed parabolas to the results shown as the solid blue curves in the right panels of Fig. 3-5. (Although $P(k_\perp)$ is a normalized probability distribution, $P_{\rm fit}$ is not normalized since as we can see in Fig. 3-5 it has less weight in its high-$k_\perp$ tail.) In order to gauge the range of $k_\perp$ out to which

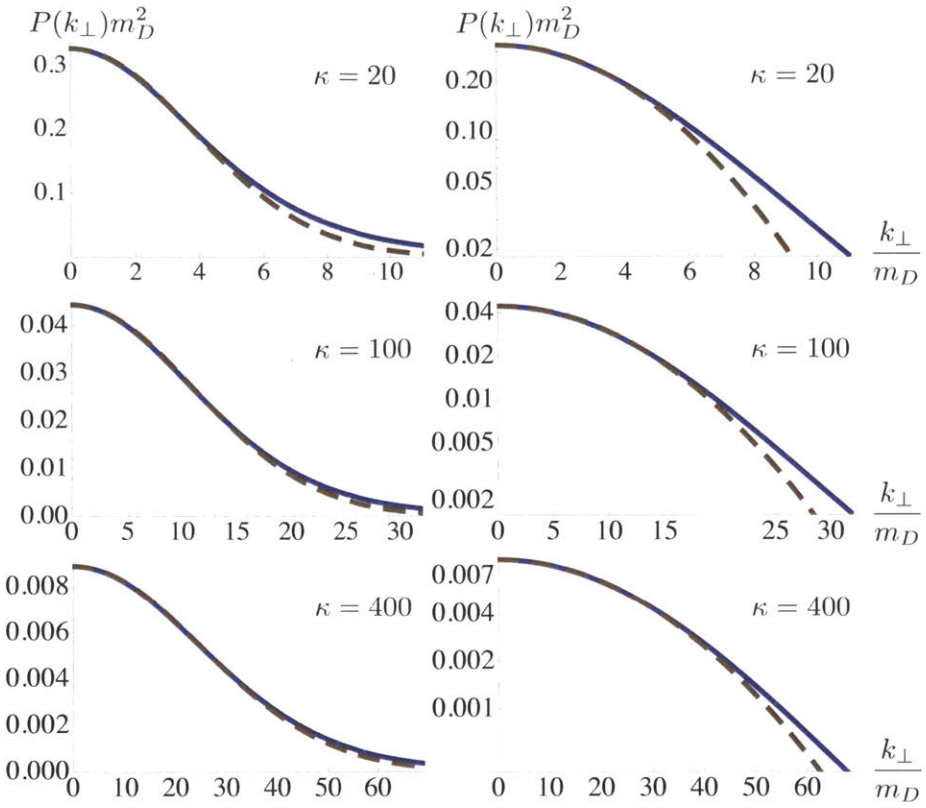

Figure 3-5: The solid blue curves show the probability distribution $P(k_\perp)$ describing momentum broadening in a weakly coupled plasma with $g = 0.1$ at three different large values of κ plotted on linear (left panels) and log (right panels) scales. For each κ, with the brown dashed curves we show a Gaussian fit of the form $P_{\rm fit}(k_\perp) = A\exp(-a\,k_\perp^2)$ to $P(k_\perp)$ at low $k_\perp$. We find $a\,m_D^2 = 0.0345$, 0.00410 and 0.000792 for $\kappa = 20$, 100 and 400. We see from the figures that at larger κ the Gaussian fit is a good approximation to $P(k_\perp)$ out to larger $k_\perp/m_D$, out to larger $k_\perp\sqrt{a}$, and down to lower probabilities. This is the central limit theorem in action.

the probability distribution $P(k_\perp)$ is well approximated by the Gaussian $P_{\rm fit}(k_\perp)$, we define $k_\perp^G$ as the value of $k_\perp$ where the Gaussian fit function starts to deviate from the actual result by 2%: $P(k_\perp^G) - P_{\rm fit}(k_\perp^G) = 0.02\,P(k_\perp^G)$. We see from Fig. 3-5 that the larger κ is, the larger is the $k_\perp^G$, both in units of m_D and in units of $1/\sqrt{a}$. More and more of the integrated probability is found in the regime in which the probability distribution is Gaussian at larger and larger κ. This is the central limit theorem in action.

We can confirm the reliability of the Gaussian fit that we have done by comparing our results for the Gaussian width parameter a to the value of a for the resummed

AGZ distribution $P^{\rm AGZ}(k_\perp)$ that we obtain in App. F. As we have already emphasized, the resummed AGZ distribution is an excellent approximation to the full probability distribution at small $k_\perp$, which is also where we find Gaussian behavior. Resumming the AGZ distribution should therefore describe the physics well in the region where we perform the fit, with the additional benefit of making it possible to do the calculation almost completely analytically. As described in detail in App. F, we fit the Gaussian (3.8) to $P^{\rm AGZ}(k_\perp)$ and find an expression for the width parameter a:

$$a\, m_D^2 = a^{\rm AGZ}\, m_D^2 \equiv \frac{1}{4}\frac{\int_0^\infty dx\, x^{3-\kappa} \exp\left[-\kappa\, K_0(x)\right]}{\int_0^\infty dx\, x^{1-\kappa} \exp\left[-\kappa\, K_0(x)\right]}\,, \tag{3.9}$$

with K_0 the modified Bessel function of the second kind. The values of a that we obtain from this expression with κ set to 20, 100 and 400, namely $a^{\rm AGZ}\, m_D^2 = 0.0362$, 0.00410 and 0.000763, are all within a few percent of those that we have obtained by fitting to our full results in Fig. 3-5. Naive application of the central limit theorem would suggest that the width of the Gaussian, $\propto 1/\sqrt{a}$, should increase like $\sqrt{L}$ and hence at fixed g it should increase with increasing κ like $\sqrt{\kappa}$. Instead we find both from our full results and from (3.9) that $1/a$ grows slightly faster than linearly with κ, apparently including a $\kappa \log \kappa$ term as well as a term proportional to κ.

We have also investigated the g-dependence of a by repeating the analysis shown in Fig. 3-5 at $g = 1$, instead of $g = 0.1$ as in the Figure. In so doing we find that a decreases by factors of 27000, 19000 and 16700 if we hold L fixed, increasing κ from the 20, 100 and 400 in the Figure to 2000, 10000 and 40000. If instead we hold κ fixed and increase g, we find that to a good approximation $1/a$ increases like g^2, as in (3.9). Our results for the width parameter a can therefore be summarized by writing $1/a = m_D^2 f(\kappa)$ for small values of g, with $f(\kappa)$ a function that grows slightly faster than linearly with κ at large κ. This means that $1/a$ grows slightly faster than like g^4 with increasing g at fixed L.

To this point we have focussed on the Gaussian behavior illustrated in Fig. 3-5 but it is just as important to see in these plots that for any κ, no matter how large, at large enough $k_\perp$ you see the $P(k_\perp) \propto 1/k_\perp^4$ behavior (3.7), which is the correct

form for $P(k_\perp)$ in the asymptotic ultraviolet $k_\perp \to \infty$ limit. This apparent failure of the central limit theorem arises because the underlying probability distribution for a thin medium $P_{\rm thin}(k_\perp)$ has a "fat tail": its power-law fall-off at large $k_\perp$ ensures that no matter how many scatterings are added up by resumming L-enhanced diagrams, i.e. no matter how thick the medium is, the behavior of $P(k_\perp)$ at large $k_\perp$ does not become Gaussian, it remains power-law. The physics behind this is that no matter how thick the medium there is a $k_\perp$ that is so large that the most probable way of picking up this much transverse momentum is via a single hard scattering. The "fat tail" of the $P_{\rm thin}(k_\perp)$ distribution ensures that, for large enough $k_\perp$, although such single hard scatterings are rare they are more probable than picking up such a large $k_\perp$ from multiple scatterings.

There are many previous analyses of momentum broadening via multiple scattering in a weakly coupled plasma in the literature in which approximations are made that result in a Gaussian form for $P(k_\perp)$. (See Refs. [66, 67, 30, 43, 42], for example, and see Appendix D for further discussion.) It is important to realize that altehough at large κ this is the correct form for "most of the probability", i.e. for a region in $k_\perp$ that contributes the lion's share of the normalization (1.3) of the probability density $P(k_\perp)$, at large enough $k_\perp$ the probability density is not Gaussian but rather a power law. And, in the $Q \to \infty$ limit (high jet-energy limit) in which the calculational framework within which we are working is controlled it is the large-$k_\perp$ power-law region of $P(k_\perp)$ that controls the jet quenching parameter $\hat{q} \propto \langle k_\perp^2 \rangle$, as we shall discuss in the next subsection. We shall see there that there is nevertheless a sense in which $1/(aL)$ can be thought of as a sort of "soft jet quenching parameter". More generally, it is interesting to ask how the width of the Gaussian component of $P(k_\perp)$ manifests itself in aspects of the phenomenology of jet quenching other than momentum broadening, even in the $Q \to \infty$ limit. However, $1/(aL)$ is *not* the jet quenching parameter. And, in fact, we shall see that in the $Q \to \infty$ limit any dependence of $\hat{q}$ on a is both subleading and implicit.

3.3 Jet quenching parameter

In this subsection we shall discuss the implications of our results for the jet quenching parameter $\hat{q}$, defined as

$$\hat{q} \equiv \frac{\langle k_\perp^2 \rangle}{L} = \frac{1}{L} \int \frac{d^2 k_\perp}{(2\pi)^2} k_\perp^2 P(k_\perp) \ . \tag{3.10}$$

Recall that in the large $k_\perp$ limit, the resummation discussed in Section 2.1 becomes unnecessary, and we recover the limiting behavior of $P_{\rm thin}(k_\perp)$ given in (3.7). We immediately see that the "fat tail" of the probability distribution, $P(k_\perp) \propto 1/k_\perp^4$ at large $k_\perp$, makes $\hat{q}$ defined in (3.10) logarithmically divergent in the ultraviolet. Hence, the jet quenching parameter $\hat{q}$ is not well-defined in a weakly coupled plasma. This UV divergence has been noted by many authors before us, for example in Refs. [20, 21, 53, 52, 54, 55]. Nevertheless, the quantity $\hat{q}$ enters in many calculations of parton energy loss, even though its definition is based entirely upon momentum broadening, and we therefore want to compare our results for this quantity to those in the literature. To that end, we shall follow standard practice in much of the literature and regulate the integral in (3.10) with an ultraviolet cutoff Λ_{UV}, which is usually thought of as being a kinematic cutoff of order $\Lambda_{\rm UV} \sim (QT)^{1/2}$, with Q the energy of the hard parton. The thinking behind this conventional choice is that $\Lambda_{\rm UV}$ should be of order the maximum $k_\perp$ that the hard parton of energy Q can pick up via a single scattering from a gluon in the medium with momentum of order T. More sophisticated, perhaps process-dependent, approaches are also possible [52, 68, 54, 69]. In the $Q \to \infty$ limit in which the calculational framework within which we are working is controlled, $\Lambda_{\rm UV}$ is much greater than the $k_\perp^G$ below which $P(k_\perp)$ is Gaussian and it must be in the regime in which $P(k_\perp) \propto 1/k_\perp^4$. We shall take this as given initially, but we shall later consider the possibility that $\Lambda_{\rm UV}$ may not always be so large for experimentally realizable values of Q.

Although our purpose in this subsection is to compare our results for $\hat{q}$ to those in the literature, we note here that for many purposes $\hat{q}$ may not be the most relevant parameter with which to characterize $P(k_\perp)$ in a weakly coupled plasma. Because $\hat{q}$

is ultraviolet-divergent in a weakly coupled plasma, in this setting it is determined by $P(k_\perp)$ at asymptotically large $k_\perp$, in a regime that contributes almost negligibly to the integrated probability. We have seen in Fig. 3-5 that although $P(k_\perp)$ has a "fat tail" that controls $\hat{q}$, most of the probability comes instead from the Gaussian region at lower $k_\perp$. So, in the case of a weakly coupled plasma the jet quenching parameter $\hat{q}$ describes only the tail, not the dog itself. In marked contrast, we shall see in the next subsection that in a plasma that is strongly coupled at all length scales, $P(k_\perp)$ is Gaussian at all momentum scales, and the jet quenching parameter $\hat{q}$ is finite, well-defined, and is the only parameter needed in order to characterize the entire probability distribution $P(k_\perp)$ [48, 41].

We turn now to the calculation of $\hat{q}$, with its ultraviolet divergence regulated in the conventional way. In Appendix G we show that for a probability distribution of the form (2.15) the jet quenching parameter $\hat{q}$ takes the form

$$\hat{q} = -\frac{1}{L}\,\nabla^2 \mathcal{W}_{\mathcal{R}}^{(2)}\Big|_{x_\perp=0} \ , \tag{3.11}$$

where ∇^2 is the Laplace operator in the transverse plane. Before proceeding to apply (3.11), we can make a very general point. If we were able to push our calculation through to all orders in perturbation theory, $\mathcal{W}_{\mathcal{R}}^{(2)}$ in (2.15) would be replaced by the sum of connected diagrams in the exponent in (2.14), which we can denote $\mathcal{W}_{\mathcal{R}}^{(c)}$. The calculation in Appendix G then still goes through, meaning that (3.11) becomes

$$\hat{q} = -\frac{1}{L}\,\nabla^2 \mathcal{W}_{\mathcal{R}}^{(c)}\Big|_{x_\perp=0} \ . \tag{3.12}$$

As we have discussed in Section 2.1, the contribution of each connected diagram to $\mathcal{W}_{\mathcal{R}}^{(c)}$ is proportional to L. We then see that (3.12) constitutes a proof that $\hat{q}$ is independent of L and, equivalently, of κ to all orders in perturbation theory. So, $\hat{q}$ can only depend on g and T as well as on $\Lambda_{\rm UV}$.

We now apply (3.11) to our weak-coupling result (2.18) for $\mathcal{W}_{\mathcal{R}}^{(2)}$ and find

$$\hat{q} = \frac{1}{L} \int \frac{d^2 k_\perp}{(2\pi)^2} k_\perp^2 P_{\rm thin}(k_\perp) \ , \tag{3.13}$$

which is divergent, as we expect. Even before we regulate the divergence, we notice the interesting result that $\hat{q}$ is the same as it would be if the probability distribution for momentum broadening were just $P_{\rm thin}(k_\perp)$, instead of $P(k_\perp)$. We have seen in the previous subsection that the resummation of length-enhanced diagrams completely changes the shape of $P(k_\perp)$, but we now see that in a weakly coupled plasma this resummation has no effect on $\hat{q}$. This makes sense since in a weakly coupled plasma $\langle k_\perp^2 \rangle$ is controlled by the ultraviolet power-law behavior of $P(k_\perp)$ which is unaffected by the resummation. In order to actually use the expression (3.13), we regulate it by introducing an ultraviolet cutoff $\Lambda_{\rm UV}$, as discussed above. (As long as $\Lambda_{\rm UV}$ is large enough, introducing the ultraviolet cutoff already in (3.10) would have been equivalent.)

Because we are assuming $\Lambda_{\rm UV} \gg k_\perp^G$, we can present our results in a semi-analytical form. First we divide the integral over the magnitude of $k_\perp$ in the expression (3.13) for $\hat{q}$ into two parts, one from 0 to $k'_\perp$ and the other from $k'_\perp$ to $\Lambda_{\rm UV}$, with $k'_\perp$ arbitrary except that it must satisfy $k'_\perp \ll \Lambda_{\rm UV}$, $k'_\perp \gg k_\perp^G$ and $k'_\perp \gg T$. We denote the two contributions to $\hat{q}$ by

$$\hat{q} = \hat{q}_{\rm IR} + \hat{q}_{\rm UV} \ . \tag{3.14}$$

Next, we observe that in the ultraviolet tail of $P_{\rm thin}(k_\perp)$ the retarded propagator in Eq. (2.23) is well approximated by the first order solution to the Dyson equation (2.20). This means that the Wightman propagator $D^>$, expressed in terms of the retarded propagator as in (2.19), takes the form

$$D^>(q_0, k_\perp) = (1 + f(q_0)) \, \frac{{\rm Im}\left(\Pi_R^L - \Pi_R^T\right)}{k_\perp^2 \left(k_\perp^2 + q_0^2\right)} \ . \tag{3.15}$$

We then define the dimensionless coefficient

$$b \equiv \int dq_0 \frac{(1+f(q_0))}{2\pi^2 T^3} \frac{k_\perp^2}{(k_\perp^2+q_0^2)} \frac{\mathrm{Im}\left(\Pi_R^L - \Pi_R^T\right)}{g^2} \ . \tag{3.16}$$

Given the behavior of the imaginary part of the self-energy in the UV limit, the constant b does not depend on either $k_\perp$ or g. We have defined b so as to allow us to write a very compact expression for the probability distribution $P_{\rm thin}(k_\perp)$ that is valid only in the ultraviolet limit,

$$P_{\rm thin}^{\rm UV}(k_\perp) = 2\pi\, b\, g^4 C_R \frac{LT^3}{k_\perp^4} \ , \tag{3.17}$$

and from this we determine that the UV contribution to the jet quenching parameter is given by

$$\hat{q}_{\rm UV} = b\, g^4 C_R\, T^3 \int_{k'_\perp}^{\Lambda} \frac{dk_\perp}{k_\perp} = b\, g^4 C_R\, T^3 \log \frac{\Lambda}{k'_\perp} \ . \tag{3.18}$$

The arbitrary scale $k'_\perp$ must be large enough that we can safely apply all the UV approximations just discussed. From its definition in Eq. (3.16), we can calculate the value of b explicitly. We find

$$b = 0.2035 \ . \tag{3.19}$$

To check our results against those in the literature, we identify the factor corresponding to b in the result (3.7) from Ref. [52], finding

$$b^{\rm AD} = \frac{1}{2\pi} \frac{7\,\zeta(3)}{4\,\zeta(2)} = 0.2035 \ . \tag{3.20}$$

Our expression for $\hat{q}_{\rm UV}$ is therefore in excellent agreement with that obtained by Arnold and Dogan.

Turning now to the IR, we have

$$\hat{q}_{\rm IR} = \frac{1}{2\pi L} \int_0^{k'_\perp} dk_\perp k_\perp^3 P_{\rm thin}(k_\perp) \ . \tag{3.21}$$

Since we chose $k'_\perp$ to be well into the UV region, the integral in (3.21) must depend

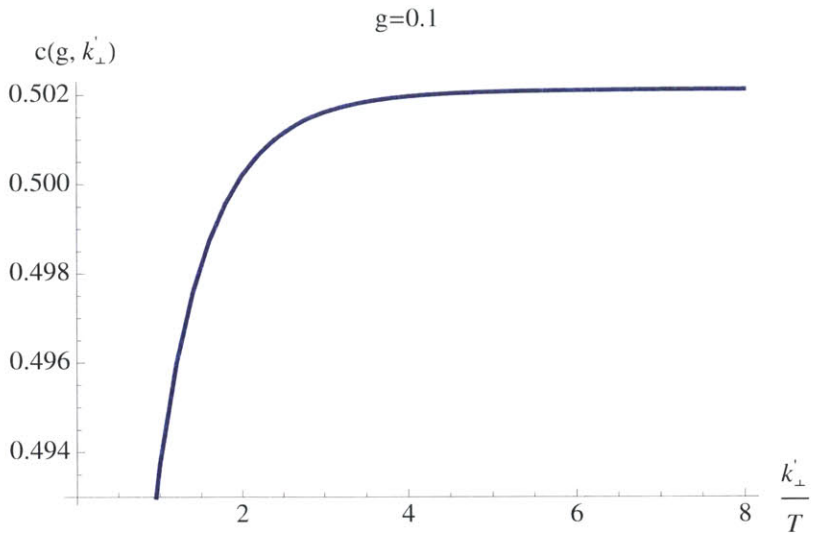

Figure 3-6: The function $c(g, k'_\perp)$ as a function of $k'_\perp$, with the gauge coupling set to $g = 0.1$. For large enough $k'_\perp$, $c(g, k'_\perp)$ becomes constant.

logarithmically on $k'_\perp$. To isolate this known logarithmic behavior, we define the function $c(g, k'_\perp)$ via the expression

$$\hat{q}_{\rm IR} = g^4 C_R T^3 \left[c(g, k'_\perp) + b \log \frac{k'_\perp}{T} \right] , \tag{3.22}$$

in which $\hat{q}_{\rm IR}$ is to be evaluated using (3.21) and which therefore serves to define c. The function $c(g, k'_\perp)$ is plotted in Fig. 3-6 as a function of $k'_\perp$ for $g = 0.1$. We see that for large enough $k'_\perp$, the function $c(g, k'_\perp)$ becomes independent of $k'_\perp$. And, we anyway needed to choose $k'_\perp \gg T$ in order to control the behavior of $\hat{q}_{\rm UV}$. Upon making this choice, $c(g, k'_\perp) \simeq c(g)$. The only way that properties of the probability distribution $P_{\rm thin}(k_\perp)$ in the IR, and indeed in any region of $k_\perp$ except the UV, enter into the calculation of $\hat{q}$ is through the function $c(g)$. In some implicit way, $c(g)$ is related to the properties of the $P(k_\perp)$ distribution that we discussed in Section 3.2, like for example the width $1/\sqrt{a}$ of its Gaussian component at large κ. Notice, however, that $c(g)$ appears only in a subleading contribution to $\hat{q}$; the dominant contribution comes from the logarithmic UV divergence. We have computed $c(g)$ for several different g

values, obtaining

$$c(g) = \begin{cases} 1.0363 \text{ for } g = 0.01 \\ 0.5023 \text{ for } g = 0.1 \\ 0.0368 \text{ for } g = 1 \\ -0.0795 \text{ for } g = 2 \end{cases} . \tag{3.23}$$

Finally, we combine the two contributions $\hat{q}_{\rm UV}$ in Eq. (3.18) and $\hat{q}_{\rm IR}$ in Eq. (3.22). Summing them, we find

$$\hat{q} = g^4 C_R T^3 \left(b \log \frac{\Lambda_{\rm UV}}{T} + c(g) \right) , \tag{3.24}$$

where the dependence on the arbitrarily chosen $k'_\perp$ has dropped out, as it must. Thus, at the end of the day we find that the jet quenching parameter is specified by the constant b and the function of the coupling constant $c(g)$, as well as T, $\Lambda_{\rm UV}$ and g itself. Our results for b and $c(g)$ are given in (3.19) and (3.23), respectively. As a comparison, the AGZ distribution in (3.5) gives

$$\hat{q}^{\rm AGZ} = g^4 C_R T^3 \frac{3}{4\pi} \log \frac{\Lambda_{\rm UV}}{m_D} , \tag{3.25}$$

from which we can read off the coefficients

$$b^{\rm AGZ} = \frac{3}{4\pi} , \qquad c^{\rm AGZ}(g) = -\frac{3}{4\pi} \log \left(g\sqrt{\frac{3}{2}} \right) . \tag{3.26}$$

The coefficients b and $b^{\rm AGZ}$ differ by $\approx 15\%$. This is the discrepancy between the ultraviolet tails of $P_{\rm thin}(k_\perp)$ and $P^{\rm AGZ}_{\rm thin}(k_\perp)$ (recall that $P^{\rm AGZ}_{\rm thin}(k_\perp)$ is not valid in the ultraviolet) that we have already seen in Fig. 3-1. The values of $c(g)$ and $c^{\rm AGZ}(g)$ are in good agreement for small values of g, and differ more for larger values of g, where $P_{\rm thin}(k_\perp)$ starts to differ from $P^{\rm AGZ}_{\rm thin}(k_\perp)$.

We can even plug in explicit values for the parameters in a range that is reasonable for jets produced in heavy ion collisions at the LHC. We pick the benchmark values $T = 300\,\text{MeV}$ and $L = 5\,\text{fm}$ for the plasma temperature and thickness, respectively.

We choose the UV cutoff to be $\Lambda_{\rm UV} = 17\,{\rm GeV}$. (This can be thought of as the kinematic limit for a 300 GeV parton scattering off a 1 GeV parton from the medium.) We consider the momentum broadening of a hard gluon, meaning that we set $C_{\mathcal{R}} = 3$, and find

$$\hat{q} = 0.411\, g^4 (0.822 + c(g))\, {\rm GeV}^2\, {\rm fm}^{-1}\ . \tag{3.27}$$

If we then choose $g = 2$, corresponding to $\alpha_{\rm QCD} = 0.32$, this would correspond to a jet quenching parameter $\hat{q} \simeq 4.9\,{\rm GeV}^2{\rm fm}^{-1}$. With these choices of parameters, $\kappa \simeq 14.5$, large enough that the resummation of length-enhanced diagrams is certainly necessary in order to obtain $P(k_\perp)$. With $\kappa \simeq 14.5$, extrapolating from Fig. 3-5 we estimate $k_\perp^G \sim 4m_D$, meaning that with the parameters we have chosen it is around 3 GeV. So, our assumption that $\Lambda_{\rm UV} \gg k_\perp^G$ is reasonable, as is our calculation in which $\hat{q}$ is dominated by the tail of the probability distribution $P(k_\perp)$.

Although the calculation breaks down if we do so, it is also interesting to speculate as to how its results differ if we attempt to use parameters more appropriate for the momentum broadening of hard partons produced in heavy ion collisions at RHIC. In the RHIC context, $\Lambda_{\rm UV}$ must be much smaller, first because the hard partons only have $Q \sim 30 - 40$ GeV and second because the temperature is somewhat lower. Likely, $\Lambda_{\rm UV}$ cannot be much more than 5 GeV. Also, the relevant values of g must be somewhat larger at RHIC than at the LHC. With κ increasing like g^2, according to Fig. 3-5 this will result in a larger $k_\perp^G$. This means that the assumption that $\Lambda_{\rm UV} \gg k_\perp^G$ has broken down, as has our calculation of (3.27). Of course, the whole calculational framework is breaking down too, for two independent reasons: g is becoming uncomfortably large and we can no longer trust the $Q \to \infty$ limit as a guide.

Motivated both by jet quenching at RHIC and by the analysis of the strongly coupled plasma that we shall discuss in the next subsection, it is worth asking what happens if $\Lambda_{\rm UV} < k_\perp^G$ even though as we have just described our weakly coupled calculation is not at all under control in this regime. If we nevertheless apply our results, when $\Lambda_{\rm UV}$ lies within the regime in which $P(k_\perp)$ is well fit by a Gaussian of

the form (3.8) then the power-law tail of the probability distribution is irrelevant in the calculation of the jet quenching parameter, since the integral in (3.13) is cutoff before the power-law tail makes its appearance. $\hat{q}$ is determined entirely from the Gaussian region, and is given in terms of the width $1/\sqrt{a}$ of the Gaussian (3.8) by

$$\hat{q}_{\rm soft} = \frac{1}{aL} \ , \tag{3.28}$$

where we have introduced the subscript "soft" to remind ourselves that this result is only valid if $\Lambda_{\rm UV} < k_\perp^G$ and in particular is not valid in the $Q \to \infty$ limit where the full calculation is controlled. Even though $\hat{q}_{\rm soft}$ is not the actual jet quenching parameter $\hat{q}$ (which is defined in the $Q \to \infty$ limit and is given by (3.24)) since $\hat{q}_{\rm soft}$ is determined by the width of the Gaussian that describes the lion's share of the probability in $P(k_\perp)$ rather than by the power-law tail it could certainly turn out that $\hat{q}_{\rm soft}$ is more relevant to the phenomenology of jet quenching than $\hat{q}$ itself. Our attempt to plug numbers into our results suggests that this circumstance is more likely to arise for jets produced in heavy ion collisions at RHIC and is less likely to arise in the case of the highest energy jets produced in heavy ion collisions at the LHC.

3.4 From weak to strong coupling

We have calculated the probability distribution $P(k_\perp)$ for momentum broadening in a weakly coupled quark-gluon plasma in QCD. We anticipate that our calculation is only quantitatively reliable for $g < 1$. For example, we argued in Section 3.2 based upon evidence visible in Fig. 3-1 that the matching that we describe in Section 2.3 is not quantitatively reliable at $g = 1$ and $g = 2$, although it is gratifying that the small kinks in the $g = 1$ and $g = 2$ curves in Fig. 3-1 have no visible effects in Fig. 3.2, and therefore no visible effects on our results, as plotted in Figs. 3-3, 3-4 and 3-5. Although it is important on theoretical grounds that we have control of the calculation for $g < 1$, this is of little phenomenological interest. The smallest values

of g that are typically used in comparisons to data from heavy ion collisions at RHIC and the LHC are around $g \sim 2$. (Note that $g = 2$ corresponds to $\alpha_{\rm QCD} \simeq 0.32$, in many other contexts a weak coupling.) There are other good reasons beyond the large value of g not to trust a weakly coupled description of the plasma produced in heavy ion collisions at RHIC and the LHC, chief among them being the suite of evidence that this plasma is a strongly coupled liquid with a shear viscosity that is so small that no description in terms of weakly interacting quark and gluon quasiparticles can be self-consistent. That said, it is nevertheless natural to ask, at least at a qualitative level, what our results suggest for $P(k_\perp)$ at $g \sim 2$ and beyond. At a qualitative level, the answer is provided by Fig. 3-5. By far the most important consequence of increasing g at fixed L is the increase in κ, and we see from Fig. 3-5 that increasing κ makes the probability distribution $P(k_\perp)$ for momentum broadening "more and more Gaussian." That is, $P(k_\perp)$ is well-approximated as Gaussian out to larger and larger $k_\perp$ and for a larger and larger fraction of the total probability, pushing the appearance of the power-law behavior that must be present at asymptotic $k_\perp$ out to larger and larger $k_\perp$.

The qualitative expectations for the behavior of $P(k_\perp)$ at strong coupling that we have gleaned by looking at how our results behave at large κ are nicely borne out in the strongly coupled plasma of $\mathcal{N} = 4$ supersymmetric Yang-Mills (SYM) theory. Taking advantage of the fact that this theory, at both zero and nonzero temperature, has a dual gravitational description [70, 85, 71, 72, 73, 74, 75, 76], holographic calculations of many aspects of its plasma phase have been used to gain varied insights into the physics of strongly coupled plasma more generally [77]. Of interest to us, the expectation value of the Wilson loop in Eq. (2.3), and from it the probability distribution for momentum broadening, have been calculated for $\mathcal{N} = 4$ SYM theory in the strong coupling and large-N_c limit [48, 41]. For a propagating gluon in the adjoint representation, the result reads

$$P^{\rm SYM}(k_\perp) = \frac{4\tilde{a}}{\pi\sqrt{\lambda}T^3L} \exp\left[-\frac{\tilde{a}\,k_\perp^2}{\pi^2\sqrt{\lambda}T^3L}\right] , \tag{3.29}$$

where $\lambda \equiv g^2 N_c$ is the 't Hooft coupling, assumed large, and where

$$\tilde{a} \equiv \sqrt{\pi}\,\Gamma(5/4)/\Gamma(3/4) \approx 1.311. \tag{3.30}$$

We see immediately that in this theory, whose plasma is strongly coupled at all scales, $P(k_\perp)$ is Gaussian out to arbitrarily large $k_\perp$, which is consistent at a qualitative level with the expectations derived from extending our calculation for a weakly coupled plasma to larger values of g and hence κ, as we have described above. At a qualitative level, the lesson from (3.29) is that in a strongly coupled plasma momentum broadening should be thought of as diffusion in transverse momentum space, even though in the calculation behind (3.29) there is no thin-medium regime, no analogue of starting with some $P_{\rm thin}$ and resumming length-enhanced diagrams, and hence no picture of multiple scattering off quasiparticles building up a Gaussian $P(k_\perp)$ via the central limit theorem. In a strongly coupled plasma, $P(k_\perp)$ is always Gaussian at any $k_\perp$, for any L. At a qualitative level, such a regime can be approached starting from a weakly coupled plasma either by increasing the coupling or by increasing L, either of which corresponds to increasing κ.

Although the qualitative picture that we have just sketched is pleasing, it is important to note that at a quantitative level the Gaussian probability distribution (3.29) is quite different from the Gaussian that we obtained by fitting to our results for a weakly coupled plasma at large κ in Fig. 3-5. In particular, the width of the Gaussian in (3.29) increases with increasing g only like $\lambda^{1/4} \sim \sqrt{g}$ while we found in Section 3.2 that the width $1/\sqrt{a}$ of the Gaussians in Fig. 3-5 increase with increasing g somewhat faster than g^2.

The result quoted in Eq. (3.29) was derived in the $\lambda \to \infty$ limit. For large but finite 't Hooft coupling λ, we cannot conclude that $P(k_\perp)$ will be Gaussian at all scales. It is reasonable to expect that in this case like at weak coupling $P(k_\perp)$ will be Gaussian only for $k_\perp$ less than some $k_\perp^G$, with $k_\perp^G \to \infty$ as $\lambda \to \infty$ and consequently $\kappa \to \infty$. The form of $P(k_\perp)$ for $k_\perp > k_\perp^G$, where the Gaussian description breaks down, is not known. However, since there are no quasiparticles off which hard scattering

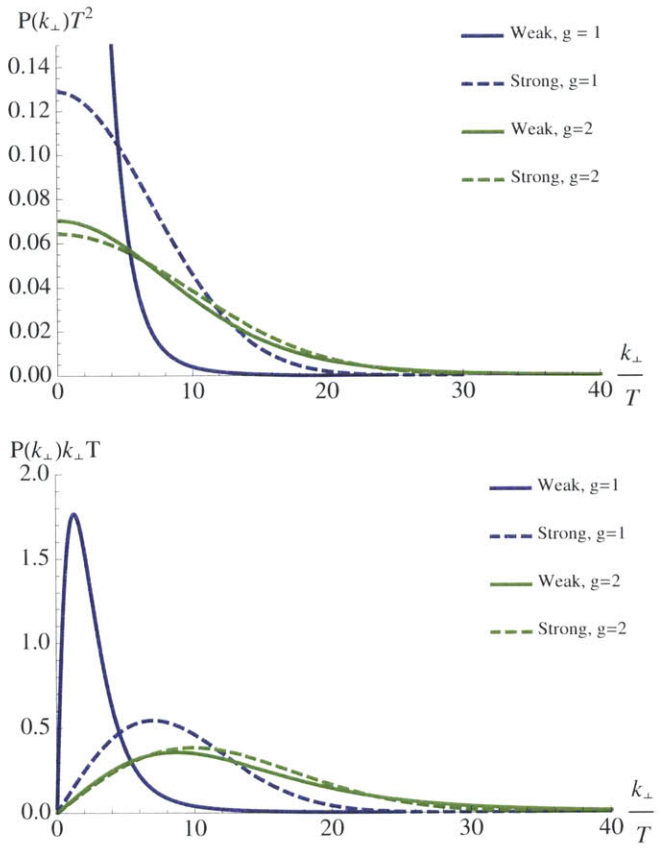

Figure 3-7: Probability distributions for momentum broadening $P(k_\perp)$ for weakly coupled QCD plasma with $g = 1$ (continuous blue curve) and $g = 2$ (continuous green) and $P^{\rm SYM}(k_\perp)$ for strongly coupled $\mathcal{N} = 4$ SYM plasma with $N_c = 3$ and $g = 1$ (blue dashed) and $g = 2$ (green dashed). The curves are for propagation of a hard gluon through a region of plasma with thickness $L = 5$ fm, and temperature $T = 300$ MeV.

can occur in the $\mathcal{N} = 4$ SYM theory plasma with large but finite λ, we anticipate that even where $P(k_\perp)$ is not Gaussian it will continue to fall off more rapidly than any power of $k_\perp$ at large $k_\perp$.

We illustrate both the qualitative and the quantitative comparisons that we have just made between $P(k_\perp)$ in weakly coupled QCD plasma and $P^{\rm SYM}(k_\perp)$ in strongly coupled $\mathcal{N} = 4$ SYM plasma in Fig. 3-7 by plotting both for $g = 1$ and $g = 2$. In QCD, $g = 1$ and 2 correspond to $\alpha_{\rm QCD} = 0.08$ and 0.32 while in $\mathcal{N} = 4$ SYM theory with $N_c = 3$, these couplings correspond to $\lambda = 3$ and 12. It is interesting to note that $g = 2$ is in a regime in which $\alpha_{\rm QCD} = 0.32$ is considered a weak coupling in some

contexts and $\lambda = 12$ is considered a strong coupling in some contexts. We perform the comparison for a plasma with temperature $T = 300\,\mathrm{MeV}$ that is $L = 5\,\mathrm{fm}$ thick. With these choices, $g = 1$ and 2 correspond to $\kappa = 3.6$ and $\kappa = 14.5$. We see in Fig. 3-7 that upon increasing g from 1 to 2, the width of $P(k_\perp)$ for the weakly coupled QCD plasma increases much more rapidly than the width of the Gaussian (3.29) for the strongly coupled plasma does, as we have described above. Perhaps the most striking aspect of Fig. 3-7 is just how similar $P(k_\perp)$ with $g = 2$ and $P^{\mathrm{SYM}}(k_\perp)$ with $g = 2$ and hence $\lambda = 12$ are, in particular when plotted as in the top and middle panels. This is an indication that at this value of the coupling the strongly coupled and weakly coupled perspectives yield comparable descriptions of momentum broadening for low and moderate values of $k_\perp/T$. We see in the bottom panel of Fig. 3-7, however, that the physics of the two descriptions is completely different at large-$k_\perp$, where we see that the probability distribution $P(k_\perp)$ has a power-law tail only for the weakly coupled plasma.

We further illustrate the sharp distinction between the behavior of $P(k_\perp)$ at large $k_\perp$ in weakly and strongly coupled plasma in Fig. 3-8. Because the probability distribution for the plasma that is strongly coupled at all scales is Gaussian whereas that for the weakly coupled plasma is proportional to $1/k_\perp^4$ at large $k_\perp$, no matter how large the coupling is there is always a $k_\perp$ beyond which $P(k_\perp)$ is greater in the weakly coupled plasma than in the strongly coupled plasma. This behavior, which at first hearing may sound counterintuitive, reflects the presence of point-like quasiparticles in the weakly coupled plasma. This means that, as Rutherford could have understood, although the probability for large-angle, large-$k_\perp$, scattering is always low it is much larger in a plasma containing point-like scatterers than it would be in a liquid plasma with no quasiparticles at any length-scale like the strongly coupled plasma of $\mathcal{N} = 4$ SYM theory. In Fig. 3-8 we plot the integrated probability that a hard parton propagating through $L = 5$ fm of either the weakly coupled QCD plasma or the strongly coupled $\mathcal{N} = 4$ SYM plasma with temperature $T = 300$ MeV picks up a transverse momentum kick $k_\perp > k_\perp^{\mathrm{min}}$. As we can see, in the strongly coupled plasma with its Gaussian $P^{\mathrm{SYM}}(k_\perp)$, this integrated probability is completely negli-

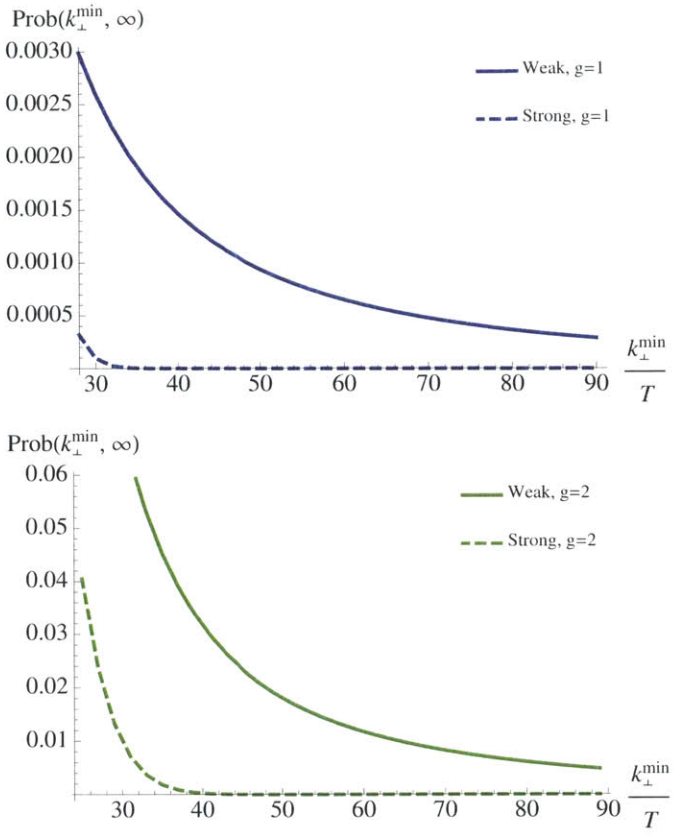

Figure 3-8: Probability that a hard gluon receives a transverse momentum greater than $k_\perp^{\min}$ after propagating a distance L through a weakly coupled QCD plasma or a strongly coupled $\mathcal{N} = 4$ SYM plasma with temperature T and coupling constant g. Values of g, T and L as well as color conventions for the curves are all as in Fig. 3-7.

gible for $k_\perp^{\min} \gtrsim 40\,T$. In stark contrast, if we assume a weakly coupled QCD plasma and then set $g = 2$, this integrated probability is still more than half a percent for $k_\perp^{\min} = 80\,T$. So, although the two probability distributions are quite similar in the regime of $k_\perp$ which is probable — indicating that momentum broadening for most partons would be comparable in these two cases — rare hard, large-angle, scatterings will be very much more common if the weakly coupled QCD analysis yields a reasonable approximation.

If we evaluate our results for the momentum broadening of a hard quark rather than a hard gluon, the conclusions of the above paragraph become even stronger. The widths of the Gaussian probability distributions $P^{\rm SYM}(k_\perp)$ describing the momentum

broadening of a hard quark in the strongly coupled $\mathcal{N} = 4$ SYM plasma are half as wide as those in Fig. 3-7 [48], meaning that the dashed curves plotted in Fig. 3-8 are pushed down so much that they are indistinguishable from the horizontal axis across the whole range of $k_\perp$ in Fig. 3-8. At weak coupling, in the ultraviolet $P(k_\perp)$ is proportional to $C_\mathcal{R}$, meaning that the solid curves in Fig. 3-8 get multiplied by a factor of 4/9 if one treats a hard quark instead of a hard gluon. So, in a weakly coupled QCD plasma with $g = 2$ and L and T as in Fig. 3-8 the integrated probability that a hard quark picks up $k_\perp^{\rm min} = 30\,T$ $(60\,T)$ or more in transverse momentum is more than two percent (about half a percent), while either of those integrated probabilities is completely negligible in the strongly coupled plasma with its Gaussian $P^{\rm SYM}(k_\perp)$. Because QCD is asymptotically free, its strongly coupled liquid quark-gluon plasma must emerge from weakly coupled quarks and gluons that can be resolved at short enough length scales. We therefore expect that for large enough $k_\perp$ our weakly coupled QCD analysis yields a reasonable approximation to $P(k_\perp)$, meaning that we expect that although large-angle scattering is rare it will be very much more common than it would be if the quark-gluon plasma were a strongly coupled liquid at all length scales.

3.5 Outlook

We have calculated the probability distribution $P(k_\perp)$ for an energetic parton that propagates for a distance L without radiating through weakly coupled quark-gluon plasma with temperature T to pick up transverse momentum $k_\perp$. Our calculation is built upon Soft Collinear Effective Theory (SCET), but to date we have not used much of the power of SCET, which could in future be brought to bear on the question of calculating corrections (for example in the ratio of T to the parton energy) to leading order results like ours. Before doing this, however, the most pressing next steps beyond our calculation are to include the radiation of collinear and soft gluons.

To date, SCET has been used to relate $P(k_\perp)$ in any medium to $\mathcal{W}_\mathcal{R}(x_\perp)$, the expectation value in that medium of a Wilson loop with two long light-like sides sep-

arated in the transverse direction by a distance $x_\perp$. What we have done here is to use standard methods from real time thermal field theory, including Hard Thermal Loop resummation where needed (see Section 2.3 for an explanation of where it is needed), to calculate the expectation value $\mathcal{W}_\mathcal{R}(x_\perp)$ and from it the probability for momentum broadening $P(k_\perp)$, for the case in which the medium is weakly coupled quark-gluon plasma in thermal equilibrium at temperature T, as in QCD at temperatures that are sufficiently high that the QCD coupling constant g is less than one.

We first obtained $P_{\rm thin}(k_\perp)$ for a "thin medium", in which κ (proportional to g^2LT and defined in (3.1)) is much less than one. We have checked that our results in this regime agree with previous determinations, both at large and small $k_\perp$. Although it is a stretch to apply a calculation that requires $g < 1$ to plasma at temperatures such that $g \sim 2$ we do so anyway, since the lowest estimates of the coupling constant in the plasma produced in heavy ion collisions at RHIC and the LHC are in this range. Doing this requires consideration of values of κ that are significantly greater than one. (A reasonable choice like $L \sim 5$ fm and $T \sim 300$ MeV corresponds to $\kappa \sim 14$ if $g \sim 2$.) Handling $\kappa > 1$ required us to resum an infinite class of length-enhanced planar diagrams in order to obtain the leading behavior of $P(k_\perp)$. After resumming the L-enhanced diagrams we obtain results valid for any value of κ including $\kappa \gg 1$. We find that in a weakly coupled plasma the properties of the plasma enter the calculation of $P(k_\perp)$ only through the retarded gluon propagator. We computed the self-energy therein using real time thermal field theory, including Hard Thermal Loop resummation in the infrared. We find that the form of $P(k_\perp)$ changes qualitatively between $\kappa < 2$, where it diverges at small $k_\perp$, and $\kappa > 4$ where it looks Gaussian at small $k_\perp$. Our entire discussion is only valid to leading order in the coupling constant g. It will be interesting in the future to quantify the effects of length-enhancement at large κ for existing next-to-leading order calculations [54].

At large κ, we find that $P(k_\perp)$ takes the form of a Gaussian at small $k_\perp$ with a power-law tail, proportional to $1/k_\perp^4$, at large $k_\perp$. As κ increases, more and more of the integrated probability resides in the Gaussian, with the power-law tail contributing less and less. Since $\kappa \to \infty$ can equally well be thought of as the strong coupling limit

as the large-L limit, at a qualitative level our large-κ results are pleasingly consistent with the known behavior of $P(k_\perp)$ in the plasma of large-N_c $\mathcal{N}=4$ SYM theory in the strong coupling limit. In this theory, $P(k_\perp)$ is precisely Gaussian, with no power-law tail at all. Although the widths of the Gaussian in the strongly coupled $\mathcal{N}=4$ SYM plasma and of the Gaussian that characterizes $P(k_\perp)$ in the weakly coupled QCD plasma for all but improbably large values of $k_\perp$ do not agree quantitatively, and in particular have different g-dependence, it is interesting to note that they are remarkably similar for $g=2$, a value of the coupling that can reasonably be thought of as weak since $g^2/(4\pi)$ is small and that can reasonably be thought of as strong since $g^2 N_c$ is large for $N_c=3$.

The most noteworthy difference between momentum broadening in the weakly coupled QCD plasma and in the strongly coupled $\mathcal{N}=4$ SYM plasma is at large $k_\perp$. Because it has $P(k_\perp) \propto 1/k_\perp^4$ at large $k_\perp$, no matter how small κ or g is there will always be a $k_\perp$ for which the weakly coupled plasma has a larger $P(k_\perp)$ than that in any strongly coupled plasma. In a weakly coupled plasma, the physics of momentum broadening is different at small $k_\perp$ than at large $k_\perp$. At small $k_\perp$ and large κ, momentum broadening in a weakly coupled plasma can be thought of as diffusion in $k_\perp$-space, as is the case at all κ and all $k_\perp$ in a plasma that is strongly coupled at all length scales. At large enough $k_\perp$, however, momentum broadening in a weakly coupled plasma is dominated by single, rare, hard, large-angle scattering off point-like quasiparticles. In the large-$k_\perp$ regime, the power-law tail of $P(k_\perp)$ is unaffected by resumming L-enhanced diagrams precisely because for any given L it arises only at values of $k_\perp$ that are so large that $P(k_\perp)$ describes rare single hard scattering. Although rare, these scatterings are more common than in a plasma that is a strongly coupled liquid at all scales, like that in strongly coupled $\mathcal{N}=4$ SYM theory, because in such a plasma there are no weakly coupled point-like constituents at any length-scale.

Although there are many reasons not to attempt a quantitative comparison between our calculation and any results from experiment (for example, we applied a leading order calculation valid for $g<1$ at $g\sim 2$; for example, we have not yet

included effects of gluon radiation) at a qualitative level it is easy to see what our calculation predicts for $P(k_\perp)$ in the QCD plasma at experimentally relevant temperatures: as long as observables that bias toward short L are not used, we should expect $P(k_\perp)$ to be Gaussian at low $k_\perp$ and to have a power-law tail at large $k_\perp$. Even if the QCD plasma can be best understood as a strongly coupled fluid without quasiparticles at its natural length scales of order $1/T$, since QCD is asymptotically free we know that at short distances the strongly coupled quark-gluon plasma is made of weakly coupled quarks and gluons and this means that at high enough $k_\perp$ a power-law tail must rise above the Gaussian in $P(k_\perp)$, as in our calculations in which the plasma is assumed to be weakly coupled at all length scales.

What about the jet quenching parameter $\hat{q} \equiv \langle k_\perp^2 \rangle / L$? Our calculation shows that its role is very different in a plasma that is weakly coupled at short distances than in one that is strongly coupled on all length scales. In the latter case, if $P(k_\perp)$ is Gaussian, as in the strongly coupled $\mathcal{N} = 4$ SYM plasma, then $\hat{q}$ is simply a measure of the width of the Gaussian probability distribution. In some other plasma that is strongly coupled on all length scales, the same would be true even if $P(k_\perp)$ were not precisely Gaussian. On the other hand, if $P(k_\perp) \propto 1/k_\perp^4$ at large $k_\perp$, as in any plasma that contains weakly coupled constituents at short enough length scales, then $\hat{q}$ is ultraviolet divergent and so is determined almost completely by the power-law tail of the probability distribution $P(k_\perp)$. In this circumstance, $\hat{q}$ knows almost nothing about the (Gaussian) behavior of $P(k_\perp)$ in the regime where almost all of the probability resides. In this circumstance, therefore, $\hat{q}$ tells us almost nothing about the momentum broadening of almost all hard partons. In this circumstance, $\hat{q}$ is almost entirely determined by the improbably small fraction of hard partons that scatter at large angles.

We close with three observations. First, the jet quenching parameter by itself is not sufficient as a characterization of $P(k_\perp)$. Depending on the circumstances, it could be a characterization of the "bulk" of the probability distribution for momentum broadening or it could be telling us only about the power-law "fat tail" of this distribution, in other words only about the physics of those few hard partons that

pick up improbably large $k_\perp$. Knowing how to interpret what a value of $\hat{q}$ means requires knowing more than $\hat{q}$; it requires further characterization of the shape of $P(k_\perp)$. Second, if at some future time it is possible to use data from heavy ion collision experiments to characterize the shape of $P(k_\perp)$ over the range of $k_\perp$ where most of the probability lies, it will take quantitative knowledge of this shape to learn about the properties of the plasma — since we have seen an example in which a very similar shape arises if the plasma is assumed weakly coupled or if the plasma is assumed to be infinitely strongly coupled. Third, the place to look in order to distinguish between these cases qualitatively is large $k_\perp$. Just as Rutherford discovered point-like nuclei within what he thought were liquid-like atoms, we can find evidence for the weakly coupled quarks and gluons that we know to be the short length-scale constituents of the strongly coupled plasma produced in heavy ion collision experiments.

It remains to be seen which experimental observables provide access to $P(k_\perp)$ at large $k_\perp$. The most direct approach that we are aware of is to analyze events in which an initial hard scattering produces an energetic photon back-to-back with an energetic quark. The photon tells us the initial energy and direction of the quark, and we can then hope to determine the $k_\perp$ relative to this initial direction that the quark has picked up as it propagates through the plasma. Fig. 3-8 suggests it would be very interesting to determine whether the quark picks up $k_\perp \sim 20$ GeV or more a fraction of a percent of the time, even a small fraction of a percent of the time, versus not at all. Seeing rare, but large, momentum kicks would confirm that (as we know) at short enough distance scales quark-gluon plasma is made of quark and gluon quasiparticles. It would then become very interesting to study the intermediate $k_\perp$-range in detail, to start to understand how a strongly coupled liquid emerges from an asymptotically free gauge theory.

Part II

Heavy quark energy loss at strong coupling

Chapter 4

Introduction to part II

In part I, we considered the case when interactions of probe particle with medium are weak – we expanded and evaluated Wilson loop for weakly coupled QCD at finite temperature. In the end, we discussed the case if the medium was strongly coupled and compared transverse momentum broadening in these two cases. In part II, we consider the case when all interactions are strong and study the question of quark energy loss directly.

The analysis of how a heavy quark moving through the strongly coupled liquid quark-gluon plasma produced in ultrarelativistic heavy ion collisions loses energy and, subsequently, diffuses in the flowing plasma is of considerable theoretical interest because experimentalists are developing the detectors and techniques needed to use heavy quarks as 'tracers' or 'probes' of the strongly coupled liquid. If one assumes that the interactions between the heavy quark and the quark-gluon plasma are weak then perturbative techniques originally formulated for energetic light quarks [19, 20, 21, 22] can be employed to analyze heavy quark energy loss [134].

The discovery that the plasma produced in heavy ion collisions is a strongly coupled liquid has prompted much interest in the real-time dynamics of strongly coupled non-Abelian plasmas and in the dynamics of heavy quarks therein. Although it remains to be seen to what degree treating all aspects of the dynamics of heavy quarks as strongly coupled is a good approximation, this approach is certainly of value as a benchmark: thorough understanding of the physics in this tractable setting can

provide valuable qualitative insights. What makes these calculations tractable is holographic duality, which maps questions of interest onto calculations done via a dual gravitational description of the strongly coupled plasma and the heavy quark probe. The simplest theory in which these holographic calculations can be done is strongly coupled $\mathcal{N} = 4$ supersymmetric Yang-Mills (SYM) theory in the large number of colors (large N_c) limit, whose plasma with temperature T is dual to classical gravity in a 4+1-dimensional spacetime that contains a $3 + 1$-dimensional horizon with Hawking temperature T and that is asymptotically anti–deSitter (AdS) spacetime, with the heavy quark represented by a string moving through this spacetime [82, 83, 84, 85, 86, 87]. The earliest work on heavy quark dynamics in the equilibrium plasma of strongly coupled $\mathcal{N} = 4$ SYM theory [82, 83, 84] yielded determinations of the drag force felt by a heavy quark moving through the static plasma and the diffusion constant that governs the subsequent diffusion of the heavy quark once its initial motion relative to the static fluid has been lost due to drag. The basic picture of heavy quark dynamics that emerges, with all but the initially most energetic heavy quarks being rapidly slowed by drag and then becoming tracers diffusing within the (moving) fluid, is qualitatively consistent with early experimental investigations [135]. For a review, see Ref. [77]. Subsequently, the holographic calculational techniques were generalized to any static plasmas whose gravitational dual has a 4+1-dimensional metric that depends only on the holographic (i.e. 'radial') coordinate in Ref. [105] and heavy quark energy loss and diffusion has by now been investigated in the equilibrium plasmas of many gauge theories with gravitational duals [136, 124, 137, 126, 138, 139, 140, 127, 125, 141, 142, 113, 112, 114].

We want a toy model in which we can reliably calculate how the energy loss rate of a heavy quark moving through the far-from-equilibrium matter present just after a collision compares to that in strongly coupled plasma close to equilibrium. We start by studying the energy loss of a heavy quark moving through the debris produced by the collision of planar sheets of energy in strongly coupled SYM theory introduced in Ref. [88] and analyzed there and in Refs. [89, 143]. The incident sheets of energy move at the speed of light in the $+z$ and $-z$ directions and collide at $z = 0$ at time

$t = 0$. They each have a Gaussian profile in the z direction and are translationally invariant in the two directions $\vec{x}_\perp = x, y$ orthogonal to z. Their energy density per unit transverse area is $\mu^3(N_c^2/2\pi^2)$, with μ an arbitrary scale with respect to which all dimensionful quantities in the conformal theory that we are working in can be measured. The width w of the Gaussian energy-density profile of each sheet is chosen to be $w = 1/(2\mu)$. We shall describe this setup, and its holographic description, in Section 5.1.1. Although there is no single right way to compare the widths of these translationally invariant sheets of energy with Gaussian profiles to the widths of a nucleus that has been Lorentz-contracted by a factor of 107 (RHIC) or 1470 (LHC), reasonable estimates suggest that our choice of $w\mu$ corresponds to sheets with a thickness somewhere between the thickness of the incident nuclei at RHIC and the LHC [88]. The recent investigations of Refs. [89, 143] suggest that it would be interesting to repeat our analyses for varying values of $w\mu$, but we leave this for future work since here we shall only be seeking to draw qualitative lessons.

The principal lesson that has been learned to date from analyses of the collisions of strongly coupled sheets of energy as in Refs. [88, 89, 143] and from many other analyses of how strongly coupled plasma forms from a large number of widely varied far-from-equilibrium strongly coupled initial collisions (for example, see Refs. [90, 91, 92, 93, 94, 95, 96, 97]) is that the fluid *hydrodynamizes*, i.e. comes to be described well by viscous hydrodynamics, after a time $t_{\rm hydro}$ that is at most around $(0.7 - 1)/T_{\rm hydro}$, where $T_{\rm hydro}$ is the effective temperature (for example, defined from the fourth root of the energy density) at the hydrodynamization time $t_{\rm hydro}$. At $t_{\rm hydro}$, the fluid can still have sufficiently large velocity gradients and pressure anisotropies that the dissipative effects of viscosity are significant. In the context of hydrodynamic modeling of heavy ion collisions at RHIC (for a recent example see Ref. [98]) $t_{\rm hydro} \sim 0.7/T_{\rm hydro}$ corresponds to a time ~ 0.3 fm/c when $T \sim 500$ MeV. This is about a factor of two earlier in time than the upper bounds on the hydrodynamization times inferred from hydrodynamic modeling of RHIC collisions [99, 100, 98]. Because QCD is asymptotically free, the dominant dynamics at the earliest moments of a sufficiently energetic heavy ion collision are expected to be weakly coupled, with the relevant

(weak) coupling being $\alpha_{\rm QCD}$ evaluated at the (short) distance scale corresponding to the mean spacing between gluons in the transverse plane at the moment when the two highly Lorentz-contracted nuclei collide. So, it would be inappropriate to take the estimates obtained in a context in which the colliding sheets of matter are strongly coupled from beginning to end as estimates for the hydrodynamization times of heavy ion collisions per se. The impact of these estimates is that they teach us that the $\sim$ 10 year old result [99, 100] that the matter produced in RHIC collisions takes at most 0.6-1 fm/c to hydrodynamize should not be seen as 'rapid thermalization' since this timescale is comfortably longer than what we now know to expect if the physics of heavy ion collisions were strongly coupled from the start. After we have calculated the drag force on a heavy quark that finds itself in the midst of the colliding sheets of energy density, we shall seek similarly qualitative lessons to those that have been drawn from the analyses of the collisions themselves.

We compute heavy quark energy loss by inserting a heavy quark moving at constant velocity $\vec{\beta}$ between the colliding sheets before the collision and calculating the force needed to keep its velocity constant throughout the collision. Via holography, the colliding planar sheets of energy in SYM theory map into colliding planar gravitational waves in asymptotically AdS_5 spacetime [88]. The addition of a heavy quark moving at constant velocity $\vec{\beta}$ amounts to including a classical string attached to the boundary of the geometry [87] and dragging the string endpoint at constant velocity $\vec{\beta}$, pulling the string through the colliding gravitational wave geometry. We show how to compute the profile of the string in this dynamical background in Section 5.1.2. The force needed to maintain the velocity of the string endpoint, which we compute in Section 5.1.3, yields the energy loss rate of the heavy quark [82, 83].

We describe our results for heavy quark moving through the colliding sheets of energy in Section 5.2, beginning in Section 5.2.1 with the case in which the heavy quark is moving with $\vec{\beta}$ perpendicular to the z-direction, meaning that it has zero rapidity. We compare the drag force that we calculate to what it would be in a homogeneous plasma in thermal equilibrium that has the same energy density or transverse pressure or longitudinal pressure as the matter that the quark finds itself

in at a given instant in time. We find that the peak value of the drag force, which occurs at a time when the matter produced in the collision is still far from equilibrium, is comparable to the peak value of the drag force in a static plasma with the same instantaneous energy density or pressure. However, we find that both the initial rise in the drag force and its peak are delayed in time relative to what they would be in a static plasma with the same instantaneous energy density or pressure. In Appendix B we provide some evidence that this time delay is of order $1/\pi T_{\rm hydro}$ at low β and increases slowly as $\gamma \equiv 1/\sqrt{1-\beta^2}$ increases. All these results are robust, in particular in the sense that we see them again when we consider a heavy quark moving with some nonzero rapidity in Sections 5.2.2 and 5.2.3.

The message from our results at early times is that there is no sign of any enhancement in the energy loss experienced by a heavy quark by virtue of the matter that it finds itself moving through being far from equilibrium. In broad terms, the energy loss is comparable to what it would be in an equilibrium plasma with the same energy density; when looked at in more detail, it can be significantly less by virtue of the initial delay in its rise. This is quite different than at weak coupling, where instabilities in the far-from-equilibrium matter can arise and can result in substantially enhanced rates of heavy-quark energy loss [101]. There are, however, no signs of any instabilities in the debris produced in the collisions of the sheets of strongly coupled matter that we analyze [88, 89] or, for that matter, in any analyses of far-from-equilibrium strongly coupled matter to date.

When we look at the drag force at late times, after the strongly coupled fluid has hydrodynamized, we find different results depending on whether the heavy quark has small or large rapidity. At small rapidity, the drag force that we calculate is described semiquantitatively by assuming a homogeneous plasma in equilibrium with an appropriate time-dependent temperature. At large rapidity, however, this approximation misses qualitative effects that, we show in Sections 5.2.2 and 5.2.3, can be attributed to the presence of gradients in the fluid velocity. We find that a velocity gradient in the fluid has the greatest effect on the energy loss of the heavy quark when the direction of motion of the heavy quark is most closely aligned with the velocity gra-

dient. As a consequence, effects of velocity gradients are larger at larger rapidity. We find generically that the force that must be exerted on the quark in order to move it along its trajectory includes a component perpendicular to the direction of motion of the quark, a component that can be substantial in magnitude. In certain cases we also find that, as a consequence of gradients in the fluid velocity, the z-component of the force that is required to move the quark in the positive-z direction points toward negative z!

After considering drag force experienced on heavy quark moving through the colliding sheet debris, we investigate the case of quark moving through the 'general' uncharged strongly coupled fluid with only requirement that fluid velocity gradients are small enough so that constituent equations of first order hydrodynamics hold. We begin by computing the drag force on a heavy quark moving through a fluid whose own motion is only in one direction, which we shall take to be the z-direction. If we denote the fluid 4−velocity by u^μ then at this stage the only gradients that we are considering are $\partial_z u^z$ and $\partial_t u^z$ as well as $\partial_z T$ and $\partial_t T$. In chapter 6, we restrict to the case of first order in gradients in the fluid temperature and velocity. The gravitational dual for a slowly changing fluid, including the effects of first order derivatives but neglecting higher derivatives, was first obtained in Ref. [122], where Einstein's equations in the 4+1-dimensional gravitational theory were solved to first order in gradients in the boundary coordinates and exactly in the radial direction. In Section 6.1.1 we describe this metric, for the case where the fluid motion is only in one direction, and then in Section 6.1.2 we introduce a heavy quark, described in the gravitational theory by a string. The endpoint lives at the boundary of the AdS space, where it follows the trajectory of the heavy quark of interest. We shall assume that it is being dragged at some constant velocity $\vec{\beta}$, which may or may not be parallel to the direction of motion of the fluid.[1] In Section 6.1.2, with the gravitational metric describing the fluid in hand, we formulate and solve the string equations of motion,

[1] We shall work throughout in the heavy quark mass, *i.e.*, $M \to \infty$, limit and we shall assume throughout that the quark is being pulled at constant velocity $\vec{\beta}$ by some external force. We leave to future work the consideration of the case where there is no external force meaning that a quark with finite M would decelerate under the influence of the force exerted on it by the fluid.

which is to say that we calculate the shape of the string attached to the heavy quark, including effects of fluid gradients up to first order. In Section 6.2.1 we use the string profile to calculate the flux of momentum down the string, which determines the drag force on the heavy quark. We first do the calculation in the fluid rest frame and then boost the result to any frame in Section 6.2.2. In Section 6.2.3 we generalize to the case in which the fluid has an arbitrary velocity and in which any of the gradients $\partial_\alpha u^\beta$ can be nonzero.

By analyzing the case in which the quark is moving with an ultrarelativistic velocity relative to the fluid we find indications that our results may not be valid in the limit in which the Lorentz factor γ of the quark velocity is large, even if the quark mass $M \to \infty$ limit has been taken first and even if fluid gradients are small. We find that in the $\gamma \to \infty$ limit the "correction" to the drag force that is first order in fluid gradients is larger than the leading (i.e. zeroth order) term by a factor that is $\mathcal{O}(\gamma^{1/2})$. This suggests that the gradient expansion may not be valid in this regime. That is, even if higher order gradients are small enough that they are not important in describing the fluid motion itself their effects on the drag force may become important at large enough γ.

In Section 6.3, we consider three consequences of our general result for the first order effects of fluid gradients on the drag force exerted by the fluid on the heavy quark. First, we point out that even if the quark has no velocity relative to the fluid the drag force on it is nonzero as long as the time derivative of the fluid velocity is nonvanishing. Next, we consider two explicit examples of a fluid whose motion is only in one direction. First, we analyze the drag force on a heavy quark moving through a fluid that is undergoing boost-invariant expansion in the z-direction, à la Bjorken. We show that even though there are gradients in this fluid, a quark that is moving along with the fluid feels no drag force. A quark whose velocity includes a component perpendicular to the direction of motion of the fluid feels a drag force that is affected by the fluid gradients. And, last of all, we return to the colliding sheets of energy density that motivated our investigation, showing that our general expression for the effects of fluid gradients on the drag force to first order does a good job of

explaining the explicit results obtained in Chapter 5, in many cases quantitatively and qualitatively in all cases, even those where the results for colliding sheets of energy appear counter-intuitive. In Section 7 we conclude and look ahead to new directions whose investigation is motivated by our results.

Chapter 5

Heavy quark energy loss far from equilibrium in a strongly coupled collision

5.1 Holographic description

In a strongly coupled conformal gauge theory with a dual gravitational description, a heavy quark moving through out-of-equilibrium matter that is on its way to becoming strongly coupled plasma consists of a string moving in some non-equilibrium, but asymptotically AdS_5, black brane spacetime. For an infinitely massive quark, the endpoint of the string is attached to the four-dimensional boundary of the geometry. The geometry of the boundary is that of Minkowski space and the trajectory of the string endpoint on the boundary coincides with the trajectory of the quark.

We shall focus on the case in which the gauge theory is $\mathcal{N} = 4$ SYM theory with N_c colors, although our results can immediately be generalized to any conformal gauge theory with a gravity dual upon making a suitable modification to the relationship between the 't Hooft coupling $\lambda \equiv g^2 N_c$ of the gauge theory with g the gauge coupling constant, and corresponding quantities in the gravity dual. In the limit of large N_c and large λ, the evolution of the black brane geometry is governed by Einstein's

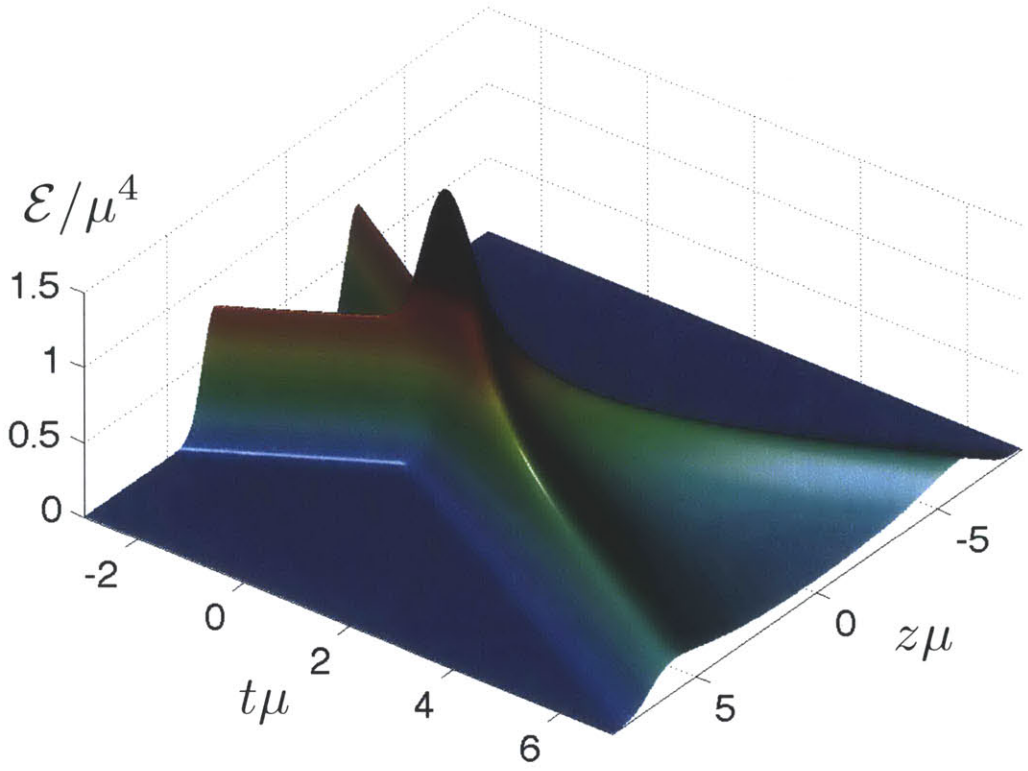

Figure 5-1: A plot of the boundary energy density as a function of time t and position along the 'beam' direction z for the colliding sheets of energy. Before $t = 0$, the energy density is that of two sheets with Gaussian profiles moving toward each other at the speed of light. The sheets collide around time $t = 0$ and leave debris in the forward light-cone that subsequently hydrodynamizes as it expands, becoming strongly coupled, liquid, plasma.

equations

$$R_{MN} - \tfrac{1}{2} G_{MN} \left(R - 2\Lambda \right) = 0, \tag{5.1}$$

with cosmological constant $\Lambda = -6$. In this limit, the back reaction of the string on the geometry is negligible meaning that we can solve Einstein's equations first, independently of the string equations, and then subsequently determine the shape of the string in a background given by the solution to Einstein's equations.

5.1.1 Gravitational description of colliding sheets of energy

The geometry we choose to study is that of the colliding gravitational shockwaves studied in Ref. [88]. In the dual gauge theory living on the boundary this geometry corresponds to colliding planar sheets of energy density. In Fefferman-Graham coordinates the pre-collision metric is given by [102]

$$ds^2 = \frac{-dx_+dx_- + d\vec{x}_\perp^2 + u^4\left[h_+dx_+^2 + h_-dx_-^2\right] + du^2}{u^2}, \tag{5.2}$$

where $x_\pm = t \pm z$ and $h_\pm \equiv h(x_\pm)$ for some function $h(x_\pm)$ that specifies the profile of the incident gravitational shockwaves and hence the incident sheets of energy in the boundary theory. The boundary of the geometry is located at AdS radial coordinate $u = 0$. The gravitational shockwaves move in the $\pm z$ direction at the speed of light. If $h(x_\pm)$ has compact support then $h(x_+)$ and $h(x_-)$ do not overlap in the distant past and the metric (5.2) is an exact pre-collision solution to Einstein's equations. Following Ref. [88], we choose Gaussian profiles

$$h(x_\perp) = \mu^3(2\pi w^2)^{-1/2}e^{-\frac{1}{2}x_\pm^2/w^2}, \tag{5.3}$$

where μ defines the energy scale, meaning that we shall measure all other dimensionful quantities in units of μ.

For a given solution to Einstein's equations, the near-boundary behavior of the metric encodes the boundary stress tensor $T^{\mu\nu}$ [103, 104]. In the boundary gauge theory the energy density of each shock is proportional $h(x_\pm)$ [102]. The metric that we have described therefore corresponds in the boundary theory to two sheets of energy density (infinite in extent, and translation-invariant, in the transverse dimensions) that are moving towards each other in the $\pm z$ directions at the speed of light. The energy density profiles of the sheets are Gaussians with widths w, and the incident sheets each have an energy per unit area that is given by $N_c^2\mu^3/(2\pi^2)$ [88]. We choose the width of each shock to be $w = 0.5/\mu$, meaning that we shall be probing the collision of sheets of energy that are thinner by a factor of 2/3 than those in Ref. [88].

Near the collision time, when the functions $h(x_\pm)$ begin to overlap, the metric (5.2) ceases to be a solution to Einstein's equations. Using (5.2) as initial data in the distant past, one must therefore compute the future evolution of the geometry numerically. Our numerical scheme for solving Einstein's equations can be found in Refs. [88, 143]. In what follows we simply state some of the salient features. A useful choice of coordinates for the numerical evolution is that of infalling Eddington-Finkelstein coordinates where the metric takes the form

$$ds^2 = \frac{-Adt^2 + \Sigma^2 \left[e^B d\vec{x}_\perp^2 + e^{-2B} dz^2\right] + 2dt\,(Fdz - du)}{u^2} \tag{5.4}$$

where A, B, Σ and F are functions of t, z and u. Lines of constant time t (and spatial coordinates $\vec{x}_\perp$ and z) are infalling null geodesics.[1]

An important practical matter when solving Einstein's equations is fixing the computational domain in u. The geometry we study in this paper contains a black brane with planar topology. Moreover, the event horizon exists in the infinite past, even before the collision takes place on the boundary [91, 88]. Therefore, a natural choice is to excise the geometry inside the horizon, as this region is causally disconnected from the outside geometry. To perform the excision we identify the location of an apparent horizon (which always lies inside the event horizon) and choose to stop integrating Einstein's equations any further into the black brane at its location. Our choice of coordinates makes this procedure particularly simple. The metric ansatz (5.4) is invariant under the residual diffeomorphism

$$\frac{1}{u} \to \frac{1}{u} + \xi(t, z), \tag{5.5}$$

where ξ does not depend on the radial coordinate u but is an arbitrary function of the boundary spacetime coordinates t and z. One may fix ξ by demanding that the location of the apparent horizon be at $u = 1$. With this choice of coordinates, the

[1] To the best of our knowledge there does not exist a closed form coordinate transformation taking the pre-collision metric (5.2) onto the metric (5.4) used for numerical evolution. Therefore, for initial data we compute the coordinate transformation required to put the initial metric (5.2) in the form of (5.4) numerically. For details see Refs. [88, 143].

boundaries of the computational domain are static: $0 < u < 1$. The numerical procedure for determining ξ and solving Einstein's equations is described in Refs. [88, 143] and we shall not review it here. Following this procedure yields ξ as well as the bulk metric functions A, B, Σ and F, whose asymptotic near-boundary behavior determines the stress-energy tensor $T^{\mu\nu}$ of the colliding sheets of energy in the boundary gauge theory, as described in Ref. [88].

In the distant past the apparent horizon lies very deep in the bulk. This presents a computational problem for solving Einstein's equations numerically as the coefficient functions in the metric (5.2) diverge deep in the bulk. As described in Ref. [88], to regulate this problem we choose to study study shocks which propagate and collide in a low temperature background plasma of temperature $T_{\rm background}$. In the distant past the effect of the background temperature is to push the apparent horizon up towards the boundary and thereby control the size of the metric coefficient functions deep in the bulk. Our choice of background temperature is $T_{\rm background} = 0.085\,\mu$ which corresponds to an initial background energy density 213 times smaller than the energy density at the center of the sheets of energy and 450 times smaller than the energy density at $t = z = 0$, during the collision.

Fig. 5-1 shows a plot of the rescaled energy density

$$\mathcal{E} \equiv \frac{2\pi^2}{N_c^2} T^{00} \tag{5.6}$$

for our colliding sheets as a function of position and time. Before $t = 0$, the energy density is that of two sheets of energy with Gaussian profiles moving toward each other at the speed of light. The sheets collide around time $t = 0$ and leave debris in the forward light-cone. We shall calculate the rate of energy loss of (i.e. the 'drag force' acting on) a heavy quark moving through the far-from-equilibrium matter right near $t = z = 0$, during the collision when the energy density is largest. We shall then follow the quark forward in time and see how it loses energy in the expanding, cooling, fluid that forms in the forward lightcone. In gravitational terms, we wish to study the dynamics of a string moving in the black brane geometry during and after the

collision.

After the collision, the fluid in the forward lightcone is expanding meaning that at $z \neq 0$ it has a velocity that points in the direction of increasing $|z|$. The fluid velocity is defined to be the future-directed time-like eigenvector of $T^{\mu}_{\ \nu}$, normalized such that $u_\mu u^\mu = -1$:

$$T^{\mu}_{\ \nu} u^\nu = -\frac{N_c^2}{2\pi^2}\,\varepsilon\, u^\mu, \tag{5.7}$$

with $-\varepsilon$ the eigenvalue, ε being the proper energy density rescaled as in (5.6). At any spacetime point, we can find the local fluid rest frame by first using (5.7) to determine $u^\mu_{\text{lab frame}}$ and then boosting to a frame in which, at this spacetime point, u^μ is given by $u^\mu_{\text{rest frame}} = (1,0,0,0)$. In this local fluid rest frame, the stress-energy tensor at the spacetime point of interest is diagonal and can be written as

$$T^{\mu\nu}_{\text{rest frame}} = \frac{N_c^2}{2\pi^2}\,\text{diag}(\varepsilon, \mathcal{P}_\perp, \mathcal{P}_\perp, \mathcal{P}_\parallel)\,. \tag{5.8}$$

Note that at $z = 0$ the velocity of the fluid vanishes by symmetry, meaning that at $z = 0$ in (5.7) we have simply $u^\mu_{\text{lab frame}} = u^\mu_{\text{rest frame}} = (1,0,0,0)$ and $\varepsilon = \mathcal{E} = T^{00}(2\pi^2)/N_c^2$.

Before we turn to describing the dynamics of the string and then to calculating the rate at which the heavy quark loses energy, we should justify referring to the matter that is formed in the forward light-cone as a fluid. In Fig. 5-2 we compare the pressures in the 'beam' direction and perpendicular to it at $z = 0$ to what those pressures would be if the matter were a fluid described by the equations of viscous hydrodynamics for the $\mathcal{N} = 4$ SYM plasma, to first order in a derivative expansion. In particular, the hydrodynamic constitutive relations allow us to determine $\mathcal{P}_\parallel$ and $\mathcal{P}_\perp$ from the proper energy density ε and the fluid velocity u^μ, determined via (5.7). (Because we are making this comparison at $z = 0$, where the fluid is at rest in the lab frame, in this instance (5.7) is trivial as described above.) We plot the pressures determined by applying the first order hydrodynamic constitutive relations to ε and u^μ as dashed curves in Fig. 5-2. We see that from a time that is clearly before $2/\mu$ onwards the flow of the fluid is described very well by hydrodynamics.

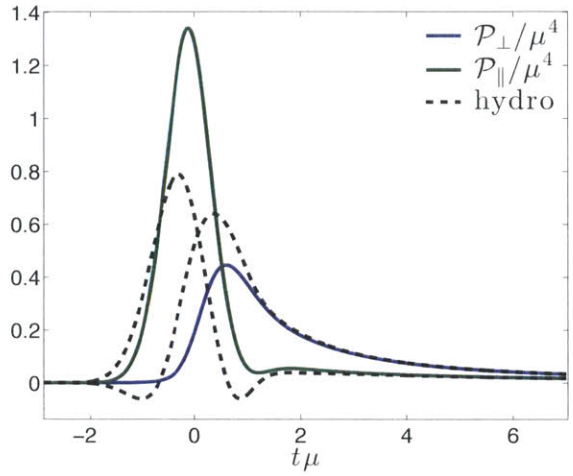

Figure 5-2: Pressure, both parallel to the direction of motion of the colliding sheets ($\mathcal{P}_\parallel$) and in the transverse directions ($\mathcal{P}_\perp$), as a function of time at $z = 0$ during the collision of the sheets of energy illustrated in Fig. 5-1. We compare the pressures in the collision, shown as solid colored curves, to what they would be if the hydrodynamic constitutive relations were satisfied, shown as dashed curves. We see that the strongly coupled fluid produced in the collision hydrodynamizes to a reasonable degree before $t = 2/\mu$, although with the more strict operational criterion defined in the text, the hydrodynamization time is $t_{\rm hydro} = 2.8/\mu$.

We can use the same operational definition of the hydrodynamization time $t_{\rm hydro}$ as in Ref. [88], namely the time after which the actual pressures within the matter produced in the initially far-from-equilibrium collision are both within 15% of the values derived from the hydrodynamic constitutive relations. With this definition, in Fig. 5-2 hydrodynamization occurs at $t = t_{\rm hydro} = 2.8/\mu$. It is clear from the Figure that one could choose a reasonable but less strict criterion for hydrodynamization with respect to which hydrodynamization occurs well before $2/\mu$. The reason that with the strict criterion $t_{\rm hydro}$ is a little later is that $\mathcal{P}_\parallel$ is so small that a 15% relative deviation corresponds to a very small absolute deviation.

We shall calculate the drag force on the heavy quark as it plows through the matter produced in the collision both before the hydrodynamization time $t_{\rm hydro}$, when the matter is far from equilibrium, and after $t_{\rm hydro}$ when we have an expanding, cooling, hydrodynamic liquid. As in Ref. [88], we see from Fig. 5-2 that at the hydrodynamization time $t_{\rm hydro}$ the parallel and transverse pressures are very different.

The fluid is very anisotropic at the time that it hydrodynamizes and becomes locally isotropic only at a much later time, beyond that shown in the Figure. We shall therefore be studying the drag force on a heavy quark when it is first in the far-from-equilibrium matter at $t \sim 0$, well before hydrodynamization, and then later in an expanding cooling hydrodynamic fluid that is far from isotropic.

5.1.2 String dynamics

For a given solution to Einstein's equations, for example the one above that describes the dynamics of a black brane in the bulk and the collision, hydrodynamization, and hydrodynamic flow of the strongly coupled matter in the boundary theory, we can add an infinitely heavy quark moving through the boundary theory matter by adding a string in the bulk geometry whose endpoint follows the trajectory of the quark along the boundary. The dynamics of the string are governed by the Polyakov action

$$S_{\rm P} = -\frac{T_0}{2}\int d^2\sigma\sqrt{-\eta}\eta^{ab}G_{MN}\partial_a X^M \partial_b X^N, \tag{5.9}$$

where $\sigma_1 \equiv \tau$ is a temporal worldsheet coordinate, $\sigma_2 \equiv \sigma$ is a spatial worldsheet coordinate, $X^M(\tau,\sigma) = (t(\tau,\sigma), \vec{x}(\tau,\sigma), u(\tau,\sigma))$ are the string embedding functions that describe where the string is located within the spacetime metric that we are interested in probing, η_{ab} is the worldsheet metric and $T_0 = \frac{\sqrt{\lambda}}{2\pi}$ is the string tension. We choose worldsheet coordinates such that the worldsheet metric takes the form

$$\eta_{ab} = \begin{pmatrix} -\alpha(\tau,\sigma) & -1 \\ -1 & 0 \end{pmatrix} \tag{5.10}$$

with $\alpha(\tau,\sigma)$ being an arbitrary function. Just as we did in the spacetime metric (5.4), we have chosen worldsheet coordinates that are infalling Eddington-Finkelstein coordinates. Lines of constant τ are infalling null worldsheet geodesics. As we describe further below, we fix the function $\alpha(\tau,\sigma)$ by demanding $\sigma = u$.

Varying the Polyakov action with respect to the embedding functions X^M yields dynamical equations of motion. Likewise, varying the Polyakov action with respect

to the worldsheet metric yields a system of constraint equations. With our choice of infalling Eddington-Finkelstein bulk and worldsheet coordinates, the dynamical equations of motion take the simple form

$$\dot{X}'^N + \Gamma^N_{AB}\dot{X}^A X'^B = 0 \tag{5.11}$$

where Γ^N_{AB} are Christoffel symbols associated with the metric (5.4) for the bulk spacetime and

$$\dot{X}^M \equiv \partial_\tau X^M - \frac{1}{2}\alpha X'^M \ , \tag{5.12a}$$

$$X'^M \equiv \partial_\sigma X^M \ . \tag{5.12b}$$

The constraint equations are even simpler:

$$X'^2 = 0, \tag{5.13a}$$

$$\dot{X}^2 = 0. \tag{5.13b}$$

The constraint equation (5.13a) is a temporal constraint. If (5.13a) is satisfied every where in space at one time, the dynamical equations (5.11) imply that it will be satisfied at all subsequent times. The constraint equation (5.13b) is a boundary constraint. If (5.13b) is satisfied at all times at one value of σ the dynamical equations (5.11) imply it will be satisfied at all σ.

Given X^M for all σ at some value of τ, the equations of motion (5.11) constitute a linear system of ordinary differential equations for $\dot{X}^M$. To solve these equations, in addition to specifying the initial conditions for X^M one must specify five boundary conditions at all τ at the AdS boundary, where the string endpoint is located. Three boundary conditions are simply that the string endpoint moves on a given trajectory $\vec{x}_o(t)$

$$\lim_{\sigma\to 0}\vec{x}(\tau,\sigma) = \vec{x}_o(t). \tag{5.14}$$

We choose the trajectory

$$\vec{x}_o(t) = \vec{\beta}t, \tag{5.15}$$

for some constant velocity $\vec{\beta}$. These boundary conditions correspond to choosing to study a heavy quark, whose location after all coincides with the location of the endpoint of the string, that is moving with constant velocity $\vec{\beta}$ and that finds itself at $z = 0$ at time $t = 0$, meaning that this heavy quark finds itself right in the center of the collision that we wish to probe. We shall present results for several different values of $\vec{\beta}$.

Two more boundary conditions are required. For convenience, we choose

$$\lim_{\sigma\to 0} t(\tau,\sigma) = \tau, \tag{5.16}$$

so that the worldsheet time τ corresponds to the coordinate time t at the boundary. The remaining boundary condition comes from demanding that the boundary constraint (5.13b) is satisfied at $\sigma = 0$. The boundary conditions (5.15) and (5.16) and the boundary constraint (5.13b) are satisfied at $\sigma = 0$ provided that [2]

$$\lim_{\sigma\to 0} \dot{t} = \frac{1}{2}\left[1 + \frac{1}{\gamma}\right], \ \lim_{\sigma\to 0} \dot{\vec{x}} = \frac{\vec{\beta}}{2}, \ \lim_{\sigma\to 0} \dot{u} = -\frac{1}{2\gamma}, \tag{5.17}$$

where $\gamma \equiv 1/\sqrt{1-\vec{\beta}^2}$ as usual.

We can now see how to evolve the string forward in τ, given an initial string profile specified by X^M at some initial τ. The algorithm has two steps. First we need to obtain $\dot{X}^M = \left(\dot{t}, \dot{\vec{x}}, \dot{u}\right)$ at the initial τ. We do this by observing that if we think of $\dot{X}^M$ as the dynamical variables, the equations of motion (5.11) are first order differential equations for $\dot{X}^M$ with the independent variable being σ. We can solve these equations for $\dot{X}^M$ as functions of σ at the initial τ as long as we know X'^M — which we do since we have been given X^M for all σ at the initial τ — and as long

[2] To see that this is true one can solve the string equations of motion (5.11) and the constraint equations (5.13) with a power series expansion in σ near $\sigma = 0$. In doing so one can directly incorporate the boundary conditions (5.15) and (5.16) into the series expansions. With the expansion known to order σ, one can easily see that the boundary limit of $\dot{X}^M$ takes the form (5.17).

as we have boundary conditions for $\dot{X}^M$ at $\sigma = 0$ — which we have in (5.17). So, we solve (5.11) starting from $\sigma = 0$ and obtain $\dot{X}^M$ at all σ at the initial τ. In the second step of the algorithm, we use (5.12a), rewritten as $\partial_\tau X^M = \dot{X}^M + \frac{1}{2}\alpha X'^M$, to compute the field velocities $\partial_\tau X^M$. To do this we need the function α. With the gauge choice $\sigma = u$, it is given simply by $\alpha = -2\dot{u}$. With $\partial_\tau X^M$ known, we can then determine X^M at the new τ, thus completing the evolution of the system from the initial τ to a τ one time-step later. We then repeat.

All that we still need to specify is our choice of initial conditions for X^M at an initial time t that we shall typically take to be $-3/\mu$, when the centers of the incident sheets of energy are $6/\mu = 12w$ apart. In the distant past, well before the sheets of energy collide, the near-boundary geometry between the sheets of energy, which is where the heavy quark is located, is that of an equilibrium black brane with a small temperature $T_{\text{background}}$. This is so provided that we do not choose $|\vec{\beta}|$ so large that at our initial time the heavy quark is within one of the incident sheets. We shall make sure not to do this, which is to say that we shall make sure that at our initial time the heavy quark has not yet felt the sheets of energy that are soon going to hit it to any significant degree. We therefore choose initial conditions such that the string profile coincides with the trailing string solution of Refs. [82, 83] moving at velocity $\vec{\beta}$, given in Appendix H. Such initial conditions satisfy the temporal constraint equation (5.13a) near the AdS boundary.[3]

Constructing initial string profiles that are equilibrium solutions to the pre-collision geometry ensures that the future non-trivial evolution of the string is entirely due to the change in the bulk geometry associated with the collision event, not due to tran-

[3] Our choice of initial conditions is slightly complicated by our choice of infalling Eddington-Finkelstein coordinates. In infalling Eddington-Finkelstein coordinates the bulk is the causal future of the boundary. At any given Eddington-Finkelstein time t, even in the distant past before the sheets of energy collide on the boundary, the gravitational shocks are colliding somewhere deep in the bulk. As a consequence of this, choosing the trailing string of Refs. [82, 83] will lead to a small violation of the temporal constraint equation (5.13a) deep in the bulk. However, as time progresses the violation of the constraint decreases in magnitude and then as time progress further towards $t = 0$ when the sheets collide on the boundary, the portion of the string that violates the temporal constraint equation is rapidly enveloped by the event horizon of the black brane. Because of this, the initial violation of the temporal constraint equation is causally disconnected from physics near the boundary and hence is of no concern. We discuss this further in Appendix H.

sients that would come along as artifacts of any other choice of initial conditions. However, as we shall describe below, although perturbing the initial string profile does result in an early-time transient before the collision happens, the change that results in the rate of energy loss of the heavy quark *during and after* the collision event is negligible. Because in an actual heavy ion collision a heavy quark is produced during the collision, we are not particularly interested in any aspect of the motion of our heavy quark before the collision of our sheets of energy. This, together with the insensitivity of the results during and after the collision that we are interested in to initial conditions and associated transients, means that our study could be repeated with other choices of initial conditions for the string without changes to our conclusions.

We discretize the σ coordinate using pseudo-spectral methods. Specifically, we decompose the σ dependence of all functions in terms of the first 20-35 Chebyshev polynomials. We then time evolve the string profile, typically from $t = -3/\mu$ to $t = +6/\mu$, according to the algorithm that we have described above using a fourth order Runge-Kutta ordinary differential equation solver.

5.1.3 Extracting the drag force acting on the quark from the string profile

Because the quark is a point-like source which is being pushed through the surrounding medium at a constant speed by some external agent, it must be transferring energy and momentum to the surrounding medium meaning that the boundary stress tensor is not conserved:

$$\partial_\mu T^{\mu\nu}(x) = F^\nu(x) = -f^\nu \delta^3(\vec{x} - \vec{\beta}t), \tag{5.18}$$

where f^ν is the four momentum lost by the quark per unit time. Note that, as always for a force, f^ν does not transform as a four-vector under Lorentz transformations. It is conventional to write

$$\frac{dp^\nu}{dt} = f^\nu, \tag{5.19}$$

with p^ν the four momentum of the quark, even though in the setup we are analyzing the four momentum of the quark does not actually change. The external agent does work in order to move the quark at constant speed and, in so doing, transfers energy and momentum to the medium surrounding the quark; the quark does not slow down. If the external agent dragging the quark is a classical background electric field, the total stress tensor

$$T^{\mu\nu}_{\rm tot} = T^{\mu\nu} + T^{\mu\nu}_{\rm EM}, \tag{5.20}$$

is conserved

$$\partial_\mu T^{\mu\nu}_{\rm tot} = 0 \ . \tag{5.21}$$

Via the quark, energy and momentum flow from the electric field into the surrounding medium. The quantity f^ν is thus given by

$$f^\nu(t) = -\int d^3x\, \partial_\mu T^{\mu\nu}(x) = \int d^3x\, \partial_\mu T^{\mu\nu}_{\rm em}(x) \ . \tag{5.22}$$

Just as the near-boundary behavior of the metric encodes the expectation value of the boundary stress tensor, the near boundary behavior of the string profile encodes f^ν. Specifically, f^ν can be identified as the flux of four momentum down the string [105]. The flux down the string can be extracted by noting that the total action for the holographic system,

$$S_{\rm tot} = S_{\rm P} + S_{\rm EM}, \tag{5.23}$$

must be diffeomorphism invariant. The electromagnetic action $S_{\rm EM}$ only has support at the boundary and couples the string endpoint to the classical background electric field used to drag the quark (which is to say the string endpoint) at constant velocity.

Under an infinitesimal diffeomorphism $X^M \to X^M + \chi^M$ the variation in the Polyakov action (5.9) only has support at the boundary and reads

$$\delta S_{\rm P} = \lim_{u\to 0} \int d^4x\, n_N\, \chi^M \sqrt{-G}\, \mathcal{T}^N_M, \tag{5.24}$$

where D_M is the covariant derivative with respect to the bulk spacetime metric (5.4),

n_N is the normal to the boundary at $u = 0$, and

$$\mathcal{T}^{MN}(Y) = \frac{-T_0}{\sqrt{-G}} \int d^2\sigma \sqrt{-\eta}\, \eta^{ab}\, \partial_a X^M\, \partial_b X^N \delta^5(Y - X), \tag{5.25}$$

is the string stress tensor. Likewise, the variation in the electromagnetic action is

$$\delta S_{\rm EM} = \int d^4x \chi^\mu \partial_\nu T^\nu_{\mu\,{\rm EM}} = -\int d^4x \chi^\mu F_\mu, \tag{5.26}$$

where in the last line we used $\partial_\nu T^\nu_{\mu\,{\rm EM}} = -F_\mu$ with F_μ defined in (5.18). Upon demanding that the variation in the action vanish for all χ^μ, we conclude that

$$F_\mu = \lim_{\rm u\to 0} n_N \sqrt{-G} \mathcal{T}^N_\mu, \tag{5.27}$$

from which the drag f^μ can easily be extracted via (5.18).

Setting the normal to the boundary $n_M = \delta_{M5}$, one might naively conclude[4] that $F_\mu = \lim_{\rm u\to 0} \sqrt{-G}\mathcal{T}^5_\mu$. However, this cannot be correct. Near the boundary some components of the string stress tensor diverge like $1/u^2$. As a consequence of this divergence $\lim_{\rm u\to 0} \sqrt{-G}\mathcal{T}^5_\mu$ transforms nontrivially under the *radial* diffeomorphism (5.5). Simply put, the expression $\lim_{\rm u\to 0} \sqrt{-G}\mathcal{T}^5_\mu$ depends on one's choice of the gauge parameter ξ used in solving Einstein's equations.

The unique remedy to the above problem is to set $n_M = \delta_{M5} + u^2 \partial_M \xi$. This choice is simply the near-boundary limit of δ_{5N}, transformed by (5.5). In other words, $n_M = \delta_{M5}$ would have been correct if we had used $\xi = 0$ but is not correct once we make the transformation (5.5) that we needed to make in order to solve Einstein's equations. With the correct choice of n_M, F_μ in (5.27) is invariant under all infinitesimal diffeomorphisms, including those arising from Eq. (5.5). We therefore conclude that

$$F_\mu = \lim_{u\to 0} \left[\sqrt{-G} \left(\mathcal{T}^5_\mu + u^2 \partial_\alpha \xi \left(\mathcal{T}^\alpha_\mu - \delta^\alpha_\mu \mathcal{T}^5_5 \right) \right) \right]. \tag{5.28}$$

[4]As we did, in a preliminary version of this study [5]. The drag forces calculated in Ref. [5] are not correct but, comparing the figures from that preliminary report to those in Section 5.2 where we present our results, the differences are not large.

We note that f^μ can also be expressed in terms of the canonical worldsheet fluxes

$$\pi^a_M \equiv \frac{\delta S_P}{\delta\left(\partial_a X^M\right)} = -T_0\sqrt{-\eta}\, G_{MN}\,\eta^{ab}\,\partial_b X^N. \tag{5.29}$$

A straightforward exercise using the string stress (5.25) and (6.34) shows that

$$f_\mu = \lim_{u\to 0}\left[\pi^\sigma_\mu + u^2\,\pi^\sigma_5\,\partial_\mu\xi - u^2\,\pi^a_\mu\,\partial_\alpha\xi\,\partial_a X^\alpha\right]\ . \tag{5.30}$$

We see that for the choice $\xi = 0$ the usual identification of force in terms of the canonical fluxes [82, 83] is reproduced.

5.2 Results

In this section we present and discuss the results that we have obtained for the drag force on a heavy quark being dragged through the colliding sheets of Fig. 5-1. We shall initially choose the quark to be moving with a velocity $\vec{\beta}$ in the plane perpendicular to the direction of motion of the colliding sheets. Later we shall consider the more general case where the velocity of the quark has components both parallel to and perpendicular to the 'beam' direction. We shall compare our results to expectations based upon comparing the drag force that we calculated to what it would have been in a static homogeneous plasma with the same instantaneous energy density or parallel pressure or transverse pressure as that at the position of the quark. To further explore the effect of a time-dependent background on the drag force, in Appendix I we consider a toy example in which the temperature increases with time but the plasma remains homogeneous and isotropic and does not undergo any expansion.

5.2.1 Heavy quark with zero rapidity

We begin with the case where the heavy quark is moving perpendicular to the 'beam' direction, which is to say perpendicular to the z-direction along which the sheets of energy collide. Although our heavy quark was present before the collision, from

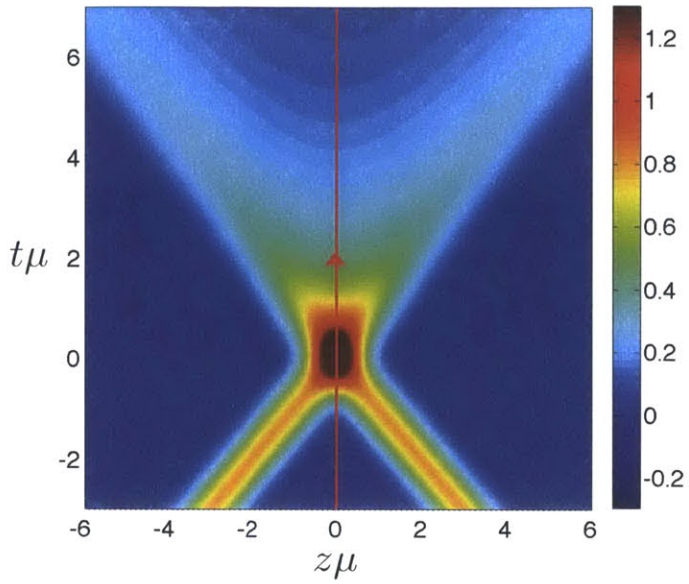

Figure 5-3: The path in the (z,t)-plane of a quark moving in the $z = 0$ direction, i.e. with zero rapidity, is shown as the red line superimposed on a color-plot of the rescaled energy density $\mathcal{E}$, see Eq. (5.6), in units of μ^4. Thinking of the x-axis as perpendicular to the page, the quark is moving out of the page with velocity β_x.

a phenomenological perspective this calculation may inform how we think about a heavy quark that is produced at $t = 0$ in a heavy ion collision with zero rapidity moving with some perpendicular velocity $\vec{\beta}$. The $z = 0$ path along which the heavy quark is moving is illustrated in Fig. 5-3, as is the energy density through which it moves. The parallel and perpendicular pressures of the material in which it finds itself are those that we plotted in Fig. 5-2. The case of a quark moving at zero rapidity is simpler than the more general case that we will turn to next for two reasons: (i) a quark moving along the $z = 0$ plane is always moving through fluid at rest, with $u^\mu = (1,0,0,0)$, meaning that in this case the local fluid rest frame is the same as the lab frame; (ii) the drag force acting on the quark with zero rapidity is directed antiparallel to the velocity vector, with no component of the force perpendicular to the direction of motion of the quark. We have calculated the drag force as described in Section 5.1. Our results for quarks moving at zero rapidity with speed $\beta_x = 0.5$ and $\beta_x = 0.95$ are shown as the solid red curves in Figs. 5-4 and 5-5, respectively.

We are interested in comparing our results to expectations based upon the classic

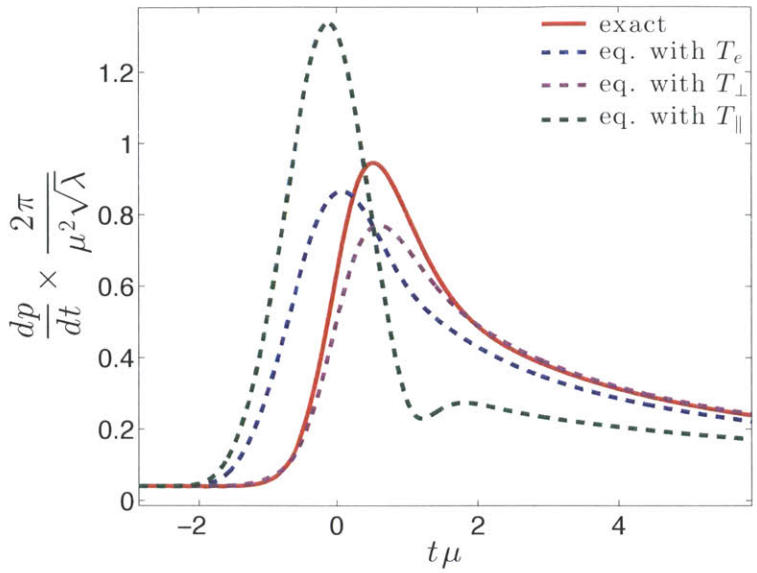

Figure 5-4: Drag force in units of $\mu^2\sqrt{\lambda}/(2\pi)$ on a quark being pulled through the collision in the x-direction at $z = 0$, i.e. at zero rapidity, with velocity $\beta_x = 0.5$. The dashed curves show the drag force that the quark would experience in an equilibrium plasma with the same instantaneous energy density, parallel pressure or perpendicular pressure as that at the location of the quark. The dashed curves are described further in the text.

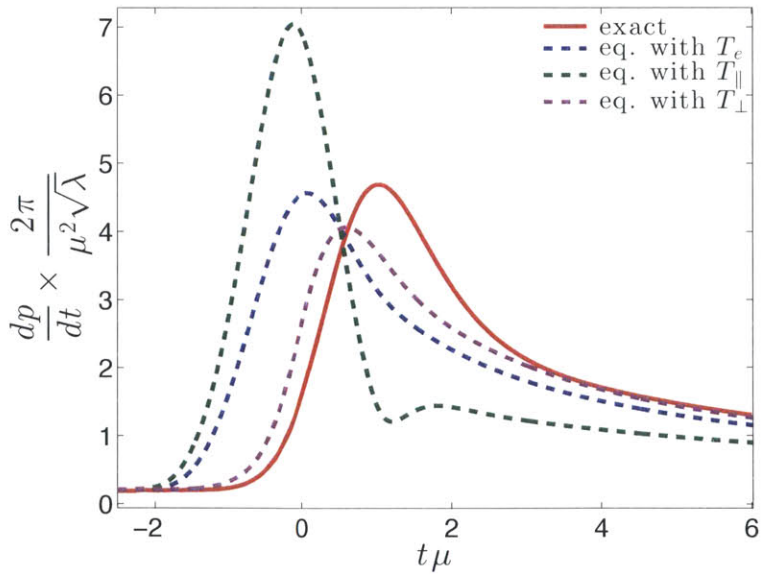

Figure 5-5: Same as Fig. 5-4 but for a quark moving at zero rapidity with a velocity $\beta_x = 0.95$.

result for the drag force required to move a heavy quark with constant velocity $\vec{\beta}$ through the *equilibrium* plasma in strongly coupled SYM theory, namely [82, 83]

$$\left.\frac{d\vec{p}}{dt}\right|_{\rm eq} = \frac{\sqrt{\lambda}}{2\pi}(\pi T)^2 \frac{\vec{\beta}}{\sqrt{1-\beta^2}}\,, \tag{5.31}$$

where T is the temperature of the equilibrium plasma. Out of equilibrium, the matter does not have a well-defined temperature. We can nevertheless use (5.31) to frame expectations for $d\vec{p}/dt$ at any point in spacetime, as follows. At $z = 0$ the fluid is at rest, meaning that the lab frame in which we are working is the local fluid rest frame and the stress tensor for the fluid takes the form (5.8) which we now rewrite as

$$T^{\mu\nu}_{\text{rest frame}} = \frac{\pi^2 N_c^2}{8}\,{\rm diag}(3T_e^4, T_\perp^4, T_\perp^4, T_\parallel^4)\,. \tag{5.32}$$

If the fluid were at rest in equilibrium, we would have $T_e = T_\perp = T_\parallel = T$. In the nonequilibrium setting of interest, through (5.32) we have defined three different "effective temperatures", no one of which is a true temperature since none can be defined. We can then use each of these three "temperatures" in the equilibrium expression (5.31), obtaining the three dashed curves in Figs. 5-4 and 5-5. Because the stress tensor is traceless, any one of the dashed curves can be obtained from the other two; only two are independent. This also explains why wherever two of the dashed curves cross the third must cross also. Note that none of the three dashed curves should be seen as a "prediction" for the actual drag force experienced by the heavy quark in the far-from-equilibrium conditions created by the collision of the sheets of energy. Rather, the three dashed curves tell us what the drag force would be in a static plasma with the same instantaneous energy density or transverse pressure or parallel pressure as that present in the far-from-equilibrium conditions at time t and position $z = 0$. The dashed curves are devices through which we use what we know about the drag force in an equilibrium plasma to frame expectations for the nonequilibrium case.[5]

[5] Some support for this strategy is provided by analyses [106, 107, 108] of the drag force on a heavy quark moving through a fluid that is undergoing boost invariant expansion in one dimension

Comparing the drag force on the heavy quark, the solid red curves in Figs. 5-4 and 5-5, to the three dashed curves yields many observations. Reading the figures from left to right, we first see that at very early times where $T_e = T_\perp = T_\parallel = T_{\rm background}$ the drag force is indeed given by the equilibrium result (5.31) for a static plasma with temperature $T_{\rm background}$. Next, we see that the increase in the drag force due to the dramatic change in the stress tensor of the fluid corresponding to the collision of the sheets of energy is delayed. And, the delay in the increase of the drag force seems to increase with increasing heavy quark velocity. We shall return to this below. Third, we see that the peak value of the drag force is comparable to the expectations provided by the dashed curves, meaning that the peak value of the drag force in the far-from-equilibrium matter produced in the collision is not dramatically smaller or larger than what it would be in a static plasma with the same instantaneous energy density. These second and third observations suggest that a reasonable first-cut approach to modelling the drag on a heavy quark in a heavy ion collision would be to turn the drag force on roughly one "sheet thickness" in time after the collision and from then on use the equilibrium expression (5.31) with an effective temperature determined by the instantaneous energy density. Fourth, at late times when the expansion of the fluid is described well by viscous hydrodynamics we see in Figs. 5-4 and 5-5 that the drag force is best approximated by the value that it would have in a static plasma with the same instantaneous transverse pressure. To some degree this agreement is coincidental as we see that for $\beta = 0.5$ our result is a little below (5.31) with the effective temperature $T_\perp$ while for $\beta = 0.95$ our result is a little above this benchmark. What seems robust is the fact that at late times the actual force required to drag the quark through the expanding, cooling, anisotropic hydrodynamic fluid lies within the band of expectations spanned by the drag force in a static plasma with the same instantaneous energy density or parallel pressure or transverse pressure. For a heavy

and is translation invariant in the other two dimensions. In this setting, the gradient expansion of hydrodynamics becomes an expansion in powers of $1/\tau^{2/3}$, with τ the proper time. (See, for example, Refs. [90, 92].) At leading order, which is to say at late times, the fluid can be treated as ideal meaning that $T_e = T_\perp = T_\parallel \equiv T(\tau)$ with $T(\tau) \propto 1/\tau^{1/3}$ [109]. In this approximation, the drag force on the heavy quark is indeed given by (5.31) with T replaced by $T(\tau)$ [106, 107]. Ref. [108] includes an investigation of the next order corrections.

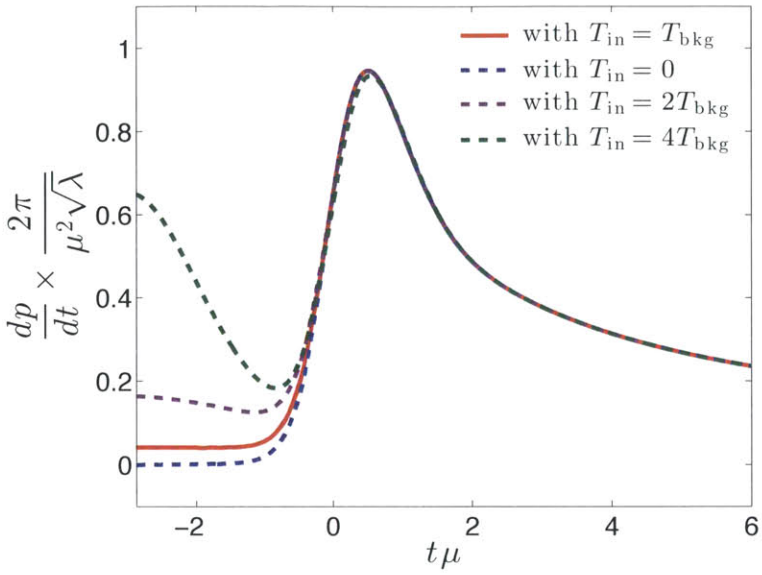

Figure 5-6: Illustration of how the drag force depends on the initial string shape. The four curves show the drag force on a quark whose string initially has the shape of the string trailing behind a heavy quark that is being dragged through an equilibrium plasma with temperatures ranging from zero to four times the actual temperature $T_{\rm background}$ of the low temperature plasma present before the collision. The solid red curve is the same as the solid red curve in Fig. 5-4. The other three curves show that by the time the collision occurs the drag force felt by the heavy quark is quite insensitive to the choice of initial conditions. Note that the initial drag force felt by the heavy quark varies between zero and sixteen times that for the red curve; the perturbations to the initial shape of the string illustrated here are not small, but their residual effects during and after the collision are. In all cases, the heavy quark is dragged with velocity $\beta_x = 0.5$ and $\beta_z = 0$.

quark with zero rapidity, we see no qualitative deviation relative to these expectations, meaning that we see no qualitative consequences of the presence of gradients of the fluid velocity.

We are using initial conditions that correspond to a heavy quark which has been dragged through an equilibrium plasma with the low temperature $T_{\rm background}$ for a long time before the collision. This, of course, is not reminiscent at all of what actually happens in a heavy ion collision, where the heavy quark is created during the collision. It is therefore important to check how sensitive our results for the drag force on the heavy quark during and after the collision are to the choices we are making for the initial shape of the string well before the collision. If our results during and after the

collision were sensitive to our choice of initial conditions this would be problematic, since there can be no right answer to the question of what the initial conditions for a heavy quark before the collision should be since in actual heavy ion collisions there are no heavy quarks present then. Fortunately, as we illustrate in Fig. 5-6 we have found that our results of interest, namely our results for the drag force on the heavy quark during and after the collision, are quite insensitive to the choice of initial conditions. The solid red curve in Fig. 5-6 is the same as that in Fig. 5-4, while the blue, purple and green dashed curves correspond to initial string profiles chosen such that the initial drag force is zero, four or sixteen times that for the red curve. [6] These perturbations to the initial shape of the string, which are in no way small, do have transient effects at early times but their effects on the drag force felt by the heavy quark during and after the collision are negligible.

Let us now return to the question of how the drag force changes with quark velocity β. Looking at Figs. 5-4 and 5-5, the biggest effect of increasing β is certainly the increase in the overall magnitude of the drag force. Since we have seen that our results are not dramatically different from the equilibrium expectations provided by the dashed curves in these figures, it is natural to look at the equilibrium formula (5.31) and ask to what degree the β-dependence in our results is described by assuming that the drag force scales with $\beta\gamma$. Fig. 5-7 provides the answer. Almost all of the change in the overall magnitude of the drag force, e.g. the change in the height at which it peaks seen by comparing Figs. 5-4 and 5-5, can be understood as scaling with $\beta\gamma$. The interesting β-dependent effect that remains in Fig. 5-7 is the time delay in the onset and peaking of the drag force. This time delay increases with increasing β. We investigate the β-dependence of the time delay in Fig. 5-8. From this figure we see that a reasonable characterization of our results for the time at which the drag force peaks is that at low velocity it peaks about one sheet thickness after the time when (around the same time as) the drag force in an equilibrium plasma with the same with the same instantaneous energy density (transverse pressure) would peak

[6] In obtaining these results, we have determined $t(\tau, \sigma)$ by solving the temporal constraint equation (5.13a) numerically; see Appendix H for a discussion.

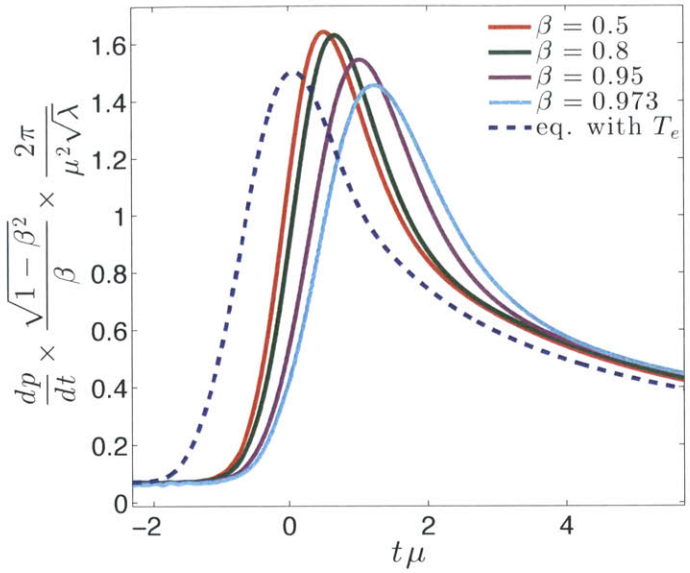

Figure 5-7: Rescaled drag force for four different quark velocities β, all in the x-direction as in Figs. 5-4 and 5-5. We see that the largest β-dependence of our results in Figs. 5-4 and 5-5 can be understood by assuming that the drag force scales roughly with $\beta\gamma$. The remaining β-dependence seen here illustrates the fact that the delay in the onset of, and subsequent peak in, the drag force increases with β. The dashed curve shows the rescaled drag force that the quark would experience in an equilibrium plasma with the same instantaneous energy density. From (5.31) we see that, once we have rescaled by $\beta\gamma$, the dashed curve is β-independent.

while at higher velocities its peak is delayed by a time that increases approximately linearly with γ. In Appendix I we investigate this time delay further by watching how the drag force responds in a background in which the temperature of the plasma is homogeneous in space but over some narrow range of time increases from a low value to a high value. This investigation indicates that the fact that the time delay increases roughly linearly with increasing γ may be generic while the fact that (for the colliding sheets of energy above) we find that at low velocity the drag force peaks close to when the transverse pressure peaks is likely a coincidence. It also indicates that at low velocity the drag force may generically peak at a time that is about $1/(\pi T_{\rm hydro})$ later than the time when the energy density peaks, where $T_{\rm hydro}$ is the temperature defined from the fourth root of the energy density of the fluid at the time when the fluid hydrodynamizes. For the collision we are analyzing, this corresponds to a time

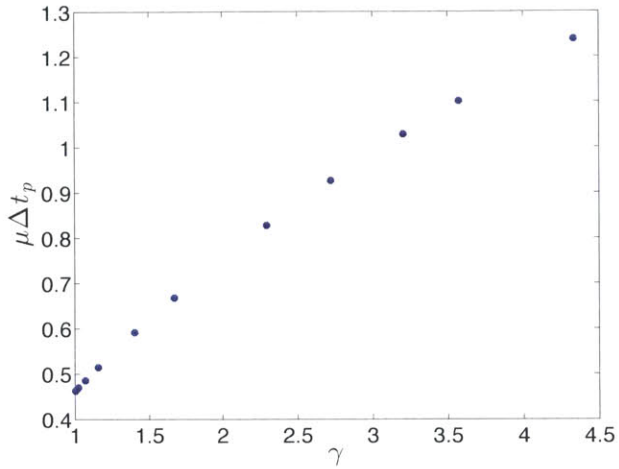

Figure 5-8: The time delay Δt_p between the time at which the drag force on a heavy quark moving with velocity β at zero rapidity peaks, i.e. the peak in the solid curve in Fig. 5-7, and the time at which the dashed curve in Fig. 5-7 peaks. We plot Δt_p vs. γ for velocities ranging from $\beta = 0.05$ to $\beta = 0.973$. The increase in Δt_p clearly has a component that is linear in γ, but the dependence is not completely linear. The value of Δt_p at $\gamma \to 1$, i.e. at $\beta \to 0$, is similar to the delay between the peaks in the purple and blue dashed curves in Figs. 5-4 and 5-5, which is $0.53/\mu$.

delay of around one sheet thickness.

The analysis in Appendix B supports a gravitationally intuitive picture in which a time delay of order $1/(\pi T_{\rm hydro})$ corresponds to the time it takes information from deep inside the bulk, near the black hole horizon, to propagate to the boundary. The information that the geometry near the horizon has changed cannot propagate in the bulk faster than the speed of light, meaning that the time it takes for such a change to affect the string near the boundary — which is what determines the drag force on the heavy quark — is at least $\sim 1/(\pi T_{\rm hydro})$. Furthermore, for a quark that is moving with a large γ the length of the string that stretches from the quark at the boundary down to the near-horizon region is proportional to γ, suggesting that the time delay for a fast quark should include a contribution that is proportional to $\gamma/(\pi T_{\rm hydro})$. These considerations are somewhat heuristic, however, since the changes in the bulk geometry to which the string dragging behind the heavy quark responds do not occur only in the near-horizon region.

A time delay between a change in the stress tensor of the plasma and the resulting

change in the drag force that is proportional to γ can be understood qualitatively in terms of the boundary gauge theory as follows. Clearly, the drag force depends not only on the instantaneous stress tensor of the plasma in which the quark finds itself and the velocity of the quark but also on the history of the quark. In particular, our results suggest that the drag force takes on its "correct" value — i.e. the value it would have in an equilibrium plasma whose stress tensor is similar to the instantaneous stress tensor of the fluid around it — only if the fields that dress the moving quark are configured appropriately. Perhaps as the energy density of the plasma increases the longer wavelength fields that dress the moving quark must be stripped off leaving only those on length scales of order $1/T_e$ and smaller. Perhaps when the energy density decreases those longer wavelength fields need to grow back. Whether or not such speculations are correct in detail, our results indicate that the drag force on the quark responds to changes in the conditions around the quark only after the fields carried along with the moving quark rearrange themselves in a way that takes some time. If the time this takes were constant in the rest frame of the quark, the time delay that we evaluate would be proportional to γ.[7]

5.2.2 Heavy quark with zero transverse momentum

In this section and the next we shall consider more general cases in which the quark has some nonzero velocity β_z in the 'beam' direction parallel to the direction of motion of the colliding sheets, which is to say that we shall allow the quark to have nonzero rapidity. As illustrated in Fig. 5-9, we shall only consider trajectories in which the velocity $\vec{\beta}$ of the quark is constant and in which the initial position of the quark has been chosen such that at $t = 0$ the quark is at $z = 0$, meaning that the quark passes through the spacetime point at which the sheets of energy collide. Although in our setup the quark has existed for all time, we are of course interested in gaining qualitative insights into circumstances in which a heavy quark is produced

[7] A time delay between some change in the environment in which a heavy quark finds itself and the resulting change in the drag force on the heavy quark has been seen in other contexts, see for example Refs. [110, 111], in which it has also been attributed to the time it takes for the gluon fields around the moving quark to rearrange.

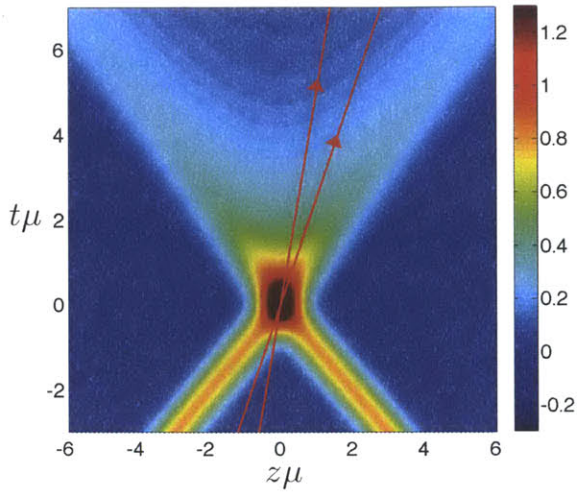

Figure 5-9: The red arrows show the trajectories in the (z,t)-plane of two quarks with nonzero rapidity, with $\beta_z = 0.2$ and $\beta_z = 0.4$. The trajectories are superimposed on the plot of the rescaled energy density $\mathcal{E}$ as in Fig. 5-3. We shall consider cases in which the quark has zero or nonzero transverse velocity β_x. In all cases that we shall consider, the quark is pulled with constant velocity $\vec{\beta}$ through the energy density produced by the colliding sheets.

at $z = t = 0$ with some velocity $\vec{\beta}$. We shall not consider values of β_z that are greater than 0.4 because we want to ensure that at the time $t = -3/\mu$ at which we choose our initial conditions the quark has not yet felt the sheet of energy that is about to catch up with it in any significant way.

In order to obtain the greatest contrast with the case in which the quark has zero rapidity, analyzed above, in this section we shall consider the case in which the quark has a nonzero β_z but has no transverse velocity, $\beta_x = 0$. We shall allow both β_x and β_z to be nonzero in the next section.

The solid red curve in Fig. 5-10 shows the force on a quark with $\beta_z = 0.4$ and $\beta_x = 0$. To interpret the force shown in Fig. 5-10, we first need to ask what the velocity of the fluid is at the location of the quark as a function of time, since the drag on the quark should depend on its velocity relative to that of the moving fluid. The fluid velocity is always in the z-direction and its magnitude is given by

$$\beta_z^{\text{fluid}} \equiv \frac{u^z}{u^0} \tag{5.33}$$

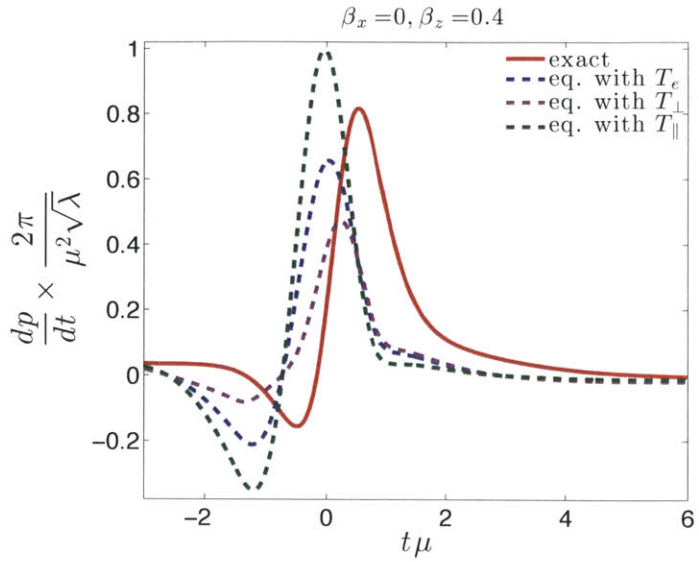

Figure 5-10: The 'drag' force (solid red curve) acting on a quark moving through the matter produced in the collision along a trajectory with $\beta_z = 0.4$ and $\beta_x = 0$. The force is shown in the lab frame. The dashed curves show what the force would be if in the local fluid rest frame it were given by the drag force that the quark would experience in an equilibrium plasma with the same instantaneous energy density, parallel pressure or perpendicular pressure as that in the local fluid rest frame at the location of the quark. The dashed curves are described further in the text.

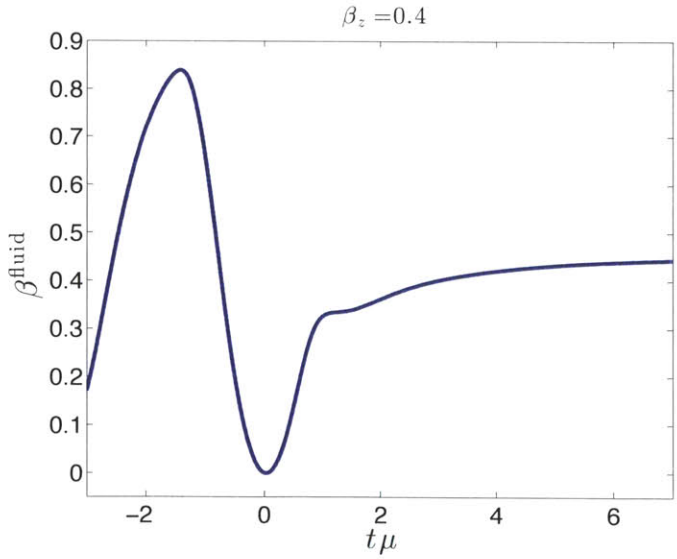

Figure 5-11: The fluid velocity β^{fluid}, defined in the text, at the location of a quark moving along the trajectory in Fig. 5-9 with $\beta_z = 0.4$. If the hydrodynamic fluid at late times were boost invariant, β^{fluid} would be given by $\beta_z = 0.4$. Note that at late times $\beta^{\text{fluid}} > 0.4$, meaning that the fluid is moving faster than the quark.

where u^μ is the fluid velocity four-vector obtained from the stress tensor in the lab frame as described by Eq. (5.7). We show $\beta^{\rm fluid}$ in Fig. 5-11. Reading this figure from left to right while referring to Fig. 5-9: (i) We see that at the time $t = -3/\mu$ at which we choose our initial conditions the quark is already feeling some effects of the fast-approaching sheet of energy. The quark is initially immersed in the background plasma, which is at rest, meaning that the fact that $\beta^{\rm fluid} \neq 0$ can be attributed to the Gaussian tail of the sheet of energy which is approaching with velocity 1. (ii) Then, the sheet of energy incident from the left catches up to the quark and as the energy of the sheet overwhelms that of the background plasma $\beta^{\rm fluid}$ rises toward the speed of light. Note that the quantity $\beta^{\rm fluid}$ can be computed as we have described even when the matter is far from equilibrium, as long as its energy density is positive [89]. At these early times $\beta^{\rm fluid}$ should not really be thought of as the velocity of a fluid, although for convenience we shall refer to it as such. (iii) Next, the left-moving sheet of energy slams into the right-moving sheet and, briefly, $\beta^{\rm fluid}$ is near zero. By symmetry, $\beta^{\rm fluid} = 0$ at all times at $z = 0$, meaning that $\beta^{\rm fluid} = 0$ at the location of the quark at $t = 0$. (iv) Finally, at late times after the fluid has hydrodynamized, $\beta^{\rm fluid}$ is close to $\beta_z = 0.4$. Note that if the hydrodynamic expansion at late times were boost invariant, the velocity of the fluid at late times on a trajectory with constant rapidity like the one that the quark is following would be given by the velocity of the quark itself. In other words, if the expanding fluid at late times were boost invariant, the curve in Fig. 5-11 would have $\beta^{\rm fluid} = 0.4$ at late times.

With an understanding of the velocity of the matter through which the heavy quark is moving now in hand, we can return to Fig. 5-10 and compare the drag force there with expectations based upon the force (5.31) on a heavy quark that is being dragged through plasma in equilibrium, as we did in Fig. 5-4. The expression (5.31) describes the force on a quark moving through matter at rest, so to use it at any given time t we must first boost to a frame in which the matter through which the quark in Fig. 5-10 is moving is at rest at that time. That is, we boost by a velocity $\beta^{\rm fluid}(t)$, plotted in Fig. 5-11, to the local fluid rest frame. In the local fluid rest frame, the

quark is moving in the z-direction with a velocity

$$\beta_{z,\mathrm{RF}} = \frac{\beta_z - \beta^{\mathrm{fluid}}}{1 - \beta_z\,\beta^{\mathrm{fluid}}} \tag{5.34}$$

that can be positive or negative depending on whether β^{fluid} is smaller or larger than the velocity β_z of the quark in the lab frame. Next, we compute the stress tensor in the local fluid rest frame, where it takes the form (5.32), and use the temperatures T_e, $T_\perp$ and $T_\parallel$ so obtained as well as the velocity $\beta_{z,\mathrm{RF}}$ from (5.34) in the expression (5.31). This gives us the drag force that the quark would experience if, in the local fluid rest frame, it were moving with velocity $\beta_{z,\mathrm{RF}}$ through an equilibrium plasma with the same instantaneous energy density, perpendicular pressure or parallel pressure as that of the matter at its location. Finally, we boost the three forces computed in this way back to the lab frame, using the appropriate Lorentz transformation for forces, given in the present context by [8]

$$f^{\mu}_{\text{eq, lab frame}} = \frac{1}{u^0 + u^z \beta_{z,\mathrm{RF}}} \begin{pmatrix} u^0 f^0_{\mathrm{eq,RF}} + u^z f^z_{\mathrm{eq,RF}} \\ f^x_{\mathrm{eq,RF}} \\ f^y_{\mathrm{eq,RF}} \\ u^0 f^z_{\mathrm{eq,RF}} + u^z f^0_{\mathrm{eq,RF}} \end{pmatrix} , \tag{5.35}$$

with u^μ the fluid four-velocity from Eq. (5.7). We plot the three lab-frame forces computed as we have just described as the three dashed curves in Fig. 5-10. If we apply this algorithm in the more general case in which in the lab frame the quark is moving with both β_z and β_x nonzero, the result is

$$\begin{aligned} f^x_{\text{eq, lab frame}} &= \frac{\sqrt{\lambda}}{2\pi}(\pi T)^2 \gamma \left(u^0 \beta_x - u^z \beta_x \beta_z\right) \\ f^z_{\text{eq, lab frame}} &= \frac{\sqrt{\lambda}}{2\pi}(\pi T)^2 \gamma \left(u^0 \beta_z + u^z (\beta_x)^2 - u^z\right) , \end{aligned} \tag{5.36}$$

[8] As it is shown in Appendix J, one can do consistency check of the formalism for extracting the drag force from the bulk gravitational quantities that we have set out in Section 5.1.3 to confirm that upon boosting the bulk black brane metric and the trailing string profile by a velocity β^{fluid} and evaluating (5.30) one obtains (5.35).

which can be written as

$$f^{\mu}_{\text{eq, lab frame}} = -\frac{\sqrt{\lambda}}{2\pi}(\pi T)^2 \frac{1}{\gamma}\left(u_\nu u_q^\nu u_q^\mu + u^\mu\right) \ , \tag{5.37}$$

where we have defined $u_q^\mu \equiv \gamma(1, \vec{\beta})$ and have allowed for a generic choice of coordinate axes. The T used in the expressions (5.36) or (5.37) can be either the T_e or the $T_\perp$ or the $T_\parallel$ obtained from the stress tensor in the local fluid rest frame.

We can now compare the actual drag force on a quark moving in the z-direction, the solid red curve in Fig. 5-10, to the expectations for an equilibrium plasma moving with velocity β^{fluid} with the same instantaneous energy density or pressure, shown as the dashed curves. In many respects, this comparison is as we found in Fig. 5-4 for a quark moving in the x-direction. As in Fig. 5-4, we see in Fig. 5-10 that the maximum value of the drag force in the far-from-equilibrium matter produced during the collision is within the expectations for the maximum drag force spanned by the three dashed curves. And, as in Fig. 5-4, we see a time delay in the rise in the magnitude of the drag force. Here, though, the drag force first goes negative as the heavy quark is hit from the left by the sheet of energy going in the same direction and only then goes positive as the second sheet of energy slams into the first.

The most interesting differences between Figs. 5-10 and 5-4 arise at late times. First, we see that the magnitude of the drag force at late times is much smaller in Fig. 5-10 than in Fig. 5-4. This reflects the fact that at late times the quark and the fluid are moving at comparable velocities, see Fig. 5-11, meaning that their relative velocity is small. In fact, at $t \simeq 2.8/\mu$ the fluid velocity and the quark velocity are equal – the dashed curves in Fig. 5-10 therefore cross zero there. Interestingly, we see that the solid curve stays positive for quite a long time afterwards until $t = 5.0/\mu$ meaning that there is an extended period of time when: (i) The fluid has hydrodynamized. (ii) The fluid is moving faster than the quark, which would suggest that the 'drag' force on the quark needed to keep it moving at constant β_z should be a force pulling backward on it, toward negative z, pulling against the push from the fluid that is moving faster than the quark. That is, we expect that dp/dt should

be negative, as is indeed the case for the dashed curves in Fig. 5-10. (iii) Instead, the quark is still being dragged forward, toward positive z, with dp/dt positive. This means that in the local fluid rest frame the force that the external agent must exert in order to move the quark towards the left acts toward the right. The quark is moving towards the left in this frame but the force exerted on it by the liquid through which it is moving is *also* acting toward the left, pushing it in the direction of its motion rather than dragging it in the opposite direction! We illustrate this in Fig. 5-12 by plotting the force exerted on the quark in the local fluid rest frame. The reason that a result as surprising as this is possible is that in formulating our expectations, as shown via the dashed curves, we are completely neglecting the effects of spatial gradients in the fluid velocity.[9] Unlike in Fig. 5-4, in Fig. 5-10 these gradients are aligned parallel to the direction in which the quark is moving; the lesson we learn is that in this circumstance the gradients in the fluid velocity can have qualitative effects on the 'drag' force that must be exerted on the quark. Qualitative effects of the gradient in the fluid velocity arise in Figs. 5-10 and 5-12 but not in Fig. 5-4 both because the effects of the gradient on the 'drag' force are larger in absolute magnitude when the gradient is aligned with the motion of the quark and because in this case the drag force in the absence of gradients would be very small since the relative velocity of the quark and the fluid is so small.

The red curves in Fig. 5-13 show the gradient of the fluid velocity in the lab frame and in the local fluid rest frame, in each case projected onto the quark velocity in that frame, namely

$$(\nabla u^z) \cdot \hat{\beta} \equiv \frac{\partial u^z}{\partial z} \frac{\beta_z}{\beta} \tag{5.38}$$

and

$$(\nabla u^z)_{\rm RF} \cdot \hat{\beta}_{\rm RF} \equiv \left.\frac{\partial u^z}{\partial z}\right|_{\rm RF} \frac{\beta_{z,\rm RF}}{\beta_{\rm RF}} \tag{5.39}$$

for the trajectory with $\beta_z = 0.4$ and $\beta_x = 0$. For trajectories with $\beta_z = 0$ and $\beta_x > 0$,

[9] We have also neglected spatial gradients in the energy density of the fluid. In the following, we will show that after hydrodynamization the effects of spatial gradients on the drag force that we compute correlate well with the behavior of the gradients of the fluid velocity. We have checked that the spatial gradients of the energy density are small at these late times, as are their effects on the force that we compute.

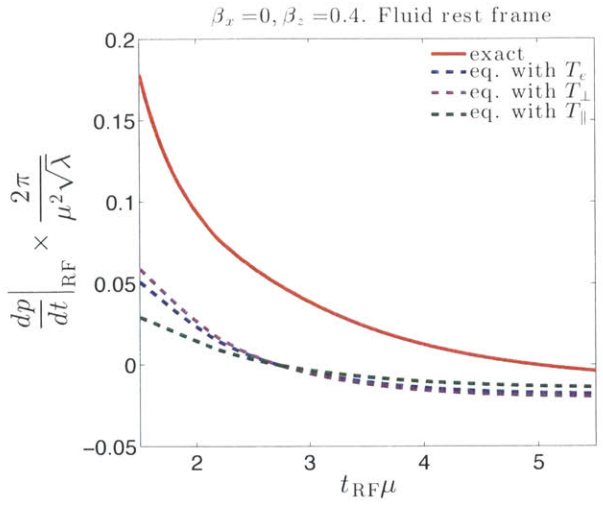

Figure 5-12: Forces as in Fig. 5-10, plotted here in the local fluid rest frame and focusing on times $t_{\rm RF} > 1.5/\mu$ to better illustrate the behavior after hydrodynamization. After $t_{\rm RF} = 2.8/\mu$, the quark is moving to the left in the local fluid rest frame (in the lab frame, the fluid is moving faster than the quark) and the dashed curves accordingly lead us to expect that the force needed to drag the quark leftward in the local fluid rest frame should be a force acting toward the left. Instead, we see that between $t_{\rm RF} = 2.8/\mu$ and $t_{\rm RF} = 5.0/\mu$, the 'drag' force that must be exerted to maintain the leftward motion acts toward the right!

both quantities vanish identically. Fig. 5-13 shows that if we start with $\beta_z = 0.4$ and add a nonzero β_x that is small compared to β_z in the lab frame but that is large compared to $|\beta_{z,\rm RF}|$, for example $\beta_x = 0.2$, the quantity $(\nabla u^z)_{\rm RF} \cdot \hat{\beta}_{\rm RF}$ is substantially reduced while in the lab frame $(\nabla u^z) \cdot \hat{\beta}$ is not much changed. This suggests that if we analyze the drag force on a quark that follows a trajectory with $\beta_z = 0.4$ and $\beta_x = 0.2$, we should find results that in the local fluid rest frame are more similar to those in Fig. 5-4 but in the lab frame are more similar to those in Fig. 5-10. We shall confirm this expectation in the next section, but in so doing we shall discover a second surprise.

5.2.3 Heavy quark with nonzero rapidity and transverse momentum

In this section we analyze the force that must be exerted in order to move a heavy quark through the colliding sheets of energy along a trajectory with nonzero β_x and

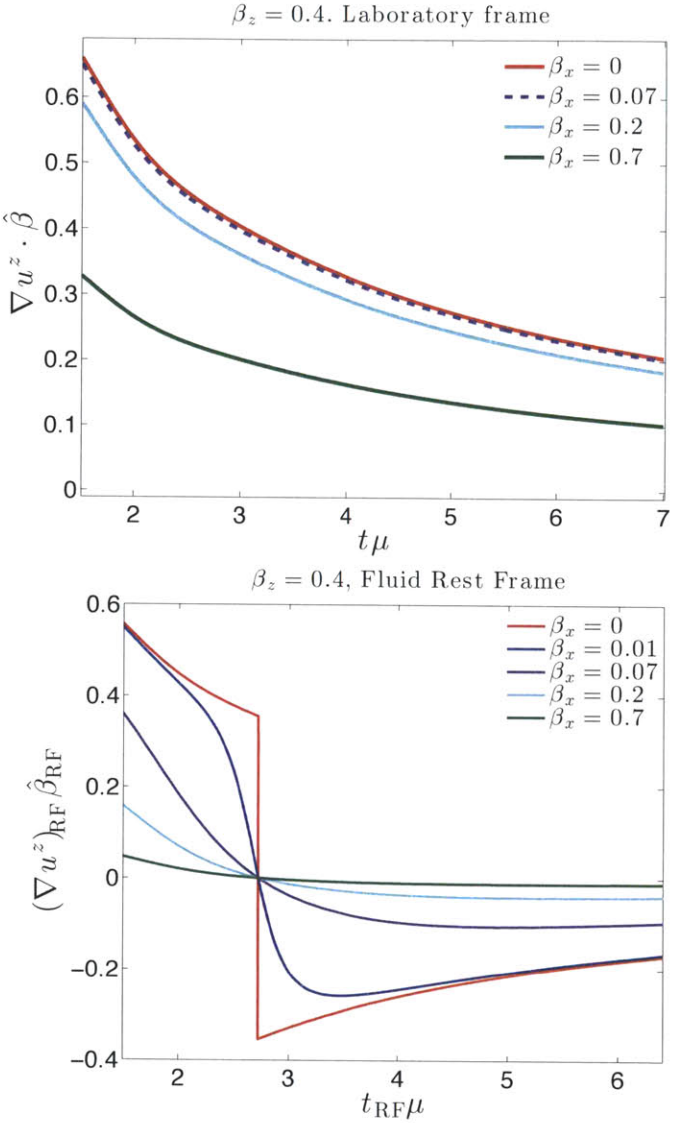

Figure 5-13: Component of the gradient of the fluid velocity in the direction of motion of the quark at the location of the quark in the lab frame (upper panel) and in the local fluid rest frame (lower panel). The differences between the two panels arises because $\beta_{z,\mathrm{RF}} \ll \beta_z$. In all curves in both panels, the trajectory of the quark has $\beta_z = 0.4$. The different curves are for trajectories with varying values of β_x. At $t_{\mathrm{RF}} = 2.8/\mu$, the sign of $\beta_{z,\mathrm{RF}}$ flips, which is to say that in the lab frame the velocity of the fluid exceeds the velocity of the quark. We see in the lower panel that adding a β_x that is quite small compared to β_z in the lab frame, but is comparable to $\beta_{z,\mathrm{RF}}$, significantly reduces $(\nabla u^z)_{\mathrm{RF}} \cdot \hat{\beta}_{\mathrm{RF}}$.

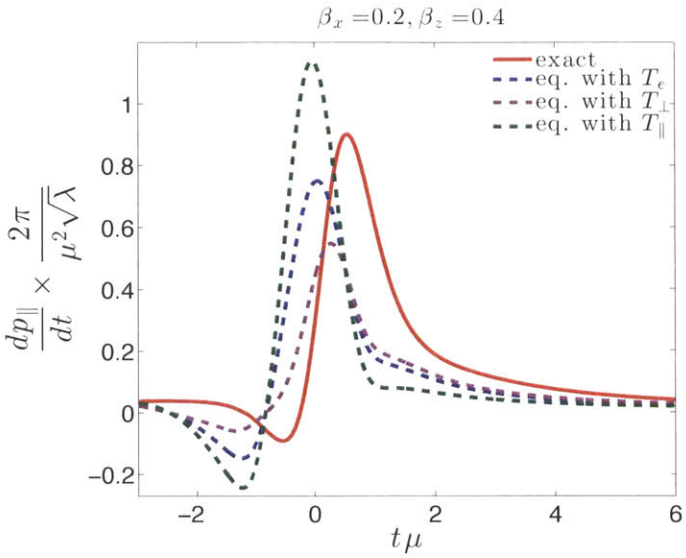

Figure 5-14: The force (solid red line) in the lab frame that must be exerted in the direction of motion of the quark (in the lab frame) in order to drag it with a velocity $\beta_x = 0.2$ and $\beta_z = 0.4$, a trajectory with nonzero transverse momentum and rapidity. The dashed curves, computed as described in the previous section, show what this force would be if in the local fluid rest frame the quark were being dragged through a plasma with the same instantaneous energy density, perpendicular pressure or parallel pressure as that at the location of the quark.

β_z, which is to say with both transverse momentum and rapidity nonzero. We start by considering a trajectory with $\beta_z = 0.4$ as in Figs. 5-10 and 5-11 but now with $\beta_x = 0.2$. Because the velocity of the quark now has a component perpendicular to the velocity of the fluid at the location of the quark (this was not the case in both previous sections) we now expect and find that the force that must be exerted in order to move the quark along this trajectory has a component perpendicular to the direction of motion of the quark.

Let us first look at the drag force parallel to the direction of motion the quark in the lab frame,

$$\frac{dp_\parallel}{dt} \equiv \frac{\vec{f}\cdot\vec{\beta}}{\beta}\,, \tag{5.40}$$

which is shown as the solid red curve in Fig. 5-14. (Note that $dp_\parallel/dt$ and, below, $dp_\perp/dt$ refer to the force parallel and perpendicular to the direction of motion of the quark; in contrast, $T_\parallel$ and $T_\perp$ are defined via the pressures in the fluid that

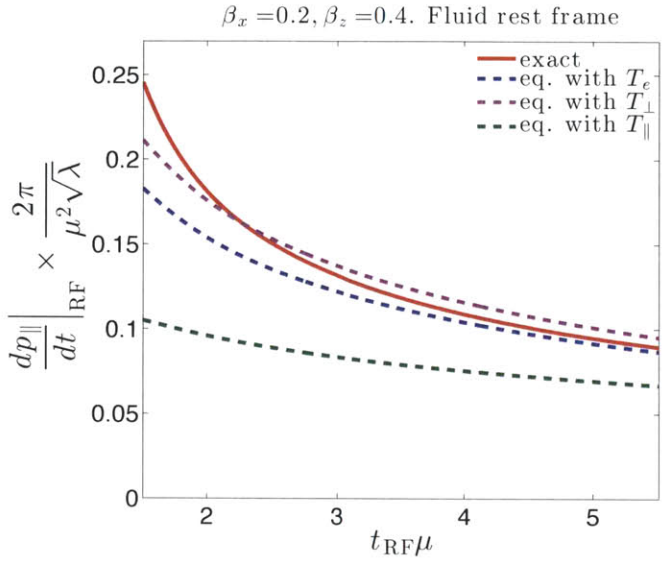

Figure 5-15: Forces as in Fig. 5-14 plotted here in the local fluid rest frame and focusing on times $t_{\rm RF} > 1.5/\mu$ to better illustrate the behavior after hydrodynamization. We saw in Fig. 5-12 that when $\beta_z = 0.4$ and $\beta_x = 0$ the dashed curves that show what the drag force in the local fluid rest frame would be in a spatially homogeneous plasma with the same instantaneous energy density or transverse pressure or parallel pressure failed to describe the actual force on the quark, because they neglected the effects of gradients in the fluid velocity on the force. Here, with $\beta_x = 0.2$, we see that after hydrodynamization the actual force on the quark falls within the range of expectations spanned by the dashed curves.

act in the directions parallel to and perpendicular to the direction of motion of the colliding sheets and hence of the fluid, i.e. the z-direction.) We see that, as in both Sections 5.2.1 and 5.2.2, the dashed curves provide a reasonable guide to the peak value of the drag force but the actual force peaks later than the dashed curves do, a time delay that is by now familiar.

At late times, after the fluid has hydrodynamized, we see behavior that is more similar to that in Section 5.2.2 in the sense that the drag force in the direction of motion of the quark is affected by the gradients in the fluid velocity to such a degree that it is well outside the expectations spanned by the three dashed curves. Unlike when β_x was zero, though, with $\beta_x = 0.2$ at least the sign of the force is the same for the solid and dashed curves. The dashed curves nevertheless fail to give a qualitative description of the actual drag force after the fluid has hydrodynamized. This is consistent with the upper panel of Fig. 5-13 which shows that, when $\beta_z = 0.4$, turning on $\beta_x = 0.2$ does not substantially reduce the magnitude of the component of the gradient of the fluid velocity in the direction of motion of the quark — in the lab frame. In Fig. 5-15 we see that the story is different in the local fluid rest frame. With $\beta_x = 0.2$, we find that the drag force in this frame does lie within the range of expectations spanned by the three dashed curves. This is consistent with the lower panel of Fig. 5-13, where we saw that, because $|\beta_{z,\mathrm{RF}}| \ll \beta_z$, when we turn on $\beta_x = 0.2$ we do substantially reduce the component of the gradient of the fluid velocity in the direction of motion of the quark — in the local fluid rest frame.

Turning now to the force acting perpendicular to the direction of motion of the quark, we fix our sign conventions by defining this as

$$\frac{dp_\perp}{dt} \equiv f^z \frac{\beta_x}{\beta} - f^x \frac{\beta_z}{\beta} \ . \tag{5.41}$$

It is plotted as the solid red curve in the upper panel of Fig. 5-16. The dashed curves show what the force perpendicular to the direction of motion of the quark would be in the lab frame if, in the local fluid rest frame, the quark were moving through an equilibrium plasma with the same instantaneous energy density, perpendicular

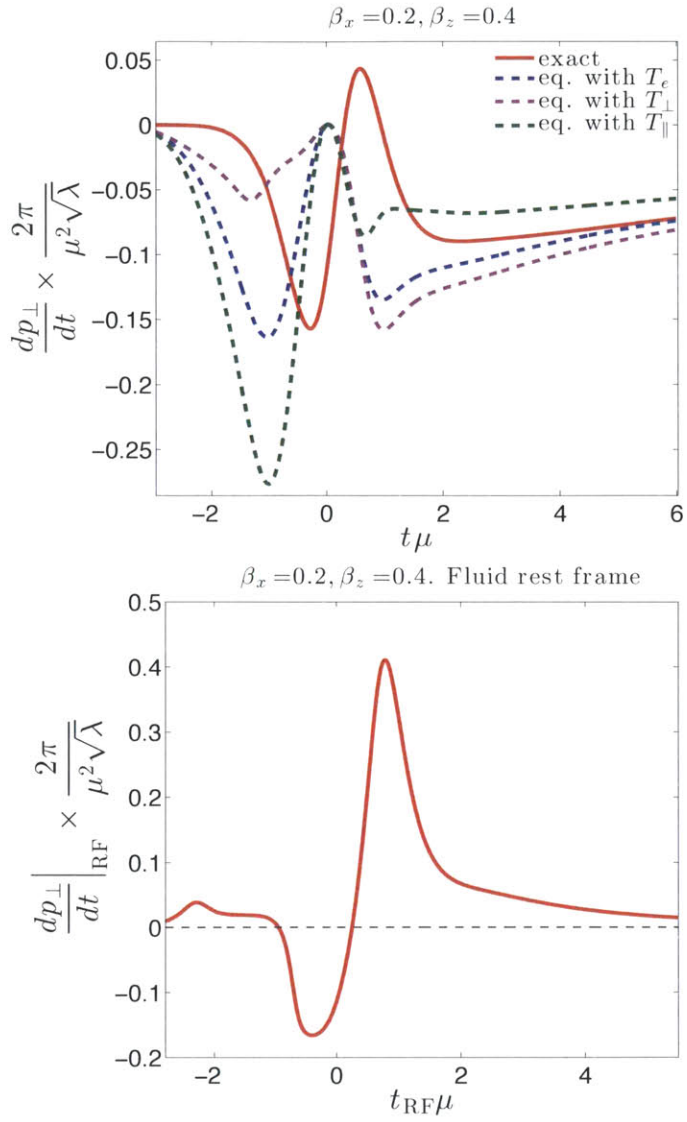

Figure 5-16: Upper panel: as in Fig. 5-14, but here we plot the force that must be exerted perpendicular to the direction of motion of the quark, in the lab frame. Note the scale on the vertical axis: this component of the force is significantly smaller than the component of the force in Fig. 5-14. Lower panel: the force that must be exerted perpendicular to the direction of motion of the quark in the local fluid rest frame. If, in this frame, the quark were moving through a homogeneous fluid (e.g. the equilibrium plasma with the same instantaneous energy density or pressure as that at the location of the quark) the force in this frame could only act parallel to the direction of the quark. The dashed curves therefore all vanish in the lower panel. The actual force does not vanish and is in fact quite substantial at its peak: even in the local fluid rest frame, the force needed to drag the quark includes a component perpendicular to its direction of motion.

pressure, or parallel pressure as that at the location of the quarks.

The force perpendicular to the direction of motion of the quark is a new development, present only when both β_x and β_z are nonzero. In the lab frame, the existence of a perpendicular force is no surprise since in this frame of reference the quark is moving through a fluid whose velocity includes a component perpendicular to its own. For this reason, in the upper panel of Fig. 5-16 the dashed curves show that even if there were no velocity gradients in the fluid the force would include a component perpendicular to the direction of motion of the quark in the lab frame. This poses an obvious question: boost to the local fluid rest frame and ask whether in that frame the drag force is parallel to the direction of motion of the quark. We show in the lower panel of Fig. 5-16 that the answer is no: even in a reference frame in which at each point in time we have boosted to a frame in which the quark is moving through a fluid at rest, the force required to drag the quark along its trajectory through this fluid includes a component perpendicular to the direction of motion of the quark! In this frame, in the absence of gradients in the fluid there could be no component of the force perpendicular to the motion of the quark. The lower panel of Fig. 5-16 thus represents a stark consequence of the presence of spatial gradients in the matter produced in the collision. The effect is largest at early times, when the matter is far from equilibrium. At these early times, the effect is large indeed: the peak value of the force perpendicular to the motion of the quark is about half as large as the peak value of the drag force that acts parallel to the velocity of the quark. The effect is also non-vanishing at late times, after the expanding fluid has hydrodynamized. We find this result to be generic, arising for any trajectory in which both β_x and β_z are nonzero. A drag force that includes a component perpendicular to the direction of motion of the quark through a medium arises in other contexts in which some anisotropy in the medium has been introduced [112, 113, 114]. Here we see this phenomenon arising as a robust consequence of gradients in the fluid velocity — a form of anisotropy that must be present in heavy ion collisions.

To get a sense of how generic our results are, we close this section by illustrating them for the case where the heavy quark is dragged along a trajectory with $\beta_x = 0.7$

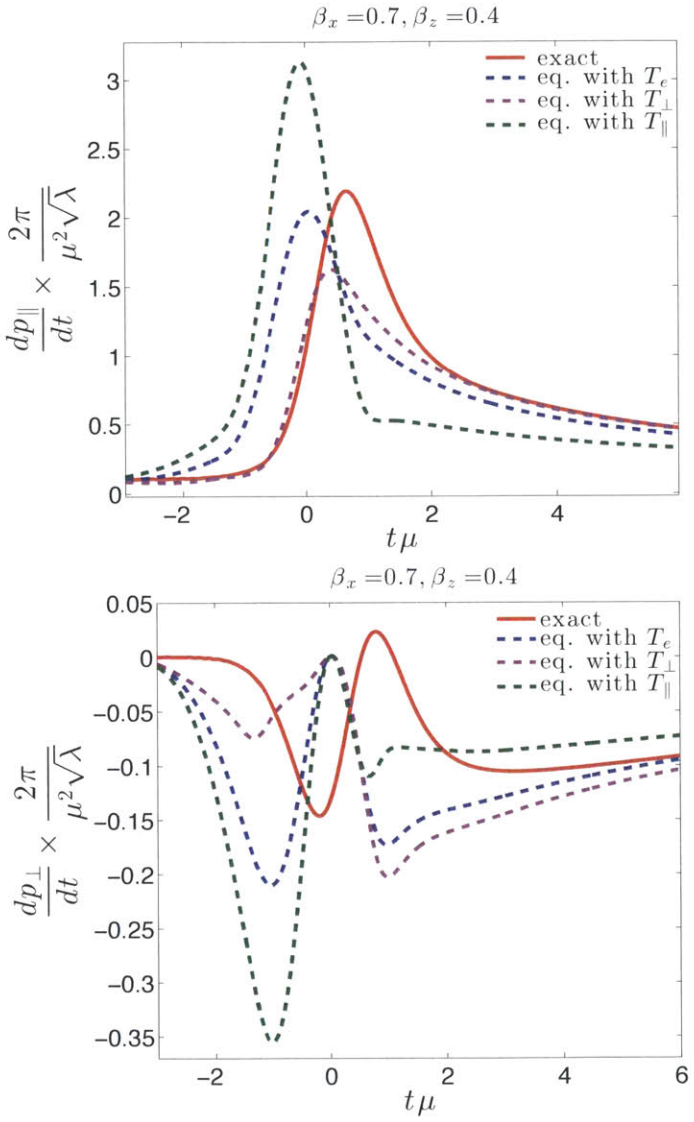

Figure 5-17: Drag force parallel to (upper panel) and perpendicular to (lower panel) the direction of motion of the quark in the lab frame, as in Fig. 5-14 and the upper panel of Fig. 5-16, but here for a quark with $\beta_x = 0.7$ and $\beta_z = 0.4$.

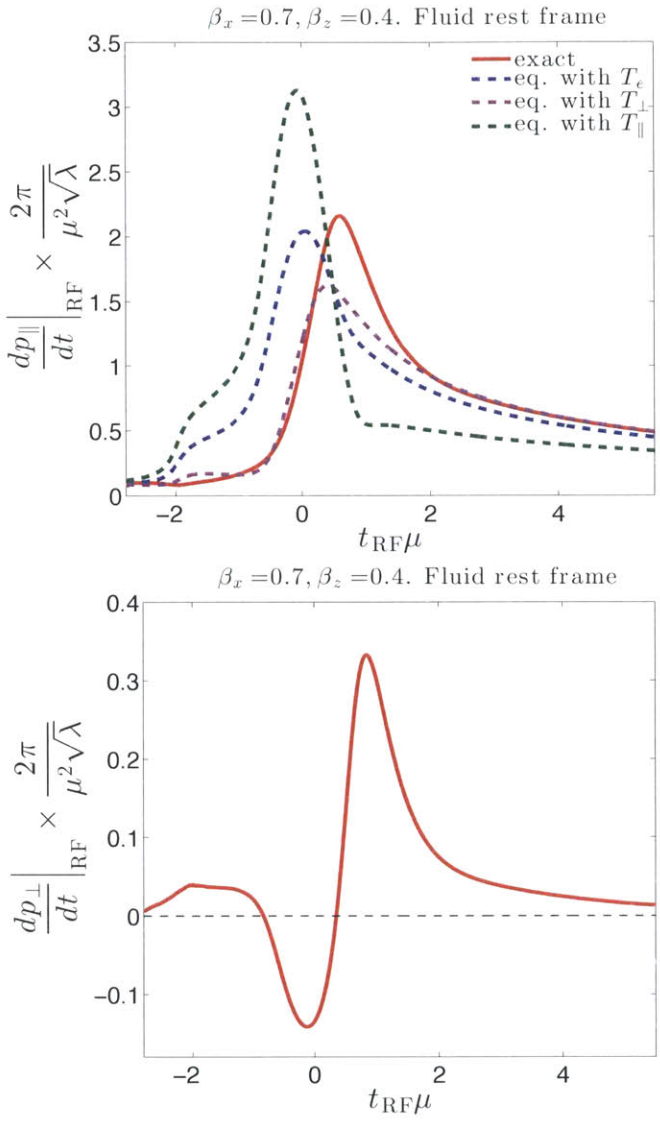

Figure 5-18: As in Fig. 5-17, but here in the local fluid rest frame.

and $\beta_z = 0.4$. In Fig. 5-17 we first show our results in the lab frame, finding results that are similar in most respects to those at smaller β_x that we saw in Figs. 5-14 and 5-16. The important distinction is that in Fig. 5-17 we see that at late times, after hydrodynamization, the drag force that we calculate is well described by the dashed curves meaning that, unlike in Fig. 5-14, here there are no qualitative effects of the gradients in the fluid velocity apparent. We can understand this by noting from the upper panel of Fig. 5-13 that by increasing β_x from 0.2 to 0.7 we have substantially reduced the component of the gradient of the fluid velocity in the direction of motion of the quark in the lab frame.

In Fig. 5-18, we show our results for the case with $\beta_x = 0.7$ and $\beta_z = 0.4$ after boosting to the local fluid rest frame. Again, we find that even in a frame in which the quark is moving through a fluid that is instantaneously at rest the force required to drag the quark along its trajectory includes a component perpendicular to the trajectory. We see that this effect of gradients in the fluid velocity is somewhat smaller in absolute terms, and much smaller relative to the drag force in the direction of motion of the quark, here where $\beta_x = 0.7$ than it was in the lower panel of Fig. 5-16, where $\beta_x = 0.2$. This reflects the fact that as β_x increases at fixed β_z the component of the gradient of the fluid velocity in the direction of motion of the quark decreases.

Chapter 6

Effects of fluid velocity gradients on heavy quark energy loss

6.1 Hydrodynamic fluid and a heavy quark moving through it

6.1.1 Gravitational description of a moving fluid

We begin with a brief description of the dual gravitational description of the stress-energy tensor for the conformal fluid of strongly coupled $\mathcal{N} = 4$ SYM theory at nonzero temperature, undulating in some generic way according to the laws of hydrodynamics. We shall work only to first order in fluid gradients. In order to keep our expressions tractable on a first pass through the calculation, we shall then specialize to the case of a fluid that fills 3-dimensional space but that moves only along a single axis, flowing in some generic way along the z-direction. (Toward the end of Section 6.2 we shall lift this restriction, returning there to the case of generic hydrodynamic motion in 3+1 dimensions, still working only to first order in gradients which is to say still assuming that the spatial and temporal variation of the thermodynamic variables and the fluid velocity occur only on length and time scales that are much longer than $1/T$, with T the fluid temperature.)

The stress-energy tensor for the conformal fluid of $\mathcal{N} = 4$ SYM theory flowing hydrodynamically in $3 + 1$-dimensions with a temperature T and 4-velocity u^μ that vary as functions of space and time is given to first order in gradients by

$$\frac{8\pi^2}{N_c^2} T^{\mu\nu} = \frac{1}{b^4} \left(\eta^{\mu\nu} + 4u^\mu u^\nu\right) - \frac{2}{b^3}\sigma^{\mu\nu}, \tag{6.1}$$

where $b \equiv 1/(\pi T)$ is the inverse temperature, $\eta^{\mu\nu} = \mathrm{diag}(-1, 1, 1, 1)$ is the Minkowski metric, and

$$\sigma^{\mu\nu} = \frac{1}{2} P^{\mu\alpha} P^{\nu\beta} (\partial_\alpha u_\beta + \partial_\beta u_\alpha) - \frac{1}{3} P^{\mu\nu} \partial_\alpha u^\alpha \tag{6.2}$$

is the symmetric tensor encoding the first order contributions of fluid gradients, with the projectors transverse to u^μ defined by $P^{\mu\nu} \equiv \eta^{\mu\nu} + u^\mu u^\nu$. With our metric conventions, u^μ is normalized such that $u^\mu u_\mu = -1$. The stress-energy tensor (6.1) describes a fluid whose equation of state is $P = \varepsilon/3$, where P and ε are its pressure and energy density respectively, and whose shear and bulk viscosities are given by $\eta = s/(4\pi)$ and $\zeta = 0$, where s is the entropy density of the fluid. $P = \varepsilon/3$ and $\zeta = 0$ follow just from conformal invariance. $4\pi\eta/s = 1$ for the fluid in any non-Abelian gauge theory with a dual gravitational description, in the strong coupling and large-N_c limit [144, 145, 146, 147]. Note that the stress-energy tensor depends on symmetric combinations of the fluid gradients $\partial_\alpha u_\beta$ and is independent of the fluid vorticity

$$\tilde{\omega}^\mu \equiv \frac{1}{2} \epsilon^{\mu\nu\alpha\beta} u_\nu \partial_\alpha u_\beta \,, \tag{6.3}$$

because the underlying microscopic theory does not violate time-reversal or parity symmetry. The vorticity will nevertheless play a role in our considerations later. Hydrodynamics is the statement that the fluid variables satisfy energy and momentum conservation,

$$\partial_\mu T^{\mu\nu} = 0 \,. \tag{6.4}$$

It is easy to see that, to first order in gradients, the hydrodynamic equations (6.4) determine the spatial and temporal variation of the temperature, or the inverse tem-

perature b, uniquely in terms of the spatially and temporally varying fluid velocities:

$$\partial_\mu b = b\left(u^\nu \partial_\nu u_\mu - \frac{1}{3} u_\mu \partial_\alpha u^\alpha\right). \tag{6.5}$$

We shall use this relation below.

The dual gravitational description of the fluid with stress-energy tensor (6.1) was obtained in Ref. [122]. (These authors worked to second order in gradients. We shall quote their results only to first order.) Upon introducing a bookkeeping parameter ϵ that we shall use to count powers of gradients and that we shall in the end set to $\epsilon = 1$, the $4+1$-dimensional metric in the dual gravitational description of the fluid takes the form

$$ds^2 = \left(G^{(0)}_{MN} + \epsilon\, G^{(1)}_{MN}\right) dX^M dX^N \tag{6.6}$$

where $X^M \equiv (x^\mu, r)$. The first term in (6.6) is given by

$$G^{(0)}_{MN} dX^M dX^N = -2u_\mu dx^\mu dr - r^2 f(br) u_\mu u_\nu dx^\mu dx^\nu + r^2 P_{\mu\nu} dx^\mu dx^\nu \tag{6.7}$$

where $f(x) \equiv 1 - 1/x^4$. If we set $u^\mu = (1,0,0,0)$ everywhere, the metric (6.7) describes a static AdS black brane with an event horizon at $r = 1/b$ and with the AdS boundary located at $r = \infty$. This is the gravitational dual of the static $\mathcal{N} = 4$ SYM plasma in equilibrium with a uniform and constant temperature $T = 1/(\pi b)$. The coordinates X^M that we are using to describe the spacetime, chosen in such a way that the metric has no dr^2 term and has no singularities at $r = 1/b$, are referred to as in-falling Eddington-Finkelstein coordinates. With a generic choice of u^μ, varying as a function of x^μ, at any given x^μ the metric (6.7) is obtained by boosting the AdS black brane metric by the boost that takes you from the instantaneous fluid rest frame, where $u^\mu = (1,0,0,0)$, to the frame in which u^μ takes on the value of interest. The metric (6.7) is therefore often said to describe a boosted black brane, but it is important to remember that b and u^μ are in fact varying. It describes a black brane whose horizon is undulating, as is its entire metric. Note that although $r = 1/b$ is the horizon of the static black brane, once $1/b$ is undulating the global event horizon

of the metric (6.6) need no longer be located at $r = 1/b$. Gradient corrections to the position of the event horizon have been computed in Ref. [148]. The metric (6.7) is the zeroth approximation to the gravitational dual of the moving fluid; it would be a complete description if gradients made no contribution to the fluid stress-energy tensor, which is to say if the fluid were an ideal fluid with zero shear viscosity.

The second term in the metric (6.6) is the dual gravitational description of the contribution of first order gradients in u^μ and b to the fluid stress-energy tensor. It is given by [122]

$$G^{(1)}_{MN} dX^M dX^N = 2r^2 b\, F(br) \sigma_{\mu\nu} dx^\mu dx^\nu + \frac{2}{3} r\, u_\mu u_\nu \partial_\lambda u^\lambda dx^\mu dx^\nu - r\, u^\lambda \partial_\lambda (u_\mu u_\nu) dx^\mu dx^\nu \tag{6.8}$$

where

$$F(x) \equiv \frac{1}{4}\left[\log\left(\frac{(1+x)^2(1+x^2)}{x^4}\right) - 2\arctan x + \pi\right]. \tag{6.9}$$

We are working in a gauge in which $G^{(1)}_{Mr} = 0$. The metric (6.8) is a good approximation to the gravitational dual of the hydrodynamics of the flowing conformal fluid as long as the length scale L over which b and u^μ vary satisfies $L \gg b$.

In the next subsection, we will compute the profile of the string that hangs "down" into the bulk metric G_{MN} from the heavy quark. To determine the profile of the string at the time t at which the heavy quark is located at a particular position $\vec{x}$, it will prove convenient to do the calculation in the frame in which the fluid is at rest at $\vec{x}$ at the instant of time t, which is to say the frame in which $u^\mu(\vec{x}, t) = (1, 0, 0, 0)$. In making this choice we do not lose any generality since we can of course later boost the result of our calculation to any frame that we like. In order to do the calculation in the instantaneous fluid rest-frame it will be helpful to have the metric G_{MN} in this frame, which we obtain by setting $u^\mu = (1, 0, 0, 0)$ in (6.7) and (6.8), keeping derivatives of u^μ. At the same time, since we will calculate the drag force on a heavy quark located at $x^\mu = 0$ we expand $b(x^\nu)$ and $u^\mu(x^\nu)$ around $x^\nu = 0$ in (6.7), keeping only terms that are first order in their gradients. Combining (6.7) and (6.8), the

metric then takes the form

$$\begin{aligned} G_{MN}dX^M dX^N &= 2dtdr - r^2 f(br)dt^2 + r^2 dx_i dx_i \\ &+ \epsilon \left(-2x^\mu \partial_\mu u_i dr dx^i - 2x^\mu \partial_\mu u_i r^2 (1 - f(br)) dt dx^i - 4\frac{x^\mu \partial_\mu b}{b^5 r^2} dt^2 \right. \\ &\left. + 2br^2 F(br)\sigma_{ij} dx^i dx^j + \frac{2}{3} r \partial_i u_i dt^2 + 2r\partial_t u_i dt dx^i \right) , \end{aligned} \tag{6.10}$$

which is the form that we shall need.

We shall begin by doing the calculation for a fluid that is only moving in one direction, that we shall choose to be the z-direction. In this case, when we boost to the instantaneous rest-frame in which $u^\mu(\vec{x}, t) = (1, 0, 0, 0)$ the only non-vanishing gradients are

$$\partial_t b(t, z) \neq 0, \quad \partial_z b(t, z) \neq 0, \quad \partial_t u^3(t, z) \neq 0, \quad \partial_z u^3(t, z) \neq 0, \tag{6.11}$$

with

$$\partial_\mu u^\perp = \partial_\perp u^\nu = \partial_\perp b = 0. \tag{6.12}$$

This fluid configuration will not be sufficient for us to determine the drag force in the most general configuration, in particular because in this configuration the fluid has zero vorticity. However, we shall see by the end of Section 6.2 that it suffices to get us most of the way. Upon making this simplifying assumption, conservation of the stress-energy tensor (6.5) takes on the particularly simple form

$$\begin{aligned} 3\partial_t b(t, z) &= b(t, z)\partial_z u^3(t, z), \\ \partial_z b(t, z) &= b(t, z)\partial_t u^3(t, z). \end{aligned} \tag{6.13}$$

We will return to the consideration of a general fluid configuration only in Section 6.2.3.

6.1.2 Gravitational description of a moving heavy quark

The dual gravitational string of a quark with mass M at the spacetime point $x^\mu = 0$ and moving with velocity $\vec{\beta}$ is, in the $M \to \infty$ limit, a string whose endpoint is at $x^\mu = 0$ moving with velocity $\vec{\beta}$ along the AdS boundary, namely at $r \to \infty$. As noted in section 5.1.2, the dynamics of the string is generally described by Polyakov action, eq. (5.9). Nevertheless, in this section we will be using simple string parametrization and it suffices to use special instance of Polyakov action – Nambu-Goto action. Nambu-Goto action is given by

$$S_{\rm NG} = -\frac{\sqrt{\lambda}}{2\pi} \int d\tau d\sigma \sqrt{-g(\tau,\sigma)} \tag{6.14}$$

where the string tension is $\frac{\sqrt{\lambda}}{2\pi}$, where $\lambda = g^2 N_c$ is the 't Hooft coupling, and where $g(\tau,\sigma) = \det g_{ab}(\tau,\sigma)$ with $g_{ab}(\tau,\sigma)$ the induced metric on the world-sheet, namely

$$g_{ab}(\tau,\sigma) = G_{MN} \partial_a X^M(\tau,\sigma) \partial_b X^N(\tau,\sigma). \tag{6.15}$$

We shall parametrize the string world-sheet in such a way that

$$\begin{aligned} t(\tau,\sigma) &= \tau, \\ r(\tau,\sigma) &= \sigma. \end{aligned} \tag{6.16}$$

We shall assume that the string is being dragged along with a constant velocity $\vec{\beta}$. Because we are treating the case where the fluid motion is only in the z-direction, without loss of generality we can choose $\vec{\beta} = (\beta_x, 0, \beta_z)$. We can think of the motion of the quark as being due to a force exerted on it by some electric field, with respect to which the quark is charged. Our task is to determine the force required to drag the quark, working to leading order in the fluid gradients. The first step in the calculation, which we shall carry out in this section, is the determination of the string profile, again to leading order in fluid gradients.

We denote the string profile to first order in gradients by

$$\vec{x}(\tau,\sigma) = \vec{x}_0(\tau,\sigma) + \epsilon\,\vec{x}_1(\tau,\sigma) \tag{6.17}$$

where $\vec{x}_0(\tau,\sigma)$ is the string profile in the case of an equilibrium fluid with a constant temperature that is moving with some uniform velocity, which is to say in the absence of any gradients in the fluid velocity or b. In the instantaneous fluid rest-frame in which we are working this means that $u^\mu = (1,0,0,0)$ and all gradients vanish. This "trailing string" solution was first obtained in Refs. [82, 83] and is given by

$$\vec{x}_0(\tau,\sigma) = \vec{\beta}\left(\tau - b\left(\tan^{-1}(b\sigma) - \frac{\pi}{2}\right)\right) \ , \tag{6.18}$$

where we note that at $\sigma \to \infty$ the endpoint of the string follows the trajectory of the heavy quark. We will need to differentiate $\vec{x}_0$, and to that end we need to keep track of how it depends on u^μ, namely

$$\vec{x}_0(\tau,\sigma) = \vec{\beta}\tau - b\left(u^0\vec{\beta} - \vec{u}\right)\left(\tan^{-1}(b\sigma) - \frac{\pi}{2}\right) \ . \tag{6.19}$$

The function $x_1(\tau,\sigma)$ in (6.17) encodes the corrections to the zeroth order profile $\vec{x}_0(\tau,\sigma)$ due to fluid gradients, up to first order in those gradients. It must vanish in the $\sigma \to \infty$ limit. Our task in the remainder of this section is to calculate $x_1(\tau,\sigma)$.

The equations of motion for the string are obtained by extremizing the Nambu-Goto action with respect to the function $\vec{x}(\tau,\sigma)$. To zeroth order we obtain $\vec{x}_0(\tau,\sigma)$. The function $\vec{x}_1(\tau,\sigma)$ is determined from

$$\partial_\tau\left(\frac{\delta\mathcal{L}}{\delta(\partial_\tau\vec{x}_1)}\right) + \partial_\sigma\left(\frac{\delta\mathcal{L}}{\delta(\partial_\sigma\vec{x}_1)}\right) = \frac{\delta\mathcal{L}}{\delta\vec{x}_1} \ . \tag{6.20}$$

Since the terms that are linear in gradients in (6.10) arose either directly from (6.8) or via expanding (6.7) to first order about $x^\mu = 0$, the terms in (6.20) that are first order in gradients can depend on time at most linearly, meaning that $x_1(\tau,\sigma)$ takes

the form

$$\vec{x}_1(\tau,\sigma) = b\,\tau\,\vec{h}(\sigma) + b\,\vec{g}(\sigma)\ , \tag{6.21}$$

with $\vec{h}(\sigma)$ and $\vec{g}(\sigma)$ being dimensionless functions that we must determine, that both have only x- and z-components, and that both vanish at $\sigma \to \infty$.

The terms in the Euler-Lagrange equation (6.20) that are proportional to τ depend only on $\vec{h}(\sigma)$, not on $\vec{g}(\sigma)$. It is in fact possible to guess the form of $\vec{h}(\tau)$. However, determining it by explicit solution is instructive, so we shall follow that route. Integrating the Euler-Lagrange equations for $\vec{h}(\sigma)$ once yields

$$\begin{aligned} h_x'(\sigma) &= \frac{c_{hx}\gamma^2(b^2\sigma^2+1)^2 - 2\beta_x D_t b(\gamma^2+2b^2\sigma^2+1)}{(\gamma^2-b^2\sigma^2)(b^2\sigma^2+1)^2}, \\ h_z'(\sigma) &= \frac{1}{(b^4\sigma^4-\gamma^2)}\times \\ &\quad \left(\frac{b\,(b^4\sigma^4+2b^2\sigma^2-\gamma^2+2)\,D_t u^3}{(b^2\sigma^2+1)} + \frac{2\beta_z\,(2b^2\sigma^2+\gamma^2+1)\,D_t b}{(b^2\sigma^2+1)^2} - \gamma^2 c_{hz}\right), \end{aligned} \tag{6.22}$$

where by $'$ we mean $d/d\sigma$ and where

$$D_t \equiv \partial_t + \beta^i\partial_i = \partial_t + \beta_z\partial_z \tag{6.23}$$

is the convective derivative along the path of the quark, with the second equality valid here because the only nonzero gradients are in the z-direction, where $\gamma = (1-\vec{\beta}^2)^{-1/2}$ is the Lorentz factor for the heavy quark, and where c_{hx} and c_{hz} are integration constants that we must now fix. The expressions for $\vec{h}'(\sigma)$ have a first order pole at the radial position

$$\sigma = \frac{\sqrt{\gamma}}{b}\ , \tag{6.24}$$

which in the case of the static fluid is identified as the location of the worldsheet horizon $\sigma_{\rm ws} \equiv \sqrt{\gamma}/b$ that arises in the calculation of $\vec{x}_0(\tau,\sigma)$ in a static fluid [82, 83].

We have found that the position on the worldsheet where the integration constants are fixed, $\sigma = \sqrt{\gamma}/b$, is the same as it would be in a static homogeneous fluid with the same instantaneous temperature. This means that our results disagree with those of Refs. [108, 149]: those authors assumed that the influence of fluid gradients on the

drag force could be described via a dependence of this radial position on the fluid gradients. We now see by explicit calculation that, at least to first order, there is no such dependence. And, indeed our results for the drag force that we shall present in Section 6.2 do differ from those in Refs. [108, 149].

As in the static fluid calculation of Refs. [82, 83], in order to obtain a regular string profile across the world-sheet horizon we must choose the integration constants in (6.22) in such a way that the numerators on the right-hand sides of (6.22) vanish at the same σ at which the denominators vanish, i.e. at the world-sheet horizon. This requirement uniquely determines the integration constants to be

$$c_{hx} = \frac{2\beta_x D_t b}{\gamma^2}, \quad c_{hz} = 2\frac{bD_t u^3 + \beta_z D_t b}{\gamma^2}. \tag{6.25}$$

The expressions (6.22) can then be integrated again, with the new integration constants being fixed via the requirement that $\vec{h}(\sigma)$ vanishes at $\sigma \to \infty$. Doing so yields

$$\begin{aligned} h_x(\sigma) =& \frac{\beta_x}{b}\left(\frac{\pi}{2} - \tan^{-1}(b\sigma) - \frac{b\sigma}{b^2\sigma^2+1}\right) D_t b, \\ h_z(\sigma) =& \frac{\beta_z}{b}\left(\frac{\pi}{2} - \tan^{-1}(b\sigma) - \frac{b\sigma}{b^2\sigma^2+1}\right) D_t b - \left(\frac{\pi}{2} - \tan^{-1}(b\sigma)\right) D_t u^3 \ , \end{aligned} \tag{6.26}$$

which we can denote more simply by

$$b\,\vec{h}(\sigma) = D_t \vec{x}_0(\tau,\sigma)\Big|_{\tau=0}, \tag{6.27}$$

a result that we now see could have been guessed. So, we have shown that

$$\vec{x}(\tau,\sigma) = \vec{x}_0(\tau,\sigma) + \epsilon\,\tau D_t \vec{x}_0(\tau,\sigma)\Big|_{\tau=0} + \epsilon\, b\,\vec{g}(\sigma) \tag{6.28}$$

to the order at which we are working, and our task now is to find $\vec{g}(\sigma)$.

Upon using the solution for $\vec{h}(\sigma)$, the Euler-Lagrange equations become differential equations for $\vec{g}(\sigma)$. As in the determination of $\vec{h}(\sigma)$, we integrate the differential equations for $\vec{g}(\sigma)$ once, obtaining expressions for $\vec{g}'(\sigma)$. Again as before, these expressions have poles at $\sigma = \sigma_{\rm ws}$ and the requirement that the string profile must be

regular there can be used to fix the integration constants in the expressions for $\vec{g}'(\sigma)$. Upon so doing, we find

$$
\begin{aligned}
g_x'(\sigma) &= \frac{b^2\beta_x\beta_z\left(\left(-\pi/2+\tan^{-1}(b\sigma)\right)\left(b^2\sigma^2+3\right)+b\sigma\right)}{\left(b^2\sigma^2+1\right)^2}\partial_t u^3 + \frac{b^2\beta_x}{3}\partial_z u^3 \times \\
&\left(\left(\gamma^2\left(3\beta_z^2+1\right)+1\right)\frac{c_1\left(-b^2\sigma^2\right)-c_1(-\gamma)}{\gamma^2-b^4\sigma^4} - \frac{1}{(\sqrt{\gamma}+b\sigma)(\gamma+b^2\sigma^2)} - \frac{\frac{\pi}{2}-\tan^{-1}(b\sigma)}{1+b^2\sigma^2}\right), \\
g_z'(\sigma) &= b^2\left(\frac{b^2\sigma^2\left(\beta_z^2-1\right)+3\beta_z^2-1}{\left(b^2\sigma^2+1\right)^2}\tan^{-1}(b\sigma)\right. \\
&\left.-\frac{1}{2}\left(\frac{\sqrt{\gamma}-b\sigma}{\gamma(b^2\sigma^2+\gamma)}+\frac{2\beta_z^2(\pi-b\sigma)}{\left(b^2\sigma^2+1\right)^2}-\frac{\pi(1-\beta_z^2)}{b^2\sigma^2+1}+\frac{1}{\gamma(b\sigma+\sqrt{\gamma})}\right)\right)\partial_t u^3 \\
&+\frac{b^2\beta_z\left(5\left(b\sigma+\sqrt{\gamma}\right)\left(b^2\sigma^2+\gamma\right)\left(\frac{\pi}{2}-\tan^{-1}(b\sigma)\right)-\left(b^2\sigma^2+1\right)\right)}{3\left(b^2\sigma^2+1\right)\left(b\sigma+\sqrt{\gamma}\right)\left(b^2\sigma^2+\gamma\right)}\partial_z u^3,
\end{aligned}
\tag{6.29}
$$

where we have defined the function

$$
\begin{aligned}
c_1(x) &\equiv \pi/2 - \tan^{-1}(\sqrt{-x}) - F(\sqrt{-x}) \\
&= \frac{1}{4}\left(2\tan^{-1}\left(\frac{1}{\sqrt{-x}}\right) - \log\left(\frac{(1-x)(1+\sqrt{-x})^2}{x^2}\right)\right).
\end{aligned}
\tag{6.30}
$$

(The way we have chosen the signs in this definition will prove convenient later.) We can see explicitly in (6.29) that $\vec{g}(\tau,\sigma)$ is regular at $\sigma = \sigma_{\rm ws}$. It is then possible to integrate the expressions (6.29) analytically, fixing the integration constants by the requirement that $\vec{g}(\tau,\sigma) = 0$ at $\sigma \to \infty$. The resulting expressions for $g_x(\sigma)$ and $g_z(\sigma)$ are unwieldy and we shall not quote them here. In Section 6.3 we shall, however, plot the string profile for several choices of fluid flow and $\vec{\beta}$. In addition to being unwieldy, the expressions for $g_x(\sigma)$ and $g_z(\sigma)$ are not of direct utility because, as we shall see in Section 6.2, it is only $\vec{g}'(\sigma)$ that enters into the calculation of the canonical momentum fluxes along the string and hence of the drag force.

6.2 Computing the drag force on the heavy quark

In this Section we calculate the drag force acting on the heavy quark moving through the strongly coupled fluid. If the fluid were static, as in the original calculations [82, 83], the drag force would be a function of the temperature and the velocity $\vec{\beta}$ of the heavy quark. In the case that we are analyzing, where the fluid is moving but we work in the instantaneous fluid rest-frame, the drag force again depends on b and $\vec{\beta}$ but, we shall show, it also depends upon the spatial gradients and time derivatives of b and the fluid 4-velocity u^μ. After computing the drag force in the instantaneous fluid rest frame in Section 6.2.1 for the case in which the fluid motion is only along the z-direction, in Section 6.2.2 we boost the result to a frame in which the fluid at the location of the heavy quark has some nonzero velocity in the z-direction, $u^3 \neq 0$. Then, in Section 6.2.3 we generalize our result to the case in which the motion of the fluid is not restricted to the z-direction and, in particular, may feature nonzero vorticity.

When the heavy quark is dragged through the fluid, in the dual gravitational description momentum and energy flow "down" the string that "hangs down" from the heavy quark at $r = \infty$, trailing into the bulk metric. In order to conserve energy and momentum, an external force must be exerted upon the heavy quark to keep it moving at constant velocity and (in the dual picture) to replace the energy and momentum flowing down the string. Consequently,

$$\partial_\nu T^{\nu\mu} = -f^\mu(\tau)\delta^3(\vec{x} - \vec{\beta}\tau) \tag{6.31}$$

where $f^\mu(\tau)$ is the drag force acting on the heavy quark, *i.e.*, on the endpoint of the string at the $r = \infty$ boundary. The drag force at the boundary is given by [82, 83]

$$f^\mu(\tau) = \lim_{\sigma\to\infty} n_M \int d^3x\sqrt{-g}\mathcal{T}^{M\mu} \tag{6.32}$$

where $\mathcal{T}^{MN}$ is the stress-energy tensor of the string obtained by varying the Nambu-Goto action (6.14) with respect to the G_{MN}, and n_M is the unit-vector normal to

the boundary at $r \to \infty$. Because we are using the simple parametrization (6.16) of the world-sheet, the normal is simply $n_M = -\delta_{M5}$ and the relevant component of the string stress-energy tensor is

$$\mathcal{T}^{5\mu}(\tau, \vec{x}, \vec{y}, \sigma) = \eta^{\mu\nu} \frac{1}{\sqrt{-g}} \pi^{\sigma}_{\nu}(\tau, \sigma) \delta^3(\vec{y} - \vec{x}) \,, \tag{6.33}$$

where the canonical energy/momentum fluxes along the string are obtained by varying $S_{\rm NG}$ with respect to $\partial_\sigma X^\mu$:

$$\pi^{\sigma}_{\mu} \equiv \frac{\delta S_{\rm NG}}{\delta(\partial_\sigma X^\mu)} = -\frac{\sqrt{\lambda}}{2\pi} G_{\mu N} \frac{1}{\sqrt{-g}} \left[g_{\tau\sigma} \partial_\tau X^N - g_{\tau\tau} \partial_\sigma X^N \right] . \tag{6.34}$$

Combining (6.32) and (6.33), the force acting on the quark at the boundary is given by

$$f^\mu(\tau) = -\frac{dp^\mu}{dt}(\tau) = -\lim_{\sigma\to\infty} \eta^{\mu\nu} \pi^{\sigma}_{\nu}(\tau, \sigma), \tag{6.35}$$

evaluated at the location of the heavy quark, $\vec{x} = \vec{\beta}\tau$. Because we have used the world-sheet parameterization (6.16) we have obtained the same expression obtained in Refs. [82, 83]; the calculation of Ref. [3] was done with a different world-sheet parametrization, one for which (6.32) yields an expression that differs from (6.35). Note also that we are using a sign convention opposite to that in Ref. [3]. In the present paper, f^μ is the force exerted on the heavy quark by some external agency (eg. an electric field) in order to keep the quark moving with constant velocity. In the classic case of a quark moving with $\beta_z > 0$ through a static plasma, $f^z > 0$ and $dp^z/dt < 0$. Note that dp^μ/dt refers to the energy/momentum lost by the quark (lost by the quark and gained by the plasma; in the dual description, lost by the quark and flowing down the string).

As is the case for any force, $f^\mu(\tau)$ is not a Lorentz 4-vector. This is most easily seen via the expression $f^\mu = -dp^\mu/dt$, in which p^μ is a 4-vector but t is not boost-invariant. We see immediately that we can define a so-called proper force $F^\mu(\tau)$ that *is* a 4-vector via

$$F^\mu(\tau) \equiv f^\mu(\tau) \frac{dt}{d\tau_p} = -\frac{dp^\mu}{d\tau_p} \tag{6.36}$$

where τ_p is the (boost-invariant) proper time of the quark. Because the heavy quark is moving with a constant velocity, $dt = \gamma d\tau_p$, with $\gamma \equiv 1/\sqrt{1-|\vec{\beta}|^2}$ the Lorentz factor for the heavy quark. Then the actual drag force f^μ and the proper drag force F^μ are simply related by

$$f^\mu(\tau) = \frac{1}{\gamma} F^\mu(\tau). \tag{6.37}$$

The distinction between actual and proper forces will play an important role in Sections 6.2.2 and 6.2.3.

Just as we did in the calculation of the string profile, we expand the drag force in powers of the fluid gradients, writing it as

$$f^\mu(\tau) = f^\mu_{(0)}(\tau) + \epsilon f^\mu_{(1)}(\tau), \tag{6.38}$$

where the first component $f^\mu_{(0)}(\tau)$ is the drag force when fluid gradients are neglected, first obtained in Refs. [82, 83], and the second component $f^\mu_{(1)}(\tau)$ is proportional to fluid gradients and is the term that we will calculate in the remainder of this Section. In the instantaneous fluid rest frame, in which $u^\mu = (1,0,0,0)$, the spatial components of the force are given by [82, 83]

$$\vec{f}_{(0),\mathrm{RF}}(\tau) = \frac{\sqrt{\lambda}}{2\pi}\frac{\gamma}{b^2}\vec{\beta} \tag{6.39}$$

which shows that this contribution to the force is proportional to $\gamma\vec{\beta}$, which is to say proportional to $\vec{p}/M$. It is because the force is proportional to the momentum that it is referred to as a drag force. We can then boost this result to any other frame, in which the fluid at the location of the heavy quark has an instantaneous three-velocity $\vec{v}$ and a Lorentz factor $\gamma_v \equiv 1/\sqrt{1-|\vec{v}|^2}$ and, hence,

$$u^\mu = \gamma_v(1,\vec{v}) \ . \tag{6.40}$$

It is also convenient to define the 4−velocity of the heavy quark

$$w^\mu = \gamma(1,\vec{\beta}) \ . \tag{6.41}$$

Upon boosting (6.39) to a frame in which $\vec{v} \neq 0$, the zeroth contribution to the drag force (i.e. the drag force obtained upon neglecting the effects of gradients) takes the form

$$f^{\mu}_{(0)}(\tau) = -\frac{\sqrt{\lambda}}{2\pi}\frac{1}{\gamma b^2}\left(s\, w^{\mu} + u^{\mu}\right), \tag{6.42}$$

where the scalar factor s is defined by

$$s \equiv u^{\nu} w_{\nu} \ . \tag{6.43}$$

If the only nonzero component of $\vec{v}$ is v_z, we find $s = -\gamma\gamma_v(1 - v_z\beta_z)$. We shall calculate $f^{\mu}_{(1)}$ in the instantaneous fluid rest frame in Section 6.2.1, and in a more general frame in Section 6.2.2.

Before turning to our calculation, one further general remark will prove useful. Starting from (6.35) and (6.34), it is possible to show by explicit calculation that $w_{\mu} f^{\mu}(\tau) = 0$. Written explicitly, this takes the form

$$\frac{dE}{dt} = \vec{\beta}\frac{d\vec{p}}{dt}, \tag{6.44}$$

relating the rate of energy loss to the rate of momentum loss. Since $\vec{\beta} = \vec{p}/E$ this implies that $E^2 = \vec{p}^2 + M^2$ for some constant M, which is to say that if the quark starts out on-shell it stays on-shell.

6.2.1 Drag force in the instantaneous fluid rest frame

We now calculate the canonical momentum flux along the string to first order in gradients, $\pi^{\sigma}_{\mu,(1)}(\tau,\sigma)$, and use it to obtain the corresponding drag force $f^{\mu}_{(1)}(\tau)$ exerted on the heavy quark at the boundary. We calculate the drag force in the instantaneous fluid rest frame using the string profile given in Eqs. (6.26) and (6.29). We need to evaluate (6.34) to linear order in ϵ after expanding the metric $G_{\mu N}$, the induced metric g_{ab}, and derivatives of the string profile $\partial_a X^N$ in powers of ϵ. Just as for the

decomposition of the string profile in Eq. (6.28), we find that

$$\pi^{\sigma}_{\mu}(\tau,\sigma) = \pi^{\sigma}_{\mu,(0)}(\tau) + \epsilon\left(\tau\, D_t \pi^{\sigma}_{\mu,(0)}(\tau)\Big|_{\tau=0} + \pi^{\sigma}_{\mu,(1)}(\sigma)\right). \tag{6.45}$$

The leading term is independent of the radial coordinate σ and, in the instantaneous fluid rest-frame, is given by

$$\pi^{\sigma}_{\mu,(0)}(\tau) = -\frac{\sqrt{\lambda}}{2\pi}\frac{1}{\gamma b^2}\left(\gamma w_\mu + \delta^0_\mu\right), \tag{6.46}$$

from which we obtain the result for the drag force absent any effects of the fluid gradients that we already quoted in Eq. (6.42). The term proportional to time τ in (6.45) is given by

$$D_t \pi^{\sigma}_{\mu,(0)}(\tau)\Big|_{\tau=0} = \frac{\sqrt{\lambda}}{2\pi}\frac{1}{\gamma b^2} \times \left[\frac{2}{b}(\gamma w^\mu - \delta^\mu_0) D_t b + (w^\mu w^z + \delta^\mu_3) D_t u^z\right], \tag{6.47}$$

where D_t was defined in (6.23). We can neglect this term since it appears in (6.45) multiplied by τ and we are evaluating the drag force on the heavy quark at $\tau = 0$.

The nontrivial part of the computation is the determination of $\pi^{\sigma}_{(1)}(\sigma)$. After collecting terms proportional to ϵ at $\tau = 0$, we find that

$$\begin{aligned}
\pi^{\sigma}_{x,(1)}(\sigma) &= \frac{\sqrt{\lambda}}{2\pi b}\gamma\beta_x\left[\beta_z\left(\frac{b\sigma}{b^2\sigma^2+1} + \pi - 2\tan^{-1}(b\sigma) - \sqrt{\gamma}\right)\partial_t u^3 + \right. \\
&\left. \frac{\left(\frac{b\sigma}{b^2\sigma^2+1} - \sqrt{\gamma} + (1+3\beta_z^2)\left(\frac{\pi}{2} - \tan^{-1}(b\sigma)\right) - c_1(-\gamma)\left(\gamma^2(1-3\beta_z^2)+1\right)\right)}{3}\partial_z u^3\right], \\
\pi^{\sigma}_{z,(1)}(\sigma) &= \frac{\sqrt{\lambda}}{2\pi b}\gamma\left[\left(-\frac{\beta_x^2 b\sigma}{b^2\sigma^2+1} + \left(2\beta_z^2+1\right)\left(\frac{\pi}{2} - \tan^{-1}(b\sigma)\right) - \sqrt{\gamma}\left(1-\beta_x^2\right)\right)\partial_t u^3 + \right. \\
&\left. \frac{\beta_z\left(\frac{b\sigma}{b^2\sigma^2+1} + (1-3\beta_x^2)\left(\frac{\pi}{2} - \tan^{-1}(b\sigma)\right) - \sqrt{\gamma} - c_1(-\gamma)\left(\gamma^2(1-3\beta_z^2)-5\right)\right)}{3}\partial_z u^3\right],
\end{aligned} \tag{6.48}$$

where $c_1(-\gamma)$ was defined in (6.30) and the conservation of the stress-energy tensor (6.13) has been used to eliminate $\partial_t b$ and $\partial_z b$ in favor of $\partial_t u^3$ and $\partial_z u^3$. We now determine the contributions of these canonical momentum fluxes to the drag force on

the heavy quark at the boundary, which is to say we take the $\sigma \to \infty$ limit. The terms $\frac{b\sigma}{b^2\sigma^2+1}$ and $\frac{\pi}{2} - \tan^{-1}(b\sigma)$ vanish in this limit, and the contribution to the drag force that is first order in gradients is given by

$$\begin{aligned} f^x_{(1)} &= \frac{\sqrt{\lambda}}{2\pi b}\gamma\beta_x\left(\sqrt{\gamma}\beta_z\partial_t u^3 + \frac{\sqrt{\gamma} + c_1(-\gamma)\left(\gamma^2\left(1-3\beta_z^2\right)+1\right)}{3}\partial_z u^3\right), \\ f^z_{(1)} &= \frac{\sqrt{\lambda}}{2\pi b}\gamma\left(\sqrt{\gamma}(1-\beta_x^2)\partial_t u^3 + \frac{\sqrt{\gamma} + c_1(-\gamma)\left(\gamma^2\left(1-3\beta_z^2\right)-5\right)}{3}\beta_z\partial_z u^3\right), \end{aligned} \tag{6.49}$$

with the t component of the force given by $f^t_{(1)} = \beta_x f^x_{(1)} + \beta_z f^z_{(1)}$, ensuring that the quark stays on shell. The complete expression for the drag force is obtained by combining the contributions from (6.46) and (6.49).

Before turning to generalizations of this result, we end this subsection by remarking that both the terms proportional to $\partial_t u^3$ and the terms proportional to $\partial_z u^3$ in (6.49) are proportional to $\gamma^{3/2}$ for large γ. This is apparent for the terms proportional to $\partial_t u^3$. To see this for the terms proportional to $\partial_z u^3$, note that in the large-γ limit

$$c_1(-\gamma) = -\frac{1}{3\gamma^{3/2}} + \mathcal{O}\left(\frac{1}{\gamma^2}\right). \tag{6.50}$$

This means that for large enough γ, the contributions to the drag force that are first order in fluid gradients, namely (6.49), dominate over the zeroth order expression (6.39) for the drag force in the absence of fluid gradients. Comparing (6.39) and (6.49) we see that the first order contributions to the drag force are smaller than the zeroth order contributions when

$$\sqrt{\gamma} < \frac{1}{b\,|\partial_t u^3|} \quad \text{and} \quad \sqrt{\gamma} < \frac{9}{5}\frac{1}{b\,|\partial_z u^3|} \tag{6.51}$$

or, using (6.13), when

$$\sqrt{\gamma} < \frac{1}{|\partial_z b|} \quad \text{and} \quad \sqrt{\gamma} < \frac{3}{5}\frac{1}{|\partial_t b|}, \tag{6.52}$$

with γ and the gradients on the right-hand sides of all these expressions evaluated in the frame of reference in which the fluid is instantaneously at rest at the location of

the moving heavy quark. This result suggests that at larger values of γ the expansion of the drag force in powers of the fluid gradients may break down, although to be sure of this it would be useful to extend our calculation to higher order in gradients. At a qualitative level, what seems to be happening is that at large enough γ the heavy quark sees a gradient in the fluid as sudden, and the gradient expansion of the drag force ceases to be valid. Note that the criterion for the validity of the hydrodynamic description of the fluid itself is $|\partial_z b| \ll 1$ and $|\partial_t b| \ll 1$, meaning that as long as the motion of the fluid is described well by hydrodynamics the limitation (6.52) on the values of γ at which the gradient expansion can be used to describe the drag force on the heavy quark sets in at some $\gamma \gg 1$. As hydrodynamics itself breaks down, the range of validity of the gradient expansion in the calculation of the heavy quark drag force becomes smaller and smaller.

Note that for quarks with finite M the description of the drag force in terms of a single trailing string is only valid for [150, 151, 77]

$$\sqrt{\gamma} \ll \frac{M}{T\sqrt{\lambda}} \ , \tag{6.53}$$

since the external force required to move a quark with mass M at a larger γ would result in copious pair-production of quark-antiquark pairs. However, we are working in the $M \to \infty$ limit throughout this paper, meaning that the criterion (6.53) by itself would allow us to consider arbitrarily large γ. Instead, even in the $M \to \infty$ limit the magnitude of the fluid gradients imposes new, lower, limits (6.52) on how large γ can be, at least if one wishes to use a gradient expansion to calculate the drag force. These considerations motivate future extensions of our calculations, both to higher order in fluid gradients and to finite quark mass M. An analysis in which one takes the $\gamma \to \infty$ limit first, with finite mass quarks, and only later takes $M \to \infty$ would necessarily look very different from the analysis in this paper.

6.2.2 Generalizing to a frame in which the fluid is moving

In Section 6.2.1 we have calculated the drag force exerted on a heavy quark moving through the fluid, in the instantaneous fluid rest frame and in a fluid that is moving only along the z-direction, obtaining the result (6.49). We can now boost this result to a frame in which the fluid at the location of the heavy quark has velocity $\vec{v} = (0, 0, v_z)$, instead of being at rest. We do this by first constructing the proper force F^μ from f^μ, according to (6.37), then applying a Lorentz transformation to the 4−vector F^μ, bringing it to the desired frame, then working out the value of γ in the desired frame, and finally using (6.37) again to obtain f^μ in the new frame. The calculation, which is tedious but straightforward, yields the following expression for the drag force exerted on a heavy quark moving with velocity $\vec{\beta}$ through a fluid that is moving only along the z-direction and that has velocity $\vec{v} = (0, 0, v_z)$ at the location of the heavy quark:

$$
\begin{aligned}
f^x_{(1)} = &-\frac{\sqrt{\lambda}}{2\pi}\frac{s\gamma_v^2\beta_x}{3b}\times \\
&\Big[\partial_t v_z\left[c_1(s)\left(s^2+1\right)\gamma_v v_z + 3c_1(s)s(s\gamma_v+\gamma)\Delta\beta_z + \sqrt{-s}\gamma_v(3\Delta\beta_z + v_z)\right] \\
&+\partial_z v_z\left[c_1(s)\left(s^2+1\right)\gamma_v + 3c_1(s)s(s\gamma_v v_z + \gamma\beta_z)\Delta\beta_z + \sqrt{-s}\gamma_v(3v_z\Delta\beta_z + 1)\right]\Big],
\end{aligned}
\tag{6.54}
$$

$$
\begin{aligned}
f^z_{(1)} = &-\frac{\sqrt{\lambda}}{2\pi}\frac{\gamma_v^2}{3b\gamma}\Big[\partial_t v_z\Big(c_1(s)\gamma_v\left[\gamma_v\left(s^2\left(v_z^2-3\right)+v_z^2\right) + s\gamma\left(\left(s^2+1\right)\beta_z v_z - 3\right)\right] \\
&+3c_1(s)s\gamma\Delta\beta_z\left[s\beta_z(s\gamma_v+\gamma) - \gamma_v v_z\right] + \gamma_v\sqrt{-s}\left[s\gamma\beta_z(3\Delta\beta_z + v_z) + \gamma_v\left(v_z^2-3\right)\right]\Big) \\
&+\partial_z v_z\Big(3c_1(s)s\gamma\beta_z\Delta\beta_z\left[\left(s^2-1\right)\gamma_v v_z + s\gamma\beta_z\right] + c_1(s)\gamma_v\left[s^3\gamma\beta_z - 2s^2\gamma_v v_z\right. \\
&\left.+s\gamma(3v_z - 5\beta_z) + \gamma_v v_z\right] + \sqrt{-s}\gamma_v\left[s\gamma\beta_z(3v_z\Delta\beta_z + 1) - 2\gamma_v v_z\right]\Big)\Big].
\end{aligned}
\tag{6.55}
$$

Here, $\Delta\beta_z$ denotes the (relativistic) difference between the velocities of the quark and the fluid in the $z-$direction

$$
\Delta\beta_z = \frac{\beta_z - v_z}{1 - \beta_z v_z} = \frac{\gamma\gamma_v}{s}(v_z - \beta_z). \tag{6.56}
$$

Recall that our notation is such that $\vec{v}$ is the velocity of the fluid, here in the z-direction, $\gamma_v = 1/\sqrt{1-v_z^2}$ is the fluid velocity Lorentz factor, and $u^\mu = \gamma_v(1,\vec{v})$. Furthermore, $\vec{\beta}$ is the velocity of the heavy quark, $\gamma = 1/\sqrt{1-\vec{\beta}^2}$, $w^\mu = \gamma(1,\vec{\beta})$, and the scalar factor s is given by

$$s \equiv u^\mu w_\mu = -\gamma\gamma_v(1 - v_z\beta_z) \ . \tag{6.57}$$

(Note that in the instantaneous fluid rest frame $s = -\gamma$. We chose the signs in our definition (6.30) of the function c_1 such that henceforth what will appear in many equations is $c_1(s)$.) In the next subsection, we shall find a much more compact way of writing the result (6.55) after first generalizing our calculation of the drag force to the case in which the fluid can move in any direction.

6.2.3 General fluid motion

Although in the explicit applications of our results that we shall present in Section 6.3 we shall only need the results we have already obtained in Sections 6.2.1 and 6.2.2, before proceeding we now wish to generalize our analysis beyond the case in which the motion of the fluid is only along a single axis to consider any possible three-dimensional motion of the fluid satisfying the hydrodynamic equations of motion (6.4). It will turn out that generalizing our analysis in this way will yield a more compact form of our result that is more user-friendly than (6.54) and (6.55), in addition to being more general. We will continue to work only to first order in fluid gradients, but we will no longer restrict to the case (6.12). That is, we will allow all the velocity gradients and time derivatives $\partial_\alpha u_\beta$ to be nonzero, but will continue to assume that they are small enough in magnitude that second and higher derivatives can be neglected. The time derivative and gradients of the temperature are then determined from $\partial_\alpha u_\beta$ via the hydrodynamic equations in the form (6.5). We will start by writing down the most general possible Lorentz covariant proper drag force F^μ, related to f^μ by (6.37), to first order in $\partial_\alpha u_\beta$, and will then use the calculations that we have done already (plus a little bit more) to fix all the coefficients in the general expression. In this

way we will obtain the drag force f^μ up to first order in $\partial_\alpha u_\beta$ for a general fluid configuration.

To zeroth order in gradients, we already have the general result for $f^\mu_{(0)}$ in (6.42), in explicit form. We now write a general, but formal, expression for the contribution to the drag force $f^\mu_{(1)}$ that is first order in the fluid gradients $\partial_\alpha u_\beta$ by writing the most general possible Lorentz covariant vector $F^\mu_{(1)}$ and, from (6.37), dividing by γ:

$$\begin{aligned} f^\mu_{(1)} = \frac{\sqrt{\lambda}}{2\pi}\frac{1}{b\gamma}\Big[& a_1\eta^{\mu\alpha}w^\beta + u^\mu(a_2\eta^{\alpha\beta} + a_3 w^\alpha w^\beta + a_4 u^\alpha w^\beta) \\ & + w^\mu(a_5\eta^{\alpha\beta} + a_6 w^\alpha w^\beta + a_7 u^\alpha w^\beta) + \eta^{\mu\beta}(a_8 u^\alpha + a_9 w^\alpha) \\ & + \epsilon^{\lambda\nu\alpha\beta}\left(a_{10}\eta^\mu{}_\lambda u_\nu + a_{11}u^\mu w_\lambda u_\nu + a_{12}w^\mu w_\lambda u_\nu + a_{13}\eta^\mu{}_\lambda w_\nu\right)\Big]\partial_\alpha u_\beta \end{aligned} \tag{6.58}$$

where the coefficients $a_1 \ldots a_{13}$ are (at present arbitrary) functions of the only possible Lorentz scalar that is zeroth order in derivatives, namely the now familiar $s \equiv u^\alpha w_\alpha$. Our task now is to determine $a_1 \ldots a_{13}$. The terms multiplied by $a_1 \ldots a_9$ in (6.58) are all the possible terms that can be written without introducing $\epsilon^{\lambda\nu\alpha\beta}$. This can be seen by noting that the index μ can be placed on the gradient direction ∂^μ (the a_1 term), on the fluid velocity 4−vector u^μ (the $a_2 \ldots a_4$ terms), on the heavy quark velocity 4−vector w^μ (the $a_5 \ldots a_7$ terms), or on the fluid velocity 4−vector that is acted upon by the derivative (the a_8 and a_9 terms). (We have used $u^\beta\partial_\alpha u_\beta = 0$, a consequence of $u^\beta u_\beta = -1$, to eliminate other terms.) The terms multiplied by $a_{10} \ldots a_{13}$ are the only allowed terms that can be constructed by contracting with the totally antisymmetric tensor $\epsilon^{\lambda\nu\alpha\beta}$. For example a_{10} multiplies the fluid vorticity $\tilde{\omega}^\mu$, defined in (6.3). Note, however, that there is a sense in which effects of vorticity are hiding among the $a_1 \ldots a_9$ terms because since

$$\epsilon^{\mu\nu\alpha\beta}\tilde{\omega}_\nu w_\alpha u_\beta = \frac{1}{2}\left[\left(\eta^{\mu\beta}w^\alpha - \eta^{\mu\alpha}w^\beta\right) - \left(u^\mu w^\beta - \eta^{\mu\beta}s\right)u^\alpha\right]\partial_\alpha u_\beta \tag{6.59}$$

there is one linear combination of the a_1, a_4, a_8 and a_9 terms that vanishes if $\tilde{\omega} = 0$, a fact that will be relevant.

There is one completely general constraint on f^μ that we have not yet imposed,

namely $w_\mu f^\mu_{(1)} = 0$. Using (6.58), this constraint takes the form

$$\begin{aligned}&\big[\eta^{\alpha\beta}(s\,a_2 - a_5) + u^\alpha w^\beta(s\,a_4 + a_8 - a_7)\\&+w^\alpha w^\beta(a_1 + s\,a_3 - a_6 + a_9) + \epsilon^{\lambda\nu\alpha\beta}w_\lambda u_\nu\,(a_{10} + s\,a_{11} - a_{12})\big]\,\partial_\alpha u_\beta = 0\end{aligned} \tag{6.60}$$

and since the relation has to be satisfied for the arbitrary vectors u^μ and w^μ independently, four out of the 13 coefficients $a_1 \ldots a_{13}$ can be eliminated, *e.g.*,

$$a_1 = a_6 - a_9 - s\,a_3, \quad s\,a_2 = a_5, \quad s\,a_4 = a_7 - a_8, \quad a_{12} = a_{10} + s\,a_{11}. \tag{6.61}$$

In this way we can replace (6.58) by

$$\begin{aligned}f^\mu_{(1)} = -\frac{\sqrt{\lambda}}{2\pi}\frac{1}{b\gamma}\,&\big[c_1(s)w^\beta(u^\mu w^\alpha - s\,\eta^{\mu\alpha}) + c_2(s)\eta^{\alpha\beta}(u^\mu + s\,w^\mu) + c_3(s)w^\beta(w^\mu w^\alpha + \eta^{\mu\alpha})\\&+\,c_4(s)u^\alpha w^\beta(u^\mu + s\,w^\mu) + c_5(s)u^\alpha(u^\mu w^\beta - s\,\eta^{\mu\beta}) + c_6(s)(w^\alpha\eta^{\mu\beta} - \eta^{\mu\alpha}w^\beta)\\&+\epsilon^{\lambda\nu\alpha\beta}\left(c_7(s)\left(\eta^\mu{}_\lambda + w^\mu w_\lambda\right)u_\nu + c_8(s)\left(u^\mu + sw^\mu\right)w_\lambda u_\nu + c_9(s)\eta^\mu{}_\lambda w_\nu\right)\big]\,\partial_\alpha u_\beta\end{aligned} \tag{6.62}$$

with a new set of nine unknown coefficients $c_1 \ldots c_9$ that are each still unknown functions of s that are related to the $a_1 \ldots a_{13}$ by

$$\begin{aligned}c_1 &= a_3, & s\,c_2 &= a_5, & c_3 &= a_6,\\ s\,c_4 &= a_7, & s\,c_5 &= -a_8, & c_6 &= a_9,\\ c_7 &= 2a_{10} + s\,a_{11}, & c_8 &= s\,a_{10} + (1+s^2)a_{11}, & c_9 &= a_{13},\end{aligned} \tag{6.63}$$

with a_1, a_2, a_4 and a_{12} related to the c's through (6.61). Note that the combination of terms (6.59) that vanishes if the vorticity vanishes is now a linear combination of the terms multiplied by c_5 and c_6.

We can now attempt to use the results of our previous calculation, namely (6.49), to fix the coefficients $c_1 \ldots c_9$ in (6.62). We start by writing (6.62) in the instantaneous fluid rest frame, in which $u^\mu = (1,0,0,0)$ and $s = -\gamma$. We then restrict to the fluid

motion that we analyzed in Sections 6.1.2 and 6.2.1, which is to say that we set the partial derivatives (6.12) to zero, keeping only those in (6.11). We then compare the expressions for $f^x_{(1)}$ and $f^z_{(1)}$ so obtained with the expressions in (6.49), term by term. By "term by term" we mean that we compare those terms in $f^x_{(1)}$ (or $f^z_{(1)}$) from (6.62) and (6.49) that are proportional to $\partial_z u^3$ (or $\partial_t u^3$) and that are proportional to β_z^0 or β_z or β_z^2 or β_z^3. In this sense, we make 16 comparisons between (6.62) and (6.49), resulting in 16 expressions that specify various of the c's. What we find when we do this exercise is that we only obtain 5 independent constraints on the c's, and that these constraints can be used to fix the values of $c_1 \ldots c_4$ and $c_5 + c_6$. However, we cannot determine $c_5 - c_6$ or $c_7 \ldots c_9$. This is not unexpected, since by setting the partial derivatives (6.12) to zero we have set the vorticity to zero and have ensured that the terms multiplied by $c_7 \ldots c_9$ in (6.62) all vanish as does (6.59).

From the above exercise we conclude that in order to complete the determination of all the $c_1 \ldots c_9$ we need to analyze a fluid configuration with nonzero vorticity. We have repeated the analysis of Sections 6.1.2 and 6.2.1 for a fluid in which $\partial_t u^1 \neq 0$, $\partial_x u^1 \neq 0$, $\partial_x u^3 \neq 0$ and $\partial_z u^1 \neq 0$, in addition to the nonzero partial derivatives in (6.11). We also allowed $\vec{\beta}$ to have nonzero components in all three directions. As a check, we first considered the case where $\partial_x u^3 = \partial_z u^1 \neq 0$, which is to say we did a much more complicated calculation than in Sections 6.1.2 and 6.2.1 but still with vanishing vorticity. We then repeated the exercise described in the preceding paragraph and once again found only 5 independent constraints on the c's that served to fix $c_1 \ldots c_4$ and $c_5 + c_6$. So, we obtained no new information at all. We then redid all the calculations with $\partial_x u^3 \neq \partial_z u^1$. In this case, we found 9 independent constraints

on the c's that, finally, served to fix them all. We find:

$$\begin{aligned}
c_1(s) &= \pi/2 - \tan^{-1}(\sqrt{-s}) - F(\sqrt{-s}), \\
c_2(s) &= \frac{1}{3}\left(\sqrt{-s} + (1+s^2)c_1(s)\right), \\
c_3(s) &= c_6(s) = -sc_1(s), \\
c_4(s) &= -c_5(s) = \frac{1}{\sqrt{-s}} - sc_1(s), \\
c_7(s) &= c_8(s) = c_9(s) = 0,
\end{aligned} \tag{6.64}$$

where $c_1(s)$ is the same function as defined in (6.30) previously. As a nontrivial check of the calculation, we note that we obtained the same results for $c_1 \ldots c_4$ and $c_5 + c_6$ when we fixed them via our calculations for configurations with or without vorticity. As another nontrivial check, we have used (6.62) with (6.64) to reproduce our results (6.54) and (6.55) from Section 6.2.2.

Although we included $c_7 \ldots c_9$ for completeness, we could have argued from the beginning that they must vanish. If any of these coefficients were nonzero, there would be a contribution to the drag force that was proportional to the vorticity, or to one of the other expressions involving an explicit $\epsilon^{\mu\nu\alpha\beta}$. This would violate time-reversal and parity symmetry. It might be interesting to repeat our analysis for a (chiral) fluid in which these symmetries are in fact violated at a microscopic level. We expect that in such a fluid these coefficients could be nonzero. Note, however, that $c_5 \neq c_6$ in our calculation. This means that the presence of nonzero vorticity in the $\mathcal{N} = 4$ SYM fluid that we have analyzed *does* affect the drag force that the fluid exerts on a heavy quark moving through it, via a contribution to the drag force that is proportional to (6.59).

The most general result of this paper is the expression (6.62) which, with (6.64), gives the contribution to the drag force on a heavy quark moving through the strongly coupled fluid in arbitrary hydrodynamic motion that is first order in fluid gradients.

By rearranging terms we have found a more compact version of this expression:

$$f^{\mu}_{(1)} = -\frac{\sqrt{\lambda}}{2\pi}\frac{1}{b\gamma}\times \left[c_1(s)\left(u^\mu w^\alpha \partial_\alpha s - s\partial^\mu s - s(su^\alpha + w^\alpha)\partial_\alpha U^\mu\right) + c_2(s)U^\mu \partial_\alpha u^\alpha - \sqrt{-s}u^\alpha \partial_\alpha U^\mu\right], \tag{6.65}$$

where $U^\mu \equiv u^\mu + sw^\mu$ denotes the component of fluid 4−velocity u^μ that is perpendicular to the heavy quark 4−velocity w^μ. This (deceptively) compact expression for the drag force arising due to fluid gradients at first order is the main result of this paper. The explicit results given in earlier subsections that we shall employ in Section 6.3 are all special cases of (6.65).

6.3 Applications

In this Section we shall apply our result (6.49) and its generalization (6.65) to analyze the effects of fluid gradients on the drag force on a heavy quark in three settings, ordered by increasing complexity. We will first consider a quark at rest in the instantaneous fluid rest frame, and show that even in this case the fluid can exert a "drag" force on the heavy quark. We will then consider two applications of our result to models of interest in the context of heavy ion collisions. In Section 6.3.2 we consider boost-invariant expansion of the fluid, à la Bjorken. In Section 6.3.3 we return to the colliding sheets of energy whose analysis in Ref. [3] provided the initial motivation for the present study, as we have described in Section 4.

6.3.1 A quark at rest in a fluid that is, instantaneously, at rest

As a very simple example with which to illustrate how fluid gradients can have non-trivial consequences for the "drag" force exerted by the fluid on a heavy quark, let us consider a heavy quark that is at rest in a fluid that is instantaneously at rest at the location of the heavy quark. However, the fluid is not static and is not spatially

uniform. If we neglect the effects of gradients, there would be no force on the quark: the quark is not moving, the fluid is not moving, so there can be no drag force. For simplicity let us consider the case where the fluid motion is only in the z-direction, as in Section 6.2.1. In this case, from (6.49) we see that as a consequence of the time variation of the fluid velocity there *is* a force acting on the quark, pushing it in the z-direction, namely

$$f^z_{(1)} = \frac{\sqrt{\lambda}}{2\pi b}\partial_t u^3 \,, \tag{6.66}$$

even though $\vec{\beta} = 0$. This shows that the force exerted by the fluid on the heavy quark cannot always be thought of as a drag force, a point that was already made in Ref. [3]. Note, however, that the sign of the force (6.66) is consistent with an interpretation in terms of drag with a time delay. If $\partial_t u^3 > 0$, then a short time ago u^3 was negative. That means that if we think in terms of drag we would expect that a short time ago the fluid was pushing the quark toward negative z, which in turn means that a short time ago the external agency holding the quark at constant $\vec{\beta} = 0$ would have been exerting a force $f^z > 0$. So, we can interpret (6.66) in terms of a time delay in the response of the drag force to changing fluid conditions. Comparing (6.66) to (6.42), we can estimate that the time delay is of order b for a quark at rest. The results of Ref. [3] indicate that a time delay like this is generic.

6.3.2 Bjorken flow

In 1982 Bjorken discovered a simple solution to the zeroth order (ideal) hydrodynamic equations of motion [109] that has since then often been used as a toy model for the longitudinal expansion of the fluid produced in heavy ion collisions. In Bjorken's solution, the fluid expands in the z-direction only and its expansion is boost invariant. The fluid 4-velocity is given by

$$u^\mu = \left(\frac{t}{\tau_p}, 0, 0, \frac{z}{\tau_p}\right) , \tag{6.67}$$

where $\tau_p \equiv \sqrt{t^2 - z^2}$ is the proper time, which is to say

$$\vec{v} = \left(0, 0, \frac{z}{t}\right) \ . \tag{6.68}$$

The solution is only defined in the forward light-cone, $z > |t|$. The temperature of the fluid, and hence its energy density and pressure, depend only on τ_p. We shall refer to this solution to hydrodynamics as Bjorken flow. If the fluid were ideal, with no viscosity and hence no contribution to the fluid stress-energy tensor from gradients, then $b(\tau_p) \propto \tau_p^{1/3}$ [109]. This dependence is modified when nonzero viscosity and hence effects of gradients are taken into account, as for example in Refs. [121, 92]. The gravitational dual of Bjorken flow was first constructed in Ref. [90]. For us, though, the calculation of the drag force on a heavy quark in a fluid expanding in a Bjorken flow is simply a special case of the calculation we have presented in Section 6.2.2. We just need to apply the result (6.55) or, in its more general form, the result (6.65), to the velocity profile (6.67). The temperature could be obtained from (6.67) but we will not need to do so, as we will leave our result written in terms of $b(t, z) = b(\tau_p)$.

Let us consider the case where the quark starts at $(t, z) = 0$ and is dragged with constant velocity $\vec{\beta} = (\beta_x, \beta_y, \beta_z)$, meaning in particular that the quark follows a trajectory whose z-component is $z = \beta_z t$. Along the trajectory of the quark, the fluid velocity is given by $v_z = z/t$, which is to say $v_z = \beta_z$, meaning that in the instantaneous fluid rest frame at all times the quark is not moving in the z-direction. The quark is moving with the fluid in the z-direction. In the laboratory frame, the fluid velocity gradients are given by

$$\begin{aligned} \partial_t u^3 &= -\partial_z u^0 = -\gamma_v^3 \frac{\beta_z}{t} = -\gamma_v^2 \frac{\beta_z}{\tau_p}, \\ \partial_z u^3 &= -\frac{\partial_t u^0}{\beta_z^2} = \frac{\gamma_v^3}{t} = \frac{\gamma_v^2}{\tau_p}, \end{aligned} \tag{6.69}$$

where $\gamma_v \equiv (1 - \beta_z^2)^{-1/2}$ is the relativistic gamma factor associated with the fluid velocity $\vec{v}$. We note that since the quark is in the local fluid rest frame at all times,

the convective derivative of u^3 along the path of the quark vanishes: $D_t u^3 = \partial_t u^3 + \beta^z \partial_z u^3 = 0$.

By substituting (6.67) and (6.69) into (6.65), simplifying the resulting expression for $\vec{f}_{(1)}$, and combining it with the zeroth order drag force (6.42) we find that the drag force needed to pull the heavy quark at velocity $\vec{\beta}$ through the Bjorken flow is given by

$$\vec{f}_{\rm BF}(\tau_p) = \vec{f}_{(0),\rm BF}(\tau_p) + \vec{f}_{(1),\rm BF}(t) = \frac{\sqrt{\lambda}}{2\pi} \frac{\gamma}{\gamma_v\, b(\tau_p)^2} \left(1 + c_2\left(-\frac{\gamma}{\gamma_v}\right) \frac{b(\tau_p)}{\tau_p}\right) \begin{pmatrix} \beta_x \\ \beta_y \\ \beta_z \gamma_v^2 \beta_\perp^2 \end{pmatrix}, \tag{6.70}$$

where $\beta_\perp^2 \equiv \beta_x^2 + \beta_y^2$ and where $c_2(-\gamma/\gamma_v)$ is defined in (6.64), noting that for Bjorken Flow $s = -\gamma/\gamma_v$. It is easiest to obtain (6.70) from (6.65), upon noting that since u^3 does not depend on x or y we have $u^\alpha \partial_\alpha u^3 = \gamma_v D_t u^3 = 0$ and $w^\alpha \partial_\alpha u^3 = \gamma D_t u^3 = 0$. It can also be shown that $\partial_z s = 0$, meaning that the only nonvanishing term in (6.65) is the term proportional to $c_2(s)$. At large τ_p, $b(\tau_p) \sim \tau_p^{1/3}$ and the first order term in (6.70) is smaller than the zeroth order term by a factor $\sim \tau_p^{-2/3}$, which is the standard power-counting for the derivative expansion in Bjorken flow.

When the quark is moving solely along the $z-$direction ($\beta_\perp = 0$), the drag force (6.70) vanishes identically at both zeroth and first order in gradients. This is because in this case the quark is at rest in the instantaneous fluid rest frame at all times and, in the frame in which both the quark and the fluid around it are at rest, there is no time derivative of the fluid velocity meaning that according to (6.66) there is no drag force. So, in this case the existence of fluid gradients does not modify the intuitive, zeroth order, result. The result that we have obtained for the case in which $\beta_\perp \neq 0$ and $\beta_z \neq 0$ looks less intuitive. However, note that it can be shown that if we boost the force (6.70) to the fluid rest frame, it has $f^z = 0$ which means that in the fluid

rest frame $\vec{f} \parallel \vec{\beta}$. If we choose $\beta_x \neq 0$ and $\beta_y = 0$, then in the fluid rest frame we find

$$f^x_{BF,RF} = \frac{\sqrt{\lambda}}{2\pi}\frac{1}{b(\tau_p)^2}\gamma\beta_x\left(1 + \frac{b(\tau_p)}{\tau_p}c_2\left(-\gamma\right)\right) . \tag{6.71}$$

So, when $\beta_\perp \neq 0$ we find that the fluid gradients do correct the result for the drag force at first order.

The drag force on a heavy quark moving through a fluid expanding in a Bjorken flow has been discussed previously in the literature. The leading term, namely $\vec{f}_{(0)}$ to zeroth order in gradients, was obtained in Refs. [106, 107]. The authors of Ref. [108] attempted the calculation of the correction to the force to first order in fluid gradients for a heavy quark moving through the Bjorken flow along a path with $z = 0$ but, as we noted previously, this calculation was based upon the assumption that the effects of fluid gradients could be attributed to their effects on the position of the world-sheet horizon in the dual gravitational description, and we have now seen that the position of the world-sheet horizon is unaffected by fluid gradients, at least to first order.

There are not many solutions to relativistic viscous hydrodynamics that are known analytically. Recently, Gubser has discovered two new such solutions, each in a different sense a deformation of Bjorken flow. In the solution of Ref. [152], the fluid expands in both the transverse and longitudinal directions, with the longitudinal expansion boost invariant as in Bjorken flow. The other solution, in Ref. [153], describes a longitudinal expansion that is not boost invariant but that can be obtained via suitable deformation of Bjorken flow. It would be interesting to apply our results to obtain expressions for the drag force on a heavy quark moving through a fluid expanding according to these hydrodynamic solutions. We leave this to future work.

6.3.3 Colliding sheets of energy

We now return to the example that prompted our study [3], namely the drag force needed to pull a heavy quark through the matter produced in the collision of two planar sheets of energy in strongly coupled SYM theory, introduced in Ref. [88] and analyzed there and in Refs. [89, 143]. The incident sheets of energy move at the

speed of light in the z and $-z$ directions and collide at $z = 0$ at time $t = 0$. They each have a Gaussian profile in the z direction and are translationally invariant in the two directions $\vec{x}_\perp = x, y$ orthogonal to z. Because this setup is translationally invariant in $\vec{x}_\perp$ throughout the collision, the motion of the fluid produced in the collision is entirely along the z direction at all times. The energy density per unit transverse area of the incident sheets is $\mu^3 N_c^2/(2\pi^2)$ with μ an arbitrary scale with respect to which all dimensionful quantities in the conformal theory can be measured. As in Ref. [3], we shall choose the width w of the Gaussian energy density profile of each sheet to be $w = 1/(2\mu)$. Although there is no single right way to compare the widths of these translationally invariant sheets of energy with Gaussian profiles to the widths of a nucleus that has been Lorentz-contracted by a factor of 107 (RHIC) or 1470 (LHC), reasonable estimates suggest that our choice of $w\mu$ corresponds to sheets with a thickness somewhere between the thickness of the incident nuclei at RHIC and LHC [88]. The matter produced in these collisions is initially far from equilibrium but it then rapidly hydrodynamizes: after a time $t_{\rm hydro}$ its subsequent expansion and cooling is well described by viscous hydrodynamics, with $t_{\rm hydro}/b(t_{\rm hydro})$ at most 2-3 [88].

In Ref. [3] we and a coauthor inserted a heavy quark moving with velocity $\vec{\beta}$ between the colliding sheets before the collision, choosing a trajectory such that the heavy quark is at $z = 0$ at $t = 0$, meaning that it finds itself in the center of the collision, and calculated the drag force needed to keep the velocity of the heavy quark constant throughout the collision. Our focus throughout much of Ref. [3] was the drag force at the earliest moments of the collision when the matter was far from equilibrium. We also calculated the drag force during the later epoch when the fluid has hydrodynamized and is expanding according to first order viscous hydrodynamics. We compared our results throughout to expectations for what the drag force would have been in a spatially homogeneous equilibrium fluid with the same instantaneous energy density, transverse pressure or longitudinal pressure. The first of these corresponds to the zeroth order drag force (6.42). To see this, note that what we did in Ref. [3] was to first boost to the instantaneous fluid rest frame, then compute the

energy density ε_{RF} in that frame, and from that define a temperature T_e as if the fluid were spatially homogeneous and in equilibrium, which is to say via $\varepsilon_{RF} = 3\pi^2 N_c^2 T_e^4/8$, and then use this T_e in the expression for the drag force on a heavy quark moving through an equilibrium fluid with no gradients. From (6.1) and (6.2) we see that in the instantaneous fluid rest frame σ^{00} vanishes, meaning that in this frame the fluid gradients do not contribute to $T^{00} = \varepsilon_{RF}$. Thus, the T_e we defined in Ref. [3] is related to b precisely by $b = 1/(\pi T_e)$. So, the dashed curves in Ref. [3] that were drawn using T_e correspond precisely to expectations for the drag force upon working to zeroth order in fluid gradients, namely (6.42). The results of Ref. [3] can be summarized as follows. First, (6.42) has roughly the right magnitude even just after the collision when the matter is far-from-equilibrium, although the time dependence of the actual force lags behind that obtained via (6.42) by a time delay that grows linearly with increasing γ. And, second, it was noted in Ref. [3] that even after the fluid has hydrodynamized the actual drag force calculated there does not agree with (6.42), an effect that was attributed to the effects of gradients in the fluid. Here we shall confirm this attribution.

We shall compare the drag force calculated in the full calculation of Ref. [3] to the zeroth order expectation (6.42), which neglects the effects of fluid gradients, and to that plus the contribution due to fluid gradients to first order which we now have at our disposal in the form (6.55) or the form (6.65). We shall do the comparison for two cases in which $\beta_z = 0$ and $\beta_x \neq 0$, meaning that the quark is moving perpendicular to the fluid motion, two cases in which $\beta_x = 0$ and $\beta_z \neq 0$, with the quark moving in the same direction as the fluid, and one case in which both β_x and β_z are nonzero.

In Fig. 6-1 we plot the drag force on a quark moving in the x-direction, perpendicular to the "beam" direction and therefore perpendicular to the direction of motion of the fluid, with $\beta_x = 0.5$ and $\beta_x = 0.95$. The red curves show the drag force obtained from the full gravitational calculation of Ref. [3], without any expansion in gradients. The blue dot-dashed curves, which were also obtained in Ref. [3], so what the drag force would be at each instant in time in a static homogeneous fluid in thermal equilibrium with the same energy density as the actual fluid has at

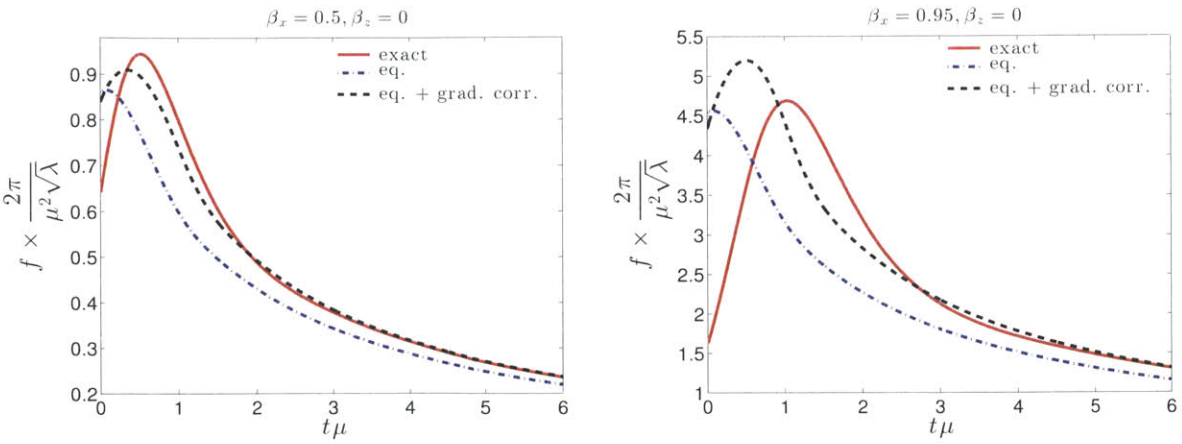

Figure 6-1: Actual drag force (red curves) from Ref. [3] on a heavy quark being dragged with $\beta_z = 0$ and $\beta_x = 0.5$ (left panel) or $\beta_x = 0.95$ (right panel) through the debris produced in the collision of two sheets of energy. We compare the actual drag force to the zeroth order calculation (blue dot-dashed curve) which neglects the effects of fluid gradients and our calculation in which the effects of fluid gradients are included up to first order (black dashed curves). At late times, when the fluid has hydrodynamized, the gradient corrections included in the black dashed curves yield a much better description of the full result.

that instant in time at the location of the quark. An equivalent description of these curves, which are obtained from our expression (6.42) that is zeroth order in fluid gradients, is that they show what the drag force would be if we neglect all effects of the spatial gradients and variation in time of the fluid at the location of the quark. The black dashed curves show how the drag force changes when we start with the blue dot-dashed curves and add the results of our calculation (6.65) of the first-order effects of fluid gradients on the drag force. Using the operational definition of the hydrodynamization time $t_{\rm hydro}$ introduced in Ref. [88], namely taking it to be the time after which the transverse and longitudinal pressure agree with those obtained via the hydrodynamic constitutive relations from the energy density and the fluid velocity, in Fig. 6-1 hydrodynamization time $t_{\rm hydro}\mu = 2.8$. We see that after $t_{\rm hydro}$ the black dashed curves are much closer to the full results shown by the red curves than the blue dot-dashed curves are, meaning that adding effects of fluid gradients to first order has resolved most of the discrepancy between the full results and the zeroth order blue dot-dashed curves. This confirms that this discrepancy was due to

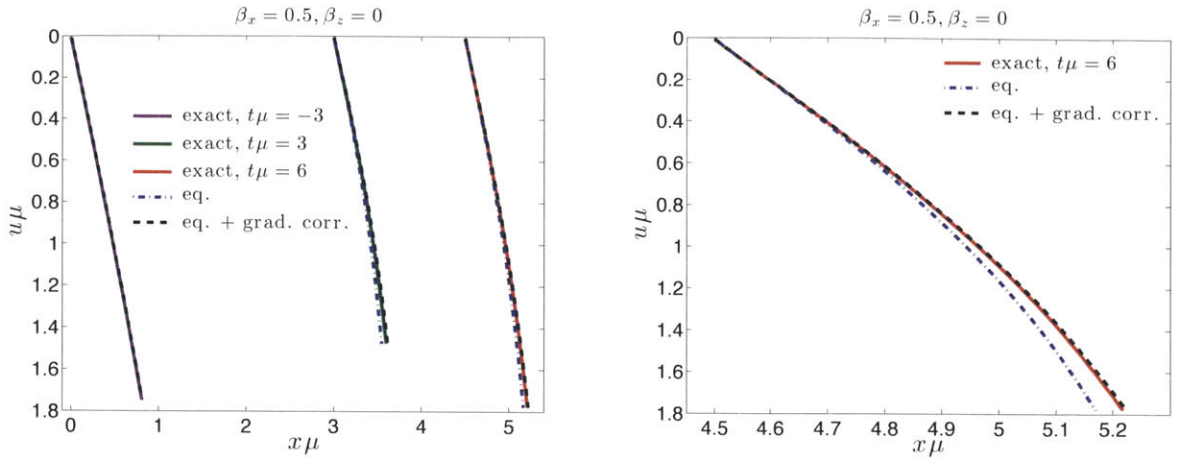

Figure 6-2: Comparison of the profile of the string trailing "down" into the bulk from the heavy quark moving with $\vec{\beta} = (0.5, 0, 0)$. The vertical axes show the radial, or holographic, coordinate $u = 1/r$, meaning that the AdS boundary at $r = \infty$ is at $u = 0$, at the top of the figures. The horizontal axes show x; the quark and hence its string is moving to the right. The curves show the shape of the string at a fixed Eddington-Finkelstein time t. The left panel shows the string at three times, $t\mu = -3, 3$ and 6. The right panel zooms in at $t\mu = 6$. In all cases, the solid curve shows the string profile obtained from the full gravitational calculation in Ref. [3], the blue dot-dashed curve shows the string profile (6.18) as it would be at that instant in time t if gradients in the fluid were neglected, and the black dashed curve shows the string profile (6.28) including the effects of fluid gradients to first order.

the effects of the fluid gradients. It is reasonable to guess that if one were to push our calculation to second order in gradients, the agreement would get even better. We leave this to future work.

We have also checked that the criteria (6.52) are well satisfied, by more than a factor of two in fact, at all times after $t_{\rm hydro}$ even for $\beta_x = 0.95$, namely for $\gamma = 3.2$. Throughout, we will only show results for cases in which these criteria are satisfied by a large margin.

To get further intuition, in Fig. 6-2 we investigate the shapes of the string hanging "down" into the gravitational spacetime from the heavy quark in the calculation of the drag force shown in the left panel of Fig. 6-1. Each string profile is plotted at fixed Eddington-Finkelstein time $t\mu$ as a function of the inverse radial coordinate $u = 1/r$. The solid curves are the exact string profiles at three times, obtained numerically in

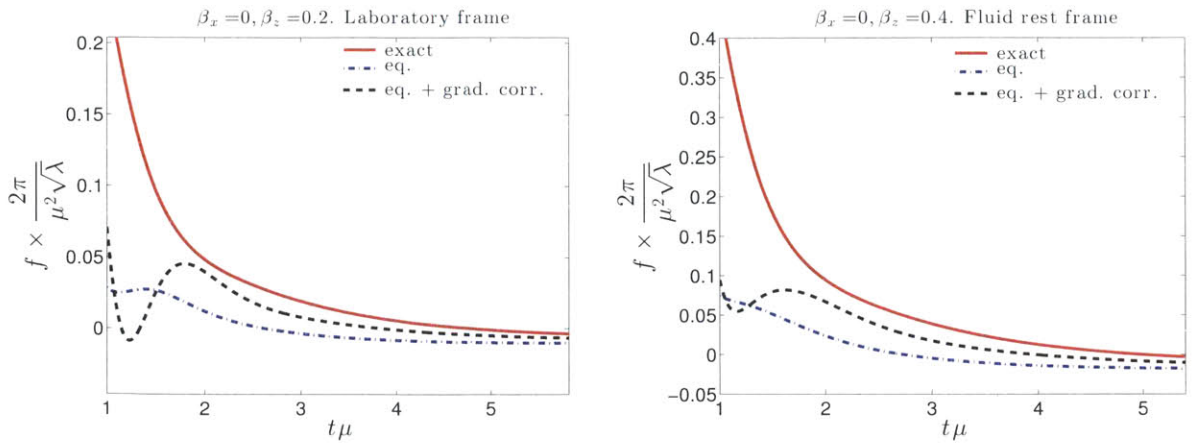

Figure 6-3: As in Fig. 6-1, except that here the quark has zero velocity in the direction perpendicular to the motion of the fluid and is moving only in the z-direction. In the left panel, $\beta_z = 0.2$ and in the right panel $\beta_z = 0.4$. We have shown the left panel in the laboratory frame while in the right panel at each time t we have boosted to the frame in which the fluid is at rest at the location of the quark. As in Fig. 6-1, we show the exact results for the drag force obtained in Ref. [3] as well as the zeroth-order approximation (i.e. the drag force in a static homogeneous fluid with the same instantaneous energy density) and the result that we have obtained upon including the effects of fluid gradients to first order.

the gravitational calculation of Ref. [3].[1] The blue dot-dashed curves are zeroth order in fluid gradients: they show the shape (6.18) that the string would have in a static, spatially homogeneous, equilibrium fluid with the same energy density as that at the location of the heavy quark. The black dashed curves are obtained by integrating $\partial_\sigma \vec{g}$ in the fluid rest frame, *i.e.*, Eqs. (6.29). In a case like those we shall turn to below, where the lab frame is not the same as the fluid rest frame, we would then boost the string profile from the fluid rest frame back to the lab frame. We see from Fig. 6-2 that including the effects of fluid gradients on the string profile to first order yields a much better description of the actual string profile, just as for the drag force itself.

In Fig. 6-3 we investigate two cases when the quark is moving with nonzero rapid-

[1] The drag force is independent of one's choice of coordinates for the 4+1-dimensional gravitational metric, but when we plot the shape of the string $u(x)$ at one value of the time coordinate t this shape does of course depend on one's definition of the coordinates u and t. The calculation in Ref. [3] was done using a metric in which $G_{tr} = 1$ and G_{Mr} vanishes for $M \neq t$. In our calculation of (6.29) we have instead used the metric given in Eqs. (6.6, 6.7, 6.8) in which $G_{rr} = 0$ and $G_{\mu r} = -u_\mu$. In order to make the comparison in Fig. 6-2, we have transformed the exact results for the string profile obtained in Ref. [3] from the metric used there to the metric we are using here. This coordinate transformation can be determined order-by-order in the fluid gradients, as described in Ref. [143].

ity, $\beta_z \neq 0$. Here we choose to set $\beta_x = 0$; below we will consider a case when both β_x and β_z are nonvanishing. In Fig. 6-3 we have chosen $\beta_z = 0.2$ and $\beta_z = 0.4$. In both cases, and as in Fig. 6-1, including the first order effects of fluid gradients on the drag force improves the agreement with the exact calculation of the drag force from Ref. [3]. In Fig. 6-3 the agreement between the black dashed curves and the solid red curves is worse than in Fig. 6-1, in fractional terms, but the more striking difference between the two Figures is that the overall magnitude of the forces plotted in Fig. 6-3 is more than an order of magnitude smaller than the forces in Fig. 6-1. This can be understood by recalling our results for Bjorken flow, from Section 6.3.2. If the longitudinal expansion of the fluid produced in the collision that we are analyzing here were boost invariant, our results from Section 6.3.2 tell us that when we choose $\beta_z \neq 0$ and $\beta_x = 0$ we would find no drag force at all, at zeroth and first order in fluid gradients. The fact that we see a nonzero drag force in Fig. 6-3 reflects the fact that the expansion of the fluid produced in the collision is not boost invariant. Since at late times the expansion is close to boost invariant [143], all the forces in Fig. 6-3 are small in magnitude. Upon realizing this, we also note that the absolute difference between the black dashed and solid curves in Fig. 6-3 is in fact quite similar to their absolute difference in Fig. 6-1, meaning that the larger fractional deviation in Fig. 6-3 is simply an artifact of the smallness of the magnitude of the drag force which is a consequence of the expansion being almost boost invariant.

In Fig. 6-4 we investigate the shapes of the string attached to the heavy quark moving with $\beta_z = 0.2$ whose drag force is shown in the left panel of Fig. 6-3 at the three Eddington-Finkelstein times $t\mu = -3, 2.5$, and 6. As in Fig. 6-2, we see that including the effects of fluid gradients on the string profile to first order improves the description of the exact string profile obtained in Ref. [3]. Just as when we compared Figs. 6-1 and 6-3, when we compare the zoomed-in panels of Fig. 6-4 to the zoomed-in panel of Fig. 6-2 we see that the absolute differences between the analytic results to first order in fluid gradients (black dashed curves) and the full results obtained numerically (solid curves) are comparable, although the fractional deviations look greater in Fig. 6-4.

We have chosen $t\mu = 2.5$ as one of the times at which we illustrate the string profile in Fig. 6-4 because it is close to the time $t\mu = 2.63$ at which the velocity of the fluid at the location of the quark, v_z, goes from below 0.2 to above 0.2, meaning that the relative velocity of the quark and the fluid changes sign at that time. At $t\mu = 2.63$, the zeroth-order approximation to the drag force therefore changes sign, as seen in the blue dot-dashed curve in the left panel of Fig. 6-3. We see that this change is also reflected in the string profile: at $t\mu = 2.63$, the string would be hanging straight down from the quark at the boundary; earlier, it angles to the right; later, it angles to the left. We see that at $t\mu = 2.5$ the orientation of the string has already changed deeper within the bulk and the change in orientation is about to reach the boundary. Note that the orientation of the string at the boundary suffices to determine the sign of the drag force only to zeroth order. Once the effects of fluid gradients are included, the drag force at time t depends on how the string is moving as well as on the orientation of the string [3]. We see in the left panel of Fig. 6-3 that the drag force including effects of fluid gradients to first order (black dashed curve) and the full drag force (red curve) change sign only considerably later than $t\mu = 2.63$. Starting at $t\mu = 2.63$, when the relative direction of the fluid flow and the quark changes, we have a period of time when the drag force exerted by the fluid on the quark points in the same direction as the velocity of the quark, an effect that was highlighted in Ref. [3]. We now see from the black dashed curve that this effect can be accounted for qualitatively by the effects of fluid gradients to first order.

The $t\mu = 2.5$ panel of Fig. 6-4 is also interesting insofar as it shows an example where although the difference between the zeroth order string profile and the full string profile is small in magnitude these two profiles have qualitatively different shapes, and we see the first order effects of gradients doing the job of turning the blue dot-dashed curve into a black dashed curve that looks much more like the red solid curve.

Finally, in Fig. 6-5 we show the results of our calculation of the effects of fluid gradients to first order on the drag force needed to move a heavy quark along a trajectory with both $\beta_x \neq 0$ and $\beta_z \neq 0$. The message from the upper two panels

is much the same as what we have already learned from Fig. 6-1. In the lower two panels, at each time we boost to a frame in which the fluid at the location of the heavy quark is instantaneously at rest. In this frame, the heavy quark is of course still moving, with a substantial velocity in the x-direction and some velocity in the z-direction. We have chosen to plot the components of the drag force in this frame in the directions parallel to and perpendicular to the direction of motion of the quark in this frame. The bottom-left plot is, again, similar to other plots that we have seen. The bottom-right plot is, however, of particular interest because the blue dot-dashed curve in this plot vanishes: in the local fluid rest frame to zeroth order in gradients the drag force must be parallel to the direction of motion of the heavy quark; without the effects of fluid gradients, there can be no perpendicular component. We have also seen in Section 6.3.2 that if the expansion were boost invariant then in the local fluid rest frame the drag force on the heavy quark would still act parallel to the direction of motion of the heavy quark even when the effects of fluid gradients are taken into account to first order. Therefore, the fact that the black dashed curve in the bottom-right panel of Fig. 6-5 is nonzero is a direct manifestation of the effects of fluid gradients *and* of the fact that the expanding fluid produced in the collision of the two sheets of energy is not boost invariant. The magnitude of the force described by this curve is small, since the expansion is close to boost invariant, but it is nonzero. We also see that the first order effects of fluid gradients push the black dashed curve toward the full result, shown as usual by the red curve.

We conclude from the investigations that we have reported in this section that the discrepancies observed in Ref. [3], and presented in Chapter 5, between the actual drag force on a heavy quark being pulled through the matter produced in the collision of sheets of energy and the drag force that would have been obtained in an static, homogeneous, plasma with the same energy density is indeed due to the effects of spatial gradients in, and time derivatives of, the fluid on the drag force. Evaluating these effects to first order in the fluid gradients explain all the qualitative aspects of the discrepancies found in Ref. [3] and do a reasonable job even at the quantitative level.

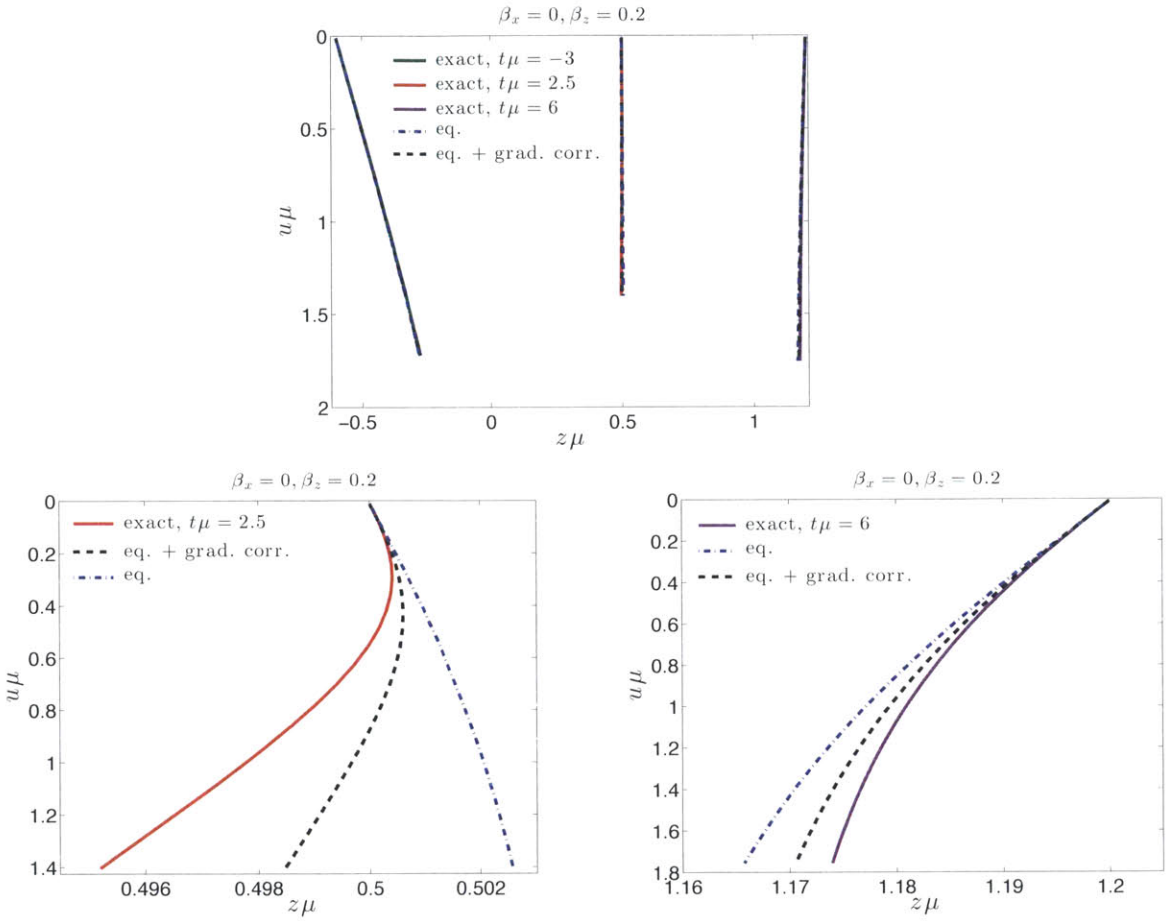

Figure 6-4: Comparison of the profile of the string trailing "down" into the bulk from the heavy quark moving with $\vec{\beta} = (0, 0, 0.2)$. The axes are as in Fig. 6-2. The solid curves show the shape of the string obtained from the full gravitational calculation of Ref. [3] at three fixed Eddington-Finkelstein times t, namely $t\mu = -3, 2.5$ and 6. As in Fig. 6-2, the blue dot-dashed curves show the string profile as if there were no gradients in the fluid and the black dashed curves show the results of this paper, with the effects of fluid gradients taken into account to first order. The lower panels zoom in on the string profiles at $t\mu = 2.5$ and 6. We have chosen $t\mu = 2.5$ as one of the times at which we illustrate the string profile because it is just before the time $t\mu = 2.63$ at which the blue dot-dashed curve in the left panel of Fig. 6-3 crosses zero, which is to say it is just before the time at which the relative velocity of the quark and the fluid changes sign, meaning that the zeroth-order estimate of the drag force changes sign.

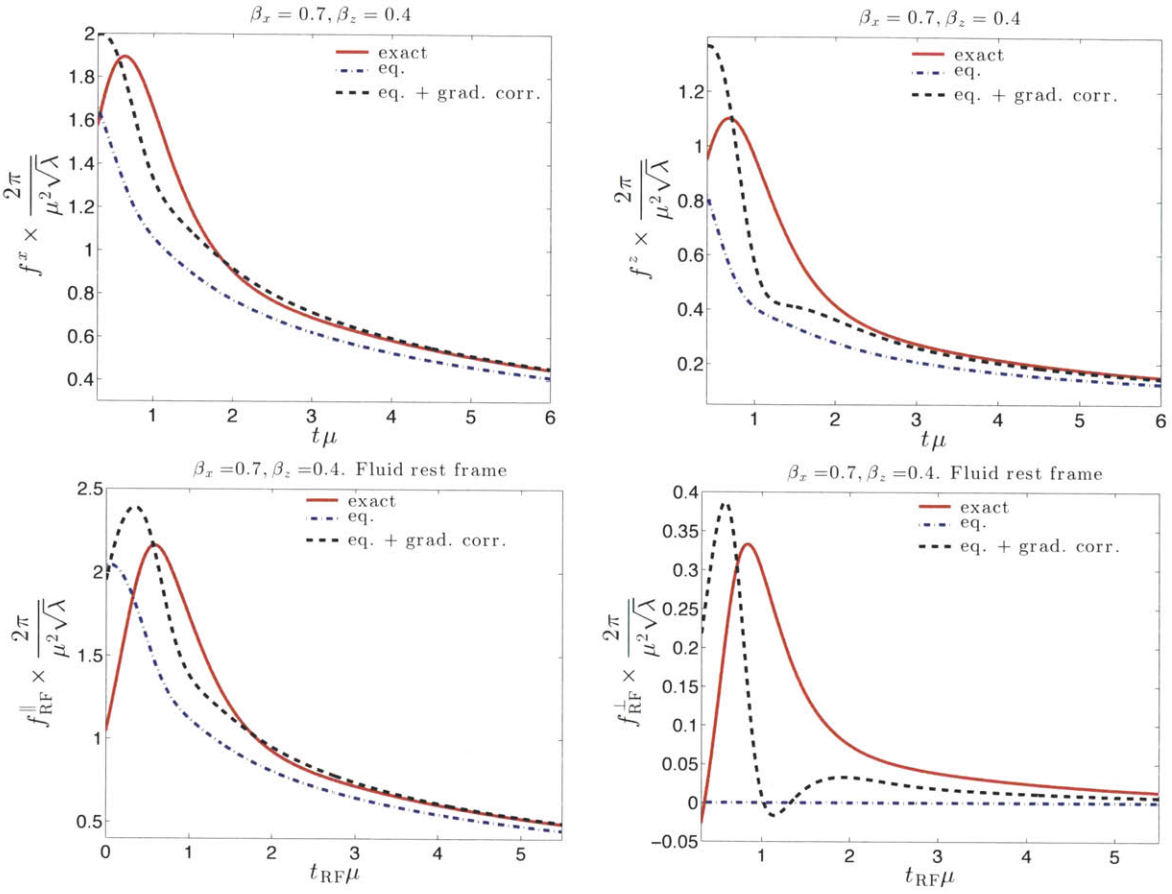

Figure 6-5: As in Fig. 6-1, but the case when quark is moving with velocity $\vec{\beta} = (0.7, 0, 0.4)$, meaning $\beta_x = 0.7$ perpendicular to the collision direction and $\beta_z = 0.4$ along the collision axis. The upper two panels show the x- and z-components (top-left and top-right panels, respectively) of the drag force as seen in the "laboratory frame", which is to say the center-of-mass frame for the collision. In the lower two panels, we boost to the frame in which the fluid at the location of the heavy quark is at rest. And, instead of showing the x- and z-components of the drag force in this frame, we show the components of the force in the directions parallel to (bottom-left panel) and perpendicular to (bottom-right panel) the direction of motion of the quark in the local fluid rest frame. In all the panels, the drag force with fluid gradient corrections included to first order (black dashed curve) gives a better description of the full drag force (red curve) than does the zeroth-order drag force with fluid gradients neglected.

Chapter 7

Conclusions and future directions for part II

In part II we calculated energy loss of a heavy quark moving through the colliding sheets of energy as well as derived the general drag force expression in case when fluid is close to equilibrium. The straightforward approach to modeling the rate of energy loss of heavy quarks produced in a heavy ion collision proceeds as follows: (i) Use the equilibrium equation of state to turn the proper energy density as a function of space and time in the collision (for example described via viscous hydrodynamics) into an effective temperature as a function of space and time; (ii) Use perturbative QCD to calculate the distribution of the initial positions and momenta of heavy quarks produced via hard scattering at the earliest moments of the heavy ion collision; (iii) Use the effective temperature from (i) in the expression (5.31) for the drag force in a homogeneous plasma in thermal equilibrium, perhaps with the overall prefactor in (5.31) turned into a parameter to be fit to data; (iv) Use the resulting spacetime-dependent drag force, and consequent energy loss rate, in a Langevin equation employed to model the dynamics of heavy quarks in heavy ion collisions, as for example in Refs. [115, 116, 117, 118, 119, 120].

Our results indicate that a straightforward approach along the lines above can reasonably be applied even at very early times, before hydrodynamics applies. In particular, even though the peak value of the energy loss in the matter produced

in the collision of the two sheets of energy that we have analyzed occurs before hydrodynamization, at a time when the matter produced in the collision is still far from equilibrium, this peak value is nevertheless reasonably well reproduced by the straightforward approach. Certainly there is no sign of any significant "extra" energy loss arising by virtue of being far from equilibrium. The message of our calculation seems to be that if we want to use (5.31) to learn about heavy quark energy loss in heavy ion collisions, it is reasonable to apply it throughout the collision, even before equilibration, defining the T that appears in it through the energy density. The error that one would make by treating the far-from-equilibrium energy loss in this way is likely to be smaller than other uncertainties. We anticipate that this is the most robust lesson for heavy ion physics that we can draw from our results for the colliding sheets of energy.

It also seems to be a generic feature of our results that there is some time delay after the collision before the rate of energy loss of the heavy quark rises to its peak value, even though it is during this very earliest time that the matter in which the quark is immersed has the very highest energy density. Although we have not characterized the delay time in the case of the collision of sheets of energy quantitatively, our analysis of this delay in a simpler setting suggests that it is of order $1/(\pi T_{\rm hydro})$ (where $T_{\rm hydro}$ is the temperature of the fluid when it hydrodynamizes) for a heavy quark whose velocity β through the matter is not relativistic, and increases slowly as $1/\sqrt{1-\beta^2}$ increases. This would correspond to a delay of something like 0.1-0.2 fm/c in a heavy ion collision at RHIC. This delay suggests that it takes a little time after the heavy quark is enveloped by matter with a high energy density before the gluon fields around the heavy quark respond to the presence of the matter, with the drag and energy loss rising only after this response. Although our strongly coupled calculation cannot provide a complete characterization of the very earliest moments of a heavy ion collision, it is possible that this qualitative lesson may carry over. It would be interesting to use a model of heavy quark dynamics in heavy ion collisions to investigate whether a time delay along these lines has observable consequences.

The straightforward approach to modelling the drag force on a heavy quark in a

heavy ion collision is built upon the result (5.31) for a homogeneous fluid and therefore neglects all effects of gradients in the fluid velocity. A third qualitative lesson that we can infer from our results is that this neglect works reasonably well for heavy quarks with small rapidity, whose velocities are close to perpendicular to the gradient in the fluid velocity.

We have found qualitative consequences for the drag force on heavy quarks with larger rapidity, moving closer to parallel to the gradient in the fluid velocity, arising from the presence of a velocity gradient, which is to say qualitative phenomena that are not present at all in the straightforward approach that we have sketched above. For example, we have found that because of the gradients in the fluid the force exerted by the fluid on a heavy quark that has a small velocity relative to the fluid at its location can sometimes point in the same direction as the velocity of the quark, rather than dragging on it. And, generically, we find that the force exerted by the fluid on a heavy quark will have a component perpendicular to the velocity of the quark, even as seen in the local fluid rest frame. This perpendicular force can be large; we found instances where at early times, before hydrodynamization, its peak value in the local fluid rest frame was about half as large as the maximum drag force acting parallel to the velocity of the quark. The perpendicular force is nonzero at late times too, when the quark is propagating through a liquid that is described well by viscous hydrodynamics. This perpendicular force can also be attributed to the presence of gradients in the fluid velocity. Here too, it would be interesting to use a model of heavy quark dynamics in heavy ion collisions to investigate the consequences of these effects. That being for the future, at present the fourth lesson from our results is that the straightforward approach to modelling heavy quark dynamics in heavy ion collisions should be used with caution for heavy quarks at high rapidity.

Motivated by observations from colliding sheets of energy, in chapter 6 we investigated the effects of gradients in any conformal zero charge fluid on the heavy quark energy loss. In (6.65) we have derived a general expression for the drag force needed to pull a heavy quark through a dynamic fluid, flowing in some arbitrary fashion described by hydrodynamics, to first order in the gradients and time derivatives

of the fluid velocity. We have applied this result to heavy quarks moving through a fluid that is expanding according to Bjorken flow and to heavy quarks moving through the expanding and cooling liquid produced in a collision of sheets of energy in strongly coupled $\mathcal{N} = 4$ SYM theory. Future directions include applying (6.65) to heavy quarks moving through strongly coupled plasma whose dynamics is described by other hydrodynamic solutions, for example including transverse expansion. It would also be interesting, and challenging, to extend (6.65) to second order in fluid gradients. Doing so could clarify how the drag force behaves in the large γ limit in the case where, as we have done, one assumes that the quark mass $M \to \infty$ limit has been taken first. We have seen that in this regime when (6.52) is not satisfied the first order contributions of the fluid gradients dominate over the zeroth order drag force, which motivates an evaluation of the magnitude of the second order contributions. Considering the effects of fluid gradients on a finite-mass quark at a large enough γ that (6.53) is not satisfied would, however, require a different calculation entirely. The right starting point for this would be an analysis of the rate of energy loss and transverse momentum broadening of a light quark in a dynamic strongly coupled fluid, including the effects of fluid gradients. In [154] it was shown that light quark radiation rate is not substantially modified after quark passes through constant temperature finite thickness slab as compared to vacuum radiation. It would be interesting to see if there are new effects of light quark radiation due to present fluid and temperature gradients in the slab.

Other interesting directions would include investigating how gradients in the fluid affect the emission of photons and dileptons or the screening of the attraction between a heavy quark and antiquark, and hence how they affect the binding or dissociation of quarkonia. We leave the holographic calculation of the effects of fluid gradients on these and other probes of the strongly coupled fluid to future work.

Part III

Appendices

Appendix A

Schwinger-Keldysh formalism

In this Appendix, we briefly review the real-time field theory tools that we use in setting up the formalism in Section II and calculating the self-energy in Section III. (The Schwinger-Keldysh formalism that we are using is standard. One of its advantages is that by formally doubling the number of degrees of freedom, pinch singularities that otherwise plague real-time quantum field theory are avoided. For a more complete review, see e.g. Ref. [78].) We present the discussion for a scalar field theory to avoid excess notation. The discussion for gauge bosons is analogous.

We allow the time coordinate x^0 to be complex, and we define thermal Green functions

$$G_C(x_1, x_2, \ldots, x_n) = \langle T_C \{\phi(x_1)\phi(x_2)\ldots\phi(x_n)\}\rangle \ , \tag{A.1}$$

where the ordering is taken along a path C in the complex plane. For the path C we choose the Schwinger-Keldysh contour in Fig. A-1. In the $t_i \to -\infty$ and $t_f \to \infty$ limit the vertical pieces of C are irrelevant for the calculation of Green functions. Thus it is convenient to label the field $\phi_i(x)$, where $i = 1$ or $i = 2$ depending on where the field is evaluated on C:

$$\phi_1(x) = \phi_1(x^0, \mathbf{x}) \ , \qquad \phi_2(x) = \phi_2(x^0 - i\epsilon, \mathbf{x}) \ . \tag{A.2}$$

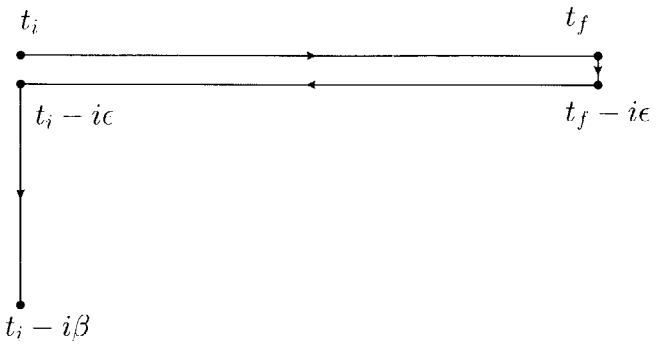

Figure A-1: Schwinger-Keldysh contour for $\sigma = \epsilon$.

Propagators then become matrices:

$$D_{ij}(x-y) = \begin{pmatrix} \langle T\{\phi(x^0,\mathbf{x})\phi(y^0,\mathbf{y})\}\rangle & \langle\phi(y^0-i\epsilon,\mathbf{y})\phi(x^0,\mathbf{x})\rangle \\ \langle\phi(x^0-i\epsilon,\mathbf{x})\phi(y^0,\mathbf{y})\rangle & \left\langle\tilde{T}\{\phi(x^0,\mathbf{x})\phi(y^0,\mathbf{y})\}\right\rangle \end{pmatrix} \tag{A.3}$$

where T and $\tilde{T}$ stand for time ordering and anti-time ordering, respectively. The generating functional for the free theory can be written as

$$\begin{aligned} Z_C^{\text{free}} &= \mathcal{N}\exp\left[-\frac{1}{2}\int_{-\infty}^{\infty} d^4x \int_{-\infty}^{\infty} d^4x'\, K(x,x')\right] , \\ K(x,x') &\equiv J_i(x) D_{ij}^{\text{free}}(x-x') J_j(x') , \end{aligned} \tag{A.4}$$

where the normalization factor $\mathcal{N}$ takes into account the multiplicative constant given by the two vertical pieces in C. In order to get the thermal Green functions we have to differentiate the above expression with respect to $J_i(x)$. For $\epsilon \to 0$, the Fourier space free propagator matrix reads

$$\begin{aligned} D_{11}^{\text{free}}(Q) &= \left[\frac{i}{Q^2+i\epsilon} + n(q_0)\, 2\pi\,\delta(Q^2)\right] , \\ D_{12}^{\text{free}}(q) &= \left[\theta(-q_0) + n(q_0)\right]\, 2\pi\,\delta(Q^2) , \\ D_{21}^{\text{free}}(Q) &= \left[\theta(q_0) + n(q_0)\right]\, 2\pi\,\delta(Q^2) , \\ D_{22}^{\text{free}}(q) &= \left[\frac{-i}{Q^2-i\epsilon} + n(q_0)\, 2\pi\,\delta(Q^2)\right] . \end{aligned} \tag{A.5}$$

The $\phi_2(x)$ field induces a modification of the naive Feynman rules. The propagator has off-diagonal elements, meaning that it mixes the two fields 1 and 2, whereas the vertices have only one type of field, and they do not induce any mixing. In addition we have a minus sign for any vertex connecting fields of type 2.

The four components of the propagator matrix in (A.3) are not independent, since

$$D_{11}(Q) + D_{22}(Q) = D_{12}(Q) + D_{21}(Q) \ , \tag{A.6}$$

and it is therefore more convenient to use a different basis including only three independent propagators. We introduce the Keldysh representation

$$\begin{aligned} &\text{Retarded :} && D_R(Q) \equiv D_{11}(Q) - D_{12}(Q) \ , \\ &\text{Advanced :} && D_A(Q) \equiv D_{11}(Q) - D_{21}(Q) \ , \\ &\text{Symmetric :} && D_S(Q) \equiv D_{11}(Q) + D_{22}(Q) \ . \end{aligned} \tag{A.7}$$

From the definitions we can derive the Fourier space expressions for the three free propagators in this new basis.

$$\begin{aligned} &\text{Retarded :} && D_R^{\text{free}}(Q) = \tfrac{i}{Q^2 + i\,\text{sgn}(q_0)\,\epsilon} \ , \\ &\text{Advanced :} && D_A^{\text{free}}(Q) = \tfrac{i}{Q^2 - i\,\text{sgn}(q_0)\,\epsilon} \ , \\ &\text{Symmetric :} && D_S^{\text{free}}(Q) = [1 + 2\,f(q_0)]\,2\pi\,\delta(Q^2) \ . \end{aligned} \tag{A.8}$$

We notice that only the symmetric propagator contains the thermal distribution $n(q_0)$ (either the Bose-Einstein distribution $n_B(q_0)$ or the Fermi-Dirac distribution $n_F(q_0)$ as appropriate) simplifying the identification of thermal contributions to diagrams.

We can now introduce the quantity that we calculate in Section III, the self-energy matrix Π_{ij} which is the building block for the propagator $D_{ij}(Q)$, as described by the Dyson equation

$$D_{ij}(Q) = D_{ij}^{\text{free}}(Q) + D_{im}^{\text{free}}(Q)\,(-i\Pi_{mn}(Q))\,D_{nj}(Q) \ . \tag{A.9}$$

In order to use the Keldysh representation also for the self-energy we define

$$D_\alpha(Q) = D_\alpha^{\text{free}}(Q) + D_\alpha^{\text{free}}(Q)\,(-i\Pi_\alpha(Q))\,D_\alpha(Q)\ , \tag{A.10}$$

where $\alpha = R, A, S$. The self-energies $\Pi_\alpha(Q)$ introduced above are linear combinations of the self-energies Π_{ij}. This is shown by plugging the propagators $D_{ij}(Q)$ into the definition (A.10), and identifying

$$\begin{aligned} &\text{Retarded}: && \Pi_R(Q) = \Pi_{11}(Q) + \Pi_{12}(Q)\ , \\ &\text{Advanced}: && \Pi_A(Q) = \Pi_{11}(Q) + \Pi_{21}(Q)\ , \\ &\text{Symmetric}: && \Pi_S(Q) = \Pi_{11}(Q) + \Pi_{22}(Q)\ . \end{aligned} \tag{A.11}$$

Appendix B

Transverse momentum broadening in a thin medium limit

In this Appendix we analyze our results in the case of a "thin medium", by which we mean L short enough such that $\kappa \equiv g^2 C_{\mathcal{R}} L\, T/(2\pi) \ll 1$. In this regime, the resummation of length-enhanced contributions performed in Sec. 2.1 is not necessary meaning that in this regime the full expression (2.15) reduces to

$$P(k_\perp) \simeq \int d^2x_\perp\, e^{-ik_\perp\cdot x_\perp} \left[1 + \mathcal{W}^{(2)}_{\mathcal{R}}(x_\perp)\right] . \tag{B.1}$$

We rewrite this expression in Fourier space, exactly as we did at the end of Sec. 2.1, and we find

$$P(k_\perp) = (2\pi)^2\delta^2(k_\perp)\left[1 - \int \frac{d^2q_\perp}{(2\pi)^2} P_{\rm thin}(q_\perp)\right] + P_{\rm thin}(k_\perp) \tag{B.2}$$

where $P_{\rm thin}(k_\perp)$ is the function defined in Eq. (3.2), a definition that we reproduce here for convenience:

$$P_{\rm thin}(k_\perp) \equiv \frac{2\sqrt{2}\pi\,\kappa}{T} \int \frac{dq^-}{2\pi} D^>(q^-, k_\perp) . \tag{B.3}$$

The probability distribution in Eq. (B.2) consists of two parts. First, we see a delta function centered at $k_\perp = 0$ whose coefficient has two terms, corresponding to no

scattering and scattering with no transverse momentum exchange. Second, we see the contribution describing scattering with nonzero final transverse momentum, given just by $P_{\rm thin}(k_\perp)$. We see that for a thin medium, and for $k_\perp \neq 0$, we have $P(k_\perp) = P_{\rm thin}(k_\perp)$.

Looking at the probability distribution (B.2), we immediately notice that the coefficient of the delta function is not finite. As we have seen in Section V.A, $P_{\rm thin}(q_\perp)$ precisely matches the AGZ distribution (3.5) in the infrared, meaning that it is $\propto q_\perp^{-2}$ for $q_\perp \ll T$. The integral in the delta function coefficient thus blows up. We shall show that, despite this divergence, the probability distribution in Eq. (B.2) is well defined. In order to do that we need to introduce the "plus distribution" $[\ldots]_+$ for a generic function $g(x)$, defined as [79]

$$\begin{aligned}[\theta(x)g(x)]_+ &\equiv \lim_{\beta\to 0}\frac{d}{dx}[\theta(x-\beta)G(x)], \text{ with} \\ G(x) &= \int_{x_0}^{x} dx' g(x') \ ,\end{aligned}$$

satisfying the boundary condition $\int_0^{x_0} dx[\theta(x)g(x)]_+ = 0$. Here, $x_0 \neq 0$ when $g(0) = \infty$. Since $P(k_\perp)$ depends only on the absolute value of transverse momentum, it is convenient to use the one-dimensional probability distributions $\tilde{P}(k_\perp) \equiv 2\pi k_\perp P(k_\perp)$ and $\tilde{P}_{\rm thin}(k_\perp) \equiv 2\pi k_\perp P_{\rm thin}(k_\perp)$. Then (B.2) becomes

$$\tilde{P}(k_\perp) = (2\pi)^2\delta(k_\perp) + \tilde{P}_{\rm thin}(k_\perp) - \delta(k_\perp)\int_0^\infty dq_\perp \tilde{P}_{\rm thin}(q_\perp) \ , \tag{B.4}$$

where the normalization now reads $\int_0^\infty dk_\perp \tilde{P}(k_\perp) = (2\pi)^2$.

We can apply the plus distribution prescription to extract the divergent term from $\tilde{P}_{\rm thin}(k_\perp)$, obtaining

$$\begin{aligned}&\left[\theta(k_\perp)\tilde{P}_{\rm thin}(k_\perp)\right]_+ = \\ &\lim_{\beta\to 0}\left[\delta(k_\perp-\beta)\int_{k_{\perp 0}}^{k_\perp} dq_\perp \tilde{P}_{\rm thin}(q_\perp) + \theta(k_\perp-\beta)\tilde{P}_{\rm thin}(k_\perp)\right] \ .\end{aligned} \tag{B.5}$$

After we take the $\beta \to 0$ limit, and noting that $k_\perp$ is always positive, the above result

takes the form

$$\left[\tilde{P}_{\rm thin}(k_\perp)\right]_+ = \tilde{P}_{\rm thin}(k_\perp) - \delta(k_\perp)\int_{k_\perp}^{k_{\perp 0}} dq_\perp \tilde{P}_{\rm thin}(q_\perp) \ . \tag{B.6}$$

This in turns implies the following facts:

- $\int_0^{k_{\perp 0}} dk_\perp \left[\tilde{P}_{\rm thin}(k_\perp)\right]_+ = 0$,
- $\left[\tilde{P}_{\rm thin}(k_\perp)\right]_+ = \tilde{P}_{\rm thin}(k_\perp)$ for $k_\perp > 0$.

Combining (B.6) and (B.4), we obtain

$$\tilde{P}(k_\parallel) = \delta(k_\parallel)\left((2\pi)^2 - \int_{k_{\perp 0}}^{\infty} dq_\parallel \tilde{P}_{\rm thin}(q_\parallel)\right) + \left[\tilde{P}_{\rm thin}(k_\parallel)\right]_+ ,$$

where $k_{\perp 0}$ is a free parameter in the range $0 < k_{\perp 0} < \infty$.

If we switch back to the two dimensional distributions, drop the tildes, and keep in mind that the plus distribution $[P(k_\perp)]_+$ is formally the one dimensional plus distribution divided by $2\pi k_\perp$, we find

$$P(k_\perp) = \delta^2(k_\perp) g(k_{\perp 0}) + [P_{\rm thin}(k_\perp)]_+^{k_{\perp 0}} \ , \tag{B.7}$$

where the factor $g(k_{\perp 0})$ reads

$$g(k_{\perp 0}) = (2\pi)^2 - 2\pi \int_{k_{\perp 0}}^{\infty} dq_\perp q_\perp P_{\rm thin}(q_\perp) \ . \tag{B.8}$$

For $k_{\perp 0} > 0$, the coefficient of the delta function in Eq. (B.7) is finite and positive, and the last term in Eq. (B.7) is the probability distribution with its value at $k_\perp = 0$ having been subtracted. Even though both terms depend on $k_{\perp 0}$, the $k_{\perp 0}$ dependence cancels when we sum the two terms. In conclusion, the probability distribution $P(k_\perp)$ in the thin medium limit $g^2 C_{\mathcal{R}} LT \ll 1$ is well defined, and the probability for no scattering plus that for scattering with no transverse momentum exchange is finite and positive, as it must be.

Appendix C

Exponentiation of $\mathcal{W}_{\mathcal{R}}^{(2)}$

In this Appendix, we show that by summing over all disconnected diagrams which involve only $\mathcal{W}_{\mathcal{R}}^{(2)}$, we obtain precisely the exponential (2.16) that we have used in (2.15). To get the lowest power in g for a given power of L, there is no need to include any connected diagrams other than $\mathcal{W}_{\mathcal{R}}^{(2)}$ in the sum. As discussed in the main text, if we ignore any factors of g that come from within the gluon propagators $\mathcal{W}_{\mathcal{R}}^{(2)}$ is of order g^2L, while any other connected diagrams give rise to g^nL with $n > 2$ and thus are of higher order. For example, $\mathcal{W}_{\mathcal{R}}^{(3)}$ is of order g^3L, while the cross diagram in Fig. 2-4 will give a factor g^4L.

To obtain the n-th order term in (2.16), we consider the expansion of $\mathcal{W}_{\mathcal{R}}$ at order $j = 2n$. For illustration here we demonstrate explicitly the exponentiation of $D^>(y^-, x_\perp)$ in (2.12) which comes from contractions of gluons with ends on different Wilson lines. The story for $D^>(y^-, 0_\perp)$ (gluons with both ends on the same Wilson line) and the cross terms between $D^>(y^-, 0_\perp)$ and $D^>(y^-, x_\perp)$ are similar and we leave it to the reader that they also exponentiate. In the notation of Eq. (2.4), we need only consider the term $W_{\mathcal{R}}^{(n,n)}$ in $\mathcal{W}_{\mathcal{R}}^{(2n)}$, which can be written as

$$W_{\mathcal{R}}^{(n,n)} = \frac{g^n}{d(\mathcal{R})} \int_{x_1^- < x_2^- < \cdots x_n^-} dx_1^- \ldots dx_n^- \int_{z_1^- < z_2^- < \cdots z_n^-} dz_1^- \ldots dz_n^-$$
$$\left\langle \mathrm{Tr}\left[A_{\mathcal{R}}^+(x_1^-, x_\perp) \ldots A_{\mathcal{R}}^+(x_n^-, x_\perp) A_{\mathcal{R}}^+(z_n^-, 0_\perp) \ldots A_{\mathcal{R}}^+(z_1^-, 0_\perp)\right]\right\rangle \qquad \text{(C.1)}$$

where we have denoted the coordinates on the two different Wilson lines by x_i^- and

z_i^- respectively and made the path ordering explicit. There are many different contractions in (C.1). The one which is relevant for our purposes here is the one in which the gluon at x_i^- is contracted with the gluon at z_i^-, for each of $i = 1, 2, \cdots n$. Other contractions will either give rise to cross terms between $D^>(y^-, x_\perp)$ and $D^>(y^-, 0_\perp)$ or create cross diagrams like that in Fig. 2-4 which are of higher order. We then find that

$$W_{\mathcal{R}}^{(n,n)} = (g^2 C_{\mathcal{R}})^n \int_{x_1^- < x_2^- < \cdots x_n^-} dx_1^- \ldots dx_n^- \int_{z_1^- < z_2^- < \cdots z_n^-} dz_1^- \ldots dz_n^- \prod_{i=1}^{n} D^>(x_i^- - z_i^-, x_\perp) \qquad \text{(C.2)}$$

$$= \frac{1}{n!} \left(g^2 C_{\mathcal{R}} L^- \int dy^- \, D^>(y^-, x_\perp) \right)^n . \qquad \text{(C.3)}$$

In the last step we have changed the integration over each pair of integration variables (x_i^-, z_i^-) to an integration over $Y_i^- = \frac{x_i^- + z_i^-}{2}$ and $y_i^- = x_i^- - z_i^-$. The integrations over y_i^- are unconstrained, while the integrations over Y_i^-, which satisfy the ordering $Y_1^- < Y_2^- < \cdots Y_n^-$, give $(L^-)^n/n!$. We have proved (2.15). The generalization of the proof of the exponentiation of $\mathcal{W}_{\mathcal{R}}^{(2)}$ that we have presented here to a proof of the exponentiation of the sum of all connected diagrams is straightforward.

Appendix D

Boltzmann equation approach to transverse momentum broadening

In this Appendix, we provide an explicit alternative derivation of the expression (2.15) for the probability distribution $P(k_\perp)$ by deriving and solving an appropriate Boltzmann equation for momentum broadening. The argument can easily be generalized to obtain the more general result (2.14) that goes beyond leading order in weak coupling. In this Appendix, it is useful to make the L-dependence of the probability distribution explicit by denoting it as $P(k_\perp, L)$.

Let us consider the hard parton after it has propagated for a distance L in the hot and dense medium. $P(k_\perp, L)$ is the probability distribution for its transverse momentum $k_\perp$. We want to relate $P(k_\perp, L)$ to $P(k_\perp, L + \Delta L)$, the probability distribution after the parton has traveled a further distance ΔL. In the $\Delta L \ll L$ limit, modifications to $P(k_\perp, L)$ are only caused by a single scattering event. We then introduce the differential collision kernel $C(q_\perp)$, defined as the differential rate for momentum broadening due to elastic collisions

$$C(q_\perp) \equiv \frac{d^2\Gamma}{dq_\perp^2} \ , \tag{D.1}$$

in terms of which the relation between the probability distributions at L and $L + \Delta L$

can be written as

$$P(k_\perp, L+\Delta L) = P(k_\perp, L)\left[1 - \Delta L \int \frac{d^2q_\perp}{(2\pi)^2} C(q_\perp)\right] + \Delta L \int \frac{d^2q_\perp}{(2\pi)^2}\, C(q_\perp)\, P(k_\perp - q_\perp, L)\ . \tag{D.2}$$

The first line describes the probability that between L and $L+\Delta L$ there is no further momentum transfer, and the probability distribution is not affected. The second line takes into account the possibility that the transverse momentum $k_\perp$ at $L+\Delta L$ arises after the hard parton picks up an additional transverse momentum $q_\perp$ in a scattering event that occurs between L and $L+\Delta L$. The Boltzmann equation for transverse momentum broadening is obtained by taking the $\Delta L \to 0$ limit in Eq. D.2, yielding

$$\frac{d\,P(k_\perp, L)}{dL} = \int \frac{d^2q_\perp}{(2\pi)^2}\, C(q_\perp)\left[P(k_\perp - q_\perp, L) - P(k_\perp, L)\right]\ . \tag{D.3}$$

Solving the Boltzmann equation (D.3) is simpler in coordinate space, where it reads

$$\frac{d\,P(x_\perp, L)}{dL} = -v\,(x_\perp)\ P(x_\perp, L)\ , \tag{D.4}$$

with

$$v\,(x_\perp) \equiv \int \frac{d^2q_\perp}{(2\pi)^2}\left[1 - e^{iq_\perp x_\perp}\right] C(q_\perp)\ , \tag{D.5}$$

a quantity often referred to as the dipole cross-section in the literature. The solution of Eq. (D.4) is just an exponential function, and upon performing the Fourier transform back to momentum space we find

$$P(k_\perp, L) = \int d^2x_\perp\, e^{ik_\perp x_\perp} e^{-v(x_\perp)L}\ . \tag{D.6}$$

This connection between multiple scattering and the dipole cross section was recognized in Refs. [20, 21, 22, 23]. In many calculations, however, the dipole cross-section was approximated as $v\,(x_\perp) \approx Cx_\perp^2$, resulting in a probability distribution that is Gaussian in $k_\perp$. As illustrated in Fig. 3-5, we find that this is a good approximation at small $k_\perp$ but not at large $k_\perp$.

Next, we present the explicit relationship between the analysis of this Appendix in terms of a Boltzmann equation and the analysis we follow throughout all other sections of this paper. The building block for deriving the Boltzmann equation was the differential elastic collision kernel $C(k_\perp)$ defined in Eq. (D.1). With a view toward making contact with results obtained in previous literature via the Boltzmann equation approach, we begin by including only elastic collisions in which one gluon exchanged. In the framework of the rest of this paper, this is obtained from the Wilson line diagrams in Fig. 2-1 with only one gluon propagator, as in Fig. 2-2. We have denoted this contribution by $P_{\rm thin}(k_\perp, L)$, defined in Eq. (3.2). The connection between $P_{\rm thin}(k_\perp, L)$ and $C(k_\perp)$ reads

$$P_{\rm thin}(k_\perp, L) = C(k_\perp)\, L \ . \tag{D.7}$$

With this identification in mind, we revisit the expression for $\mathcal{W}_{\mathcal{R}}^{(2)}$ found in Eq. (2.18), and we recognize

$$\mathcal{W}_{\mathcal{R}}^{(2)}(x_\perp) = -\int \frac{d^2q_\perp}{(2\pi)^2}\, \left[1 - e^{iq_\perp \cdot x_\perp}\right] P_{\rm thin}(q_\perp, L) = -v\,(x_\perp)\, L \ . \tag{D.8}$$

The solution to the Boltzmann equation found in Eq. (D.6), with $v\,(x_\perp)$ connected to $\mathcal{W}_{\mathcal{R}}^{(2)}$ as in Eq. (D.8), is therefore identical to the expression in Eq. (2.15) obtained by resumming length-enhanced diagrams.

The manipulations in this Appendix are completely general in the sense that they do not rely on any specific form for the collision kernel $C(k_\perp)$ in Eq. (D.1). If we were to include contributions to $C(k_\perp)$ that are higher order in the coupling, solving the Boltzmann equation would resum these higher order effects as needed when L is not small. If we were to include all contributions to $C(k_\perp)$ to arbitrarily high order in the coupling, we would recover our general result (2.14).

It has long been understood (in the QCD context, since Refs. [21, 66, 67]; in the context of electrons propagating through ordinary matter, at least since Refs. [80]) that if L is long enough that multiple scattering is important, the dipole cross section

can to a degree be approximated as $v(x_\perp) \propto x_\perp^2$, corresponding to a probability distribution for transverse momentum broadening (D.6) that is Gaussian in $k_\perp$. It was also understood by all these authors that, at large enough $k_\perp$, $P(k_\perp)$ must have a power-law tail corresponding to Rutherford scattering off a single point-like scatterer. In the QCD context, this was demonstrated in a model context by Wiedemann and Gyulassy in Appendix A of Ref. [66], where they showed that in the Gyulassy-Wang model [19] (in which the medium consists of static scattering centers which the hard parton sees as Debye-screened Yukawa potentials) the dipole cross section takes the form $v(x_\perp) \propto x_\perp^2 \log(R^2/x_\perp^2)$ at small $|x_\perp|$ for some constant R. (This form was known earlier in a different context [81].) Evaluating (D.6), we see that this form for $v(x_\perp)$ corresponds to $P(k_\perp) \propto 1/k_\perp^4$ at large $k_\perp$.

In the calculation we have presented in this paper, we need make no model assumptions about the nature of the medium. It is a weakly coupled quantum field theoretical plasma, as in QCD in thermal equilbrium at asymptotically high temperatures. And, as illustrated in Fig. 3-5, when L is large enough that multiple scattering is important we find by direct calculation both the Gaussian behavior at small $k_\perp$ and the $1/k_\perp^4$ behavior at large $k_\perp$.

Appendix E

A tensor basis for the self-energy

In this Appendix we define the projectors used to expand the retarded self-energy in tensor components in Section III and describe their properties. The presence of the thermal bath breaks Lorentz invariance by specifying a preferred frame in which the medium is at rest. We shall work in the medium rest frame, in which its four-velocity U^μ is $U^\mu = (1, 0)$, but in this Appendix we keep U^μ unspecified, defining these projectors for any frame. It is convenient to introduce another four-vector N^μ by projecting the four-velocity U^μ onto the direction orthogonal to the external momentum Q^μ:

$$\begin{aligned} N^\mu &\equiv P^{\mu\nu}U_\nu = U^\mu - \frac{Q\cdot U}{Q^2}Q^\mu \ , \\ P_{\mu\nu} &= g_{\mu\nu} - \frac{Q_\mu Q_\nu}{Q^2} \ , \qquad Q\cdot N = 0 \ . \end{aligned} \tag{E.1}$$

The self-energy is a symmetric rank-2 tensor. It can therefore be expressed as a linear combination of the following tensors:

$$\begin{aligned} P^T_{\mu\nu} &= -g_{\mu\nu} + \frac{Q_\mu Q_\nu}{Q^2} + \frac{N_\mu N_\nu}{N^2} \ , & P^L_{\mu\nu} &= -\frac{N_\mu N_\nu}{N^2} \ , \\ J_{\mu\nu} &= \frac{Q_\mu N_\nu + N_\mu Q_\nu}{\sqrt{-2N^2Q^2}} \ , & K_{\mu\nu} &= \frac{Q_\mu Q_\nu}{Q^2} \ . \end{aligned} \tag{E.2}$$

It is useful to build a multiplication table for the tensor basis, keeping in mind that the tensors in (E.2) are symmetric in their Lorentz indices. We find

$$\begin{aligned}
&P^T \cdot P^T = -P^T \ , && P^L \cdot P^L = -P^L \ , \\
&J \cdot J = \tfrac{1}{2}(P^L - K) \ , && K \cdot K = K \ , \\
&P^T \cdot P^L = 0 \ , && P^T \cdot J = 0 \ , \\
&P^T \cdot K = 0 \ , && P^L \cdot K = 0 \ , \\
&\mathrm{Tr}\left(P^L \cdot J\right) = 0 && \mathrm{Tr}\,(J \cdot K) = 0 \ .
\end{aligned} \tag{E.3}$$

Appendix F

Resumming AGZ

As we noted in Section V.A, some years ago Aurenche, Gelis and Zaraket derived an analytic expression (3.5) for $P_{\rm thin}(k_\perp)$ that is valid in the IR region, $k_\perp \ll T$, but not in the UV. In this Appendix we pursue the exercise of assuming that $P_{\rm thin}(k_\perp) = P^{\rm AGZ}_{\rm thin}(k_\perp)$ at all $k_\perp$, not just in the IR, and then resumming L-enhanced diagrams to obtain an expression for $P(k_\perp)$ that we shall denote by $P^{\rm AGZ}(k_\perp)$. Even though $P^{\rm AGZ}_{\rm thin}(k_\perp)$ is not in fact correct beyond the IR, there are two reasons to pursue this exercise. First, we anticipate that the $P^{\rm AGZ}(k_\perp)$ we obtain by resumming the AGZ expression will agree with our complete result at small enough $k_\perp$. This makes sense on physical grounds, as we have argued in Section 3.2. Here we confirm this expectation by explicit calculation. And, second, starting with the AGZ expression for $P_{\rm thin}$ allows us to do almost all of the calculation analytically. This makes it of value as a benchmark, even though the result is not valid beyond the IR. And, because the calculation *is* valid in the IR it will allow us to gain an analytic understanding of the κ-dependence of the low-$k_\perp$ behavior of $P(k_\perp)$.

In order to resum L-enhanced diagrams upon assuming that $P_{\rm thin}(k_\perp) = P^{\rm AGZ}_{\rm thin}(k_\perp)$ we proceed as follows. We first note from (2.19) and (3.2) that

$$\mathcal{W}^{(2)}_{\mathcal{R}}(x_\perp) = -\int \frac{d^2q_\perp}{(2\pi)^2}\left(1 - e^{i\,q_\perp\cdot x_\perp}\right) P_{\rm thin}(q_\perp)\ , \tag{F.1}$$

regardless of the form of $P_{\rm thin}$. In the case where $P_{\rm thin} = P^{\rm AGZ}_{\rm thin}$, given in (3.5), the

integral in (F.1) can be done analytically, yielding

$$\mathcal{W}_{\mathcal{R}}^{(2)}(x_\perp) = \mathcal{W}_{\mathcal{R}}^{(2),\mathrm{AGZ}}(x_\perp) \equiv -\kappa \left[\gamma + \log\left(\frac{x}{2}\right) + K_0(x)\right], \tag{F.2}$$

where we have defined $x \equiv x_\perp m_D$ and where $K_0(x)$ is the modified Bessel function of the second kind and $\gamma \approx 0.577$ is the Euler gamma constant. Note that $\mathcal{W}_{\mathcal{R}}^{(2)}(x) \to 0$ as $x \to 0$ since $K_0(x) \to -\gamma - \log(x/2)$ as $x \to 0$. The dipole cross-section $v(x_\perp)$ corresponding to (F.2) (see Appendix D and in particular (D.8)) is very similar to that found in Eq. (A11) of Ref. [66] for the case of the Gyulassy-Wang model where the medium consists of static Debye-screened scattering centers. This similarity is not surprising: when Fourier transformed, the screened Yukawa potentials in the Gyulassy-Wang model are similar to $P_{\mathrm{thin}}^{AGZ}(k_\perp)$ of Eq. (3.5), and in particular they agree at large $k_\perp$ where multiple scattering is not important. We therefore find that (F.2) and (A11) of Ref. [66] agree at small $x_\perp$.

Next, we must substitute (F.2) into (2.15) in order to obtain $P^{\mathrm{AGZ}}(k_\perp)$. The angular integral in (2.15) can be performed analytically, yielding the full, L-resummed, probability distribution

$$P(k_\perp) = P^{AGZ}(k_\perp) \equiv \frac{2\pi}{m_D^2} \int_0^\infty dx\, x\, J_0\left(\frac{k_\perp x}{m_D}\right) \times \exp\left[-\kappa\left(\gamma + \log\left(x/2\right) + K_0(x)\right)\right], \tag{F.3}$$

in which only a single integral remains to be evaluated numerically.

In Fig. F-1, we plot the result (F.3) for the L-resummed AGZ distribution for various values of κ. In the middle and lower panels, which are analogous to the middle and lower panels of Fig. 3-3, we show explicitly that the L-resummed AGZ distribution agrees with our full result in the IR, as anticipated. This confirms for us that when we inspect the κ-dependence of $P^{\mathrm{AGZ}}(k_\perp)$ as we do in the top panel, we can trust that at small $k_\perp$ these results agree quantitatively with our full results. The first thing that we see in the top panel is that at $\kappa = 0.1$ the L-resummed result agrees with that for a thin medium, namely $P_{\mathrm{thin}}^{\mathrm{AGZ}}(k_\perp)$, since when the medium is thin

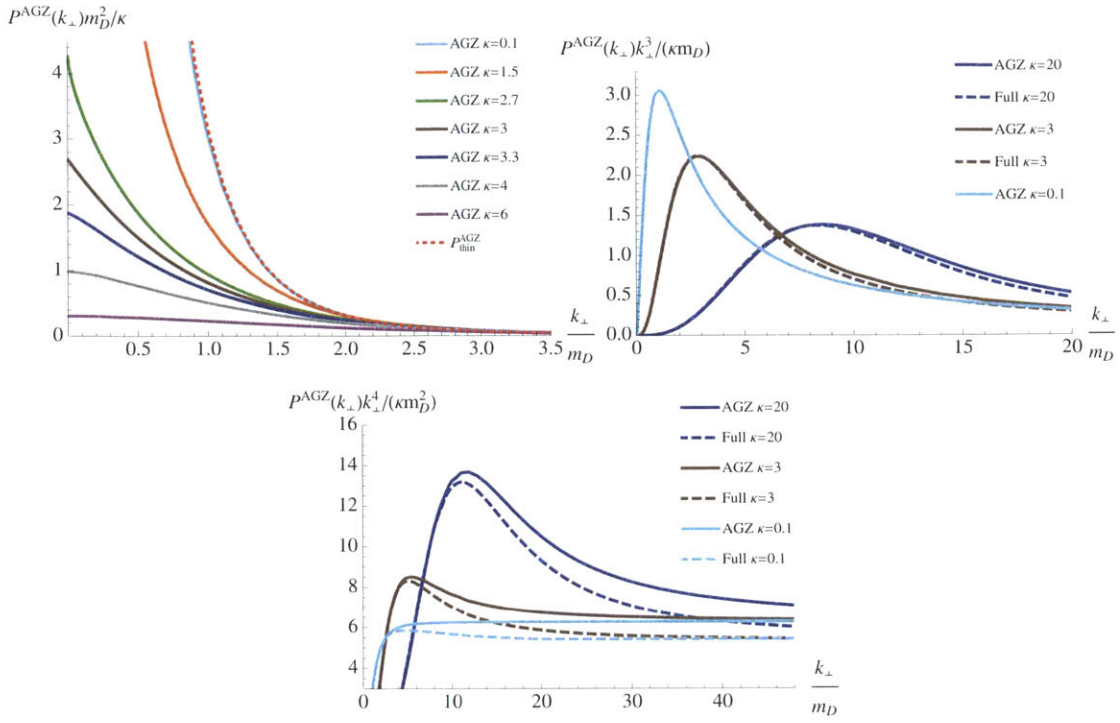

Figure F-1: The solid curves in the top panel show the L-resummed $P^{\rm AGZ}(k_\perp)$ for (top to bottom) $\kappa = 0.1$, 1.5, 2.7, 3, 3.3, 4 and 6. The dashed curve shows $P^{\rm AGZ}_{\rm thin}(k_\perp)$; this curve is κ-independent because we have divided by κ. We see the $k_\perp \to 0$ behavior of $P^{\rm AGZ}(k_\perp)$ changing as κ increases. In the middle and lower panels, both $P^{\rm AGZ}(k_\perp)$ (solid curves) and our full results for $P(k_\perp)$ from the middle and lower panels of Fig. 3.2 (dashed curves) are plotted, multiplied by $k_\perp^3$ and $k_\perp^4$. We see that, as expected, the L-resummed AGZ distribution agrees with our full result in the IR, but not in the UV. All plots are for $g = 0.1$.

there is no need to resum L-enhanced diagrams. Next, by plotting (F.3) for varying κ as in this panel we discover that for $\kappa < 2$, the resummed result $P^{\rm AGZ}(k_\perp)$ diverges as $\kappa \to 0$ while for $\kappa \geq 2$, the resummed result is finite in this limit. Careful inspection of the curves with $\kappa > 2$ shows that for $\kappa = 3$ the probability $P^{\rm AGZ}(k_\perp)$ is linear in $k_\perp$ as $k_\perp \to 0$, for $2 < \kappa < 3$ it grows faster than linear in this limit, for $3 < \kappa < 4$ it grows slower than linear in this limit, and for all $\kappa \geq 4$ the curve is quadratic in $k_\perp$ at small $k_\perp$. We find the same nontrivial κ-dependence of our full results at small $k_\perp$. The advantage of reproducing these results in the L-resummed AGZ distribution (F.3) is that in this simpler setting we can understand them all analytically, as we now explain.

The first step to understanding the κ-dependence of (F.3) at small $k_\perp$ is to divide the x-integration in (F.3) into an integral from $x = 0$ to some $x = x_0$ with x_0 chosen to be very much greater than 1, and an integral from $x = x_0$ to $x = \infty$. The integral over $0 < x < x_0$ yields a result that is analytic as $k_\perp \to 0$, whose leading small-$k_\perp$ dependence includes a constant term and a term quadratic in $k_\perp$. The only place where divergent, or other nonanalytic, behavior can arise as $k_\perp \to 0$ is from the integral over $x_0 < x < \infty$. In the $k_\perp \to 0$ limit, this integral can be evaluated analytically in terms of generalized hypergeometric functions, whose asymptotic behavior determines that as $k_\perp \to 0$ the probability distribution $P^{\rm AGZ}(k_\perp)$ must include a term with the form

$$-\frac{2\pi}{m_D^\kappa}\left(2e^{-\gamma}\right)^\kappa f(\kappa)\, k_\perp^{\kappa-2} \tag{F.4}$$

with

$$f(\kappa) \equiv \frac{\kappa}{2^\kappa}\frac{\Gamma\left(-\frac{\kappa}{2}\right)}{\Gamma\left(\frac{\kappa}{2}\right)} \tag{F.5}$$

for $\kappa \neq 2, 4, 6, \ldots$ and

$$f(\kappa) \equiv \frac{4}{4^{\kappa/2}}\frac{(-1)^{\kappa/2}}{\Gamma(\frac{\kappa}{2})^2}\left(\frac{1}{\kappa} + \psi(\frac{\kappa}{2})\right), \tag{F.6}$$

for $\kappa = 4, 6, 8, \ldots$, where $\Gamma(n)$ and $\psi(n)$ are gamma and digamma functions respectively. The $k_\perp$-dependence of this analytic result explains the $k_\perp \to 0$ behavior of all the curves in the top panel of Fig. F-1. For $\kappa > 4$, the term (F.4) is subleading relative to the regular $k_\perp^2$-dependent term at small $k_\perp$ and so, for $\kappa \geq 4$, $P^{\rm AGZ}(k_\perp)$ is quadratic at small $k_\perp$. For $\kappa < 4$, (F.4) dominates as $k_\perp \to 0$. And, it is linear in $k_\perp$ for $\kappa = 3$, grows nonanalytically and slower (faster) than linear for $3 < \kappa < 4$ ($2 < \kappa < 3$) and diverges for $\kappa < 2$. So, we have a complete analytic understanding of the nontrivial κ-dependence of $P^{\rm AGZ}(k_\perp)$ as $k_\perp \to 0$, and consequently of the same nontrivial κ-dependence of $P(k_\perp)$ that we described in Section 3.2.

We saw in Section 3.2, in particular in Fig. 3-5, that for large enough κ the probability distribution $P(k_\perp)$ is well-approximated as a Gaussian at values of $k_\perp$

that are not too large. Given how similar $P^{\rm AGZ}(k_\perp)$ and $P(k_\perp)$ are at small $k_\perp$, see Fig. F-1, we can conclude that $P^{\rm AGZ}(k_\perp)$ is also well-approximated as a Gaussian at small values of $k_\perp$. Because we have an (almost) analytic understanding of $P^{\rm AGZ}$ in the form (F.3) we can now obtain an (almost) analytic expression for the width of the Gaussians in Fig. 3-5 that describe $P(k_\perp)$ at not too large $k_\perp$.

In order to find the Gaussian approximation $P^{\rm AGZ}(k_\perp) \simeq A_{\rm AGZ}\exp(-a_{\rm AGZ}\,k_\perp^2)$ to $P^{\rm AGZ}(k_\perp)$ at low $k_\perp$, we Taylor expand the logarithm of $P^{\rm AGZ}(k_\perp)$. Recall that $P^{\rm AGZ}(k_\perp)$ is given by (F.3), which we obtained upon resumming length-enhanced diagrams as is necessary at large κ. We write the expansion as

$$\log P^{\rm AGZ}(k_\perp) = \log A_{\rm AGZ} - a_{\rm AGZ}\,k_\perp^2 + \ldots \tag{F.7}$$

and find

$$\begin{aligned} A_{\rm AGZ} &= \int_0^\infty dx\, b_{\rm AGZ}(x)\ , \\ a_{\rm AGZ} &= \frac{1}{4\,A_{\rm AGZ}\,m_D^2}\int_0^\infty dx\, x^2\, b_{\rm AGZ}(x)\ , \end{aligned} \tag{F.8}$$

where we have defined

$$b_{\rm AGZ}(x) \equiv \frac{2\pi}{m_D^2}\,x\exp\left[-\kappa\left(\gamma + \log\left(x/2\right) + K_0(x)\right)\right]\ . \tag{F.9}$$

The expression for $a_{\rm AGZ}$ in (F.8) can be rewritten as

$$a_{\rm AGZ} = \frac{1}{4m_D^2}\frac{\int_0^\infty dx\, x^2\, b_{\rm AGZ}(x)}{\int_0^\infty dx\, b_{\rm AGZ}(x)}\ , \tag{F.10}$$

from which we notice that any x-independent overall factor in $b_{\rm AGZ}(x)$ does not affect the final result for $a_{\rm AGZ}$, i.e. for the width of the Gaussian. We can therefore simplify the expression for $a_{\rm AGZ}$ further, obtaining

$$a_{\rm AGZ}\,m_D^2 = \frac{1}{4}\frac{\int_0^\infty dx\, x^{3-\kappa}\exp\left[-\kappa\,K_0(x)\right]}{\int_0^\infty dx\, x^{1-\kappa}\exp\left[-\kappa\,K_0(x)\right]}\ , \tag{F.11}$$

which is Eq. (3.9).

Appendix G

Simple formula to compute $\hat{q}$

In this Appendix, we derive the simple expression (3.11) for the jet quenching parameter $\hat{q}$, valid for any probability distribution of the form (2.15). We start from the definition of $\hat{q}$ in Eq. (3.10) which, with (2.15), reads

$$\hat{q} = \frac{1}{L} \int \frac{d^2k_\perp}{(2\pi)^2} k_\perp^2 \int d^2x_\perp e^{-ik_\perp \cdot x_\perp} e^{\mathcal{W}_\mathcal{R}^{(2)}} \,. \tag{G.1}$$

By performing the integration over $d^2k_\perp$, we obtain the two dimensional Laplace operator ∇^2 in the transverse plane, acting on a delta function:

$$\hat{q} = -\frac{1}{L} \int d^2x_\perp \left[\nabla^2 \delta^2(\vec{x}_\perp)\right] e^{\mathcal{W}_\mathcal{R}^{(2)}(x_\perp)}. \tag{G.2}$$

We can then integrate the above equation by parts, drop the vanishing boundary terms in our notation, and express $\hat{q}$ as

$$\hat{q} = -\frac{1}{L} \int d^2x_\perp \delta^2(x_\perp) \nabla^2 e^{\mathcal{W}_\mathcal{R}^{(2)}} = -\frac{1}{L} \nabla^2 e^{\mathcal{W}_\mathcal{R}^{(2)}} \Big|_{x_\perp=0} \,. \tag{G.3}$$

We can further simplify this expression. By explicit calculation, the Laplace operator acting on the exponential reads

$$\nabla^2 e^{\mathcal{W}_\mathcal{R}^{(2)}} = e^{\mathcal{W}_\mathcal{R}^{(2)}} \left[\nabla^2 \mathcal{W}_\mathcal{R}^{(2)} + \left(\partial_x \mathcal{W}_\mathcal{R}^{(2)}\right)^2 + \left(\partial_y \mathcal{W}_\mathcal{R}^{(2)}\right)^2\right], \tag{G.4}$$

where we have written the vector in the perpendicular plane as $x_\perp = (x, y)$. The last two terms vanish once they are evaluated at $x_\perp = 0$, since the medium is isotropic in the transverse plane, and we therefore find

$$\hat{q} = -\frac{1}{L} \nabla^2 \mathcal{W}_{\mathcal{R}}^{(2)}\Big|_{x_\perp=0} \ , \tag{G.5}$$

which is the result (3.11) that we used in Sec. 3.

As an example of its use, the result (G.5) can be applied in a straightforward fashion in any case where the physics of momentum broadening can be understood as diffusion in $k_\perp$-space, as for example in the strong-coupling regime that we have discussed in Section V.D. In any such context,

$$\mathcal{W}_{\mathcal{R}}^{(2)} = -D\, x_\perp^2 \ , \tag{G.6}$$

for some diffusion constant D, and applying (G.5) yields

$$\hat{q} = \frac{4D}{L} \ , \tag{G.7}$$

immediately. This is of course what we also find by applying the definition of $\hat{q}$ in Eq. (G.1).

Applying the result (G.5) to the case of a weakly-coupled plasma, as we analyze in this paper, must come with a further subtlety since, as we have discussed in Section V.C, in this case the jet quenching parameter $\hat{q}$ is not well defined! The result of the integration in Eq. (G.1) is logarithmically divergent, meaning that it must be regulated in some way. Similarly, if we simply apply (G.5) to our weak-coupling result (2.18) for $\mathcal{W}_{\mathcal{R}}^{(2)}$ we find a divergent result. To regulate this divergence, we write the result (G.5) in Fourier space, and regulate the momentum integral by imposing a UV cutoff $\Lambda_{\rm UV}$, as discussed in Section V.C. Upon doing so with $\mathcal{W}_{\mathcal{R}}^{(2)}$ given by (2.18), we obtain

$$\hat{q} = \frac{1}{L} \int^{\Lambda_{\rm UV}} \frac{d^2k_\perp}{(2\pi)^2} k_\perp^2 P_{\rm thin}(k_\perp) \ , \tag{G.8}$$

which is the expression (3.13) that we used to evaluate the jet quenching parameter $\hat{q}$ in Section V.C.

Appendix H

Trailing string solution in an equilibrium background

The trailing string solution that describes an infinitely heavy quark being dragged in the $\vec{x}$-direction with velocity $\vec{\beta}$ through an equilibrium plasma with temperature $T_{\text{background}}$ is [82, 83]

$$\vec{x} = \vec{\beta}\left(t + u_h \tan^{-1}\frac{u}{u_h}\right), \tag{H.1}$$

where we have not yet made the transformation (5.5) meaning that the event horizon of the black brane in the bulk is located at $u_h = 1/(\pi T_{\text{background}})$. With this choice of string profile, when we choose worldsheet coordinates of the form (5.10) the temporal constraint (5.13a) becomes a differential equation for t as a function of τ and u that, in the case of a time-independent metric corresponding to a static plasma with temperature $T_{\text{background}}$, has the solution

$$t + u_h \tan^{-1}\frac{u}{u_h} = \tau + u_h\sqrt{\gamma}\tan^{-1}\frac{u\sqrt{\gamma}}{u_h} \tag{H.2}$$

where $\gamma = 1/\sqrt{1-\vec{\beta}^2}$. After we make the transformation (5.5), the trailing string profile (H.1) is given by

$$\vec{x} = \vec{\beta}\left(t + u_h \tan^{-1}\frac{u}{(1+u\xi)u_h}\right) \tag{H.3}$$

and for the case of a static plasma the solution to the temporal constraint equation is now

$$t + u_h \tan^{-1} \frac{u}{(1+u\xi)u_h} = \tau + u_h\sqrt{\gamma} \tan^{-1} \frac{u\sqrt{\gamma}}{(1+u\xi)u_h} \ . \tag{H.4}$$

As we have described in Section 5.1.2, upon making the transformation (5.5) we choose worldsheet coordinates in which $u = \sigma$. This together with the expressions (H.3) and (H.4) give us our initial conditions for X^M, which is to say u, t and $\vec{x}$, as functions of τ and σ.

If all we were interested in doing was dragging a heavy quark through static plasma, there would be nothing to add. The background of interest to us, however, is one where the heavy quark is initially in a region of spacetime filled with static plasma but in which in the future the quark will be slammed by two sheets of energy, incident upon it from the $+z$ and $-z$ directions. As we mentioned in Sec. 5.1.2, at any given early Eddington-Finkelstein time t, even well before the sheets of energy collide on the boundary, the gravitational shocks are already colliding somewhere deep in the bulk. Eddington-Finkelstein coordinates on the worldsheet are advantageous from the point of view of making it possible to solve the evolution equations but from the point of view of specifying the initial conditions this feature is a complication. There are two possible ways to proceed. The route that we have followed in obtaining all the results that we show is to use (H.3) and (H.4) as our initial conditions at all σ, even deep in the bulk, even though deep in the bulk where the gravitational shocks are already colliding at the early t at which we are initializing the string profile the choice (H.4) does not satisfy the temporal constraint equations. The other option is to use (H.3) and then to solve the temporal constraint differential equation numerically, replacing (H.4) by a numerically determined $t(\tau, \sigma)$. Because we are initializing at a time t when the quark at the boundary is in a region of static plasma, these two options yield identical results close to the boundary, where (H.4) itself solves the temporal constraint equation. They are inequivalent deep in the bulk, and indeed there is no one "right answer" for how to initialize the string profile deep in the bulk in Eddington-Finkelstein coordinates. We have checked, however, that these

two options yield identical results for the drag force on the heavy quark, meaning that for our purposes they are equivalent. The reason that the distinction between them is irrelevant is that it arises only deep enough within the bulk that well before the sheets collide at the boundary the region of the string that is affected by these considerations has been enveloped by the event horizon of the black brane. Because of this, the initial violation of the temporal constraint equation (assuming we pursue the first option) and the initial arbitrariness associated with choosing the profile (H.3) where there is no reason to do so (in either the first or second option) are causally disconnected from the boundary. Since the drag force on the heavy quark is computed from the near-boundary asymptotics of the string profile, nothing in this paragraph affects it.

Appendix I

Varying temperature model

We discovered in Section 5.2.1 that when the energy density and pressures of the matter through which the heavy quark is moving change there seems to be a time delay in the response of the drag force experienced by the heavy quark, relative to the way in which the drag force would change if it were given by its value in a static plasma with the same instantaneous energy density or pressure. In this Appendix we shall quantify this time delay in a time-dependent background that is much simpler than the colliding sheets of energy that are our focus throughout the rest of this paper. We shall consider a background that, at all times, is a spatially homogeneous plasma whose properties are exactly as if it is in thermal equilibrium at temperature T, and in particular which always has zero fluid velocity throughout, but by hand we shall make $T(t)$ change with time. This of course violates energy conservation in the boundary theory. It is therefore no surprise that the bulk metric that provides the dual gravitational description of this *ad hoc* setup is not a solution to Einstein's equations. The setup in this Appendix is therefore not a model for anything; it is simply a device with which to evaluate the time delay in the response of the drag force on a heavy quark to a change in the conditions in which the heavy quark finds itself. Note that in this setup there are no spatial gradients of the fluid velocity since $u^\mu = (1, 0, 0, 0)$ at all times. Also, $T_e = T_\perp = T_\parallel = T(t)$ at all times.

The metric that describes a spatially homogeneous plasma with a time-dependent

temperature is given in Eddington-Finkelstein coordinates by (5.4) with

$$\begin{aligned} A &= \left(\left(\frac{1}{u} + \xi(t) \right)^2 f(u,t) - 2\frac{\partial \xi}{\partial t} \right), \\ \Sigma &= \frac{1}{u} + \xi(t), \quad B = F = 0, \end{aligned} \tag{I.1}$$

with

$$f(u,v) = 1 - \left(\frac{u}{(1+u\xi(t))u_h(t)} \right)^4 \tag{I.2}$$

where $u_h(t) = 1/(\pi T(t))$ and where $\xi(t)$ describes the residual diffeomorphism introduced in (5.5). As we discussed there, we fix ξ by demanding that the apparent horizon be at $u = 1$. In this simplified setup, in coordinates in which $\xi = 0$ the apparent horizon is at $u = u_h(t)$ whereas ensuring that it is at $u = 1$ corresponds to choosing

$$\xi(t) = \frac{1}{u_h(t)} - 1 \ , \tag{I.3}$$

which ensures that $f(u = 1, t) = 0$.

We shall choose a time-dependent temperature that starts at $\pi T = \mu$ at early times and ends at $\pi T = 2\mu$ at late times, rising smoothly during a window in time that is $\sim 1/(k\mu)$ wide, with k a parameter. We choose

$$u_h(t) = 1 - \frac{1}{4}\left(1 + \mathrm{erf}(k\, t\, \mu)\right) \ . \tag{I.4}$$

For large values of k, $u_h(t)$ (and therefore $T(t)$) becomes a step function at $t = 0$. In Fig. I-1, we choose $k = 3$. We have plotted the drag force rescaled in such a way that the dashed curve, which is obtained by substituting $T(t)$ into (5.31) and shows what the drag force would be in an equilibrium plasma with the instantaneous temperature $T(t)$, is independent of the quark velocity β and is a plot of $(\pi T(t)/\mu)^2$. We see that the actual drag force, shown as the solid curves, is β-dependent even when rescaled as in the Figure and shows a significant, and somewhat β-dependent, time delay. The temperature of the plasma has risen quite significantly before the drag force begins to rise; once the temperature reaches its final plateau the drag force is only about half

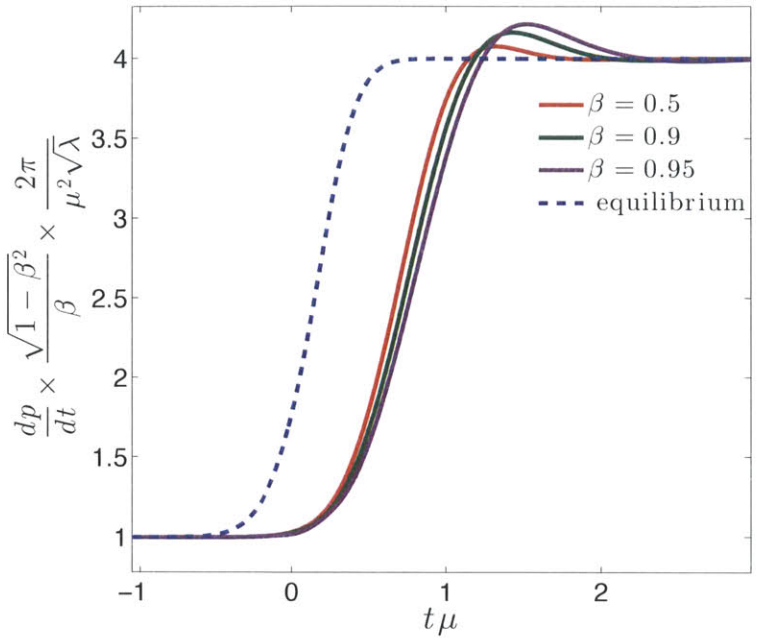

Figure I-1: Drag force, scaled by $\beta\gamma$, for a heavy quark with velocity β moving through a spatially homogeneous plasma with a time dependent temperature $T(t)$ that increases from $\pi T = \mu$ at early times to $\pi T = 2\mu$ at late times and is described by (I.4). The different solid curves show the scaled drag force on quarks with different velocities. The dashed curve is the equilibrium expectation (5.31). Because $T_e = T_\perp = T_\parallel = T(t)$ there is only a single dashed curve.

way up its rise; and, finally, the drag force over-shoots before approaching its new equilibrium value from above.

There are various ways in which we could choose an operational definition of the time delay from the results in Fig. I-1. We shall define the time delay Δt as the delay between the times when the dashed and solid curves cross the midpoint between the initial drag force and the final drag force, i.e. in Fig. I-1 when they cross 2.5. In Fig. I-2 we show how Δt depends on the quark velocity for two different values of k, the parameter that controls the rapidity with which $T(t)$ changes. For both values of k we see that at low velocities there is a time delay of around 0.5, which we note is around $1/(\pi T_{\rm final})$ where $T_{\rm final}$ is the final temperature. And, for both values of k we see that the time delay increases with increasing β in a way that is close to, but not exactly, linear with γ.

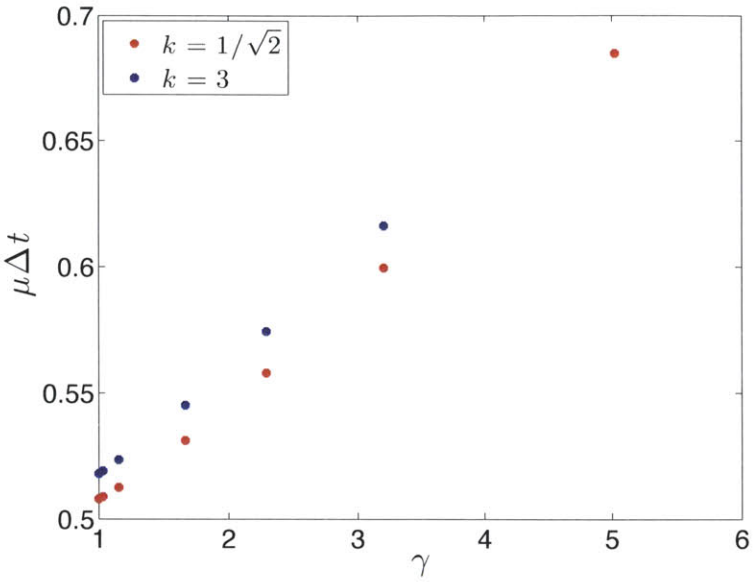

Figure I-2: The delay time Δt, defined from results as in Fig. I-1 as described in the text, as a function of γ for two values of the parameter k that controls the rapidity with which the temperature increases.

From a gravitational perspective, the fact that there is a time delay can be described in qualitative terms as if when the horizon at $u = u_h$ moves the drag force only learns of this at a time that is delayed by of order the light-travel-time for information from the horizon travelling through the bulk to reach the near-boundary region, where the drag on the heavy quark is encoded. If taken literally, this interpretation would suggest that in the setup of this Appendix the time delay should start out around $1/(\pi T_{\text{initial}})$ and then drop to around $1/(\pi T_{\text{final}})$. This interpretation should not be taken too literally, however, because making u_h time dependent makes the entire bulk metric at all u time dependent, not just the metric near the horizon.

Appendix J

Boosted black brane and drag force

Let's consider Lorentz boost transformations on the metric and string solution embedded in the two dimensional world-sheet parametrized by coordinates $\sigma^a = (\tau, \sigma)$. The boosts are parametrized by 4−velocity u^μ so that when the coordinates transform

$$X^M \to \Lambda^M{}_N X^N \tag{J.1}$$

the metric transforms as

$$G_{MN} \to \Lambda_M^A \Lambda_N^B G_{AB} \tag{J.2}$$

with the boost tensors given by

$$\Lambda^M{}_N = \begin{pmatrix} -u_0 & u_x & u_y & u_z & 0 \\ u_x & 1+\frac{u_x^2}{1-u_0} & \frac{u_x u_y}{1-u_0} & \frac{u_x u_z}{1-u_0} & 0 \\ u_y & \frac{u_x u_y}{1-u_0} & 1+\frac{u_y^2}{1-u_0} & \frac{u_y u_z}{1-u_0} & 0 \\ u_z & \frac{u_x u_z}{1-u_0} & \frac{u_y u_z}{1-u_0} & 1+\frac{u_z^2}{1-u_0} & 0 \\ 0 & 0 & 0 & 0 & 1 \end{pmatrix} \tag{J.3}$$

leaving the the radial coordinate r unmodified, and here $u_\mu = \eta_{\mu\nu} u^\nu$.

Under the boost, the canonical momentum fluxes π^a_μ do not just transform as 4−vectors because it is necessary to take into account the change of time coordinate. This is related to the fact, that the force which is associated with the fluxes is not a

4−vector. More specifically, under both Lorentz transformation and the world-sheet re-parametrization $\sigma_0^a \to \sigma^a$ the canonical momentum densities and fluxes transform as

$$\pi_M^a \to \frac{1}{|\det(\partial\vec{\sigma}/\partial\vec{\sigma}_0)|}\frac{\partial\sigma^a}{\partial\sigma_0^b}\Lambda_M^{\ N}\pi_N^b \tag{J.4}$$

In the new boosted reference frame, the τ world sheet variable is associated with the new time coordinate t which implies that when keeping σ unchanged (for simplicity considering the boost in $z-$direction only, $u^x = u^y = 0$),

$$\left.\frac{\partial\tau}{\partial\tau_0}\right|_{\sigma\to\infty} = u^0 + u^z\beta_{0,z} \quad \text{and} \quad \frac{\partial\sigma}{\partial\sigma_0} = 1 \tag{J.5}$$

where we used the fact that for the trailing string solution in the original frame is dragged with velocity $\beta_{0,z}$ at the boundary. Combining Lorentz boost transformation in the z-direction together with world sheet re-parametrization so that time is associated with τ at the boundary, we obtain

$$\begin{aligned} \pi_M^\tau &\to \Lambda_M^{\ N}\pi_N^\tau \\ \pi_M^\sigma &\to \frac{\Lambda_M^{\ N}\pi_N^\sigma}{u^0 + u^z\beta_{0,z}} \end{aligned} \tag{J.6}$$

Therefore the force associated with the canonical momentum flux π_μ^σ transforms as

$$f^M \to \frac{1}{u^0 + u^z\beta_{0,z}}\Lambda^M_{\ N} f^N \tag{J.7}$$

After relating the drag velocities $\vec{\beta}$ and $\vec{\beta}_0$ in the two frames, which for the boost only in the $z-$direction are simply related

$$\beta_\perp = \frac{\beta_{0,\perp}}{u^0 + u^z\beta_{0,z}}, \quad \beta_z = \frac{u^0\beta_{0,z} + u^z}{u^0 + u^z\beta_{0,z}} \tag{J.8}$$

the string profile in the boosted frame as well as force is obtained, which for the static metric are given in eqs. (6.18) and (6.42).

Bibliography

[1] F. D'Eramo, M. Lekaveckas, H. Liu and K. Rajagopal, "Momentum Broadening in Weakly Coupled Quark-Gluon Plasma (with a view to finding the quasiparticles within liquid quark-gluon plasma)," JHEP **1305**, 031 (2013) [arXiv:1211.1922 [hep-ph]].

[2] F. D'Eramo, C. Lee, M. Lekaveckas, H. Liu and K. Rajagopal, "Momentum Broadening in Weakly Coupled Quark-Gluon Plasma," AIP Conf. Proc. **1441**, 895 (2012) [arXiv:1110.5363 [hep-ph]].

[3] P. M. Chesler, M. Lekaveckas and K. Rajagopal, "Heavy quark energy loss far from equilibrium in a strongly coupled collision," JHEP **1310**, 013 (2013) [arXiv:1306.0564 [hep-ph]].

[4] M. Lekaveckas and K. Rajagopal, "Effects of Fluid Velocity Gradients on Heavy Quark Energy Loss," JHEP **1402**, 068 (2014) [arXiv:1311.5577 [hep-th]].

[5] P. Chesler, M. Lekaveckas and K. Rajagopal, "Far-from-equilibrium heavy quark energy loss at strong coupling," Nucl. Phys. A904-905 **2013**, 861c (2013) [arXiv:1211.2186 [hep-th]].

[6] S. Borsanyi, G. Endrodi, Z. Fodor, A. Jakovac, S. D. Katz, S. Krieg, C. Ratti and K. K. Szabo, JHEP **1011**, 077 (2010) [arXiv:1007.2580 [hep-lat]].

[7] M. Cheng, S. Ejiri, P. Hegde, F. Karsch, O. Kaczmarek, E. Laermann, R. D. Mawhinney and C. Miao *et al.*, Phys. Rev. D **81**, 054504 (2010) [arXiv:0911.2215 [hep-lat]].

[8] I. Arsene *et al.* [BRAHMS Collaboration], "Transverse momentum spectra in Au + Au and d + Au collisions at s(NN)**(1/2) = 200-GeV and the pseudorapidity dependence of high p(T) suppression," Phys. Rev. Lett. **91**, 072305 (2003) [arXiv:nucl-ex/0307003]; S. S. Adler *et al.* [PHENIX Collaboration], "Absence of suppression in particle production at large transverse momentum in s(NN)**(1/2) = 200-GeV d + Au collisions," Phys. Rev. Lett. **91**, 072303 (2003) [arXiv:nucl-ex/0306021]; B. B. Back *et al.* [PHOBOS Collaboration], "Centrality dependence of charged hadron transverse momentum spectra in d + Au collisions at s(NN)**(1/2) = 200-GeV," Phys. Rev. Lett. **91**, 072302 (2003) [arXiv:nucl-ex/0306025]; J. Adams *et al.* [STAR Collaboration], "Evidence from d + Au measurements for final-state suppression of high p(T) hadrons in Au + Au collisions at RHIC," Phys. Rev. Lett. **91**, 072304 (2003) [arXiv:nucl-ex/0306024].

[9] G. Aad *et al.* [Atlas Collaboration], "Observation of a Centrality-Dependent Dijet Asymmetry in Lead-Lead Collisions at sqrt(S(NN))= 2.76 TeV with the ATLAS Detector at the LHC," Phys. Rev. Lett. **105**, 252303 (2010) [arXiv:1011.6182 [hep-ex]].

[10] K. Aamodt *et al.* [ALICE Collaboration], "Suppression of Charged Particle Production at Large Transverse Momentum in Central Pb Pb Collisions at $\sqrt{s_{NN}} = 2.76$ TeV," Phys. Lett. B **696**, 30 (2011) [arXiv:1012.1004 [nucl-ex]].

[11] S. Chatrchyan *et al.* [CMS Collaboration], "Observation and studies of jet quenching in PbPb collisions at nucleon-nucleon center-of-mass energy = 2.76 TeV," Phys. Rev. C **84**, 024906 (2011) [arXiv:1102.1957 [nucl-ex]].

[12] S. Chatrchyan *et al.* [CMS Collaboration], "Study of high-pT charged particle suppression in PbPb compared to pp collisions at sqrt(sNN)=2.76 TeV," Eur. Phys. J. C **72**, 1945 (2012) [arXiv:1202.2554 [nucl-ex]].

[13] S. Chatrchyan *et al.* [CMS Collaboration], "Jet momentum dependence of jet quenching in PbPb collisions at sqrt(sNN)=2.76 TeV," Phys. Lett. B **712**, 176 (2012) [arXiv:1202.5022 [nucl-ex]].

[14] S. Chatrchyan *et al.* [CMS Collaboration], "Studies of jet quenching using isolated-photon+jet correlations in PbPb and pp collisions at sqrt(s[NN]) = 2.76 TeV," arXiv:1205.0206 [nucl-ex].

[15] S. Chatrchyan *et al.* [CMS Collaboration], "Measurement of jet fragmentation into charged particles in pp and PbPb collisions at sqrt(s[NN])= 2.76 TeV," arXiv:1205.5872 [nucl-ex].

[16] G. Aad *et al.* [ATLAS Collaboration], "Jet size dependence of single jet suppression in lead-lead collisions at sqrt(s(NN)) = 2.76 TeV with the ATLAS detector at the LHC," arXiv:1208.1967 [hep-ex].

[17] Talks by R. Granier de Cassagnac, G. Roland, M. Spousta, P. Steinberg, G. Veres and B. Wosiek at Quark Matter 2012 conference, Washington, DC, August 2012.

[18] Talks by M. McCumber and T. Sakaguchi at Quark Matter 2012 conference, Washington, DC, August 2012.

[19] M. Gyulassy and X. N. Wang, "Multiple collisions and induced gluon Bremsstrahlung in QCD," Nucl. Phys. B **420**, 583 (1994) [arXiv:nucl-th/9306003].

[20] R. Baier, Y. L. Dokshitzer, A. H. Mueller, S. Peigne and D. Schiff, "Radiative energy loss of high-energy quarks and gluons in a finite volume quark - gluon plasma," Nucl. Phys. B **483**, 291 (1997) [hep-ph/9607355].

[21] R. Baier, Y. L. Dokshitzer, A. H. Mueller, S. Peigne and D. Schiff, "Radiative energy loss and p(T)-broadening of high energy partons in nuclei," Nucl. Phys. B **484**, 265 (1997) [arXiv:hep-ph/9608322].

[22] B. G. Zakharov, "Radiative energy loss of high energy quarks in finite-size nuclear matter and quark-gluon plasma," JETP Lett. **65**, 615 (1997) [arXiv:hep-ph/9704255].

[23] U. A. Wiedemann, "Gluon radiation off hard quarks in a nuclear environment: Opacity expansion," Nucl. Phys. B **588**, 303 (2000) [arXiv:hep-ph/0005129].

[24] M. Gyulassy, P. Levai and I. Vitev, "NonAbelian energy loss at finite opacity," Phys. Rev. Lett. **85**, 5535 (2000) [nucl-th/0005032].

[25] M. Gyulassy, P. Levai and I. Vitev, "Reaction operator approach to non-Abelian energy loss," Nucl. Phys. B **594**, 371 (2001) [arXiv:nucl-th/0006010].

[26] X. F. Guo and X. N. Wang, "Multiple Scattering, Parton Energy Loss and Modified Fragmentation Functions in Deeply Inelastic eA Scattering," Phys. Rev. Lett. **85**, 3591 (2000) [arXiv:hep-ph/0005044].

[27] X. N. Wang and X. F. Guo, "Multiple parton scattering in nuclei: Parton energy loss," Nucl. Phys. A **696**, 788 (2001) [arXiv:hep-ph/0102230].

[28] P. B. Arnold, G. D. Moore and L. G. Yaffe, "Photon emission from ultrarelativistic plasmas," JHEP **0111**, 057 (2001) [hep-ph/0109064]; P. B. Arnold, G. D. Moore and L. G. Yaffe, "Photon emission from quark gluon plasma: Complete leading order results," JHEP **0112** (2001) 009 [hep-ph/0111107]; P. B. Arnold, G. D. Moore and L. G. Yaffe, "Photon and gluon emission in relativistic plasmas," JHEP **0206** (2002) 030 [hep-ph/0204343]; S. Jeon and G. D. Moore, "Energy loss of leading partons in a thermal QCD medium," Phys. Rev. C **71**, 034901 (2005) [hep-ph/0309332]; S. Turbide, C. Gale, S. Jeon and G. D. Moore, "Energy loss of leading hadrons and direct photon production in evolving quark-gluon plasma," Phys. Rev. C **72**, 014906 (2005) [hep-ph/0502248].

[29] C. A. Salgado and U. A. Wiedemann, "Calculating quenching weights," Phys. Rev. D **68**, 014008 (2003) [hep-ph/0302184].

[30] A. Majumder and B. Muller, "Higher twist jet broadening and classical propagation," Phys. Rev. C **77**, 054903 (2008) [arXiv:0705.1147 [nucl-th]].

[31] R. Baier, D. Schiff and B. G. Zakharov, "Energy loss in perturbative QCD," Ann. Rev. Nucl. Part. Sci. **50**, 37 (2000) [arXiv:hep-ph/0002198].

[32] A. Kovner and U. A. Wiedemann, "Gluon radiation and parton energy loss," arXiv:hep-ph/0304151.

[33] M. Gyulassy, I. Vitev, X. N. Wang and B. W. Zhang, "Jet quenching and radiative energy loss in dense nuclear matter," arXiv:nucl-th/0302077.

[34] P. Jacobs and X. N. Wang, "Matter in extremis: Ultrarelativistic nuclear collisions at RHIC," Prog. Part. Nucl. Phys. **54**, 443 (2005) [arXiv:hep-ph/0405125].

[35] J. Casalderrey-Solana and C. A. Salgado, "Introductory lectures on jet quenching in heavy ion collisions," Acta Phys. Polon. B **38**, 3731 (2007) [arXiv:0712.3443 [hep-ph]].

[36] A. Accardi, F. Arleo, W. K. Brooks, D. D'Enterria and V. Muccifora, "Parton Propagation and Fragmentation in QCD Matter," Riv. Nuovo Cim. **032**, 439 (2010) [arXiv:0907.3534 [nucl-th]].

[37] U. A. Wiedemann, "Jet Quenching in Heavy Ion Collisions," arXiv:0908.2306 [hep-ph].

[38] A. Majumder and M. Van Leeuwen, "The theory and phenomenology of perturbative QCD based jet quenching," arXiv:1002.2206 [hep-ph].

[39] C. W. Bauer, S. Fleming and M. E. Luke, "Summing Sudakov logarithms in B $\to$ X/s gamma in effective field theory," Phys. Rev. D **63**, 014006 (2000) [arXiv:hep-ph/0005275]; C. W. Bauer, S. Fleming, D. Pirjol and I. W. Stewart, "An effective field theory for collinear and soft gluons: Heavy to light decays," Phys. Rev. D **63**, 114020 (2001) [arXiv:hep-ph/0011336]; C. W. Bauer and I. W. Stewart, "Invariant operators in collinear effective theory," Phys. Lett. B **516**, 134 (2001) [arXiv:hep-ph/0107001]; C. W. Bauer, D. Pirjol and I. W. Stewart, "Soft-Collinear Factorization in Effective Field Theory," Phys. Rev. D **65**, 054022 (2002) [arXiv:hep-ph/0109045].

[40] A. Idilbi and A. Majumder, "Extending Soft-Collinear-Effective-Theory to describe hard jets in dense QCD media," Phys. Rev. D **80**, 054022 (2009) [arXiv:0808.1087 [hep-ph]];

[41] F. D'Eramo, H. Liu and K. Rajagopal, "Transverse Momentum Broadening and the Jet Quenching Parameter, Redux," Phys. Rev. D **84**, 065015 (2011) [arXiv:1006.1367 [hep-ph]].

[42] G. Ovanesyan and I. Vitev, "An effective theory for jet propagation in dense QCD matter: jet broadening and medium-induced bremsstrahlung," JHEP **1106**, 080 (2011) [arXiv:1103.1074 [hep-ph]]; G. Ovanesyan and I. Vitev, "Medium-induced parton splitting kernels from Soft Collinear Effective Theory with Glauber gluons," Phys. Lett. B **706**, 371 (2012) [arXiv:1109.5619 [hep-ph]].

[43] Z. -t. Liang, X. -N. Wang and J. Zhou, "The Transverse-momentum-dependent Parton Distribution Function and Jet Transport in Medium," Phys. Rev. D **77**, 125010 (2008) [arXiv:0801.0434 [hep-ph]].

[44] R. Baier, A. Kovner and U. A. Wiedemann, "Saturation and parton level Cronin effect: Enhancement versus suppression of gluon production in p-A and A-A collisions," Phys. Rev. D **68**, 054009 (2003) [hep-ph/0305265].

[45] J. L. Albacete, N. Armesto, A. Kovner, C. A. Salgado and U. A. Wiedemann, "Energy dependence of the Cronin effect from nonlinear QCD evolution," Phys. Rev. Lett. **92**, 082001 (2004) [hep-ph/0307179].

[46] D. Kharzeev, Y. V. Kovchegov and K. Tuchin, "Cronin effect and high p(T) suppression in pA collisions," Phys. Rev. D **68**, 094013 (2003) [hep-ph/0307037].

[47] M. Benzke, N. Brambilla, M. A. Escobedo and A. Vairo, "Gauge invariant definition of the jet quenching parameter," arXiv:1208.4253 [hep-ph].

[48] H. Liu, K. Rajagopal and U. A. Wiedemann, "Calculating the jet quenching parameter from AdS/CFT," Phys. Rev. Lett. **97**, 182301 (2006) [hep-ph/0605178].

[49] A. D. Linde, "Infrared Problem in Thermodynamics of the Yang-Mills Gas," Phys. Lett. B **96**, 289 (1980).

[50] O. K. Kalashnikov and V. V. Klimov, "Infrared Behavior Of Green Functions In Yang-mills Theory At Finite Temperatures," Sov. J. Nucl. Phys. **33**, 443 (1981) [Yad. Fiz. **33**, 848 (1980)].

[51] E. Braaten and R. D. Pisarski, "Resummation and Gauge Invariance of the Gluon Damping Rate in Hot QCD," Phys. Rev. Lett. **64**, 1338 (1990); J. Frenkel, J. C. Taylor, "High Temperature Limit of Thermal QCD," Nucl. Phys. **B334**, 199 (1990); E. Braaten, R. D. Pisarski, "Soft Amplitudes in Hot Gauge Theories: A General Analysis," Nucl. Phys. **B337**, 569 (1990); E. Braaten, R. D. Pisarski, "Deducing Hard Thermal Loops From Ward Identities," Nucl. Phys. **B339**, 310-324 (1990); E. Braaten and R. D. Pisarski, "Simple effective Lagrangian for hard thermal loops," Phys. Rev. D **45**, 1827 (1992).

[52] P. B. Arnold and C. Dogan, "QCD Splitting/Joining Functions at Finite Temperature in the Deep LPM Regime," Phys. Rev. D **78**, 065008 (2008) [arXiv:0804.3359 [hep-ph]].

[53] P. B. Arnold and W. Xiao, "High-energy jet quenching in weakly-coupled quark-gluon plasmas," Phys. Rev. D **78**, 125008 (2008) [arXiv:0810.1026 [hep-ph]].

[54] S. Caron-Huot, "O(g) plasma effects in jet quenching," Phys. Rev. D **79**, 065039 (2009) [arXiv:0811.1603 [hep-ph]].

[55] A. Majumder, B. Muller and S. Mrowczynski, "Momentum Broadening of a Fast Parton in a Perturbative Quark-Gluon Plasma," Phys. Rev. D **80**, 125020 (2009) [arXiv:0903.3683 [hep-ph]].

[56] M. Le Bellac, Thermal Field Theory, Cambridge monographs on Mathematical Physics, Cambridge University Press (1996).

[57] K. Kajantie and J. I. Kapusta, "Behavior of Gluons at High Temperature," Annals Phys. **160**, 477 (1985).

[58] R. Kobes, G. Kunstatter and K. W. Mak, "Linear Response Of The Hot Qcd Plasma From The Gluon Propagator," Z. Phys. C **45**, 129 (1989).

[59] H. A. Weldon, "Structure of the gluon propagator at finite temperature," Annals Phys. **271**, 141 (1999) [hep-ph/9701279].

[60] F. T. Brandt and J. Frenkel, "Generalized forward scattering amplitudes in QCD at high temperature," Phys. Rev. D **56**, 2453 (1997) [hep-th/9703165].

[61] O. K. Kalashnikov and V. V. Klimov, "Polarization Tensor in QCD for Finite Temperature and Density," Sov. J. Nucl. Phys. **31**, 699 (1980) [Yad. Fiz. **31**, 1357 (1980)].

[62] O. K. Kalashnikov, "Magnetic mass in hot scalar electrodynamics," Kratk. Soobshch. Fiz. (1996) Nos. 7-8 52-57 [hep-ph/9602308].

[63] H. A. Weldon, "Covariant Calculations at Finite Temperature: The Relativistic Plasma," Phys. Rev. D **26**, 1394 (1982); V. V. Klimov, "Collective Excitations in a Hot Quark Gluon Plasma," Sov. Phys. JETP **55**, 199 (1982) [Zh. Eksp. Teor. Fiz. **82**, 336 (1982)].

[64] M. Laine, "A non-perturbative contribution to jet quenching," arXiv:1208.5707 [hep-ph].

[65] P. Aurenche, F. Gelis and H. Zaraket, "A simple sum rule for the thermal gluon spectral function and applications," JHEP **0205**, 043 (2002) [arXiv:hep-ph/0204146].

[66] U. A. Wiedemann and M. Gyulassy, "Transverse momentum dependence of the Landau-Pomeranchuk-Migdal effect," Nucl. Phys. B **560**, 345 (1999) [hep-ph/9906257].

[67] M. Gyulassy, P. Levai and I. Vitev, "Reaction operator approach to multiple elastic scatterings," Phys. Rev. D **66**, 014005 (2002) [nucl-th/0201078].

[68] P. B. Arnold, "Simple Formula for High-Energy Gluon Bremsstrahlung in a Finite, Expanding Medium," Phys. Rev. D **79**, 065025 (2009) [arXiv:0808.2767 [hep-ph]].

[69] A. Peshier, "QCD running coupling and collisional jet quenching," J. Phys. G G **35**, 044028 (2008).

[70] E. Witten, "Anti-de Sitter space, thermal phase transition, and confinement in gauge theories," Adv. Theor. Math. Phys. **2**, 505 (1998).

[71] O. Aharony, S. S. Gubser, J. M. Maldacena, H. Ooguri and Y. Oz, "Large N field theories, string theory and gravity," Phys. Rept. **323**, 183 (2000) [arXiv:hep-th/9905111].

[72] J. M. Maldacena, "Wilson loops in large N field theories," Phys. Rev. Lett. **80**, 4859 (1998);

[73] S. J. Rey and J. T. Yee, "Macroscopic strings as heavy quarks in large N gauge theory and anti-de Sitter supergravity," Eur. Phys. J. C **22**, 379 (2001);

[74] S. J. Rey, S. Theisen and J. T. Yee, "Wilson-Polyakov loop at finite temperature in large N gauge theory and anti-de Sitter supergravity," Nucl. Phys. B **527**, 171 (1998);

[75] A. Brandhuber, N. Itzhaki, J. Sonnenschein and S. Yankielowicz, "Wilson loops in the large N limit at finite temperature," Phys. Lett. B **434**, 36 (1998);

[76] J. Sonnenschein, "What does the string / gauge correspondence teach us about Wilson loops?," arXiv:hep-th/0003032.

[77] J. Casalderrey-Solana, H. Liu, D. Mateos, K. Rajagopal and U. A. Wiedemann, "Gauge/String Duality, Hot QCD and Heavy Ion Collisions," arXiv:1101.0618 [hep-th].

[78] M. H. Thoma, "New developments and applications of thermal field theory," hep-ph/0010164.

[79] Z. Ligeti, I. W. Stewart, F. J. Tackmann, "Treating the b quark distribution function with reliable uncertainties," Phys. Rev. **D78**, 114014 (2008). [arXiv:0807.1926 [hep-ph]]; I. W. Stewart, F. J. Tackmann and W. J. Waalewijn, "The Quark Beam Function at NNLL," JHEP **1009**, 005 (2010) [arXiv:1002.2213 [hep-ph]].

[80] G. Molière, Z. Naturforsch **3a**, 78 (1948); H. A. Bethe, Phys. Rev. **89**, 1256 (1953).

[81] B. G. Zakharov, Sov. J. Nucl. Phys. **46**, 1 (1987); N. N. Nikolaev and B. G. Zakharov, "Color transparency and scaling properties of nuclear shadowing in deep inelastic scattering," Z. Phys. C **49**, 607 (1991).

[82] C. P. Herzog, A. Karch, P. Kovtun, C. Kozcaz and L. G. Yaffe, "Energy loss of a heavy quark moving through N=4 supersymmetric Yang-Mills plasma," JHEP **0607**, 013 (2006) [hep-th/0605158].

[83] S. S. Gubser, "Drag force in AdS/CFT," Phys. Rev. D **74**, 126005 (2006) [hep-th/0605182].

[84] J. Casalderrey-Solana and D. Teaney, "Heavy quark diffusion in strongly coupled N=4 Yang-Mills," Phys. Rev. D **74**, 085012 (2006) [hep-ph/0605199].

[85] J. M. Maldacena, "The large N limit of superconformal field theories and supergravity," Adv. Theor. Math. Phys. **2**, 231 (1998);

[86] E. Witten, "Anti-de Sitter space and holography," Adv. Theor. Math. Phys. **2**, 253 (1998) [hep-th/9802150].

[87] A. Karch and E. Katz, "Adding flavor to AdS / CFT," JHEP **0206**, 043 (2002) [hep-th/0205236].

[88] P. M. Chesler and L. G. Yaffe, "Holography and colliding gravitational shock waves in asymptotically AdS5 spacetime," Phys. Rev. Lett. **106**, 021601 (2011) [arXiv:1011.3562 [hep-th]].

[89] J. Casalderrey-Solana, M. P. Heller, D. Mateos and W. van der Schee, "From full stopping to transparency in a holographic model of heavy ion collisions," arXiv:1305.4919 [hep-th].

[90] R. A. Janik and R. B. Peschanski, "Asymptotic perfect fluid dynamics as a consequence of Ads/CFT," Phys. Rev. D **73**, 045013 (2006) [hep-th/0512162].

[91] P. M. Chesler and L. G. Yaffe, "Horizon formation and far-from-equilibrium isotropization in supersymmetric Yang-Mills plasma," Phys. Rev. Lett. **102**, 211601 (2009) [arXiv:0812.2053 [hep-th]].

[92] P. M. Chesler and L. G. Yaffe, "Boost invariant flow, black hole formation, and far-from-equilibrium dynamics in N = 4 supersymmetric Yang-Mills theory," Phys. Rev. D **82**, 026006 (2010) [arXiv:0906.4426 [hep-th]].

[93] I. Booth, M. P. Heller and M. Spalinski, "Black brane entropy and hydrodynamics: The Boost-invariant case," Phys. Rev. D **80**, 126013 (2009) [arXiv:0910.0748 [hep-th]].

[94] M. P. Heller, R. A. Janik and P. Witaszczyk, "The characteristics of thermalization of boost-invariant plasma from holography," Phys. Rev. Lett. **108**, 201602 (2012) [arXiv:1103.3452 [hep-th]].

[95] M. P. Heller, D. Mateos, W. van der Schee and D. Trancanelli, "Strong Coupling Isotropization of Non-Abelian Plasmas Simplified," Phys. Rev. Lett. **108**, 191601 (2012) [arXiv:1202.0981 [hep-th]].

[96] W. van der Schee, "Holographic thermalization with radial flow," Phys. Rev. D **87**, 061901 (2013) [arXiv:1211.2218 [hep-th]].

[97] M. P. Heller, D. Mateos, W. van der Schee and M. Triana, "Holographic isotropization linearized," arXiv:1304.5172 [hep-th].

[98] C. Shen, U. Heinz, P. Huovinen and H. Song, "Systematic parameter study of hadron spectra and elliptic flow from viscous hydrodynamic simulations of

Au+Au collisions at $\sqrt{s_{NN}}$ = 200 GeV," Phys. Rev. C **82**, 054904 (2010) [arXiv:1010.1856 [nucl-th]].

[99] P. F. Kolb and U. W. Heinz, "Hydrodynamic description of ultrarelativistic heavy ion collisions," in Hwa, R.C. (ed.) et al.: *Quark gluon plasma* 634-714 (2003) [nucl-th/0305084].

[100] U. W. Heinz, "Thermalization at RHIC," AIP Conf. Proc. **739**, 163 (2005) [nucl-th/0407067].

[101] M. E. Carrington, K. Deja and S. Mrowczynski, "Parton Energy Loss in the Extremly Prolate Quark-Gluon Plasma," PoS ConfinementX , 175 (2012) [arXiv:1301.4563 [hep-ph]].

[102] D. Grumiller and P. Romatschke, "On the collision of two shock waves in AdS(5)," JHEP **0808**, 027 (2008) [arXiv:0803.3226 [hep-th]].

[103] S. de Haro, S. N. Solodukhin and K. Skenderis, "Holographic reconstruction of space-time and renormalization in the AdS / CFT correspondence," Commun. Math. Phys. **217**, 595 (2001) [hep-th/0002230].

[104] K. Skenderis, "Asymptotically Anti-de Sitter space-times and their stress energy tensor," Int. J. Mod. Phys. A **16**, 740 (2001) [hep-th/0010138].

[105] C. P. Herzog, "Energy Loss of Heavy Quarks from Asymptotically AdS Geometries," JHEP **0609**, 032 (2006) [hep-th/0605191].

[106] G. C. Giecold, "Heavy quark in an expanding plasma in AdS/CFT," JHEP **0906**, 002 (2009) [arXiv:0904.1874 [hep-th]].

[107] A. Stoffers and I. Zahed, "Holographic Jets in an Expanding Plasma," Phys. Rev. C **86**, 054905 (2012) [arXiv:1110.2943 [hep-th]].

[108] N. Abbasi and A. Davody, "Moving Quark in a Viscous Fluid," JHEP **1206**, 065 (2012) [arXiv:1202.2737 [hep-th]].

[109] J. D. Bjorken, "Highly Relativistic Nucleus-Nucleus Collisions: The Central Rapidity Region," Phys. Rev. D **27**, 140 (1983).

[110] S. Peigne, P. -B. Gossiaux and T. Gousset, "Retardation effect for collisional energy loss of hard partons produced in a QGP," JHEP **0604**, 011 (2006) [hep-ph/0509185].

[111] A. Guijosa and J. F. Pedraza, "Early-Time Energy Loss in a Strongly-Coupled SYM Plasma," JHEP **1105**, 108 (2011) [arXiv:1102.4893 [hep-th]].

[112] M. Chernicoff, D. Fernandez, D. Mateos and D. Trancanelli, "Drag force in a strongly coupled anisotropic plasma," JHEP **1208**, 100 (2012) [arXiv:1202.3696 [hep-th]].

[113] A. Nata Atmaja and K. Schalm, "Anisotropic Drag Force from 4D Kerr-AdS Black Holes," JHEP **1104**, 070 (2011) [arXiv:1012.3800 [hep-th]].

[114] K. B. Fadafan and H. Soltanpanahi, "Energy loss in a strongly coupled anisotropic plasma," JHEP **1210**, 085 (2012) [arXiv:1206.2271 [hep-th]].

[115] G. D. Moore and D. Teaney, "How much do heavy quarks thermalize in a heavy ion collision?," Phys. Rev. C **71**, 064904 (2005) [hep-ph/0412346].

[116] H. van Hees, V. Greco and R. Rapp, "Heavy-quark probes of the quark-gluon plasma at RHIC," Phys. Rev. C **73**, 034913 (2006) [nucl-th/0508055].

[117] H. van Hees, M. Mannarelli, V. Greco and R. Rapp, "Nonperturbative heavy-quark diffusion in the quark-gluon plasma," Phys. Rev. Lett. **100**, 192301 (2008) [arXiv:0709.2884 [hep-ph]].

[118] Y. Akamatsu, T. Hatsuda and T. Hirano, "Heavy Quark Diffusion with Relativistic Langevin Dynamics in the Quark-Gluon Fluid," Phys. Rev. C **79**, 054907 (2009) [arXiv:0809.1499 [hep-ph]].

[119] R. Rapp and H. van Hees, "Heavy Quarks in the Quark-Gluon Plasma," in R. C. Hwa, X.-N. Wang (eds.) *Quark Gluon Plasma 4*, World Scientific, 111 (2010) [arXiv:0903.1096 [hep-ph]].

[120] W. M. Alberico, A. Beraudo, A. De Pace, A. Molinari, M. Monteno, M. Nardi and F. Prino, "Heavy-flavour spectra in high energy nucleus-nucleus collisions," Eur. Phys. J. C **71**, 1666 (2011) [arXiv:1101.6008 [hep-ph]].

[121] R. Baier, P. Romatschke, D. T. Son, A. O. Starinets and M. A. Stephanov, "Relativistic viscous hydrodynamics, conformal invariance, and holography," JHEP **0804**, 100 (2008) [arXiv:0712.2451 [hep-th]].

[122] S. Bhattacharyya, V. EHubeny, S. Minwalla and M. Rangamani, "Nonlinear Fluid Dynamics from Gravity," JHEP **0802**, 045 (2008) [arXiv:0712.2456 [hep-th]].

[123] J. P. Boyd, *Chebyshev and Fourier spectral methods.* Dover, 2nd ed. (2001).

[124] E. Caceres and A. Guijosa, "On Drag Forces and Jet Quenching in Strongly Coupled Plasmas," JHEP **0612**, 068 (2006) [hep-th/0606134].

[125] U. Gursoy, E. Kiritsis, G. Michalogiorgakis and F. Nitti, "Thermal Transport and Drag Force in Improved Holographic QCD," JHEP **0912**, 056 (2009) [arXiv:0906.1890 [hep-ph]].

[126] E. Nakano, S. Teraguchi and W. -Y. Wen, "Drag force, jet quenching, and AdS/QCD," Phys. Rev. D **75**, 085016 (2007) [hep-ph/0608274].

[127] H. Liu, K. Rajagopal and Y. Shi, "Robustness and Infrared Sensitivity of Various Observables in the Application of AdS/CFT to Heavy Ion Collisions," JHEP **0808**, 048 (2008) [arXiv:0803.3214 [hep-ph]].

[128] B. Wu and P. Romatschke, "Shock wave collisions in AdS5: approximate numerical solutions," Int. J. Mod. Phys. C **22**, 1317 (2011) [arXiv:1108.3715 [hep-th]].

[129] P. Romatschke and J. D. Hogg, "Pre-Equilibrium Radial Flow from Central Shock-Wave Collisions in AdS5," arXiv:1301.2635 [hep-th].

[130] S. S. Gubser, S. S. Pufu and A. Yarom, "Entropy production in collisions of gravitational shock waves and of heavy ions," Phys. Rev. D **78**, 066014 (2008) [arXiv:0805.1551 [hep-th]].

[131] L. Alvarez-Gaume, C. Gomez, A. Sabio Vera, A. Tavanfar and M. A. Vazquez-Mozo, "Critical formation of trapped surfaces in the collision of gravitational shock waves," JHEP **0902**, 009 (2009) [arXiv:0811.3969 [hep-th]].

[132] S. Lin and E. Shuryak, "Grazing Collisions of Gravitational Shock Waves and Entropy Production in Heavy Ion Collision," Phys. Rev. D **79**, 124015 (2009) [arXiv:0902.1508 [hep-th]].

[133] J. L. Albacete, Y. V. Kovchegov and A. Taliotis, "Asymmetric Collision of Two Shock Waves in AdS(5)," JHEP **0905**, 060 (2009) [arXiv:0902.3046 [hep-th]].

[134] Y. L. Dokshitzer and D. E. Kharzeev, "Heavy quark colorimetry of QCD matter," Phys. Lett. B **519**, 199 (2001) [hep-ph/0106202].

[135] A. Adare *et al.* [PHENIX Collaboration], "Energy Loss and Flow of Heavy Quarks in Au+Au Collisions at s(NN)**(1/2) = 200-GeV," Phys. Rev. Lett. **98**, 172301 (2007) [nucl-ex/0611018].

[136] E. Caceres and A. Guijosa, "Drag force in charged N=4 SYM plasma," JHEP **0611**, 077 (2006) [hep-th/0605235].

[137] T. Matsuo, D. Tomino and W. -Y. Wen, "Drag force in SYM plasma with B field from AdS/CFT," JHEP **0610**, 055 (2006) [hep-th/0607178].

[138] P. Talavera, "Drag force in a string model dual to large-N QCD," JHEP **0701**, 086 (2007) [hep-th/0610179].

[139] S. S. Gubser, "Comparing the drag force on heavy quarks in N=4 super-Yang-Mills theory and QCD," Phys. Rev. D **76**, 126003 (2007) [hep-th/0611272].

[140] G. Bertoldi, F. Bigazzi, A. L. Cotrone and J. D. Edelstein, "Holography and unquenched quark-gluon plasmas," Phys. Rev. D **76**, 065007 (2007) [hep-th/0702225].

[141] C. Hoyos-Badajoz, "Drag and jet quenching of heavy quarks in a strongly coupled N=2* plasma," JHEP **0909**, 068 (2009) [arXiv:0907.5036 [hep-th]].

[142] F. Bigazzi, A. L. Cotrone, J. Mas, A. Paredes, A. V. Ramallo and J. Tarrio, "D3-D7 Quark-Gluon Plasmas," JHEP **0911**, 117 (2009) [arXiv:0909.2865 [hep-th]].

[143] P. M. Chesler and L. G. Yaffe, "Numerical solution of gravitational dynamics in asymptotically anti-de Sitter spacetimes," arXiv:1309.1439 [hep-th].

[144] G. Policastro, D. T. Son and A. O. Starinets, "The Shear viscosity of strongly coupled N=4 supersymmetric Yang-Mills plasma," Phys. Rev. Lett. **87**, 081601 (2001) [hep-th/0104066].

[145] P. Kovtun, D. T. Son and A. O. Starinets, "Holography and hydrodynamics: Diffusion on stretched horizons," JHEP **0310**, 064 (2003) [hep-th/0309213].

[146] A. Buchel and J. T. Liu, "Universality of the shear viscosity in supergravity," Phys. Rev. Lett. **93**, 090602 (2004) [hep-th/0311175].

[147] P. Kovtun, D. T. Son and A. O. Starinets, "Viscosity in strongly interacting quantum field theories from black hole physics," Phys. Rev. Lett. **94**, 111601 (2005) [hep-th/0405231].

[148] S. Bhattacharyya, V. E. Hubeny, R. Loganayagam, G. Mandal, S. Minwalla, T. Morita, M. Rangamani and H. S. Reall, "Local Fluid Dynamical Entropy from Gravity," JHEP **0806**, 055 (2008) [arXiv:0803.2526 [hep-th]].

[149] N. Abbasi and A. Davody, "Moving Quark in a General Fluid Dynamical Flow," arXiv:1310.4105 [hep-th].

[150] H. Liu, K. Rajagopal and U. A. Wiedemann, "Wilson loops in heavy ion collisions and their calculation in AdS/CFT," JHEP **0703**, 066 (2007) [hep-ph/0612168].

[151] J. Casalderrey-Solana and D. Teaney, "Transverse Momentum Broadening of a Fast Quark in a N=4 Yang Mills Plasma," JHEP **0704**, 039 (2007) [hep-th/0701123].

[152] S. S. Gubser, "Symmetry constraints on generalizations of Bjorken flow," Phys. Rev. D **82**, 085027 (2010) [arXiv:1006.0006 [hep-th]].

[153] S. S. Gubser, "Complex deformations of Bjorken flow," Phys. Rev. C **87**, 014909 (2013) [arXiv:1210.4181 [hep-th]].

[154] P. M. Chesler and K. Rajagopal, "Jet quenching in strongly coupled plasma," arXiv:1402.6756 [hep-th].